APPLIED COMPUTATIONAL ELECTROMAGNETICS SOCIETY JOURNAL

October 2016
Vol. 31 No. 10
ISSN 1054-4887

The ACES Journal is abstracted in INSPEC, in Engineering Index, DTIC, Science Citation Index Expanded, the Research Alert, and to Current Contents/Engineering, Computing & Technology.

The illustrations on the front cover have been obtained from the research groups at the Department of Electrical Engineering, The University of Mississippi.

THE APPLIED COMPUTATIONAL ELECTROMAGNETICS SOCIETY

JOURNAL

Vol. 31 No. 10 October 2016

TABLE OF CONTENTS

Numerical Simulation of High Electron Mobility Transistors based on the Spectral Element Method

Feng Li [1], Qing H. Liu [2], and David P. Klemer [3]

[1] Department of Electrical and Computer Engineering
University of Idaho, Moscow, ID 83844, USA
fengli@uidaho.edu

[2] Department of Electrical and Computer Engineering
Duke University, Durham, NC 27708, USA
qhliu@ee.duke.edu

[3] K2 BioMicrosystems, LLC, Geneva, IL 60134, USA
david.klemer@k2biomicrosystems.com

Abstract **─** The spectral element method (SEM) is implemented for the numerical simulation of high electron mobility transistors (HEMTs) through a self-consistent solution of the Schrödinger-Poisson equations. The electron conduction band structure and electron density distribution are calculated and plotted, and results compared to those based on methods utilizing a finite-difference approach. Simulation accuracy and efficiency are analyzed and compared with traditional finite difference method (FDM). DC current-voltage (I-V) characteristics for the HEMT structure are simulated, based on a quasi-2D current model. The SEM approach offers advantages in speed and efficiency over FDM, while yielding results which conform well to reported experimental results. These advantages are particularly important for compound heterojunction devices with complex material profiles, for which FDM methods may be inefficient and computationally slow.

Index Terms **─** Heterojunction, Schrödinger equation, spectral element method, transistor.

I. INTRODUCTION

High Electron Mobility Transistors (HEMTs) – also referred to as modulation-doped FETs (MODFETs), or heterostructure FETs (HFETs) – are field-effect transistors which utilize a channel region formed by a heterojunction of (typically III-V) materials having different band gaps, in contrast to the conventional MOSFET channel formed as a three-dimensional region of doped semiconductor. The characteristics of the HEMT two-dimensional electron gas (2DEG) within the channel are typically studied by solving the Poisson-Schrödinger equations in a self-consistent matter, using various techniques such as the finite difference method [1], finite element method [2], and multigrid method [3], among others. HEMTs and related heterojunction solid-state devices can have highly complex material profiles with very small dimensions (on the scale of angstroms); accordingly, traditional numerical methods may be numerically inefficient and computationally slow, limiting their usefulness in device/circuit design and analysis applications.

The spectral element method (SEM) is a high-order finite element method which combines the advantages of the finite element method and the spectral method, resulting in computational speed advantages – by two to three orders of magnitude – when compared to conventional finite difference methods [4]. Furthermore, application of the spectral element method can result in high accuracy in numerical simulations with reasonable computational effort.

Our present research suggests that, to date, few efforts have been made to apply the spectral element method to the simulation of widely-used semiconductor devices such as the HEMT device. In this work we develop a spectral element method approach for the simulation of the HEMT structure. Although the implementation of the SEM is more complex than that of the finite difference method, we demonstrate that improvements in computational accuracy and efficiency are highly significant. This will be illustrated through comparison with computational results using the finite difference method and analysis of relative L_2 errors, (i.e., the root mean square of the error components). In addition, a quasi-two-dimensional scheme is used to study current-voltage characteristics of the HEMT device model in the triode region, based on the electron density distribution calculated from the Schrödinger-Poisson equations describing the HEMT structure,

Submitted On: November 3, 2015
Accepted On: August 18, 2016

demonstrating the further advantage of the SEM approach for device/circuit modeling and analysis.

II. THE SCHRÖDINGER-POISSON EQUATIONS

Given the idealized two-dimensional nature of the 2DEG, a quantum mechanical approach must be incorporated into the simulation in order to accurately represent carrier motion. Accordingly, the one-dimensional, single-electron, time-independent Schrödinger equation (TISE) applies:

$$-\frac{\hbar^2}{2}\frac{d}{dx}\left(\frac{1}{m^*(x)}\frac{d}{dx}\right)\psi(x)+V(x)\psi(x)=E\psi(x), \quad (1)$$

where ψ is the wave function, E represents energy, V is potential energy, $\hbar$ is Planck's constant over 2π, and m^* is the effective mass for the electron.

As is typical in semiconductor device modeling, we assume that permittivity is independent of time, and that polarization due to mechanical forces is negligible. Accordingly, the one dimensional Poisson equation is written as:

$$\frac{d}{dx}\left(\epsilon_0\epsilon_r(x)\frac{d}{dx}\right)\phi(x)=-q[N_D^+(x)-n(x)]=-\rho(x), \quad (2)$$

where ϵ_r is the relative dielectric constant, ϵ_0 is the vacuum permittivity, ϕ is the electrostatic potential, n is the electron density distribution, and N_D^+ is the ionized donor concentration. The relationship between N_D^+ and the donor concentration N_D is given by:

$$N_D^+(x)=\frac{N_D(x)}{1+2\exp\left[\frac{E_f-(V-E_D)}{k_BT}\right]}, \quad (3)$$

where E_D is the donor energy level, k_B is Boltzmann's constant, and E_f is the energy of the Fermi level.

The electron density n includes the subband electron density n_{2D} and the bulk electron density n_{3D} [5]:

$$n=n_{2D}+n_{3D}, \quad (4)$$

and the subband electron density can be expressed as:

$$\mathrm{n_{2D}(x)}=\sum_{\mathrm{j=1}}^{\mathrm{m}}\left|\psi_{\mathrm{j}}(\mathrm{x})\right|^2\mathrm{n_j}, \quad (5)$$

where m is the number of bound states, and n_j represents the electron occupation for each state, expressed as [1]:

$$n_j=\frac{m^*kT}{\pi\hbar^2}ln\left[1+exp\left(\frac{E_f-E_j}{k_BT}\right)\right]. \quad (6)$$

The 3-D bulk electron density can be expressed as [6]:

$$n_{3D}(x)=\frac{(2m^*)^{\frac{3}{2}}}{2\pi^2\hbar^3}\int_V^\infty\frac{(E-V)^{\frac{1}{2}}dE}{1+exp\left[\frac{(E-V_f)}{k_BT}\right]}, \quad (7)$$

where the potential energy V may be related to the electrostatic potential ϕ through the equation:

$$V(x)=-q\phi(x)+\Delta E_c(x), \quad (8)$$

where ΔE_c is the conduction band offset at the heterointerface.

III. NORMALIZATION AND THE STURM-LIOUVILLE DIFFERENTIAL EQUATION

The Schrödinger equation can be normalized in one dimension as [7]:

$$\left[-\frac{1}{\pi^2}\frac{d}{d\tilde{x}}\left(\frac{1}{m_r^*(\tilde{x})}\frac{d}{d\tilde{x}}\right)+\tilde{V}(\tilde{x})\right]\psi(\tilde{x})=\tilde{E}\psi(\tilde{x}), \quad (9)$$

where $\tilde{x}=\frac{x}{d_0}$, $\tilde{V}(x)=\frac{V(x)}{E_1}=\frac{[V_h(x)-q\phi]}{E_1}$, $\tilde{E}=\frac{E}{E_1}$, $E_1=\frac{\pi^2\hbar^2}{2m^*(0)d_0^2}$, $m_r^*(\tilde{x})=m^*(x)/m^*(0)$, with d_0 a reference thickness, e.g., the AlGaAs spacer thickness in the HEMT structure.

The one dimensional Poisson equation can be normalized as:

$$\frac{d}{d\tilde{x}}\left(\epsilon_r(\tilde{x})\frac{d}{d\tilde{x}}\right)\phi(\tilde{x})=-\tilde{\rho}(\tilde{x}), \quad (10)$$

where $\epsilon_r(\tilde{x})=\frac{\epsilon_0\epsilon_r(x)}{\epsilon(0)}$ and $\tilde{\rho}(\tilde{x})=\frac{d_0^2}{\epsilon(0)}\rho(x)$.

These normalized Schrödinger and Poisson equations can be treated as special forms of the Sturm-Liouville differential equation:

$$\left[-\frac{d}{d\tilde{x}}\left(\eta(\tilde{x})\frac{d}{d\tilde{x}}\right)+\tilde{V}(\tilde{x})\right]u(\tilde{x})=\tilde{E}u(\tilde{x})+\tilde{\rho}(\tilde{x}), \quad (11)$$

which becomes the Schrödinger equation for $\tilde{\rho}(\tilde{x})=0$ and $\eta(\tilde{\boldsymbol{x}})=\frac{1}{\pi^2m_r^*(\tilde{x})}$, and the Poisson equation for $\tilde{V}(\tilde{x})=0$, $\tilde{E}=0$, and $\eta(\tilde{x})=\epsilon_r(\tilde{x})$.

Finally, multiplying the above equation by a time-independent test function v on both sides, and integrating the equation over the spatial domain Ω, a weak formulation of the Sturm-Liouville differential equation can be obtained:

$$\int_\Omega\left(\eta\frac{du}{d\tilde{x}}\right)\cdot\frac{dv}{d\tilde{x}}d\tilde{x}+\int_\Omega\tilde{V}uvd\tilde{x}=\int_\Omega\tilde{E}uvd\tilde{x}+\int_\Omega\tilde{\rho}vd\tilde{x}. \quad (12)$$

IV. DISCRETIZATION AND MATRIX FORMULATION

One characteristic of the spectral element method is adopted from the finite element method, i.e., the domain under study is divided into K elements. In implementing this division, the spatial location of any semiconductor device inhomogeneity, e.g., a material heterojunction, must be considered in order to avoid an ambiguity which occurs when different materials (e.g., AlGaAs and GaAs) appear within a single element of the numerical grid. After discretization into elements, integrations involved in the original equations may be performed individually on each element, specifically:

$$\int_{\Omega_k}\left(\eta\frac{du}{d\tilde{x}}\right)\cdot\frac{dv}{d\tilde{x}}d\tilde{x}+\int_{\Omega_k}\tilde{V}uvd\tilde{x}=\int_{\Omega_k}\tilde{E}uvd\tilde{x}+\int_{\Omega_k}\tilde{\rho}vd\tilde{x}, \quad (13)$$

for $k=1,\ldots,K$.

A mathematical mapping is then implemented, and a global physical coordinate $x\in[x_k,x_{k+1}]$ for each element K is mapped into a local coordinate $\xi\in\Lambda=[-1,1]$ for the Gauss-Lobatto-Legendre (GLL) integration quadrature. The mapping function takes the form of:

$$x(\xi)=x_k+\Delta x\frac{\xi+1}{2}, \quad (14)$$

where $\Delta x=x_{k+1}-x_k$ is the length of element Ω_k, and

x_k and x_{k+1} represent respectively the left and right endpoints of element Ω_k.

As usual, this coordinate transformation requires the inclusion of the so-called Jacobian J_k within the integrand:

$$\int_{\Omega_k} f(x)dx = \int_{\Lambda} f^{(k)}(\xi)\frac{dx^{(k)}}{d\xi}d\xi = \int_{-1}^{1} f^{(k)}(\xi)J_k d\xi, \tag{15}$$

where the integrand function $f(x)$ is an arbitrary function and the superscript (k) denotes the restriction of $f(x)$ to element k. $J_k = \frac{dx^{(k)}}{d\xi} = \frac{\Delta x^{(k)}}{2}$ is the Jacobian for the k^{th} element. To perform the integration over Λ, GLL quadrature is applied, reducing the integral to a finite weighted sum:

$$\int_{\Lambda} f(\xi)\, d\xi \approx \sum_{i=0}^{N} w_i f(\xi_i), \tag{16}$$

where w_i represents the weights of the GLL quadrature.

Following domain decomposition, a GLL interpolation scheme is applied to the function u in the one-dimensional Sturm-Liouville differential equation above, applied to each element. A test function v is also defined:

$$u^{(k)}(\tilde{x}) = \sum_{j=0}^{N} u^{(k)}(\tilde{x}_j)b_j^{(k)}(\tilde{x}), \tag{17}$$

$$v_i^{(k)}(\tilde{x}) = b_i^{(k)}(\tilde{x}), \tag{18}$$

where $b_j\ (\tilde{x})$ represents the N$^{\text{th}}$-order GLL interpolation polynomial:

$$b_j(x) = \frac{-1}{N(N+1)L_N(\tilde{x}_j)}\frac{(1-\tilde{x}^2)L_N{'}(\tilde{x})}{\tilde{x}-\tilde{x}_j}, \tag{19}$$

in which L_N represents the Legendre polynomial of the Nth order, and L_N' its derivative.

Finally, the Sturm-Liouville differential equation can be transformed to:

$$\begin{gathered}\sum_{j=0}^{N}\left\{u^{(k)}(\xi_j)\cdot\sum_{i=0}^{N}\sum_{l=0}^{N}\left[\frac{db_i^{(k)}(\xi_l)}{d\xi}\frac{db_j^{(k)}(\xi_l)}{d\xi}\cdot\right.\right. \\ w_l^{(k)}\eta(\xi_l)\cdot\frac{1}{J_k}+\tilde{V}(\xi_l)b_i^{(k)}(\xi_l)b_j^{(k)}(\xi_l)\cdot \\ \left.\left. w_l^{(k)}\eta(\xi_l)\cdot J_k\right]\right\} = \sum_{j=0}^{N}\left\{u^{(k)}(\xi_j)\cdot\right. \\ \sum_{i=0}^{N}\sum_{l=0}^{N}\left[\tilde{E}\cdot b_i^{(k)}(\xi_l)b_j^{(k)}(\xi_l)\cdot w_l^{(k)}\eta(\xi_l)\cdot\right. \\ \left.\left.J_k\right]\right\}+\sum_{i=0}^{N}\sum_{l=0}^{N}\left[b_i^{(k)}(\xi_l)\cdot w_l^{(k)}\tilde{\rho}(\xi_l)\cdot J_k\right],\end{gathered} \tag{20}$$

which can be written succinctly in matrix notation as:

$$\boldsymbol{A}U = \lambda\boldsymbol{B}U + \hat{f}(\Phi). \tag{21}$$

As mentioned earlier, the Sturm-Liouville equation reduces to the Schrödinger equation for $\tilde{\rho} \equiv 0$, which can be written in the matrix form:

$$\boldsymbol{A}\Psi = \lambda\boldsymbol{B}\Psi, \tag{22}$$

where $\boldsymbol{A}$ is the stiffness matrix, $\boldsymbol{B}$ is the diagonal matrix by virtue of the quadrature, and Ψ is the wavefunction to be determined.

Since the matrix $\boldsymbol{B}$ is a diagonal matrix, equation (22) can be written as a regular eigenvalue problem, which can be solved more efficiently:

$$\widetilde{\boldsymbol{A}}\widetilde{\Psi} = \lambda\widetilde{\Psi}, \tag{23}$$

where $\widetilde{\boldsymbol{A}} = \boldsymbol{B}^{-1/2}\boldsymbol{A}\boldsymbol{B}^{-1/2}$, and $\widetilde{\Psi} = \boldsymbol{B}^{1/2}\Psi$.

Similarly, the Sturm-Liouville equation reduces to the Poisson equation for $\tilde{V} = 0$ and $\tilde{E} = 0$, which can also be expressed in matrix form:

$$\boldsymbol{A}\Phi = \hat{f}(\Phi). \tag{24}$$

This equation can be solved using Newton-Raphson iteration in the usual manner:

$$\Phi^{(n+1)} = \Phi^{(n)} - \left[\boldsymbol{A} - \frac{\partial\hat{f}\left(\Phi_i^{(n)}\right)}{\partial\Phi_j}\right]^{-1}\left(\boldsymbol{A}\Phi^{(n)} - \hat{f}\left(\Phi^{(n)}\right)\right), \tag{25}$$

where the index n denotes the nth iteration.

V. BOUNDARY CONDITIONS

At this point, we consider a typical AlGaAs/GaAs HEMT structure, with the conduction band profile schematically shown in Fig. 1. When solving the Poisson equation for HEMTs, we may choose $E_f = 0$; the electrostatic potential at the gate ($x = 0$) is determined by the Schottky barrier height and the applied gate voltage: $\phi(x_0) = \phi_{ms} - V_{gate}$. At the gate ($x = 0$), $\phi(x_0) = \phi_0$, the value of the electrostatic potential applied to the HEMT gate, a function of the choice of Fermi level E_f.

Intrinsic to the derivation of the weak formulation, Neumann-type boundary conditions are naturally included for the Schrödinger equation in the spectral element method; this is a significant advantage of the SEM approach for solving the Schrödinger equation, as compared with the FDM approach. In contrast, with FDM, the process of handling Neumann-type boundary conditions for the Schrödinger equation is awkward and requires significant numerical effort.

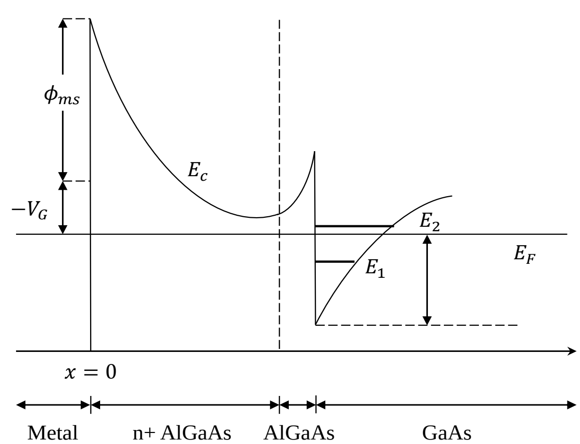

Fig. 1. Conduction band profile for a typical HEMT device.

VI. ELECTRON CONDUCTION BAND AND ELECTRON DENSITY DISTRIBUTION

The physical parameters of a typical AlGaAs/GaAs HEMT device used for numerical testing are summarized in Table 1 below. The device consists of a doped

$Al_{0.3}Ga_{0.7}As$ layer, 20 nm in depth, with a doping density of $3 \times 10^{18}/cm^3$, above an undoped $Al_{0.3}Ga_{0.7}As$ barrier (spacer) layer, 5 nm in depth, positioned above a deep (175 nm) GaAs buffer layer.

Figure 2 illustrates computational results for the electron conduction band energy and electron density distribution with no external bias, with results shown using both FDM- and SEM-based simulations.

Table 1: HEMT physical parameters used for simulation

Material	x	Thickness (Å)	Doping (/cm^3)	Relative Dielectric Constant	Effective Mass (m_0)
n+ Al_xGa_{1-x} As	0.3	200	3E+18	12.2	0.092
Al_xGa_{1-x} As	0.3	50	0	13.1	0.092
GaAs	0	1750	0	13.1	0.067

x represents the Al mole fraction for the Al_xGa_{1-x} As material; m_0 is the effective mass for electrons.

The expected quantum well at the heterojunction (x=250 Angstroms) is clearly evident, as is the accumulation of electron charge carriers (the 2DEG) in the region of the quantum well. The electron distribution "spills out" slightly into the material above the heterojunction ($x < 250$ Angstroms), illustrating the need for an undoped spacer layer to avoid Coulombic interactions between electrons and ionized dopant atoms. It can be seen that FDM and SEM simulations provide consistent results with regard to electron conduction band energy and electron density distribution, supporting the validity of the SEM implementation for numerical solution of the Schrödinger-Poisson equation.

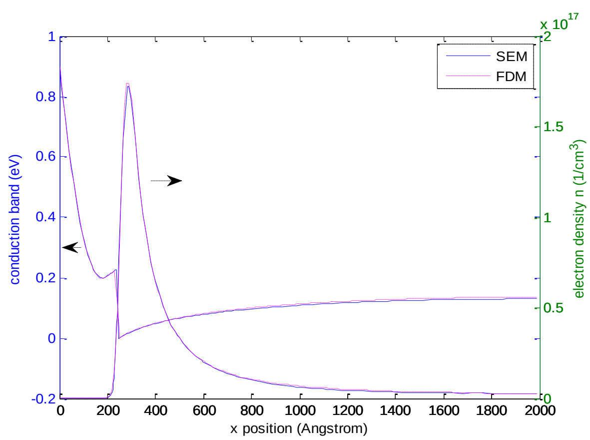

Fig. 2. Conduction band energy value and electron density distribution for the HEMT device of Table 1, calculated from SEM and FDM simulations.

VII. SIMULATION EFFICIENCY AND ACCURACY ANALYSIS

Visual comparisons of graphically plotted solutions (e.g., in Fig. 2) are qualitatively helpful, but lack quantitative rigor. One formal quantitative metric would be the rate of numerical convergence as a function of an increasing number of unknowns. The comparison of simulation time is also useful. Figure 3 shows a comparison of error as a function of simulation CPU time for FDM and SEM. It can be seen that, to reach similar accuracy, SEM is nearly 40 times faster than FDM for this one dimensional simulation.

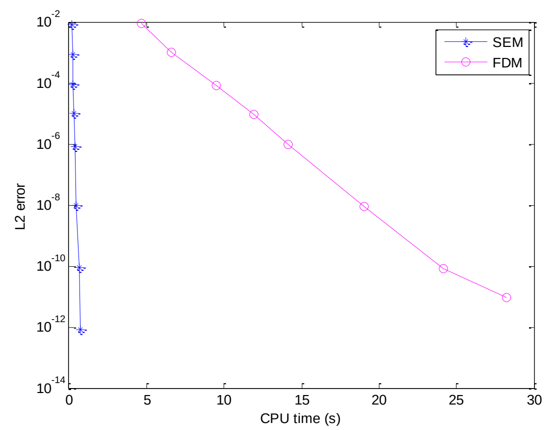

Fig. 3. Error as a function of CPU time for FDM and SEM.

Given that computational (CPU) time is directly related to the number of nodes defined for the computer simulation, we can also study L_2 errors as a function of grid size (i.e., number of nodes) in lieu of CPU time. Furthermore, instead of directly using grid size in a direction along an axis perpendicular to the device surface, the parameter number of points per wavelength (PPW) is used for normalization.

Figure 4 shows relative L_2 error for a simulated static potential computed using the FDM approach, as a function of PPW. It is apparent that L_2 error drops below approximately 0.5% if a minimum of 100 points-per-wavelength are chosen for the FDM simulation. In contrast, the SEM-based approach (with GLL order of 2) requires only 3 points-per-wavelength to achieve this level of accuracy, as shown in Fig. 5, demonstrating a significant improvement in efficiency and accuracy over the FDM approach. It is also apparent that L_2 error decreases approximately linearly with increases in PPW, as evident in the log-log graphs for both FDM- and SEM-based computational approaches.

Finally, Fig. 5 illustrates that the rate of decrease in L_2 error as a function of increasing PPW is greater for higher-order GLLs. To achieve errors in the range 0.1% to 1%, a GLL order of $N = 4$ and PPW value of 4 points per wavelength would suffice for spectral element simulations of HEMT device structures.

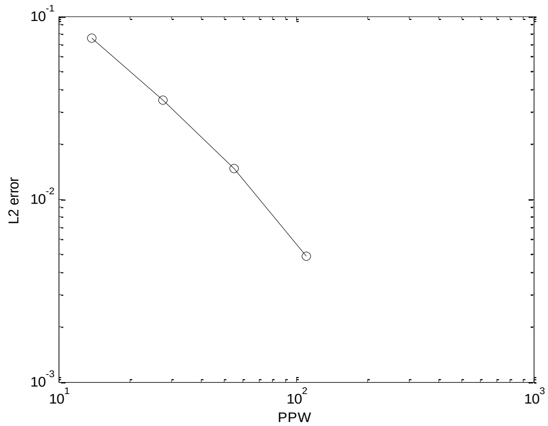

Fig. 4. Relative L_2 error in computed electrostatic potential as a function of points-per-wavelength, for FDM-based simulations.

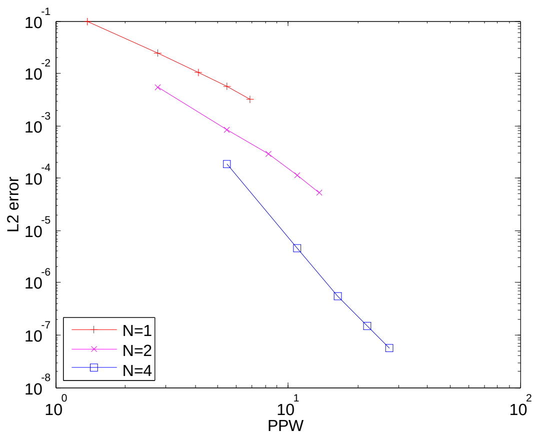

Fig. 5. L_2 error in computed electrostatic potential as a function of PPW, for SEM-based simulations having various GLL orders N (N = 1, 2 and 4).

VIII. HEMT CURRENT-VOLTAGE CHARACTERISTICS

The direct-current (DC) current-voltage (I-V) characteristics for a HEMT device can be calculated based on a quasi-two-dimensional (quasi-2D) drift-diffusion current model, using computational results of the electron density distribution [8, 9]. Figure 6 shows a schematic illustration of the quasi-2D current model which applies to the HEMT device structure under consideration.

The 2DEG sheet charge density is a function of voltage along the channel:

$$n_s(V) = \int n(V,z)dz, \tag{26}$$

and the drain current is:

$$I_D = -qWv(x)n_s. \tag{27}$$

The computation of drain current requires knowledge of the relationship between drift velocity and electric field (the v - E relationship); for increased accuracy, experimental measurements of the nonlinear v - E relationship (from [10]) are used for current calculations. Device parameters for the simulated AlGaAs/GaAs HEMT are taken from [11], specifically: gate width $W = 60\mu m$, gate length $L = 0.5\mu m$, gate metallization Ti/Pt/Au, Schottky barrier height $\phi_B = 0.58V$, Si-doped n- $Al_{0.28}Ga_{0.72}As$ layer thickness $d_{n^+} = 30nm$ with doping concentration $N_D = 1.5 \times 10^{18}/cm^3$, undoped $Al_{0.28}Ga_{0.72}As$ spacer layer thickness of $\delta d = 4\,nm$ and mole fraction $x = 0.28$. Source and drain resistances are assumed to be $R_s = R_d = 0.05\ \Omega cm$ [12, 13]. These values are highly process-dependent, thus typical values are chosen empirically here.

Based on this quasi-2D current model and knowledge of the electron density distribution (calculated from the Schrödinger-Poisson equations using the spectral element method), the current-voltage characteristics for the HEMT triode region can be determined (Fig. 7). Simulated points are shown by discrete markers in Fig. 7; the solid lines which interconnect simulation points of like gate voltage are provided for convenience in visualizing trends only. These results conform well to experimental data obtained for the triode region in Thomasian et al. [11].

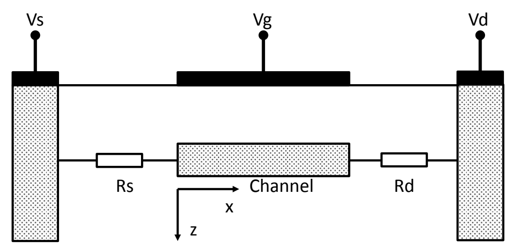

Fig. 6. A quasi-2D current model for the HEMT device.

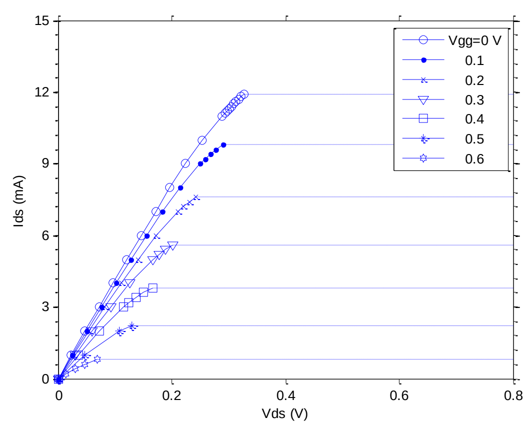

Fig. 7. I-V characteristics of an AlGaAs/GaAs HEMT.

IX. CONCLUSIONS

It is clear that implementation of the spectral element method in numerical simulations of the conduction band structure and 2DEG electron distribution in HEMT devices offers significant advantages in numerical efficiency and relative accuracy when compared to less-complex methods, such as the finite difference method. Furthermore, results from SEM-based simulation can facilitate the determination of device terminal I-V characteristics in a much more computationally-efficient manner, as compared to traditional methods. Estimation of AC small-signal parameters from large-signal data now becomes numerically feasible given the greater computational speed associated with an SEM-based method. This can facilitate both small-signal analysis and design and nonlinear large-signal analysis. Given the increasing interest in applying heterostructure-based compound semiconductor devices to new application areas (e.g., optical, chemical, and biological sensors), the SEM-based approach demonstrated herein can permit efficient numerical design of complex device structures having novel material profiles.

REFERENCES

[1] I.-H. Tan, G. L. Snider, L. D. Chang, and E. L. Hu, "A self-consistent solution of Schrödinger-Poisson equations using a nonuniform mesh," *J. Appl. Phys.*, vol. 68, no. 8, pp. 4071-4076, Oct. 1990.

[2] S. Lapaul, A. de Lustrac, and F. Bouillault, "Solving the Poisson's and Schrödinger's equations to calculate the electron states in quantum nano-structures using the finite element method," *IEEE Trans. Magnetics*, vol. 32, no. 3, pp. 1018-1021, May 1996.

[3] E. A. B. Cole, C. M. Snowden, and T. Boettcher, "Solution of the coupled Poisson-Schrödinger equations using the multigrid method," *Int. J. Numer. Model E. L.*, vol. 10, no. 2, pp. 121-136, Mar. 1997.

[4] C. Cheng, J.-H. Lee, H. Z. Massoud, and Q. H. Liu, "3-D self-consistent Schrödinger-Poisson solver: The spectral element method," *J. Comput. Electron.*, vol. 7, no. 3, pp. 337-341, Feb. 2008.

[5] A. Abou-Elnour and K. Schuenemann, "A comparison between different numerical methods used to solve Poisson's and Schrödinger's equations in semiconductor heterostructures," *J. Appl. Phys.*, vol. 74, no. 5, pp. 3273-3276, Sep. 1993.

[6] H. C. Casey, *Devices for Integrated Circuits: Silicon and III-V Compound Semiconductors.* Wiley, 1998.

[7] Q. H. Liu, C. Cheng, and H. Z. Massoud, "The spectral grid method: a novel fast Schrödinger-equation solver for semiconductor nanodevice simulation," *IEEE Trans. Comput. Aid. Des. Integr. Circ. Syst.*, vol. 23, no. 8, pp. 1200-1208, Aug. 2004.

[8] F. Sacconi, A. Di Carlo, P. Lugli, and H. Morkoc, "Spontaneous and piezoelectric polarization effects on the output characteristics of AlGaN/GaN heterojunction modulation doped FETs," *IEEE Trans. Electron Devices*, vol. 48, no. 3, pp. 450-457, Mar. 2001.

[9] J. S. Blakemore, "Semiconducting and other major properties of gallium arsenide," *J. Appl. Phys.*, vol. 53, no. 50, pp. 123-181, Oct. 1982.

[10] A. Thomasian, A. A. Rezazadeh, and L. G. Hipwood, "Observation and mechanism of kink effect in depletion-mode AlGaAs/GaAs and AlGaas/GaInAs HEMTs," *Electron Lett.*, vol. 25, no. 5, pp. 351-353, Mar. 1989.

[11] K. A. Christianson and W. T. Anderson, "Determination of AlGaAs/GaAs HEMT parasitic resistance," *Solid State Electron.*, vol. 39, no. 12, pp. 1757-1760, Dec. 1996.

[12] K. L. Priddy, D. R. Kitchen, J. A. Grzyb, C. W. Litton, T. S. Henderson, C.-K. Peng, W. F. K. Kopp, and H. Morkoc, "Design of enhanced Schottky-barrier AlGaAs/GaAs MODFET's using highly doped p surface layers," *IEEE Trans. Electron Devices*, vol. 34, no. 2, pp. 175-180, Aug. 2005.

[13] K. L. Priddy, D. R. Kitchen, J. A. Grzyb, C. W. Litton, T. S. Henderson, C. K. Peng, W. F. K. Kopp, and H. Morkoc, "Design of enhanced Schottky-barrier AlGaAs/GaAs MODFET's using highly doped p surface layers," *IEEE Trans. Electron Device*, vol. 34, no. 2, pp. 175-180, 2005.

Feng Li received the Ph.D. degree in Electrical Engineering from the University of Wisconsin-Milwaukee in 2012, and M.S. degree in Electrical Engineering from the University of Texas at Arlington in 2004. He is currently an Assistant Professor of Electrical and Computer Engineering at University of Idaho. From 2004 to 2014, he was doing research at Duke University and University of Wisconsin-Milwaukee. His research interests include simulation, design, fabrication and characterization of III-V compound semiconductor microelectronic and optoelectronic devices.

Qing Huo Liu received the Ph.D. degree in Electrical Engineering from the University of Illinois at Urbana-Champaign, in 1989.

From January 1989 to February 1990, he was a Postdoctoral Research Scientist and Program Leader with Schlumberger-Doll Research, Ridgefield, CT. From 1996 to May 1999, he was an

Associate Professor with New Mexico State University, Since June 1999, he has been with Duke University, Durhm, NC, where he is currently a Professor of Electrical and Computer Engineering. He has authored or co-authored over 450 papers in refereed journals and conference proceedings. His research interests include computational electromagnetics and acoustics, inverse problems, geophysical subsurface sensing, biomedical imaging, electronic packaging, and the simulation of photonic devices and nanodevices.

He is a Fellow of IEEE, and a Fellow of the Acoustical Society of America. He is a member of Phi Kappa Phi and Tau Beta Pi. He is a Full Member of the U.S. National Committee, URSI commissions B and F. He is an Associate Editor for the IEEE Transactions and Geoscience and Remote Sensing. He was the recipient of the 1996 Presidential Early Career Award for Scientists and Engineers (PECASE) presented by the White House, the 1996 Early Career Research Award presented by the Environmental Protection Agency, and the 1997 CAREER Award presented by the National Science Foundation (NSF).

David P. Klemer received an M.D. degree from Columbia University, New York City, NY, in 1999, and Ph.D. degree in Electrical Engineering from The University of Michigan, Ann Arbor, MI, in 1982. His research interests are based on an interdisciplinary background in engineering and medicine, with past research activities including optical imaging at near-infrared wavelengths, microelectronic device/circuit fabrication based on Si and III-V compounds, and the design of solid-state devices and circuits for biosensing and medical diagnostics. His interests include the broad application of biomedical imaging systems, biophotonics and biomedical instrumentation to explorations of human pathophysiology, disease diagnosis and management, and physiologic monitoring in critical care environments. Klemer completed a residency in Internal Medicine at NYU Medical Center/Bellevue Hospital in New York City, and is a Diplomat of the National Board of Physicians and Surgeons.

An Efficient ACA Solution for Electromagnetic Scattering from Discrete Body of Revolution

Z. H. Fan, Z. He, and R. S. Chen

Department of Communication Engineering
Nanjing University of Science and Technology, Nanjing, 210094, China
eerschen@njust.edu.cn

Abstract **─** Discrete body of revolution (DBoR) enhanced method of moments (MoM) is a specialized technique to analyze electromagnetic scattering from the object with discrete cylindrical periodicity. By exploiting the block circulant property of the impedance matrix of MoM, both filling time and storage requirement for the matrix are reduced. The matrix-vector product can be further accelerated by using the fast Fourier transform (FFT) technique. However, the matrix filling time and memory requirement of DBoR-FFT are the same as those of DBoR-MoM, which are still expensive when the number of unknowns in each sector becomes larger. Meanwhile, the DBoR-FFT scheme works inefficiently for the small number of periodic sectors. In this paper, the adaptive cross approximation (ACA) technique is employed to enhance the DBoR-MoM. Numerical examples are given to demonstrate the efficiency of the proposed method.

Index Terms **─** Adaptive cross approximation, discrete body of revolution, electromagnetic scattering, method of moments.

I. INTRODUCTION

Method of moments (MoM) is a popular tool to analyze the electromagnetic scattering from the conducting objects [1-3]. For objects with general shape, MoM costs $O(N^3)$ CPU time and $O(N^2)$ memory, where N is the number of unknowns, which prohibits its application to electrically large objects.

There are mainly two types of techniques to conquer this difficulty. On one hand, a series of fast algorithms have been proposed for general geometry [2-4]. Among them, adaptive cross approximation (ACA) algorithm [4] is one of the popular techniques. It makes use of the fact that the approximate rank of submatrix is deficient when the source group and the observation group are sufficiently separated. Hence the submatrix can be computed efficiently by invoking low-rank decomposition technique. On the other hand, specialized codes are developed to save the time and memory cost of the ordinary MoM for the structures bearing the symmetry, uniformity or periodicity. Bodies of revolution [5-7], bodies of translation [8], and periodic frequency selective surface [9] are several well-known structures. Recently, discrete body of revolution (DBoR) based integral equation approach [10-14] is proposed to analyze the structures with discrete cylindrical periodicity.

Many structures encountered in practical application possess discrete cylindrical periodicity, such as windmill, turbine and jet-engine. In the original DBoR schemes [10-11], a matrix equation with multiple right-hand sides has to be solved since the decomposition of incident field are required. A direct solution scheme of DBoR is discussed in [13-14], and it usually requires a parallel out-of-core solver for the electrically large geometries whereas the in-core solution is preferred in most situations. An efficiently iterative DBoR solver, which is free of decomposition of incident field, is proposed in [12]. It exploits the block circulant property of the whole impedance matrix, thus the storage requirement and filling time of the matrix are of order N^2/M, where M denotes the number of discrete sectors. The time complexity of one matrix-vector product scales $O(N^2)$ if FFT technique is not adopted, and scales $\mathrm{O}[(N^2 \log M)/M]$ if fast Fourier transform (FFT) technique is adopted.

However, the efficiency of DBoR-FFT is still required to be improved since FFT works inefficiently when the number of discrete sectors M is small and the storage requirement and filling time are of $O(N^2/M)$, which is still large. In this paper, a DBoR-ACA scheme is developed which exploits ACA to accelerate the solution of DBoR. Numerical experiments demonstrate that DBoR-ACA is an efficient solution scheme.

The remainder of this paper is organized as follows. In Section II, the theory and the formulations are given. Three numerical experiments are presented in Section III to show the efficiency of the proposed method. Section IV concludes this paper.

Submitted On: July 15, 2015
Accepted On: June 5, 2016

II. THEORY AND FORMULATIONS

A. DBoR-MoM and DBoR-FFT

As shown in Fig. 1, consider a DBoR geometry comprised of *M* discrete cylindrically periodic sectors, each sector occupying an angular width of $\Delta\varphi = 2\pi / M$. In the analysis, the mesh is generated for sector S_1 and then rotated to obtain the meshes for other sectors S_i, i = 2, 3, …, M. The meshes must remain conformal on truncated boundary between two neighbor sectors for current continuity and satisfy cylindrically periodical condition to take advantage of DBoR, as discussed in [11]. The surface current density $\mathbf{J}(\mathbf{r})$ is expanded by the RWG basis functions [1] divided into sectors:

$$\boldsymbol{J}(\boldsymbol{r}) = \sum_{m=1}^{M}\sum_{q=1}^{Q} I_m^q \boldsymbol{f}_m^q(\boldsymbol{r}), \tag{1}$$

where Q denotes the number of unknowns in each sector, and $N = M \times Q$ is the number of total unknowns. I_m^q and $\boldsymbol{f}_m^q$ represent the corresponding expansion coefficient and the RWG function for *q*th basis function in *m*th sector. $\boldsymbol{r} \in S_m$ is position vector. The impedance matrix $\boldsymbol{Z}$ of combined field integral equation (CFIE) is correspondingly partitioned into blocks. As shown in Eq. (2), each block is denoted as $\boldsymbol{Z}_{nm}$, which represents the interactions between sector S_n and sector S_m, each with the size of $Q \times Q$:

$$\begin{bmatrix} \boldsymbol{Z}_{11} & \boldsymbol{Z}_{12} & \boldsymbol{Z}_{13} & \cdots & \boldsymbol{Z}_{1M} \\ \boldsymbol{Z}_{21} & \boldsymbol{Z}_{22} & \boldsymbol{Z}_{23} & \cdots & \boldsymbol{Z}_{2M} \\ \boldsymbol{Z}_{31} & \boldsymbol{Z}_{32} & \boldsymbol{Z}_{33} & \cdots & \boldsymbol{Z}_{3M} \\ \vdots & \vdots & \vdots & \vdots & \vdots \\ \boldsymbol{Z}_{M1} & \boldsymbol{Z}_{M2} & \boldsymbol{Z}_{M3} & \cdots & \boldsymbol{Z}_{MM} \end{bmatrix} \begin{bmatrix} \boldsymbol{I}_1 \\ \boldsymbol{I}_2 \\ \boldsymbol{I}_3 \\ \vdots \\ \boldsymbol{I}_M \end{bmatrix} = \begin{bmatrix} \boldsymbol{V}_1 \\ \boldsymbol{V}_2 \\ \boldsymbol{V}_3 \\ \vdots \\ \boldsymbol{V}_M \end{bmatrix}. \tag{2}$$

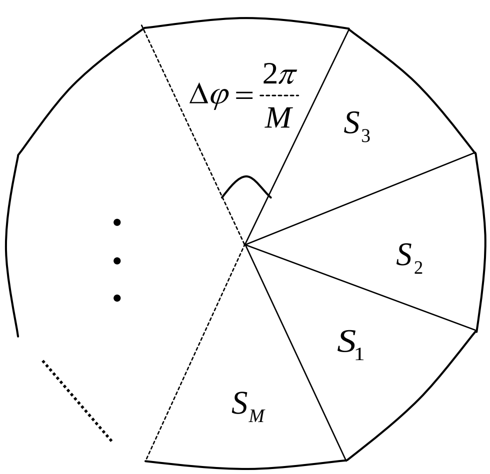

Fig.1. A geometry with *M* cylindrical periodic sectors.

Similar to the procedure for electric field integral equation in [12], $\boldsymbol{Z}_{nm}$ for CFIE can be represented as $\boldsymbol{Z}_{m-n}$ since it depends only on the value of $m-n$. Also, due to the rotational symmetry, it exists $\boldsymbol{Z}_{m-n} = \boldsymbol{Z}_{M+m-n}$. As a result, only $\boldsymbol{Z}_i$, i=0, 1,…, M-1, are required to be computed and stored. One can also use Q^2 times FFT of *M*-points to compute the matrix-vector product [12] since the impedance matrix is in the block circulant form. In this letter, the scheme without FFT is referred to as DBoR-MoM whereas the scheme with FFT is referred to as DBoR-FFT.

B. DBoR-ACA

DBoR-FFT does not work well when the number of discrete sectors *M* is small. A scheme of DBoR-ACA is developed by employing the ACA algorithm to compress each block of $\boldsymbol{Z}_i$. A multilevel spatial partitioning is used to group the RWG functions in each sector. The groups are recorded using octree data at all levels. The touching groups at the finest level are near groups and the others are well-separated groups. The interactions of near groups are computed via DBoR-MoM directly, while the interactions of others are accelerated by the ACA algorithm. Consider two well-separated groups, one group containing *s* testing functions residing in sector S_1, and the other group containing *t* basis functions residing in sector S_m. The interactions between them lead to a submatrix $\boldsymbol{Z}^{s\times t}$, which is one of the submatrices of block $\boldsymbol{Z}_{M+1-m}$. Here, the superscript $s\times t$ denotes the size of the submatrix. Suppose that $\boldsymbol{Z}^{s\times t}$ is rank-deficient with an effectively approximate rank *r*. The rank *r* is usually far smaller than *s* and *t* when both *s* and *t* are large. By utilizing the ACA algorithm, the matrix $\boldsymbol{Z}^{s\times t}$ can be approximated as:

$$\boldsymbol{Z}^{s\times t} \approx \bar{\boldsymbol{Z}}^{s\times t} = \boldsymbol{U}^{s\times r}\boldsymbol{V}^{r\times t}, \tag{3}$$

where $\boldsymbol{U}^{s\times r}$ and $\boldsymbol{V}^{r\times t}$ are two decomposition matrices. The rank *r* is determined adaptively by ACA algorithm to satisfy the following condition:

$$\left\| \boldsymbol{Z}^{s\times t} - \boldsymbol{U}^{s\times r}\boldsymbol{V}^{r\times t} \right\| \le \tau \left\| \boldsymbol{Z}^{s\times t} \right\|, \tag{4}$$

where τ denotes the truncated tolerance of the ACA algorithm and is set as 10^{-3} in this paper. The details of the ACA algorithm to fulfill (3) are referred to [4]. DBoR-ACA fills only a fraction of entries for each block $\boldsymbol{Z}_i$. As shown by numerical observation in [4], both the memory and CPU time requirements of the ACA algorithm scale as $N^{4/3}\log N$ for electrically moderate size problems, while those of MoM scale N^2. Thus DBoR-ACA can reduce both the memory requirement and simulation time for DBoR-MoM. Table 1 lists a comparison of predictions of the computational complexity for the scheme of DBoR-MoM, DBoR-FFT, and DBoR-ACA, where MVP time denotes the time required to compute matrix-vector product once.

Table 1: Predictions of computational complexity

	DBoR		
	MoM	FFT	ACA
Matrix-filling time	N^2/M	N^2/M	$N^{4/3}\log N/M$
Storage of matrix	N^2/M	N^2/M	$N^{4/3}\log N/M$
MVP time	N^2	$N^2\log N/M$	$N^{4/3}\log N$

III. NUMERICAL RESULTS

To demonstrate the efficiency of the DBoR-ACA scheme in comparison with DBoR-MoM and DBoR-FFT, codes are developed for all schemes and numerical examples are presented for typical geometries. In the simulations, the frequency f is 300 MHz unless otherwise specified. The electric field of incident wave is $\boldsymbol{E}^i = \hat{x}\exp(j2\pi z/\lambda)$, where λ is the wavelength. The discrete rotational axis of DBoR is z axis. CFIE is employed with combination coefficient of 0.5. The resulting matrix equations are iteratively solved by restarted GMRES [16] where the restarted number is set to be 30. The stop criterion for iteration is relative residual norm less than 10^{-3}. The bistatic radar cross section (RCS) results are observed at the plane with fixed azimuthal angle $\varphi^s = 0^\circ$ and varied polar angles θ^s. All the simulations are carried out in single precision arithmetic on a computer equipped with a 2.83 GHz Intel® Core2 Quad processor, with one core being used.

A. Efficiency test for a conducting ring

The first example is selected to test the performance of different schemes varying with number of sectors. The configuration is a conducting ring with inner radius a=2 m, outer radius b=3 m, and height h=0.1 m, as shown in Fig. 2 (a). To take advantage of DBoR, the mesh has to be changed each time when the number of sectors is increased. Here, the total number of unknowns is kept at a fixed level approximately. Table 2 lists the number of unknowns corresponding to each number of sectors.

Table 2: The number of unknowns and number of sectors for the first example

M	8	16	32	64	80	100	128
N	47304	46560	46752	46848	44880	45600	45312

Figure 2 (a) plots the memory requirement for DBoR-MoM and DBoR-ACA. The memory requirement of DBoR-FFT is same as that of DBoR-MoM. It can be observed that the memory requirement of DBoR-MoM is scaled as $1/M$, while the DBoR-ACA grows a few larger than $O(1/M)$ as M increases. The reason is that the dividing strategy of the DBoR-ACA group is controlled by both the octree structure and the sectors. Increasing number of divided sectors brings two burdens which lessening the compressed efficiency of DBoR-ACA against the case when ACA algorithm is utilized for objects of general shape. The first one is that it produces more groups belonging simultaneously to more than one sector, which resulting in more groups with small number of unknowns. The second burden is that the size of the largest group of DBoR-ACA is reduced since the size of each sector is reduced. But even for as many as 128 sectors, the performance of DBoR-ACA has not been reduced by much.

Figure 2 (b) shows the CPU time cost of one MVP. It can be found that the computational time for DBoR-MoM and DBoR-ACA changes slightly as number of sectors increases, whereas the computational time of DBoR-FFT reduces dramatically. The complexity of DBoR-FFT is consistent with $O(N^2\log N/M)$ for large value of number of sectors M, however the computational time is even greater than that of DBoR-MoM for $M<32$. It is because the implementation of FFT with small number of points is not that efficient. In addition, it destroys the CPU cache friendly feature of the submatrices of original DBoR-MoM. It can be observed that a slightly decrease of the CPU time for DBoR-MoM for large number of sectors. This owes to a slightly decreasing of the total number of unknowns as given in Table 2. The slightly increase of the CPU time for DBoR-ACA with large number of sectors is ascribed to the same burdens for the memory requirement. It should be noted that the DBoR-ACA scheme takes more CPU time to perform one MVP than the DBoR-FFT scheme does for large M. For DBoR configuration of practical engineering M is usually not very big, hence, DBoR-ACA is still a faster solver by considering the filling time of the impedance matrix together. Table 3 shows the case for 128 sectors. Here the total time denotes the whole analysis time including the time for pre-processing, matrix filling and solving, and RCS calculating. It can be observed that FFT takes effect in accelerating the DBoR-MoM. However, the total simulation time of DBoR-ACA is still less than that of DBoR-FFT due to saving of matrix filling time.

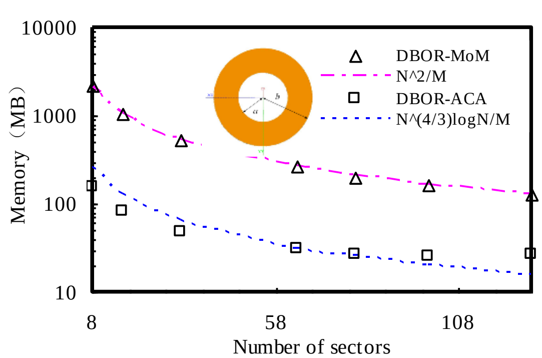

(a)

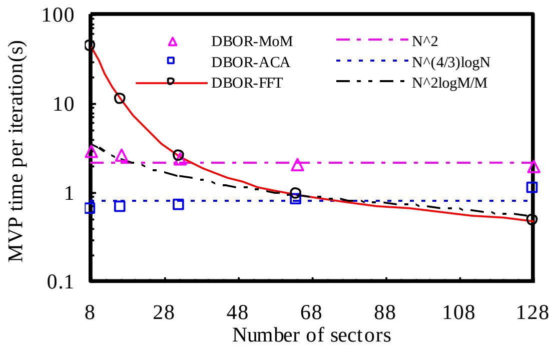

(b)

Fig. 2 Comparisons of the complexity for DBoR-MoM, DBoR-FFT, and DBoR-ACA schemes by increasing the number of divided sectors while keep approximately the total number of unknowns of 46000. (a) Memory, and (b) CPU time for one matrix-vector multiplication.

Table 3: Comparisons of the CPU time and memory requirement for the conducting ring with 128 cylindrical sectors and each with 354 unknowns

	DBoR		
	MoM	FFT	ACA
Memory (MB)	125	125	26
Matrix filling time (s)	72	73	13
Number of iteration	39	39	39
Iteration time (s)	105	19	42
Total time (s)	180	95	58

B. Computation complexity test for a conducting ring

The second example is a conducting ring with inner radius a = 2 m, outer radius b = 4 m, and height h = 0.1 m. This example is to show the complexity of various DBoR schemes for electrically increasing large problems. The ring is discretized with a mesh size of h = 0.05 m and the frequency f is increased from 214.3 MHz to 333.3 MHz. This leads to an increase of the total number of unknowns from 54528 to 129600 as the relation $N \propto f^2$. The ring is modeling with 64 sectors. The size of group box at finest level is 0.2λ in DBoR-ACA scheme. The complexity of memory requirements and CPU time of one MVP for DBoR-MoM and DBoR-ACA are illustrated in Fig. 3 (a) and Fig. 3 (b), respectively. The memory requirement of DBoR-FFT is same as that of DBoR-MoM. It can be observed the practical implementation is consistent with the prediction of the complexity as listed in Table 1. Also both the memory requirement and CPU time cost of DBoR-ACA are less than those of DBoR-FFT when the number of unknowns becomes large in each sector.

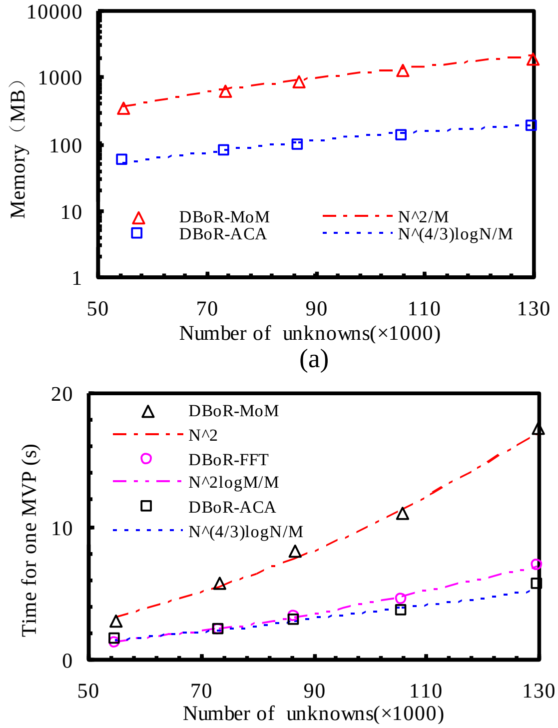

(b)

Fig. 3. Comparisons of the complexity between DBoR-MoM, DBoR-FFT, and DBoR-ACA algorithms for a conducting ring varying with number of unknowns. (a) Memory, and (b) CPU time for one matrix-vector product.

C. Bistatic RCS for a conducting jet-engine inlet

The last example is a conducting jet-engine inlet as shown in Fig. 4 (a). The configuration has 16 sectors and each sector has 4932 unknowns. The size of group box at finest level of DBoR-ACA algorithm is 0.4 m. This example is to show the efficiency for the small number of sectors of various DBoR schemes. The geometry and dimension of one sector of jet-engine is shown in Fig. 4 (b) and of shell is shown in Fig. 4 (c). For the cylindrical shell, the radius is 2.1 m and the height is 4.0 m for the inner side and the thickness is 0.1 m. The jet-engine is placed at a distance of 0.1 m above the bottom of the shell. The bistatic RCS results are illustrated in Fig. 5 for the various DBoR schemes and fast multipole solver in FEKO®. It can be observed that they are in agreement with each other. Table 4 shows the CPU time and memory requirement for this example. It can be found that DBoR-FFT fails to accelerate DBoR-MoM while DBoR-ACA successes to spend less memory and less CPU time.

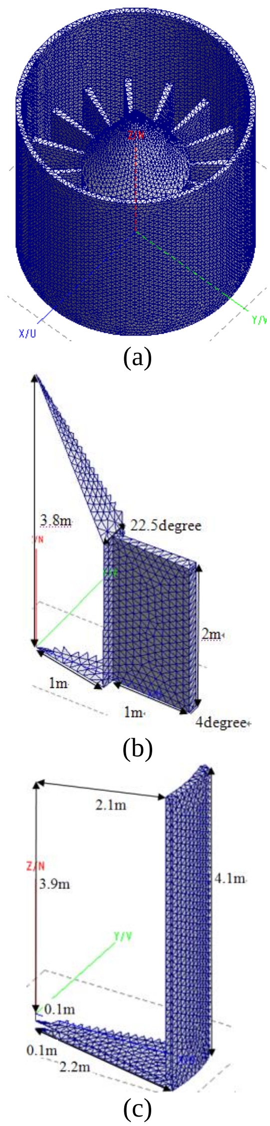

Fig. 4. The geometry and mesh of: (a) jet-engine inlet, (b) single sector of jet-engine, and (c) single sector of the shell.

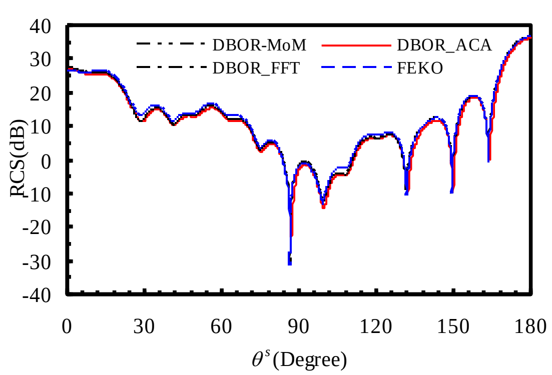

Fig. 5. The bistatic radar cross section of conducting jet-engine inlet.

Table 4: Comparison of the CPU time and memory requirement for the jet-engine inlet with 16 sectors and each sector with 4932 unknowns

	DBoR		
	MoM	FFT	ACA
Memory (MB)	3008	3008	396
Matrix filling time (s)	1530	1532	244
Number of iteration	344	344	348
Iteration time (s)	4953	9013	1072
Total time (s)	6490	10552	1321

IV. CONCLUSION

The DBoR-MoM has been extended to CFIE for the analysis of electromagnetic scattering from discrete body of revolution in free space. The ACA technique was exploited to accelerate both matrix-filling operation and matrix-vector product of the DBoR-MoM. Numerical examples validate the efficiency and accuracy of the proposed method in comparison with DBoR-MoM and DBoR-FFT. The numerical results suggest that DBoR-FFT fails to accelerate DBoR-MoM for the DBoR with small number of sectors whereas the proposed DBoR-ACA method is appropriate for accelerating the solution of all types of cylindrically periodic geometries. At the end, it is worthwhile to note that a faster scheme can be obtained if sparsified ACA [17] is applied into the DBoR.

ACKNOWLEDGMENT

This work was supported in part by Natural Science Foundation of 61371037, 61431006, 61271076, the Fundamental Research Funds for the Central Universities of No. 30920140111003, No. 30920140121004.

REFERENCES

[1] S. M. Rao, D. R. Wilton, and A. W. Glisson, "Electromagnetic scattering by surfaces of arbitrary shape," *IEEE Trans. Antennas Propag*., vol. 30, no. 3, pp. 409-418, 1982.

[2] W. C. Chew, J.-M. Jin, E. Michielssen, and J. Song, *Fast and Efficient Algorithms in Computational Electromagnetics*. Boston, MA: Artech House, 2001.

[3] W. C. Chew and L. J. Jiang, "Overview of large-scale computing: The past, the present, and the future," *Proceedings of the IEEE*, vol. 101, no. 2, pp. 227-241, 2013.

[4] K. Z. Zhao, M. N. Vouvakis, and J.-F. Lee, "The adaptive cross approximation algorithm for accelerated method of moments computations of EMC problems," *IEEE Transactions on Electromagnetic Compatibility*, vol. 47, no. 4, pp. 763-773, 2005.

[5] J. R. Mautz and R. F. Harrington, "Radiation and scattering from bodies of revolution," *Applied*

Scientific Research, vol. 20, no. 1, pp. 405-435, 1969.

[6] Z. He, H. H. Zhang, and R. S. Chen, "Parallel marching-on-in-degree solver of time-domain combined field integral equation for bodies of revolution accelerated by MLACA," *IEEE Trans. Antennas Propag.*, vol. 63, no. 8, pp. 3705-3710, 2015.

[7] Z. He, Z. H. Fan, D. Z. Ding, and R. S. Chen, "Solution of PMCHW integral equation for transient electromagnetic scattering from dielectric body of revolution," *IEEE Trans. Antennas Propag.*, vol. 63, no. 11, pp. 5124-5129, 2015.

[8] L. Medgyesi-Mitschang and J. Putnam, "Scattering from finite bodies of translation: Plates, curved surfaces, and noncircular cylinders," *IEEE Trans. Antennas Propag*., vol. 31, no. 6, pp. 847-852, 1983.

[9] B. Munk, *Frequency Selective Surfaces: Theory and Design*. John Wiley, 2000.

[10] H. T. Anastassiu, J. L. Volakis, and D. S. Fili, "Integral equation modeling of cylindrically periodic scatterers in the interior of a cylindrical waveguide," *IEEE Transactions on Microwave Theory and Techniques*, vol. 46, no. 11, pp. 1713-1720, 1998.

[11] M. A. Carr, J. L. Volakis, and D. C. Ross, "Acceleration of moment method solutions for discrete bodies of revolution in free space," *IEEE Antennas and Propagation Society International Symposium*, vol. 4, pp. 2286-2289, 2000.

[12] M. A. Carr, J. L. Volakis, and D. C. Ross, "Acceleration of free-space discrete body of revolution codes by exploiting circulant submatrices," *IEEE Trans. Antennas Propag*., vol. 50, no. 9, pp. 1319-1322, 2002.

[13] P. Soudais, P. Leca, J. Simon, and T. Volpert, "Computation of the scattering from inhomogeneous objects with a discrete rotational symmetry and a nonsymmetric part," *IEEE Trans. Antennas Propag*., vol. 50, no. 2, pp. 168-174, 2002.

[14] H. T. Anastassiu, N. L. Tsitsas, and P. J. Papakanellos, "Electromagnetic scattering and radiation by discrete bodies of revolution," *URSI Int. Symp. on Electromagnetic Theory*, Berlin, Germany, pp. 657-659, 2010.

[15] J. M. Song and W. C. Chew, "Multilevel fast-multipole algorithm for solving combined field integral equations of electromagnetic scattering," *Microwave Opt. Tech. Lett*., vol. 10, no. 1, pp. 14-19, 1995.

[16] Y. Saad and M. H. Schultz, "GMRES: A generalized minimal residual algorithm for solving nonsymmetric linear systems," *SIAM Journal on Scientific & Statistical Computing*, vol. 7, no. 3, pp. 856-869, 1986.

[17] A. Heldring, J. M. Tamayo, C. Simon, E. Ubeda, and J. M. Rius, "Sparsified adaptive cross approximation algorithm for accelerated method of moments computations," *IEEE Trans. Antennas Propag*, vol. 61, no. 1, pp. 240-246, 2013.

Zhenhong Fan was born in Jiangsu, China, in 1978. He received the M.Sc. and Ph.D. degrees in Electromagnetic Field and Microwave Technique from Nanjing University of Science and Technology (NJUST), Nanjing, China, in 2003 and 2007, respectively.
During 2006, he was with the Center of Wireless Communication in the City University of Hong Kong, Kowloon, as a Research Assistant. He is currently an Associate Professor with the Electronic Engineering of NJUST. He is the author or co-author of over 20 technical papers. His current research interests include computational electromagnetics, electromagnetic scattering and radiation.

Zi He received the B.Sc. degree in Electronic Information Engineering from the School of Electrical Engineering and Optical Technique, Nanjing University of Science and Technology, Nanjing, China, in 2011.

She is currently working towards the Ph.D. degree in Electromagnetic Fields and Microwave Technology at the School of Electrical Engineering and Optical Technique, Nanjing University of Science and Technology. Her research interests include antenna, RF-integrated circuits, and computational electromagnetics.

Rushan Chen (M'01) was born in Jiangsu, China. He received the B.Sc. and M.Sc. degrees from the Department of Radio Engineering, Southeast University, China, in 1987 and 1990, respectively, and the Ph.D. degree from the Department of Electronic Engineering, City University of Hong Kong, in 2001.

He joined the Department of Electrical Engineering, Nanjing University of Science and

Technology (NJUST), China, where he became a Teaching Assistant in 1990 and a Lecturer in 1992. Since September 1996, he has been a Visiting Scholar with the Department of Electronic Engineering, City University of Hong Kong, first as Research Associate, then as a Senior Research Associate in July 1997, a Research Fellow in April 1998, and a Senior Research Fellow in 1999. From June to September 1999, he was also a Visiting Scholar at Montreal University, Canada. In September 1999, he was promoted to Full Professor and Associate Director of the Microwave and Communication Research Center in NJUST, and in 2007, he was appointed as the Head of the Department of Communication Engineering, NJUST. He was appointed as the Dean in the School of Communication and Information Engineering, Nanjing Post and Communications University in 2009. And in 2011 he was appointed as Vice Dean of the School of Electrical Engineering and Optical Technique, NJUST. Currently, he is a Principal Investigator of more than 10 national projects. His research interests mainly include computational electromagnetics, microwave integrated circuit and nonlinear theory, smart antenna in communications and radar engineering, microwave material and measurement, RF-integrated circuits, etc. He has authored or co-authored more than 260 papers, including over 180 papers in international journals.

Chen is an Expert enjoying the special government allowance, Member of Electronic Science and Technology Group, Fellow of the Chinese Institute of Electronics (CIE), Vice-Presidents of Microwave Society of CIE and IEEE MTT/APS/EMC Nanjing Chapter and an Associate Editor for the International Journal of Electronics. He was also the recipient of the Foundation for China Distinguished Young Investigators presented by the China NSF, a Cheung Kong Scholar of the China Ministry of Education, New Century Billion Talents Award. Besides, he received several Best Paper Awards from the National and International Conferences and Organizations. He serves as the Reviewer for many technical journals, such as the IEEE Transactions on Antennas and Propagation, the IEEE Transactions on Microwave Theory and Techniques, Chinese Physics, etc.

Electromagnetic Scattering from a PEMC Circular Cylinder Coated by Topological Insulator (TI)

A. Shahzad [1], A. Illahi [2], S. Ahmed [1], A. Hussain [1], and Q. A. Naqvi [1]

[1] Department of Electronics, Quaid-i-Azam University, Islamabad, Pakistan (45320)
gondalanjum@yahoo.com, snfawan@yahoo.com, akhtar_h@yahoo.com, nqaisar@yahoo.com

[2] Research in Modeling and Simulation (RIMS) Group, Department of Physics
COMSATS Institute of Information Technology, Islamabad, Pakistan
ahsanillahi@comsats.edu.pk

Abstract **─** Scattering of electromagnetic plane wave from a perfect electromagnetic conducting (PEMC) cylinder coated with a topological insulating (TI) material has been presented. The core (PEMC) and cladding material (TI) produce co- and cross-polarized components of electromagnetic field in response to the incident plane wave for a given polarization (TE or TM). When the value of θ is made zero, TI material becomes ordinary dielectric and the results of PEMC coated with TI with $\theta = 0$ (dielectric material) have been compared with the previously published literature and are found in good agreement. When the coating is removed, same results as that of isolated PEMC circular cylinder have also been reproduced.

Index Terms **─** Cladding, insulating, isolated, polarization, topological.

I. INTRODUCTION

Topological insulator's states in 2D and 3D materials were observed theoretically in 2005 and 2007 while their experimental discovery won the 2010 Nobel Prize. Topological insulator material is currently the hottest topic in condensed matter and quantum physics, and is hard to understand. Topological insulator is a type of material that conducts electricity on its surface due to special surface electronic states. The surface states of TI are topologically protected, i.e., they cannot be destroyed by impurities. TIs are made possible due to the combination of time-reversal symmetry and interaction of spin-orbit coupling, which occurs in heavy elements like mercury and bismuth.

TIs are defined by the constitutive relations:

$$\boldsymbol{D} = \epsilon_r \epsilon_0 \boldsymbol{E} - \epsilon_0 \alpha \frac{\theta}{\pi}(c_0 \boldsymbol{B}), \quad (1)$$

$$c_0 \boldsymbol{H} = \frac{c_0}{\mu_0 \mu_r} \boldsymbol{B} + \alpha \frac{\theta}{\pi} \frac{1}{\mu_0 \mu_r} \boldsymbol{B}, \quad (2)$$

where ϵ_r, μ_r are relative permeability and permittivity and ϵ_0, μ_0 are the permeability and permittivity of free space respectively. c_0 is the speed of light in vacuum, $\alpha = e^2/4\pi\epsilon_0\hbar c_0$ is the fine structure constant, $\hbar$ is Plank constant, e is the electric charge and θ is axion parameter which is uniquely determined by band structure. Only two values of θ are possible: $\theta = 0$ (i.e., conventional dielectric) and $\theta = \pi$ (i.e., topological insulator), which gives time reversal symmetry. When time reversal symmetry is broken, the θ is quantized in odd integer values of π [1].

Due to these attractive properties many scientists started studying TI. Surface plasmons localized on the topologically nontrivial interface have been studied by Karch [1]. Qi and Zhang studied the theory of topological superconductors in close analogy to the theory of topological insulators [2]. Scattering results from topological insulator cylinders are very few [3-6]. Scattering by TI circular cylinder is discussed in [3]. Scattering from buried TI circular cylinder in a slightly rough surface has been investigated in [4] and buried in a semi infinite medium has been discussed in [5]. In [6], it has been shown that what will happen when a TI cicular cylinder is placed in chiral medium? Electromagnetic scattering from coated cylinder is a more challenging task and is therefore addressed in the present paper.

PEMC is a new class of materials introduced by Lindell and Sihvola [7]. It is the generalization of perfect electric conductor (PEC) and perfect magnetic conductor (PMC) material. It is defined by the boundary conditions:

$$\boldsymbol{n} \times (\boldsymbol{H} + M\boldsymbol{E}) = 0, \quad (3)$$

$$\boldsymbol{n}.(\boldsymbol{D} - M\boldsymbol{B}) = 0, \quad (4)$$

where M denotes the admittance of the PEMC boundary. $M = 0$ for PMC and $M \to \pm\infty$ for PEC. The circular cylinders are the most basic canonical shape for the study of electromagnetic waves scattering. Cylindrical geometry has a long history in EM problems [8-9, 12-18, 22-26]. Scientists had studied the problems of circular cylinder using composition of different materials, e.g., dielectric, negative refractive index materials (NRM),

Submitted On: May 3, 2014
Accepted On: August 1, 2016

PEMC, chiral, and nihility [10-14, 16, 17, 19-24].

In this paper, an infinite PEMC circular cylinder coated with TI material is considered. The purpose of the study is to explore important scattering characteristics and to provide physical insight of this geometry. Using the large argument approximation of Hankel function, the bi-static echo widths in the far zone are calculated. For the verification of analytical formulation and numerical code, numerical results are compared with the published work. We have used $e^{-i\omega t}$ time dependence which is suppressed throughout the analysis.

In the next few sections, analytical formulation, numerical results and discussion, and conclusions are described.

II. ANALYTICAL FORMULATION

Geometry of problem is shown in Fig. 1. Inner cylinder is PEMC while the outer cylinder shows the coating layer of TI material. PEMC circular cylinder coated with TI material is of uniform thickness. The cylinder is supposed to be of infinite length along z-axis. Radius of PEMC cylinder is 'a' while radius of PEMC cylinder coated with TI is 'b'. The region outside the coating $\rho > b$ is free space and is mentioned as region 0 with wave number $k_0 = \omega\sqrt{\mu_0\epsilon_0}$. The region between $a < \rho < b$ is termed as region 1 with wave number as $k_1 = \omega\sqrt{\mu_1\epsilon_1}$.

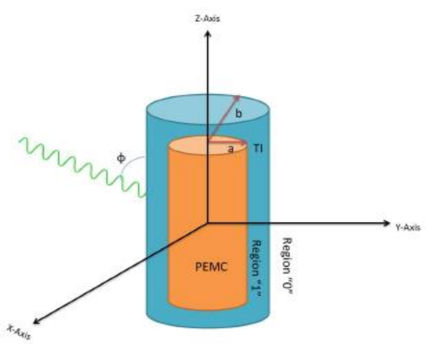

Fig. 1. PEMC Cylinder coated with topological insulator.

The polarization of the incident electric field is taken parallel to the axis of the cylinder. The incident electric field is given by:

$$E_{0z}^{i} = e^{ik_0\rho\cos\varphi}. \tag{5}$$

The incident electric field can be written in terms of cylindrical wave function as:

$$E_{0z}^{i} = \sum_{n=-\infty}^{\infty} i^n J_n\,(k_0\rho)e^{jn(\varphi)}. \tag{6}$$

Using Maxwell's equations, the corresponding magnetic field in φ direction can be written as:

$$H_{0\varphi}^{i} = -\frac{E_0}{i\eta_0}\sum_{n=-\infty}^{\infty} J_n'\,(k_0\rho)e^{jn(\varphi)}. \tag{7}$$

The scattered co-polarized electric field in region 0 can be written as:

$$E_{0z}^{s} = \sum_{n=-\infty}^{\infty} i^n a^n\, H_n^{(1)}(k_0\rho)e^{jn(\varphi)}. \tag{8}$$

And the corresponding φ component of scattered co-polarized magnetic field can be written as:

$$H_{0\varphi}^{s} = -\frac{E_0}{i\eta_0}\sum_{n=-\infty}^{\infty} i^n a^n H_n^{(1)'}\,(k_0\rho)e^{jn(\varphi)}. \tag{9}$$

As the core material of the cylinder is of PEMC, so in addition to co-polarized component cross-polarized component will also appear. The scattered cross-polarized magnetic field in region 0 can be written as:

$$H_{0z}^{s} = -\frac{iE_0}{\eta_0}\sum_{n=-\infty}^{\infty} i^n b^n H_n^{(1)}\,(k_0\rho)e^{jn(\varphi)}. \tag{10}$$

And the corresponding φ component of scattered cross-polarized electric field can be expressed as:

$$E_{0\varphi}^{s} = -E_0\sum_{n=-\infty}^{\infty} i^n a^n H_n^{(1)'}\,(k_0\rho)e^{jn(\varphi)}. \tag{11}$$

Region 1 has two interfaces at $\rho = a$ and $\rho = b$; therefore, co- and cross-polarized electric and magnetic fields in region 1 can be expressed in terms of oppositely traveling cylindrical waves as:

$$E_{1z} = E_0\sum_{n=-\infty}^{\infty} i^n[c^n H_n^{(2)}\,(k_1\rho) + d^n H_n^{(1)}(k_1\rho)]e^{jn(\varphi)}, \tag{12}$$

$$H_{1\varphi} = -\frac{E_0}{i\eta_1}\sum_{n=-\infty}^{\infty} i^n[c^n H_n^{(2)'}\,(k_1\rho) + d^n H_n^{(1)'}(k_1\rho)]e^{jn(\varphi)}, \tag{13}$$

$$E_{1z} = -\frac{iE_0}{\eta_1}\sum_{n=-\infty}^{\infty} i^n[e^n H_n^{(2)}\,(k_1\rho) + f^n H_n^{(1)}(k_1\rho)]e^{jn(\varphi)}, \tag{14}$$

$$H_{1\varphi} = -E_0\sum_{n=-\infty}^{\infty} i^n[e^n H_n^{(2)'}\,(k_1\rho) + f^n H_n^{(1)'}(k_1\rho)]e^{jn(\varphi)}. \tag{15}$$

In above expressions $J_n(.)$ is the Bessel functions of first kind, while $H_n^{(1)}(.)$ and $H_n^{(2)}(.)$ are the Hankel functions of first and second kinds respectively. Also a_n, b_n, c_n, d_n, e_n and f_n are the unknown scattering coefficients. These unknown coefficients can be found by using boundary conditions at the interfaces $\rho = a$ and $\rho = b$.

At $\rho = a$, boundary conditions are:

$$H_{1z} + ME_{1z} = 0 \quad \rho = a, \quad 0 \le \varphi \le 2\pi, \tag{16}$$

$$H_{1\varphi} + ME_{1\varphi} = 0 \quad \rho = a, \quad 0 \le \varphi \le 2\pi. \tag{17}$$

At $\rho = b$, boundary conditions are:

$$H_{0\varphi}^{i} + H_{0\varphi}^{s} = H_{1\varphi} - \alpha\frac{\theta}{c_0\pi}E_{1\varphi} \quad \rho = b,\ 0 \le \varphi \le 2\pi, \tag{18}$$

$$H_{0z}^{s} = H_{1z}^{s} - \alpha\frac{\theta}{c_0\pi}E_{1z} \quad \rho = b,\ 0 \le \varphi \le 2\pi, \tag{19}$$

$$H_{0z}^{s} = H_{1z} \quad \rho = b,\ 0 \le \varphi \le 2\pi, \tag{20}$$

$$E_{0\varphi}^{s} = H_{1\varphi} \quad \rho = b,\ 0 \le \varphi \le 2\pi, \tag{21}$$

where

$$E_{0z} = E_{0z}^{i} + E_{0z}^{s}, \tag{22}$$

$$H_{0\varphi} = H_{0\varphi}^{i} + H_{0\varphi}^{s}. \tag{23}$$

By the application of above boundary conditions at interface $\rho = a$ and $\rho = b$, a linear matrix is obtained in terms of the unknown scattering coefficients. Solution of this matrix gives unknown scattering coefficients. The values of a_n and b_n give us co- and cross-polarized components of scattered field due to PEMC cylinder coated with TI.

III. BACK SCATTERING CROSS-SECTIONS (σ)

The ratio of the total power scattered by the scatter to the incident power per unit area on the scatterer is called back scattering cross-section and is given as:

$$\sigma = 2\pi\rho\frac{W^s}{W^i} = 2\pi\rho\frac{| E^s |^2}{| E^i |^2}.$$

For parallel polarization, the normalized bi-static echo width (RCS) of the co-polarized and cross-polarized field components is given by:

$$\sigma_{co}/\lambda_0 = \frac{2}{\pi}\left| \sum_{n=-\infty}^{n=\infty} a_n e^{in(\varphi)} \right|^2,$$

$$\sigma_{cross}/\lambda_0 = \frac{4}{\pi}\left| \sum_{n=-\infty}^{n=\infty} b_n e^{in(\varphi)} \right|^2,$$

where a_n is the scattering coefficient of co-polarized field and b_n is the scattering coefficient of cross-polarized field. For perpendicular polarization, the duality principle for the above formulation may be used.

IV. NUMERICAL RESULTS AND DISCUSSION

In this section numerical results are described. The numerical results are based on the above analytical formulations for PEMC coated with TI material. For Figs. 2-8, $k_0a = 1.05$, $k_0b = 2.1$, $e = 1.6*10^{-19}$C, speed of light is $c_0 = 3*10^8 m/s$ and permeability $\mu = 1$.

In Fig. 2 echo width of PEMC circular cylinder coated with TI material has been plotted with observation angle from 0 to 2π radians. In this figure, $M\eta_1 = 0$, $\epsilon = 9.8$ and $\theta = 0$, which is a case for PMC circular cylinder coated with dielectric material. This result when compared with [24], excellent agreement is found.

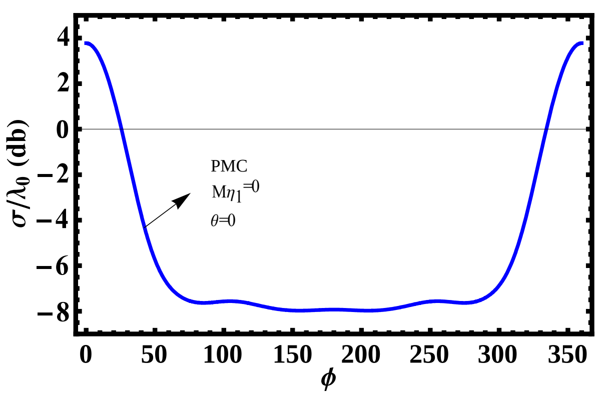

Fig. 2. Echo width from PMC coated with dielectric material with $\epsilon = 9.8$.

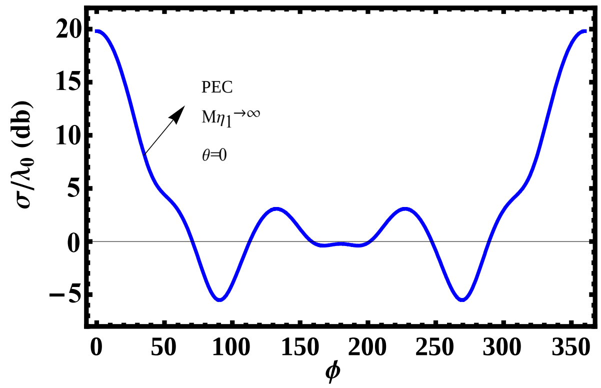

Fig. 3. Echo width from PEC coated with dielectric material $\epsilon = 9.8$.

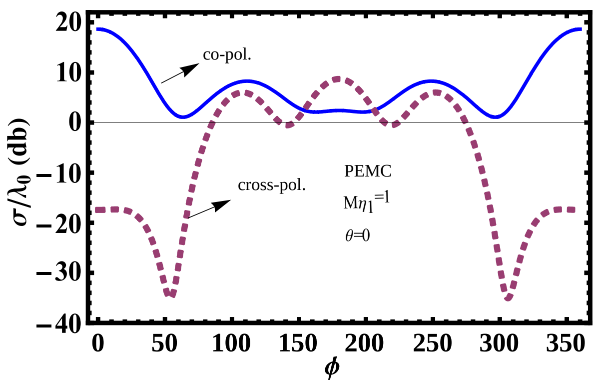

Fig. 4. Echo width of co- and cross-polarized from PEMC coated with dielectric material $\epsilon = 9.8$.

In Figs. 3 and 4, the numerical result is repeated for $M\eta_1\to\infty$, $\epsilon = 9.8$ and $\theta = 0$ and $M\eta_1 = 1$, $\epsilon = 9.8$ and $\theta = 0$. Comparison is made for PEC circular cylinder coated with dielectric material. Again, the obtained nice comparison and validated our formulation. With this confidence, the numerical code has been run for different values of $M\eta_1$ and θ, while $\epsilon = 100$ which is the characteristic value of TI material (i.e., ϵ= 50 to 100) and Figs. 5-8 are obtained.

In Figs. 5-8, scattering behavior of PEMC circular cylinder coated with TI material has been highlighted. With these results one can understand the composition of the highly focused material, i.e., TI material with PEMC (which is the most fundamental material for electromagnetic analysis).

Figure 5 represents echo width of co- and cross-polarized components for PMC circular cylinder coated with TI material. In this figure, $M\eta_1 = 0$, $\epsilon = 100$ and $\theta = 41\pi$, which is the case of PMC circular cylinder coated with TI material. In this plot, cross-polarized component has also been appeared along with co-polarized component. This cross-polarized component is due to TI material. Figure 6 shows the case when PEMC circular cylinder coated with TI material has been taken. For this figure, parameters are taken as $M\eta_1 = 1$, $\epsilon = 100$ and $\theta = 41\pi$. On comparing Fig. 5 and Fig. 6, it has been observed co-polarized component is same, while cross-polarized component of Fig. 5 is greater than the cross-polarized component of Fig. 6. This greater contribution in the cross-polarized component is because of PEMC core when coated with TI material.

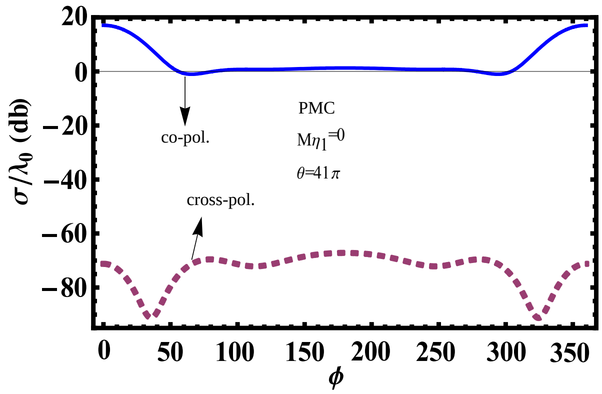

Fig. 5. Echo width of co- and cross-polarized components for PMC with $\epsilon = 100$.

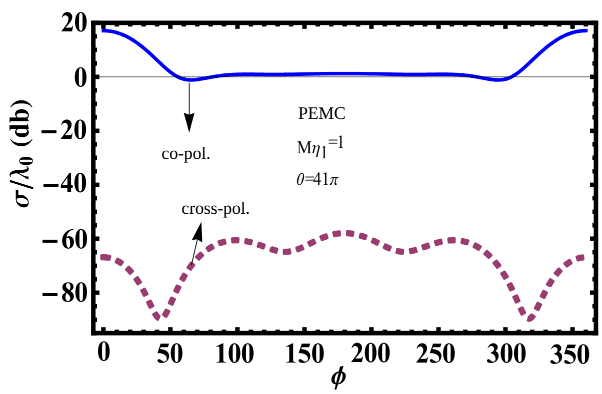

Fig. 6. Echo width of co- and cross-polarized components for PEMC with $\epsilon = 100$.

Figure 7 shows the comparison between co-polarized components for different of θ, i.e., for $\theta = 0$ and $\theta = 41\pi$; when PEMC circular cylinder coated with TI material is considered. It is observed that the behavior of co-polarized component for $\theta = 0$ is same as co-polarized component for $\theta = 41\pi$ near 0-80 and 310-360 but different for 80-310 regardless of the amplitude.

Figure 8 shows the comparison between cross-polarized components for $\theta = 0$ and $\theta = 41\pi$ respectively, when PEMC circular cylinder coated with TI material is considered. It is observed that the behavior of cross-polarized component for $\theta = 0$ is different from co-polarized component for $\theta = 41\pi$ near0-80 and 310-360 but same for 80-310 regardless of the amplitude.

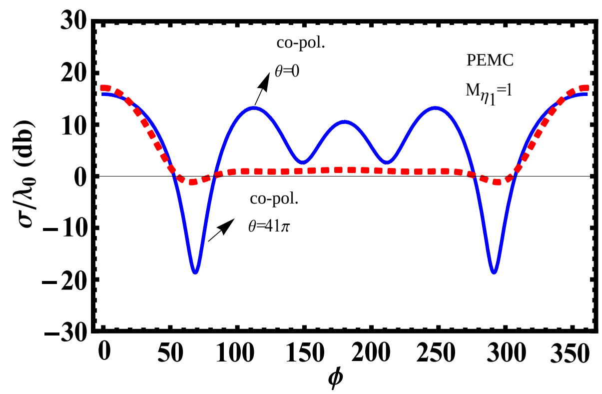

Fig. 7. Echo width of co- and co-polarized components for different values of θ when core is PEMC with $\epsilon = 100$.

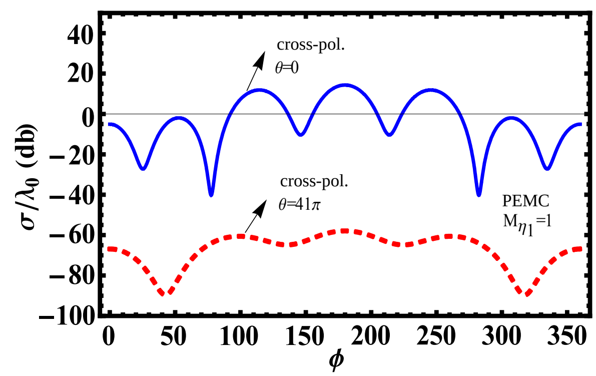

Fig. 8. Echo width of cross- and cross-polarized components for different values of θ when core is PEMC with $\epsilon = 100$.

V. NUMERICAL VERIFICATION

In Fig. 2 the code has been verified with the limiting parameters $M\eta_1 = 0$, $\epsilon = 9.8$ and $\theta = 0$ and compared with the literature [24]. The code is further verified in Figs. 3 and 4, the parameters used are: $M\eta_1 \rightarrow \infty$, $\epsilon = 9.8$ and $\theta = 0$ and $M\eta_1 = 1$, $\epsilon = 9.8$ and $\theta = 0$. Comparison is made with [24]. In both the cases excellent agreement is found. The proposed study can also be verified with the help of experiments as well as commercially available simulation software which will be our task.

VI. CONCLUSIONS

In the present paper analytical formulation of a perfect electromagnetic conducting (PEMC) circular cylinder of infinite length coated with a topological insulating (TI) material has been presented. The core (PEMC) and cladding (TI) material produces co- and cross-polarized components of electromagnetic magnetic field in response to the incident plane wave for a given polarization (TE or TM). By coating TI material on PEMC circular cylinder, again co- and cross-polarized components of the scattered field has been obtained. When the value of θ is made zero, TI material becomes ordinary dielectric and the results of PEMC coated with dielectric material has been reproduced. When the coating is removed, the same results, as that of isolated PEMC circular cylinder, have been reproduced. Making $M\eta_1 \rightarrow \infty$ or 0, PEC and PMC coated with TI material results. By using both aforementioned conditions, results of PEC and PMC coated with ordinary dielectric material have been obtained. Thus, in short, it can be said that the present problem is the most fundamental and generalized which contains all the special cases, i.e., PEC coated with dielectric, PMC coated with dielectric, PEMC coated with dielectric, PEC coated with TI, PMC coated with TI, PEMC coated with TI material can be conveniently achieved. It can also be concluded that the behavior of co- and cross- polarized components vary both in amplitude and shape with variation in geometrical parameters, i.e., $M\eta_1$, θ and ϵ.

ACKNOWLEDGEMENT

The authors of this paper would like to thank the respected anonymous reviewers for their valuable suggestions and comments to improve the quality and worth of the paper.

REFERENCES

[1] A. Karch "Surface plasmons and topological insulators," *Physical Review B*, vol. 83, pp. 245-432, 2011.

[2] X. L. Qi and S. C. Zhang, "Topological insulators and superconductors," *Rev. Mod. Phys.*, vol. 83, pp. 1057-1110, 2011.

[3] L. Zeng, R. Song, and X. Jian, "Scattering of electromagnetic radiations by time reversal perturbation topological circular cylinder," *Modern Physics Letters B*, vol. 27, pp. 13500981-7, 2013.

[4] M. A. Ashraf and M. A. Fiaz, "Scattering from a topological insulator cylinder buried below a slightly rough surface," *Journal of Modern Optics*, vol. 62, pp. 340-347, 2015.

[5] M. Akhtar, N. A. Naz, M. A. Fiaz, and Q. A. Naqvi, "Scattering from topological insulator circular cylinder buried in a semi-infinite medium," *Journal of Modern Optics*, vol. 61, pp. 697-702, 2014.

[6] F. Ashraf, S. Ahmed, A. A. Syed, and Q. A. Naqvi, "Electromagnetic scattering from a topological insulator cylinder placed in chiral medium," *International Journal of Applied Electromagnetics and Mechanics*, vol. 47, pp. 237-244, 2015.

[7] I. V. Lindell and A. H. Sihvola, "Realization of the PEMC boundary," *IEEE Trans. Antennas Propagat.*, vol. 53, no. 9, pp. 3012-3018, 2005.

[8] J. R. Wait, "Scattering of plane waves from a circular dielectric cylinder at oblique incidence," *Can. J. of Phys.*, vol. 33, pp. 189-195, 1995.

[9] H. C. Chen and D. K. Cheng, "Scattering of electromagnetic waves by an anisotropic plasma-coated conducting cylinder," *IEEE Trans. Antennas Propagat.*, vol. AP-12, pp. 348-353, 1964.

[10] M. W. McCall, A. Lakhtakia, and W. S. Weiglhofer, "The negative index of refraction demystify," *Eur. J. Phys.*, vol. 23, pp. 353-359, 2002.

[11] K. E Peiponen, V. Lucarini, E. M. Artiainen, and J. J. Saarinen, "Kramer-Kronig relations and sum rules of negative refractive index media," *Eur. Phys. J. B*, vol. 41, pp. 61-65, 2004.

[12] A.-K. Hamid "Scattering from an arbitrarily incident plane wave by a PEMC elliptic cylinder confocally coated with a chiral material," *ACES Journal*, vol. 30, no. 5, pp. 503-509, May 2015.

[13] S. Shoukat, S. Ahmed, M. A. Ashraf, A. A. Syed, and Q. A. Naqvi, "Scattering of electromagnetic plane wave from a chiral cylinder placed in chiral metamaterials," *Journal of Electromagnetic Waves and Applications*, vol. 27, no. 9, pp. 1127-1135, 2013.

[14] K. Muhammad, A. A. Syed, and Q. A. Naqvi, "Circular cylinder with DB boundary conditions in chiral and chiral nihility media," *International Journal of Applied Electromagnetic and Mechanics*, vol. 44, pp. 59-68, Jan. 2014.

[15] D. Cheng and Y. M. M. Antar, "Scattering from a perfect electric conductor cylinder with inhomogeneous coating thickness of gyroelectric chiral medium extended mode-matching method," *ACES Journal*, vol. 14, no. 2, pp. 59-66, July 1999.

[16] S. Ahmed and Q. A. Naqvi, "Electromagnetic scattering from chiral coated nihility cylinder," *Progress In Electromagnetic Research Letters*, vol. 18, pp. 41-50, 2010.

[17] S. Ahmed and Q. A. Naqvi, "Scattering of electromagnetic waves by a coated nihility cylinder," *Int. Journal of Infrared and Millimeter Waves*, vol. 30, pp. 1044-1052, 2009.

[18] A. Lakhtakia, "An electromagnetic trinity from "negative permittivity" and "negative permeability"," *Int. J. Infrared Millim. Waves*, vol. 23, pp. 813-8, 2002.

[19] A. Lakhtakia, "An electromagnetic trinity from "negative permittivity" and "negative permeability"," *Int. J. Infrared Millim. Waves*, vol. 22, pp. 1731-1734, 2001.

[20] I. V. Lindell and A. H. Sihvola, "Perfect electromagnetic conductor," *Journal of Electromagnetic Waves and Applications*, vol. 19, no. 7, pp. 861-869, 2005.

[21] I. V. Lindell and A. H. Sihvola, "Possible applications of perfect electromagnetic conductor (PEMC) media," *First European Conference on Antennas and Propagation, EuCAP*, 2006.

[22] R. Ruppin, "Scattering of electromagnetic radiation by a perfect electromagnetic conductor cylinder," *J. of Electromagnetic. Waves and Appl*., vol. 20, no. 13, pp. 1853-1860, 2006.

[23] S. Ahmed and Q. A. Naqvi, "Electromagnetic scattering from a perfect electromagnetic conductor cylinder coated with a metamaterial having negative permittivity and/or permeability," *Opt. Communication*, vol. 281, pp. 5664-5670, 2008.

[24] A. Shahzad, S. Ahmed, and Q. A. Naqvi, "Analysis of electromagnetic field due to a buried coated PEMC circular cylinder," *Optics Communications*, vol. 283, pp. 4563-4571, 2010.

[25] A. Shahzad, F. Qasim, S. Ahmed, and Q. A. Naqvi, "Cylindrical invisibility cloak incorporating PEMC at perturbed void region," *Progress in Electromagnetics Research M*, vol. 21, pp. 61-76, 2011.

[26] A. Ghaffar, M. Z. Yaqoob Majeed, A. S. Alkanhal, M. Sharif, Q. A. Naqvi, and Y. Ando, "Electromagnetic scattering from anisotropic plasma-coated perfect electromagnetic conductor cylinders," *AEUE International Journal of Electronics and Communication*, vol. 68, pp. 767-772, 2014.

Anjum Shahzad was born in Malakwal Mandi Bauh-ud-Din (Pakistan) in December, 1985. He received his M.Sc. and M.Phil. degrees in Electronics from Quaid-i-Azam University in 2007 and 2010, respectively. He received Gold Medal from the Quaid-i-Azam University. He is the author of three international publications. He is currently working towards his Ph.D. His current research interest includes techniques used in buried landmines detection and stealing, electromagnetic cloaks and scattering from canonical objects.

Ahsan Illahi received his Ph.D. degree in Electromagnetics from Quaid-i-Azam University in 2010. Currently he is working as Assistant Professor of Physics in COMSATS Institute of Information Technology (CIIT), Islamabad Pakistan. He is active member of RIMS (Research in Modeling and Simulation) Group at CIIT, Islamabad. His research interests include Modeling and Simulations of physical systems in various fields of science along with the Electromagnetics.

Shakeel Ahmed was born in a village Baldher (KPK), Pakistan. He received his initial education from his native town. He graduated from the University of Peshawer and received his Ph.D. from Quaid-i-Azam University, Islamabad (Pakistan). He is author of over twenty (20) international journal publications. His current research interests include electromagnetic scattering from different types of geometries and materials.

Akhtar Hussain was born in a small village of district Narowal (Pakistan). He received the degrees of M.Sc. in Physics and Nuclear Engineering from the University of the Punjab and Pakistan Institute of Engineering and Applied Sciences Islamabad, respectively. He received the degree of Ph.D. from Qauid-e-Azam University Islamabad in 2010. He is the author of over a dozen research papers. His research interests include Fractional electromagnetics, Computational electromagnetics Wave guides, Transmission lines and Scattering.

Qaisar Abbas Naqvi was born in village of District Narowal (Pakistan). He received his M.Sc., M. Phil. and Ph.D. from Quaid-i-Azam University Islamabad (Pakistan). He has published over one hundred and fifty (150) papers in international journals. He also author of a book and chapters in different books. He has successfully supervised eight Ph.D.'s and more than 80 M. Phil. students after his Ph.D. in 1998. His research interests are: Kobyashi potential, Maslov's Method, GTD, Fractional electromagnetics, buried cylinders, waveguides, slits, strips, antennas and numerical electromagnetics.

Nonlinear Analysis and Performance Improvement of Amplifying Aperture Coupled Reflectarray Antenna

I. Aryanian, A. Abdipour, and G. Moradi

Department of Electrical Engineering
Amirkabir University of Technology, Tehran, 15914, Iran
iman_aryanian@aut.ac.ir, abdipour@aut.ac.ir, ghmoradi@aut.ac.ir

Abstract **─** Amplifying reflectarray antenna can be used to increase the overall gain of the antenna in large distance communication systems. However, amplifying reflectarray antenna may become nonlinear in some incident powers which may lead to performance degradation. In this paper nonlinear behavior of an amplifying reflectarray antenna is studied and a new method is proposed to improve the performance of the antenna. Nonlinear analysis of the active unit cell is performed using harmonic balance method considering nonlinear model of the amplifier. Then, the effect of nonlinear element in radiation pattern of the antenna is studied. Aperture coupled patch structure is used to analyze amplifying unit cell. Finally, an amplifying reflectarray antenna considering nonlinear behavior of the active elements is designed and the proposed balanced amplifier structure is used to improve performance of the amplifying antenna.

Index Terms **─** Active antenna, antenna array, harmonic balance method, nonlinear analysis, reflectarray antenna.

I. INTRODUCTION

Printed reflectarray has some advantages compared to the usual reflectors, four of which - i.e., saving volume, simplifying the mechanical design, applying easily to deployable reflectors, and capability of integrating active elements by the antenna structure are of great importance. Different unit cell shapes are proposed to improve the reflectarray antenna performance which introduce the required phase-shift on the reflected field to produce a focused or shaped beam. Required phase shift can be obtained using resonating patches [1] or by a transmission line of proper length connected [2] or aperture-coupled to the patches [3, 4] with different size or using active elements like PIN diodes [5] or varactor diodes [6].

Using high gain antenna for large distance communication is necessary to improve performance of communication link. In these cases, usually reflector antenna or phased array antenna is used. However, manufacturing reflector antenna is difficult especially in high frequencies and phased array antenna may have some problems like unwanted radiation from the feed network. Amplifying reflectarray antenna is proposed in [3, 4, 7] which uses amplifier in each unit cell to increase gain of the antenna. Using an amplifier in the antenna structure results in difficulties in the antenna design and some issues should be determined like stability of the antenna. Moreover, the active element acts nonlinear and this necessitates the nonlinear analysis of the antenna structure. So, [8] studies nonlinear analysis of amplifying reflectarray antenna and [6] studies nonlinear analysis of reflectarray antenna containing varactor diodes.

This paper shows the importance of nonlinear analysis of active reflectarray antenna, and also the influence of nonlinear element in radiation pattern is clarified. The main output of this work is that by the explained method, the impact of nonlinearities on the performance of reflectarrays can be investigated. Furthermore, any active reflectarray cell having active device by any nonlinear model can be used in the analysis and the impact of the model parameters can be studied. Also, a new structure using balanced amplifier is used to improve antenna performance. This performance improvement will be cleared by designing a sample antenna with and without using the proposed cell.

To analyze the active reflectarray antenna, first the cell removing the amplifier is simulated using HFSS software considering infinite array approach to obtain the passive unit cell scattering parameters in which the amplifier is replaced by a two port network and two spatial ports modelled as Floqute port are assumed representing two orthogonal polarizations. So, a 4 port network is obtained which its scattering parameters are known. In the next step, an amplifier which has nonlinear model is connected to the 4 port network and the active cell performance is studied to obtain the cell amplitude response by varying the incident power to the cell. Finally, obtained nonlinear response of the cell is used to design the antenna. Verification of the nonlinear response of the unit cell is done by ADS simulation.

Submitted On: July 4, 2015
Accepted On: August 1, 2016

This process is carried out for a sample active unit cell in the center frequency of 6.2 GHz and detailed steps are explained.

II. UNIT CELL MODELING

In aperture coupled microstrip antenna structure, each cell consists of a microstrip line coupled to the radiating patch on the opposite side of the substrate via an aperture in the ground plane as shown in Fig. 1. In this paper cross-polarized element configuration is used like [3, 4] to prevent instability, where the incident and scattered fields are orthogonally-polarized. Unit cell consists of a dual-polarized aperture coupled microstrip patch and an amplifier connected between the two ports in the microstrip line path. Also, as in this paper our goal is to evaluate the performance of the active element, an ideal phase shifter is used to control the phase of the reflected signal. Parameters of the unit cell are given in Table 1. Dielectric constant of top substrate is 3.02 with a height of 1.524 mm, and dielectric constant of bottom substrate is 6.15 with a height of 1.28 mm.

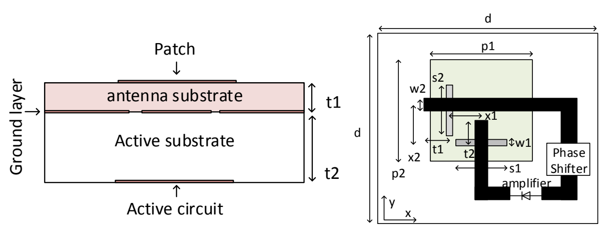

Fig. 1. Antenna unit cell schematic.

Table 1: Unit cell parameters

Parameter	Value	Parameter	Value
d	33.56 mm	t1	6 mm
p1	14.3 mm	t2	2.5 mm
P2	13.9 mm	W2	1.87 mm
S1	6.3 mm	X1	1.5 mm
S2	8.8 mm	X2	5.7 mm
W1	0.75 mm		

The passive part of the cell is modelled as a 4 port network in which ports 3 and 4 are spatial ports modelled as Floqute port [9], and the amplifier is connected between ports 1 and 2. So, the passive part of the unit cell removing the amplifier is simulated using HFSS software supposing infinite array to obtain 4 port scattering parameters as shown in Fig. 2.

Next, active element is connected between ports 1 and 2 of the obtained 4 port network as shown in Fig. 2 to obtain the active cell response in linear or nonlinear states. Active element used in this work is NE4210 which has nonlinear TOM model [10] and can be simulated in ADS software. Nonlinear TOM model is shown in Fig. 3 which has two nonlinear capacitances of C_{gs} and C_{gd}, and one nonlinear current source of I_{ds}. Relations for current source of I_{ds}, and capacitances of C_{gs} and C_{gs} of TOM model are given in (1) to (5) and parameters of the nonlinear model of NE4210 are given in Table 2.

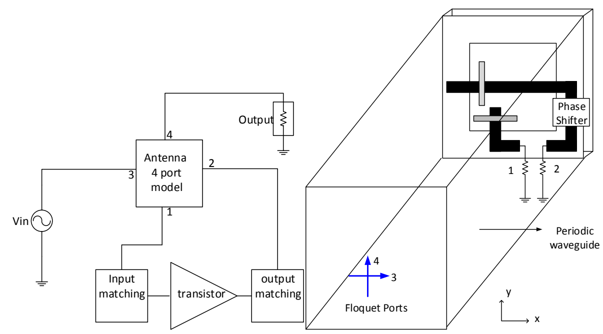

Fig. 2. Four port modelling of the unit cell.

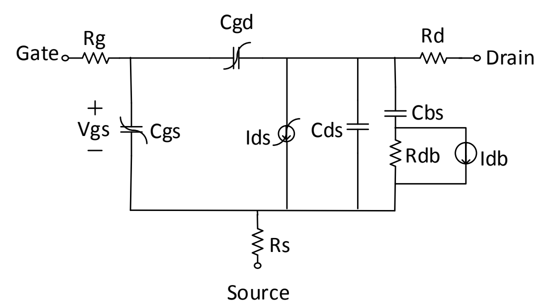

Fig. 3. Nonlinear TOM model.

Table 2: Parameters of the nonlinear model

Parameter	Value	Parameter	Value
V_{t_0}	-0.798 (V)	C_{gs0}	0.36 pF
α	8 (1/V)	C_{gd0}	0.014 pF
β	0.0952 (A/V^Q)	Δ_1	0.3 (V)
$T_{q\Delta}$	0.5 (1/W)	Δ_2	0.6 (V)
$T_{q\gamma}$	0.065	Rg	8 Ohm
Q	2.5	Rd	0.5 Ohm
Cds	0.12 pF	Rs	3 Ohm
Rdb	5 KOhm	Cbs	1 nF
F_c	0.5	V_{bi}	0.6 (V)

Current source of I_{ds} in TOM model is given as:

$$I_{ds} = \frac{I_{ds_0}}{1 + T_{q\Delta} \times V_{ds} \times I_{ds_0}}, \tag{1}$$

where

$$I_{ds_0} = \begin{cases} \beta\left(V_{gs} - V_t\right)^Q \times \left[1 - \left[1 - \dfrac{\alpha V_{ds}}{3}\right]^3\right] & 0 < V_{ds} < 3/\alpha, \\ \beta\left(V_{gs} - V_t\right)^Q & V_{ds} \geq 3/\alpha, \end{cases} \tag{2}$$

$$V_t = \left(V_{t0} + V_{t0sc}\right) - T_{q\gamma} \times V_{ds}, \tag{3}$$

and Q, $T_{q\gamma}$, $T_{q\Delta}$, α, V_{t_0}, β are parameters of the model. Also, capacitances of C_{gs} and C_{gs} in TOM model are obtained as:

$$C_{gs} = \frac{\partial Q_{gs}}{\partial V_{gs}} + \frac{\partial Q_{gd}}{\partial V_{gs}} = \frac{C_{gs0}}{2\sqrt{1 - \dfrac{V_n}{V_{bi}}}}\left[1 + \frac{V_{eff} - V_{t_0}}{\sqrt{\left(V_{eff} - V_{t_0}\right)^2 + \Delta^2}}\right] \times \frac{1}{2} \times \left(1 + \frac{V_{gs} - V_{gd}}{\sqrt{\left(V_{gs} - V_{gd}\right)^2 + \Delta^2}}\right) + \frac{C_{gd0}}{2}\left(1 - \frac{V_{gs} - V_{gd}}{\sqrt{\left(V_{gs} - V_{gd}\right)^2 + \Delta^2}}\right), \tag{4}$$

$$C_{gd} = \frac{\partial Q_{gd}}{\partial V_{gd}} + \frac{\partial Q_{gs}}{\partial V_{gd}} = \frac{C_{gs0}}{2\sqrt{1 - \dfrac{V_n}{V_{bi}}}}\left[1 + \frac{V_{eff} - V_{t_0}}{\sqrt{\left(V_{eff} - V_{t_0}\right)^2 + \Delta^2}}\right] \times \frac{1}{2} \times \left(1 + \frac{V_{gs} - V_{gd}}{\sqrt{\left(V_{gs} - V_{gd}\right)^2 + \Delta^2}}\right) + \frac{C_{gd0}}{2}\left(1 + \frac{V_{gs} - V_{gd}}{\sqrt{\left(V_{gs} - V_{gd}\right)^2 + \Delta^2}}\right), \tag{5}$$

where

$$V_{new} = \frac{1}{2}\left(V_{eff} + V_{t_0}\right) + \sqrt{\left(V_{eff} - V_{t_0}\right)^2 + \Delta_2{}^2}, \tag{6}$$

$$V_{eff} = \frac{1}{2}\left[\left(V_{gs} + V_{gd}\right) + \sqrt{\left(V_{gs} - V_{gd}\right)^2 + \Delta^2}\right], \tag{7}$$

$$\Delta = \begin{cases} \Delta_1 & if \quad \Delta_1 \, is \quad specified \\ 1/\alpha & else \end{cases}, \tag{8}$$

$$V_n = \begin{cases} V_{new} & if \quad V_{new} < \min(\mathrm{F}_c \times \mathrm{V}_{bi}, \mathrm{V}_{\max}) \\ \min(\mathrm{F}_c \times \mathrm{V}_{bi}, \mathrm{V}_{\max}) & else \end{cases}. \tag{9}$$

III. HARMONIC BALANCE ANALYSIS

Using harmonic balance method [11], the nonlinear analysis of the unit cell is performed by dividing the unit cell into two nonlinear and linear networks as shown in Fig. 4. Nonlinear part consists of nonlinear capacitances and nonlinear current source. Also, linear part consists of 4-port network of the unit cell and passive elements. Voltages of V_1, V_2 and V_3 of Fig. 4 should be evaluated so that $I_i + \tilde{I}_i = 0$. Harmonic balance equation can be solved with different methods, among which the Newton-Raphson [11] technique is the most common technique and is used in this paper. Assuming nonlinear TOM model for the transistor, total directivity of the unit cell will be obtained in Section V for different incident power which will show the nonlinear behavior of the cell.

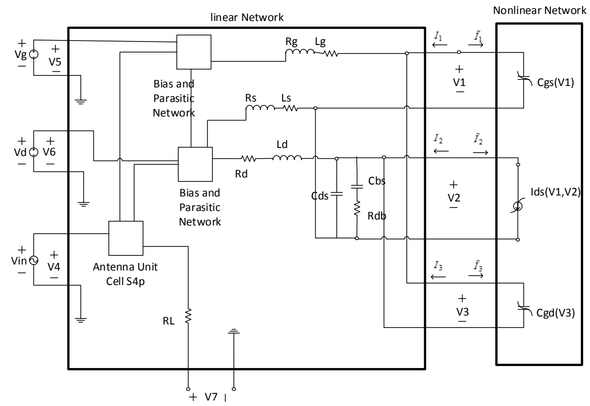

Fig. 4. Dividing the unit cell to nonlinear and linear networks.

IV. PERFORMANCE IMPROVRMENT OF THE CELL

In this part a new configuration using balanced amplifier is introduced to improve stability of the designed amplifying reflectarray antenna as shown in Fig. 5. Also, this configuration increases the power compression point of the cell which improves the antenna gain in nonlinear states. Using balanced amplifier in amplifying reflectarray antenna has some advantages. First, if the amplifiers are identical, the VSWR from the balanced structure is near 1 and it improves stability of the structure which is a problem in active reflectarray antenna. Moreover, output power is twice that achieved from the single amplifier, and if one of the amplifiers fails, the balanced amplifier unit will still work with reduced gain. Another important advantage of using balanced amplifier in amplifying reflectarray antenna is the ability of easily cascading active unit with other units, like phase shifter, since each unit is isolated by the coupler.

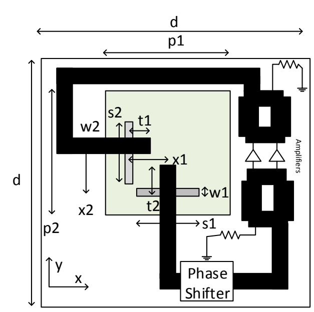

Fig. 5. Proposed unit cell for performance improvement.

V. RESULTS

Stability of the active part is identified by geometrically derived stability factor M [12]. This measurement gives the distance from the center of the Smith chart to the nearest output (load) stability circle. This stability factor is given by:

$$M = \left(\frac{1-|S_{11}|^2}{|S_{22} - conj\,(S_{11}) * \Delta| + |S_{12} * S_{21}|} \right), \qquad (10)$$

where Δ is determinant of the S-parameter matrix. Having $M > 1$ is the single necessary and sufficient condition for unconditional stability of a 2-port network. M factor for one stage amplifier is given in Fig. 6, which shows that the active part may become unstable in the frequency of operation.

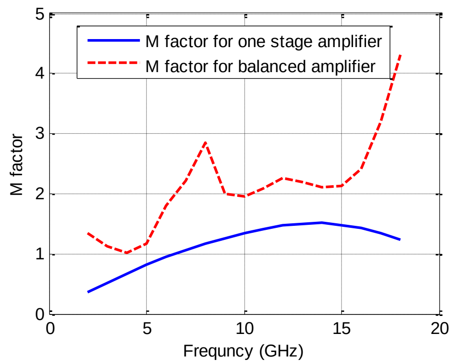

Fig. 6. M factor for one stage amplifier and balanced amplifier.

M factor for balanced amplifier is shown in Fig. 6 which has minimum of 1.01 and shows improvement in stability of the active part. Also, output power of the cell versus incident power for first design and improved cell is shown in Fig. 7 and gain of the cell versus incident power for first design and improved cell is shown in Fig. 8.

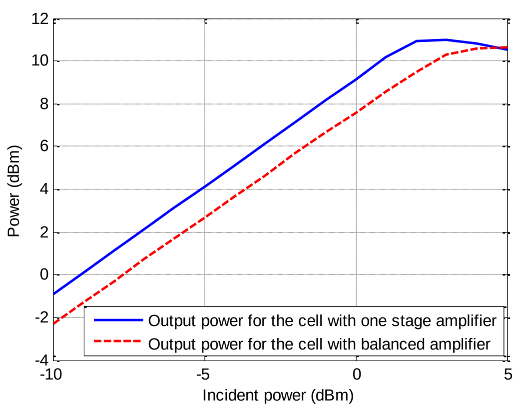

Fig. 7. Output power of the cell versus incident power for the first design and improved cell.

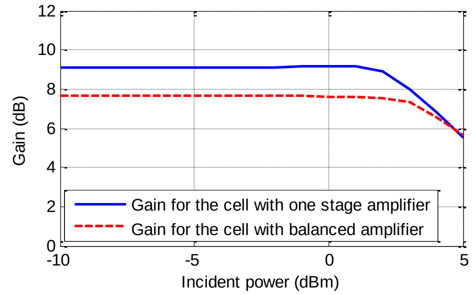

Fig. 8. Gain of the cell versus incident power for the first design and improved cell.

VI. SAMPLE ANTENNA DESIGN

In this section it is shown that the power received in each cell is different and as a result each cell may have different gain and phase. Phase of the received field from the feed antenna at each cell is shown in Fig. 9.

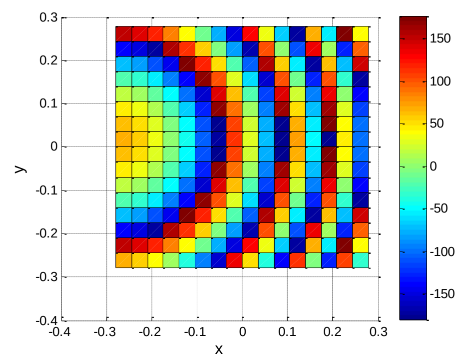

Fig. 9. Phase of the received field from the feed antenna at each cell.

Knowing the magnitude of y polarization electric field in each cell $\tilde{E}_y^R(u,v)$, power delivered to each cell is obtained as:

$$P(x,y) = \frac{\left(\tilde{E}_y^R(u,v)\right)^2}{2*\eta_0}. \qquad (11)$$

To simulate the active antenna, a 59.2 cm * 59.2 cm antenna is designed in the center frequency of 6.2 GHz by focal length of 74 cm. If we assume center of the antenna as center of Cartesian coordinates, feed antenna is placed in (-29.6 cm, 0, 74 cm). Assuming transmitted feed antenna power in a way that the power distribution on the antenna surface is like Fig. 10, most active elements become nonlinear, and the impact of nonlinearity of each cell should be considered. For this reason amplitude and phase differences caused by the nonlinear amplifier in each cell should be considered.

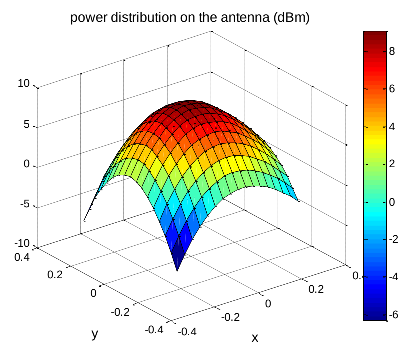

Fig. 10. Supposed power on the antenna surface.

Considering amplitude behavior of the unit cell shown in Fig. 8, and the power distribution on antenna surface shown in Fig. 10, amplitude error of each unit cell is calculated as shown in Fig. 11.

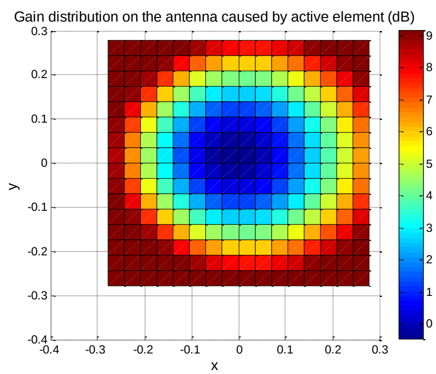

Fig. 11. Amplitude error of each unit cell.

The errors in the amplitude and phase of the reflected signal from each cell can cause gain reduction. However, phase error is low in comparison to amplitude error and can be neglected in this scenario. Antenna directivity with and without considering the nonlinear effect of active elements is shown in Fig. 12, when feed power is so that some cells are in nonlinear region and maximum difference between linear and nonlinear analysis can be obtained. In this case, nonlinear analysis shows degradation in gain which cannot be assessed by linear analysis. So, because of the nonlinear behavior of the active elements, maximum gain of the designed antenna decreases from 41 dBi to 37.5 dBi as shown in Fig. 12. Therefore, to assess the pattern of the active reflectarray antenna correctly, for all feed power, the nonlinear impact of amplifier should be considered. It is worth mentioning when feed power is so that all cells are in linear region, linear and nonlinear simulations have the same results.

Using the balanced amplifier by nonlinear response shown in Fig. 8 and considering the power distribution like Fig. 10, the antenna is analyzed again which shows that the antenna gain is increased to 40.2 dBi where gain reduction is decreased to about 0.8 dB and 2.7 dB improvement is reached.

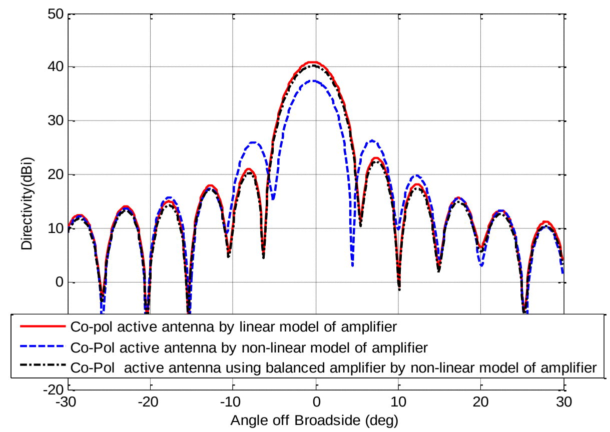

Fig. 12. Performance improvement of the antenna using balanced amplifier when feed power is so that some cells are in nonlinear region.

VII. CONCLUSION

It is shown that in some cases, nonlinear analysis of amplifying reflectarray antenna is needed. This paper uses a method combining linear full-wave simulations with the harmonic balance method to predict impact of nonlinearities on the unit cell characteristics of active reflectarrays, as well as on the pattern produced by the reflectarrays. Next, result of nonlinear analysis has been used to design a sample antenna which shows that predicting pattern of the antenna with linear modelling of the active element has error. Finally, a new structure is proposed to improve performance of amplifying reflectarray antenna which improves stability of the antenna and increases total gain of the antenna when incident power is such that the active elements are in nonlinear state. Using the proposed cell, antenna gain reduction in nonlinear state is decreased.

ACKNOWLEDGEMENTS

The authors would like to thank Mr. Hamed Golestaneh for his helpful comments.

REFERENCES

[1] D. Pozar and T. Metzler, “Analysis of a reflectarray antenna using microstrip patches of variable size,” *Electronics Letters*, vol. 29, pp. 657-658, 1993.

[2] R. S. Malfajani and Z. Atlasbaf, “Design and implementation of a broadband single-layer reflectarray antenna with large-range linear phase

elements," *Antennas and Wireless Propagation Letters, IEEE*, vol. 11, pp. 1442-1445, 2012.

[3] M. E. Bialkowski, A. W. Robinson, and H. J. Song, "Design, development, and testing of X-band amplifying reflectarrays," *Antennas and Propagation, IEEE Transactions on*, vol. 50, pp. 1065-1076, 2002.

[4] K. K. Kishor and S. V. Hum, "An amplifying reconfigurable reflectarray antenna," *Antennas and Propagation, IEEE Transactions on*, vol. 60, pp. 197-205, 2012.

[5] I. Aryanian, A. Abdipour, and G. Moradi, "Design fabrication and test of an X-band dual polarized aperture coupled reflectarray element for beam switching," *Turkish Journal of Electrical Engineering and Computer Sciences*, pp. 1-10, 2016.

[6] I. Aryanian, A. Abdipour, and G. Moradi, "Nonlinear analysis of active aperture coupled reflectarray antenna containing varactor diode," *Applied Computational Electromagnetics Society Journal*, vol. 30, 2015.

[7] R. W. Clark, G. H. Huff, and J. T. Bernhard, "An integrated active microstrip reflectarray element with an internal amplifier," *Antennas and Propagation, IEEE Transactions on*, vol. 51, pp. 993-999, 2003.

[8] I. Aryanian, A. Abdipour, and G. Moradi, "Studying the nonlinear performance of an amplifying reflectarray antenna," *International Journal of Microwave and Wireless Technologies*, pp. 1-11, 2016.

[9] J. Huang, *Reflectarray Antenna*. Wiley Online Library, 2005.

[10] A. J. McCamant, G. D. McCormack, and D. H. Smith, "An improved GaAs MESFET model for SPICE," *Microwave Theory and Techniques, IEEE Transactions on*, vol. 38, pp. 822-824, 1990.

[11] S. A. Maas, *Nonlinear Microwave and RF Circuits*. Artech House, 2003.

[12] M. L. Edwards and J. H. Sinsky, "A new criterion for linear 2-port stability using a single geometrically derived parameter," *IEEE Transactions on Microwave Theory and Techniques*, vol. 40, pp. 2303-2311, 1992.

Iman Aryanian was born in Iran in 1986. He obtained his B.Sc. in Electrical Engineering from Amirkabir University of Technology, Tehran, Iran in 2008. Then he received his M.Sc. in Electrical Communication Engineering from Amirkabir University of Technology, Tehran, Iran in 2010, and his Ph.D. degree in the same field from Amirkabir University of Technology, Tehran, Iran in 2016. His research interests are in the areas of reflectarray antenna, computational electromagnetic, semiconductor RF modeling, electromagnetic theory, and computational electromagnetics.

Abdolali Abdipour was born in Alashtar, Iran, in 1966. He received his B.Sc. degree in Electrical Engineering from Tehran University, Tehran, Iran, in 1989, his M.Sc. degree in Electronics from Limoges University, Limoges, France, in 1992, and his Ph.D. degree in Electronic Engineering from Paris XI University, Paris, France, in 1996. He is currently a Professor with the Electrical Engineering Department, Amirkabir University of Technology (Tehran Polytechnic), Tehran, Iran.

Gholamreza Moradi was born in Shahriar, Iran in 1966. He received his B.Sc. in Electrical Communication Engineering from Tehran University, Tehran, Iran in 1989, and the M.Sc. in the same field from Iran University of Science and Technology in 1993. Then he received his Ph.D. degree in Electrical Engineering from Tehran Polytechnic University, Tehran, Iran in 2002. His research areas include applied and numerical Electromagnetics, Microwave measurement and antenna.

Parameterized Model Order Reduction for Efficient Time and Frequency Domain Global Sensitivity Analysis of PEEC Circuits

L. De Camillis [1], G. Antonini [1], and F. Ferranti [2]

[1]UAq EMC Laboratory, Dipartimento di Ingegneria Industriale e dell'Informazione e di Economia, Università degli Studi dell'Aquila, Via G. Gronchi 18, 67100, L'Aquila, Italy
luca.decamillis@gmail.com, giulio.antonini@univaq.it

[2]Department of Fundamental Electricity and Instrumentation, Vrije Universiteit Brussel, Pleinlaan 2, B-1050 Brussels, Belgium
francesco.ferranti@vub.ac.be

Abstract – This paper presents a new parameterized model order reduction technique to efficiently perform global time- and frequency-domain sensitivity analysis of electromagnetic systems over the design space of interest. The partial element equivalent circuit (PEEC) method is adopted to build the electromagnetic system model at a set of initial samples in the design space. The block Laguerre-SVD algorithm is proposed to reduce the size of the original equations of the PEEC-based equivalent circuit along with those describing the port voltage and current sensitivities. Then, a multivariate cubic spline interpolation method is used to build a parameterized compact model of port voltages and currents along with their corresponding sensitivities over the entire design space of interest. Finally, two numerical examples are presented, which confirm the accuracy and efficiency of the proposed method.

Index Terms – Parameterized model order reduction, partial element equivalent circuit, sensitivity analysis, time- and frequency-domain circuit simulation.

I. INTRODUCTION

The need to improve the performances of electromagnetic (EM) structures during their early design stage has made sensitivity analysis a necessary tool. The sensitivities represent the system response gradients in the design parameter space, where the design parameters are related to the geometry and/or the materials of the EM structure.

The simplest way to compute sensitivities is represented by the perturbation method, which requires to analyze the EM structure for two different values of each design parameter for a specific nominal point in the design space. It is computationally expensive and often inaccurate, therefore impractical when the number of design parameters to take into account is large and a global sensitivity analysis over the design space of interest is required. Recently, significant progress has been made towards the development of sensitivity analysis approaches to be used along with EM simulators, involving conducting and dielectric objects, both in time- and frequency-domain [1–8]. Differential and integral equation-based methods have been considered for sensitivity analysis [9, 10]. Typical fields of applications are optimization of microwave devices, modeling of signal integrity (SI)/power integrity (PI) problems, control of crosstalk for electromagnetic compatibility (EMC) purposes. These techniques usually turn to be highly demanding in terms of both CPU time and memory resources, since they perform the sensitivity analysis using EM solvers and/or manipulating matrices describing the EM system which are typically very large.

Among EM methods, the partial element equivalent circuit (PEEC) [11] has gained increasing popularity because of its ability to transform the EM system under examination into an equivalent circuit [11–16] that can be represented by modified nodal analysis (MNA) matrix circuit equations [17], studied by means of Kirchoff principles and simulated using circuit solvers. The PEEC method uses a circuit interpretation of the electric field integral equation (EFIE) [18].

In the context of sensitivity analysis, a PEEC-based method to carry out parameterized sensitivity analysis of EM systems that depend on multiple design parameters has been proposed in [19]. The PEEC method is used to compute state-space matrices of the MNA equations for a set of values of design parameters (e.g., geometrical and substrate parameters). An interpolation process provides parameter-

Submitted On: August 25, 2015
Accepted On: January 25, 2016

ized models of these matrices as functions of design parameters [20]. The proposed interpolation scheme is able to compute derivatives of EM matrices, which are needed to perform the system sensitivity analysis. Thus, the algorithm provides sensitivity information over the entire design space of interest (global sensitivity), and not only around one operating point (local sensitivity). Although the method [19] is very accurate and more efficient with respect to the perturbative approach, it suffers from a high computational cost when the size of the MNA matrices of the PEEC circuits becomes large. In [21], a parameterized sensitivity analysis based on a parameterized model order reduction (PMOR) technique is presented. The finite element method is used to generate the equations of the original network, a multiparameter moment matching PMOR technique and an adjoint variable method are used to calculate frequency-domain sensitivities.

In this paper, we propose a new parameterized model order reduction (PMOR) technique to efficiently perform global time- and frequency-domain sensitivity analysis of electromagnetic systems over the design space of interest. The PEEC method is adopted to generate a set of PEEC MNA equations and corresponding state-space matrices at a set of design space points. For each of these points in the design space, the block Laguerre-SVD algorithm is proposed to reduce the size of the original equations of the PEEC-based equivalent circuit along with those describing the port voltage and current sensitivities. Then, a methodology based on a multivariate cubic spline interpolation is used to build a parameterized compact model of port voltages and currents along with their corresponding sensitivities over the entire design space of interest. The proposed technique shows a significantly improved efficiency when performing a global sensitivity analysis with respect to the method [19], while maintaining a high accuracy.

The paper is organized as follows. Section II briefly describes the PEEC formulation and the sensitivity formulation while Section III presents the proposed parameterized model order reduction algorithm. Finally some numerical examples are presented in Section IV to validate the proposed technique.

II. PEEC SENSITIVITY FORMULATION

In what follows, we consider a quasi-static PEEC formulation [12]. The Galerkin's approach is applied to convert the continuous electromagnetic problem described by the EFIE to a discrete problem in terms of electrical circuit quantities, i.e., currents $\boldsymbol{i}(t)$ and

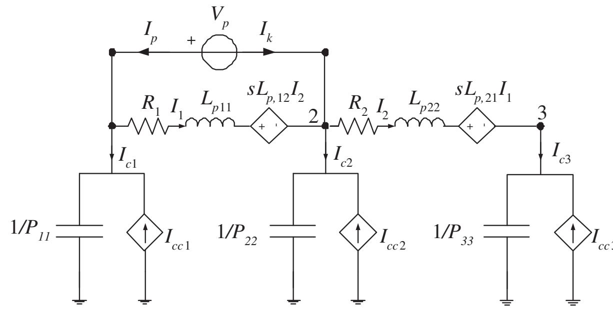

Fig. 1. Illustration of PEEC circuit electrical quantities for a conductor elementary cell.

node potentials $\boldsymbol{v}(t)$. An example of PEEC electrical quantities for a conductor elementary cell is illustrated, in the Laplace domain, in Fig. 1 where the current controlled voltage sources $sL_{p,ij}I_j$ and the current controlled current sources I_{cci} model the magnetic and electric field coupling, respectively. Let us denote with n_n the number of the nodes and with n_b the number of branches where currents flow. Among this latter, n_c and n_d represent the branches of conductors and dielectrics, respectively. Furthermore, let us assume to be interested in generating an admittance ($\mathbf{Y}$) representation having n_p output currents $\boldsymbol{i}_p(t)$ under voltage excitation $\boldsymbol{v}_p(t)$. Using the MNA formulation [17], the following admittance representation is obtained [20]:

$$\begin{bmatrix} \mathbf{P} & \mathbf{0}_{n_n,n_b} & \mathbf{0}_{n_n,n_d} & \mathbf{0}_{n_n,n_p} \\ \mathbf{0}_{n_b,n_n} & \mathbf{L}_p & \mathbf{0}_{n_b,n_d} & \mathbf{0}_{n_b,n_p} \\ \mathbf{0}_{n_d,n_n} & \mathbf{0}_{n_d,n_b} & \mathbf{C}_d & \mathbf{0}_{n_d,n_p} \\ \mathbf{0}_{n_p,n_n} & \mathbf{0}_{n_p,n_b} & \mathbf{0}_{n_p,n_d} & \mathbf{0}_{n_p,n_p} \end{bmatrix} \frac{d}{dt} \begin{bmatrix} \boldsymbol{q}(t) \\ \boldsymbol{i}(t) \\ \boldsymbol{v}_d(t) \\ \boldsymbol{i}_k(t) \end{bmatrix} =$$
$$- \begin{bmatrix} \mathbf{0}_{n_n,n_n} & -\mathbf{P}\mathbf{A}^{\mathrm{T}} & \mathbf{0}_{n_n,n_d} & \mathbf{P}\mathbf{K}^{\mathrm{T}} \\ \mathbf{A}\mathbf{P} & \mathbf{R} & \boldsymbol{\Phi} & \mathbf{0}_{n_b,n_p} \\ \mathbf{0}_{n_d,n_n} & -\boldsymbol{\Phi}^{\mathrm{T}} & \mathbf{0}_{n_d,n_d} & \mathbf{0}_{n_d,n_p} \\ -\mathbf{K}\mathbf{P} & \mathbf{0}_{n_p,n_b} & \mathbf{0}_{n_p,n_d} & \mathbf{0}_{n_p,n_p} \end{bmatrix} \cdot \begin{bmatrix} \boldsymbol{q}(t) \\ \boldsymbol{i}(t) \\ \boldsymbol{v}_d(t) \\ \boldsymbol{i}_k(t) \end{bmatrix} +$$
$$\begin{bmatrix} \mathbf{0}_{n_n+n_b+n_d,n_p} \\ -\mathbf{I}_{n_p,n_p} \end{bmatrix} \cdot \begin{bmatrix} \boldsymbol{v}_p(t) \end{bmatrix}, \quad (1)$$

$$\boldsymbol{i}_p(t) = \begin{bmatrix} \mathbf{0}_{n_n+n_b+n_d,n_p} \\ -\mathbf{I}_{n_p,n_p} \end{bmatrix}^T \cdot \begin{bmatrix} \boldsymbol{q}(t) \\ \boldsymbol{i}(t) \\ \boldsymbol{v}_d(t) \\ \boldsymbol{i}_k(t) \end{bmatrix}, \quad (2)$$

where $\mathbf{P} \in \mathbb{R}^{n_n \times n_n}$ and $\mathbf{L}_p \in \mathbb{R}^{n_b \times n_b}$ are the coefficients of potential and partial inductance matrices, respectively, $\mathbf{R} \in \mathbb{R}^{n_b \times n_b}$ is a diagonal matrix containing the resistances of volume cells and $\mathbf{C}_d \in \mathbb{R}^{n_d \times n_d}$ is the excess capacitance matrix describing the polarization charge in dielectrics [22]. $\mathbf{A} \in \mathbb{R}^{n_b \times n_n}$ is the connectivity matrix, while $\mathbf{K} \in \mathbb{R}^{n_p \times n_n}$ is a selection matrix introduced to define the port voltages in terms of node potentials:

$$\boldsymbol{v}_p(t) = \mathbf{K}\ \boldsymbol{v}(t). \quad (3)$$

In (1), $\boldsymbol{q}(t) \in \mathbb{R}^{n_n \times 1}$ represents the charges on the conductors, $\boldsymbol{i}(t) \in \mathbb{R}^{n_b \times 1}$ is the vector of volume currents, $\boldsymbol{v}_d(t) \in \mathbb{R}^{n_d \times 1}$ describes the voltage drop across the excess capacitance and $\boldsymbol{i}_k(t) \in \mathbb{R}^{n_p \times 1}$ represents the port currents. $\mathbf{I}_{n_p,n_p}$ is the identity matrix of dimension equal to the number of ports and $\mathbf{\Phi}$ is:

$$\mathbf{\Phi}=\begin{bmatrix}\mathbf{0}_{n_c,n_d}\\ \mathbf{I}_{n_d,n_d}\end{bmatrix}. \tag{4}$$

The vector $\boldsymbol{i}_p(t)$ describes the n_p port currents that are of opposite sign with respect to $\boldsymbol{i}_k(t)$. The system of equations (1)-(2) is typically ill-conditioned because the values of charges are usually much smaller than those of currents and voltages. In order to mitigate such a problem, a scaling scheme can be adopted [20]. Equations (1)-(2) can be easily translated from the $\mathbf{Y}$ representation to an impedance ($\mathbf{Z}$) representation [19] that can be expressed in a compact form as:

$$\begin{aligned}\mathbf{C}\,\dot{\boldsymbol{x}}(t)&=-\mathbf{G}\,\boldsymbol{x}(t)+\mathbf{B}\,\boldsymbol{i}_p(t)\\ \boldsymbol{v}_p(t)&=\mathbf{L}^{\mathrm{T}}\boldsymbol{x}(t),\end{aligned} \tag{5}$$

where $\mathbf{C} \in \mathbb{R}^{n_s \times n_s}$, $\mathbf{G} \in \mathbb{R}^{n_s \times n_s}$, $\mathbf{B} \in \mathbb{R}^{n_s \times n_p}$, $\mathbf{L} = \mathbf{B}$, $\boldsymbol{x}(t) = [\boldsymbol{q}(t)\ \boldsymbol{i}(t)\ \boldsymbol{v}_d(t)]^{\mathrm{T}} \in \mathbb{R}^{n_s \times 1}$ and $n_s = n_n + n_b + n_d$ is the number of state variables [19].

Considering now the influence of the design parameters $\boldsymbol{g} = (g_1, ..., g_{\mathrm{M}})$, the formulation (5) becomes:

$$\begin{aligned}\mathbf{C}(\boldsymbol{g})\,\dot{\boldsymbol{x}}(t,\boldsymbol{g})&=-\mathbf{G}(\boldsymbol{g})\mathbf{x}(t,\boldsymbol{g})+\mathbf{B}(\boldsymbol{g})\,\boldsymbol{i}_p(t)\\ \boldsymbol{v}_p(t,\boldsymbol{g})&=\mathbf{L}^{T}(\boldsymbol{g})\mathbf{x}(t,\boldsymbol{g}).\end{aligned} \tag{6}$$

In [19], the sensitivity of the voltage outputs with respect to M design parameters $\boldsymbol{g} = (g_m)_{m=1}^{M}$ was computed deriving (6). Merging the original system and corresponding sensitivity system, a new full system can be written as:

$$\begin{aligned}\begin{bmatrix}\mathbf{C}(\boldsymbol{g}) & 0\\ \widehat{\mathbf{C}}(\boldsymbol{g}) & \mathbf{C}(\boldsymbol{g})\end{bmatrix}\begin{bmatrix}\dot{\boldsymbol{x}}(t,\boldsymbol{g})\\ \dot{\widehat{\boldsymbol{x}}}(t,\boldsymbol{g})\end{bmatrix} &= -\begin{bmatrix}\mathbf{G}(\boldsymbol{g}) & 0\\ \widehat{\mathbf{G}}(\boldsymbol{g}) & \mathbf{G}(\boldsymbol{g})\end{bmatrix}\begin{bmatrix}\boldsymbol{x}(t,\boldsymbol{g})\\ \widehat{\boldsymbol{x}}(t,\boldsymbol{g})\end{bmatrix}\\ &\quad+\begin{bmatrix}\mathbf{B}(\boldsymbol{g}) & 0\\ \widehat{\mathbf{B}}(\boldsymbol{g}) & \mathbf{B}(\boldsymbol{g})\end{bmatrix}\begin{bmatrix}\boldsymbol{i}_p(t,\boldsymbol{g})\\ \widehat{\boldsymbol{i}}_p(t,\boldsymbol{g})\end{bmatrix}\\ \begin{bmatrix}\boldsymbol{v}_p(t,\boldsymbol{g})\\ \widehat{\boldsymbol{v}}_p(t,\boldsymbol{g})\end{bmatrix} &= \begin{bmatrix}\mathbf{L}(\boldsymbol{g}) & \widehat{\mathbf{L}}(\boldsymbol{g})\\ 0 & \mathbf{L}(\boldsymbol{g})\end{bmatrix}^{\mathrm{T}}\begin{bmatrix}\boldsymbol{x}(t,\boldsymbol{g})\\ \widehat{\boldsymbol{x}}(t,\boldsymbol{g})\end{bmatrix},\end{aligned} \tag{7}$$

where $\widehat{\cdot}$ denotes the derivatives with respect to the design parameters. Equation (7) can be solved, applying appropriate termination conditions, by the means of differential equations solvers, upon the knowledge of the system matrices and their derivatives. However, the simulations become slow and difficult to manage when the dimensions of the original PEEC matrices become large. Therefore, it is fundamental to obtain a parameterized reduced order model able to reduce the CPU time effort needed to carry out the desired simulations.

III. PARAMETERIZED MODEL ORDER REDUCTION ALGORITHM

In this section, we describe the proposed PMOR algorithm applied to the system (7) in order to perform parameterized (global) time- and frequency-domain sensitivity analysis with respect to design parameters in a more efficient way in comparison with the technique [19], where a parameterized sensitivity analysis was performed using interpolation models of the original PEEC matrices without any order reduction scheme.

A. Block model order reduction

The first step of the proposed PMOR algorithm is to generate a set of PEEC matrices $\{\mathbf{P}(\boldsymbol{g}_k), \mathbf{L}_p(\boldsymbol{g}_k), \mathbf{C}_d(\boldsymbol{g}_k), \mathbf{R}(\boldsymbol{g}_k)\}_{k=1}^{K_{tot}}$ corresponding to a set of K_{tot} initial samples $\boldsymbol{g}_k$ in the design space. We assume that a topologically fixed discretization mesh is used and that it is independent from the specific design parameter values as in [19]. When geometrical parameters are modified, the mesh is only locally stretched or shrunk. Therefore, the PEEC matrices $\mathbf{A}, \mathbf{\Phi}, \mathbf{K}$ are uniquely determined by the circuit topology and do not depend on $\boldsymbol{g}$. Then, a model order reduction (MOR) is proposed to generate the Krylov matrix $\mathbf{K}_q(\boldsymbol{g}_k)$ of the system (7) for each initial sample in the design space. In [23, 24], block structure preserving MOR methods were presented, where blocks were derived based on the specific application. This concept of block structure preserving MOR is used in this paper to generalize the Laguerre-SVD MOR (LSVD-MOR) algorithm [25]. The standard LSVD-MOR is listed in Algorithm 1, where α is a positive scaling parameter, $q-1$ is the order of approximation and:

$$\mathbf{K}_q = \left[\mathbf{R}^{(0)}, \mathbf{R}^{(1)}, \ldots, \mathbf{R}^{(q-1)}\right], \tag{8}$$

is the Krylov matrix of order $q-1$ [25]. The LSVD-MOR algorithm can be extended to a block LSVD-MOR method, considering the block form of the matrices in (7). If we replace the set of matrices $\{\mathbf{C}, \mathbf{G}, \mathbf{B}, \mathbf{L}\}$ in Algorithm 1 with that block form, the step $k = 0$ of the standard LSVD-MOR algorithm can be re-written as:

$$\begin{bmatrix}\mathbf{G}+\alpha\mathbf{C} & 0\\ \widehat{\mathbf{G}}+\alpha\widehat{\mathbf{C}}\mathbf{G}+\alpha\mathbf{C}\end{bmatrix}\begin{bmatrix}\mathbf{R}_{11}^{(0)}\mathbf{R}_{12}^{(0)}\\ \mathbf{R}_{21}^{(0)}\mathbf{R}_{22}^{(0)}\end{bmatrix} = \begin{bmatrix}\mathbf{B}\,0\\ \widehat{\mathbf{B}}\mathbf{B}\end{bmatrix}. \tag{9}$$

After some manipulation it follows:

$$\begin{aligned}\begin{bmatrix}\mathbf{R}_{11}^{(0)}\mathbf{R}_{12}^{(0)}\\ \mathbf{R}_{21}^{(0)}\mathbf{R}_{22}^{(0)}\end{bmatrix} &= \begin{bmatrix}\mathbf{G}_N^{-1} & 0\\ \widehat{\mathbf{G}}_N^{-1}\mathbf{G}_N^{-1}\end{bmatrix}\begin{bmatrix}\mathbf{B}\,0\\ \widehat{\mathbf{B}}\mathbf{B}\end{bmatrix} =\\ &\begin{bmatrix}\mathbf{G}_N^{-1}\mathbf{B} & 0\\ \widehat{\mathbf{G}}_N^{-1}\mathbf{B}+\mathbf{G}_N^{-1}\widehat{\mathbf{B}}\mathbf{G}_N^{-1}\mathbf{B}\end{bmatrix} = \begin{bmatrix}\mathbf{R}_1^{(0)} & 0\\ \mathbf{R}_2^{(0)}\mathbf{R}_1^{(0)}\end{bmatrix},\end{aligned} \tag{10}$$

where we have defined $\mathbf{G}_N$ and $\widehat{\mathbf{G}}_N$ as

$$\begin{aligned}\mathbf{G}_N &= \mathbf{G} + \alpha\mathbf{C}\\ \widehat{\mathbf{G}}_N &= \widehat{\mathbf{G}} + \alpha\widehat{\mathbf{C}}.\end{aligned} \tag{11}$$

At the step $k = 0$, the Krylov matrix $\mathbf{K}_q$ is composed of two components:

$$\begin{cases}\mathbf{R}_1^{(0)} = \mathbf{G}_N^{-1}\mathbf{B}\\ \mathbf{R}_2^{(0)} = \widehat{\mathbf{G}}_N^{-1}\mathbf{B} + \mathbf{G}_N^{-1}\widehat{\mathbf{B}}.\end{cases} \tag{12}$$

The first component is related to the Krylov matrix of the original system (5) for $k = 0$, while the second one is the derivative of this first component:

$$\mathbf{R}_2^{(0)} = \widehat{\mathbf{R}}_1^{(0)}. \tag{13}$$

This means that the Krylov matrix of the original system and its derivative are enough to finalize the first step of the block LSVD-MOR algorithm. The other steps for for $k > 0$ lead to:

$$\begin{bmatrix}\mathbf{G} + \alpha\mathbf{C} & 0\\ \widehat{\mathbf{G}} + \alpha\widehat{\mathbf{C}} & \mathbf{G} + \alpha\mathbf{C}\end{bmatrix}\begin{bmatrix}\mathbf{R}_{11}^{(k)} & \mathbf{R}_{12}^{(k)}\\ \mathbf{R}_{21}^{(k)} & \mathbf{R}_{22}^{(k)}\end{bmatrix} = \begin{bmatrix}\mathbf{G} - \alpha\mathbf{C} & 0\\ \widehat{\mathbf{G}} - \alpha\widehat{\mathbf{C}} & \mathbf{G} - \alpha\mathbf{C}\end{bmatrix}\begin{bmatrix}\mathbf{R}_{11}^{(k-1)} & \mathbf{R}_{12}^{(k-1)}\\ \mathbf{R}_{21}^{(k-1)} & \mathbf{R}_{22}^{(k-1)}\end{bmatrix}. \tag{14}$$

Likewise, after some manipulations:

$$\begin{bmatrix}\mathbf{R}_{11}^{(k)} & \mathbf{R}_{12}^{(k)}\\ \mathbf{R}_{21}^{(k)} & \mathbf{R}_{22}^{(k)}\end{bmatrix} = \begin{bmatrix}\mathbf{G}_N^{-1} & 0\\ \widehat{\mathbf{G}}_N^{-1} & \mathbf{G}_N^{-1}\end{bmatrix}\begin{bmatrix}\mathbf{G}_R & 0\\ \widehat{\mathbf{G}}_R & \mathbf{G}_R\end{bmatrix}\begin{bmatrix}\mathbf{R}_{11}^{(k-1)} & \mathbf{R}_{12}^{(k-1)}\\ \mathbf{R}_{21}^{(k-1)} & \mathbf{R}_{22}^{(k-1)}\end{bmatrix} = \begin{bmatrix}\mathbf{G}_N^{-1}\mathbf{G}_R & 0\\ \widehat{\mathbf{G}}_N^{-1}\mathbf{G}_R + \mathbf{G}_N^{-1}\widehat{\mathbf{G}}_R & \mathbf{G}_N^{-1}\mathbf{G}_R\end{bmatrix}\begin{bmatrix}\mathbf{R}_1^{(k-1)} & 0\\ \mathbf{R}_2^{(k-1)} & \mathbf{R}_1^{(k-1)}\end{bmatrix}, \tag{15}$$

where we have defined $\mathbf{G}_R$ and $\widehat{\mathbf{G}}_R$ as:

$$\begin{aligned}\mathbf{G}_R &= \mathbf{G} - \alpha\mathbf{C}\\ \widehat{\mathbf{G}}_R &= \widehat{\mathbf{G}} - \alpha\widehat{\mathbf{C}}.\end{aligned} \tag{16}$$

The blocks of the Krylov matrix for $k > 0$ are also composed of two components:

$$\begin{cases}\mathbf{R}_1^{(k)} = \mathbf{G}_N^{-1}\mathbf{G}_R\mathbf{R}_1^{(k-1)}\\ \mathbf{R}_2^{(k)} = \mathbf{G}_N^{-1}\mathbf{G}_R\mathbf{R}_2^{(k-1)} + \underbrace{\left(\widehat{\mathbf{G}}_N^{-1}\mathbf{G}_R + \mathbf{G}_N^{-1}\widehat{\mathbf{G}}_R\right)}_{\widehat{\mathbf{G}_N^{-1}\mathbf{G}_R}}\mathbf{R}_1^{(k-1)}.\end{cases} \tag{17}$$

As previously, equation (17) shows that the first component $\mathbf{R}_1^{(k)}$ is the component of the Krylov matrix of the original system (5) for $k > 0$, and the second component $\mathbf{R}_2^{(k)}$ is the corresponding derivative:

$$\mathbf{R}_2^{(k)} = \widehat{\mathbf{R}}_1^{(k)}. \tag{18}$$

According to Algorithm 1, the Krylov matrix $\mathbf{K}_q$ reads:

$$\mathbf{K}_q = \left[\begin{array}{cc|cc|c|cc}\mathbf{R}_1^{(0)} & 0 & \mathbf{R}_1^{(1)} & 0 & \cdots & \mathbf{R}_1^{(q-1)} & 0\\ \hline \mathbf{R}_2^{(0)} & \mathbf{R}_1^{(0)} & \mathbf{R}_2^{(1)} & \mathbf{R}_1^{(1)} & \cdots & \mathbf{R}_2^{(q-1)} & \mathbf{R}_1^{(q-1)}\end{array}\right], \tag{19}$$

and by a column permutation:

$$\mathbf{K}_q = \left[\begin{array}{ccc|ccc}\mathbf{R}_1^{(0)} & \cdots & \mathbf{R}_1^{(q-1)} & 0 & \cdots & 0\\ \hline \mathbf{R}_2^{(0)} & \cdots & \mathbf{R}_2^{(q-1)} & \mathbf{R}_1^{(0)} & \cdots & \mathbf{R}_1^{(q-1)}\end{array}\right], \tag{20}$$

where $\mathbf{R}_1^{(i)} = \mathbf{R}^{(i)}$ is the i-th component of the Krylov matrix of the original system and $\mathbf{R}_2^{(i)} = \widehat{\mathbf{R}}^{(i)}$ is its derivative (see (13) and (18)). For each initial sample $\boldsymbol{g}_k$ the corresponding Krylov matrix $\mathbf{K}_q(\boldsymbol{g}_k)$ is computed using the block LSVD-MOR method.

To compute the reduced system of (7), an orthonormalization step is applied to the Krylov matrix $\mathbf{K}_q$ using a Singular Value Decomposition (SVD) algorithm to obtain the projection matrix:

$$\mathbf{V} \to \mathbf{V}\,\Sigma\,\mathbf{U}^{\mathrm{T}} = \mathrm{SVD}\left(\mathbf{K}_q\right), \tag{21}$$

that is then used for the congruence transformations to compute the reduced matrices. In order to preserve the block structure of the system (7), the projection matrix $\mathbf{V} \in \mathbb{R}^{2n_s \times n_r}$ is partitioned in a block fashion [23, 24]:

$$\mathbf{V} = \begin{bmatrix}\mathbf{V}_1\\ \mathbf{V}_2\end{bmatrix}, \tag{22}$$

where $n_r = q \cdot n_p$ denotes the column size of the Krylov matrix $\mathbf{K}_q$. The projection matrix blocks may not have a full column rank n_r, in particular the first block $\mathbf{V}_1$, due to the presence of a block of zeros. An orthonormalization step is applied to $\mathbf{V}_1$ in order to obtain a matrix $\widetilde{\mathbf{V}}_1$ whose columns span the same space as the columns of $\mathbf{V}_1$, while having however a full column rank [24]. The same operation is performed on $\mathbf{V}_2$ to obtain $\widetilde{\mathbf{V}}_2$. The second block $\mathbf{V}_2$ has generally full column rank n_r. After this step the column size of the two blocks $\widetilde{\mathbf{V}}_1$ and $\widetilde{\mathbf{V}}_2$ may differ with respect to the column size of $\mathbf{V}_1$ and $\mathbf{V}_2$. However, this does not influence the reduction of the full system (7). Finally the projection matrix is written as [23, 24]:

$$\widetilde{\mathbf{V}} = \begin{bmatrix}\widetilde{\mathbf{V}}_1 & 0\\ 0 & \widetilde{\mathbf{V}}_2\end{bmatrix}. \tag{23}$$

In order to reduce the overall system in (7), the projection matrix (23) is used to compute the reduced matrices by congruence transformations:

$$\begin{aligned}\begin{bmatrix}\mathbf{C}_{r,1} & 0\\ \widehat{\mathbf{C}}_{r,2} & \mathbf{C}_{r,2}\end{bmatrix} &= \begin{bmatrix}\widetilde{\mathbf{V}}_1^{\mathrm{T}} & 0\\ 0 & \widetilde{\mathbf{V}}_2^{\mathrm{T}}\end{bmatrix}\begin{bmatrix}\mathbf{C} & 0\\ \widehat{\mathbf{C}} & \mathbf{C}\end{bmatrix}\begin{bmatrix}\widetilde{\mathbf{V}}_1 & 0\\ 0 & \widetilde{\mathbf{V}}_2\end{bmatrix}\\ \begin{bmatrix}\mathbf{G}_{r,1} & 0\\ \widehat{\mathbf{G}}_{r,2} & \mathbf{G}_{r,2}\end{bmatrix} &= \begin{bmatrix}\widetilde{\mathbf{V}}_1^{\mathrm{T}} & 0\\ 0 & \widetilde{\mathbf{V}}_2^{\mathrm{T}}\end{bmatrix}\begin{bmatrix}\mathbf{G} & 0\\ \widehat{\mathbf{G}} & \mathbf{G}\end{bmatrix}\begin{bmatrix}\widetilde{\mathbf{V}}_1 & 0\\ 0 & \widetilde{\mathbf{V}}_2\end{bmatrix}\\ \begin{bmatrix}\mathbf{B}_{r,1} & 0\\ \widehat{\mathbf{B}}_{r,2} & \mathbf{B}_{r,2}\end{bmatrix} &= \begin{bmatrix}\widetilde{\mathbf{V}}_1^{\mathrm{T}} & 0\\ 0 & \widetilde{\mathbf{V}}_2^{\mathrm{T}}\end{bmatrix}\begin{bmatrix}\mathbf{B} & 0\\ \widehat{\mathbf{B}} & \mathbf{B}\end{bmatrix}\\ \begin{bmatrix}\mathbf{L}_{r,1} & \widehat{\mathbf{L}}_{r,2}\\ 0 & \mathbf{L}_{r,2}\end{bmatrix} &= \begin{bmatrix}\widetilde{\mathbf{V}}_1^{\mathrm{T}} & 0\\ 0 & \widetilde{\mathbf{V}}_2^{\mathrm{T}}\end{bmatrix}\begin{bmatrix}\mathbf{L} & \widehat{\mathbf{L}}\\ 0 & \mathbf{L}\end{bmatrix}.\end{aligned} \tag{24}$$

Algorithm 2 lists the steps of the proposed block LSVD-MOR method to perform in order to obtain

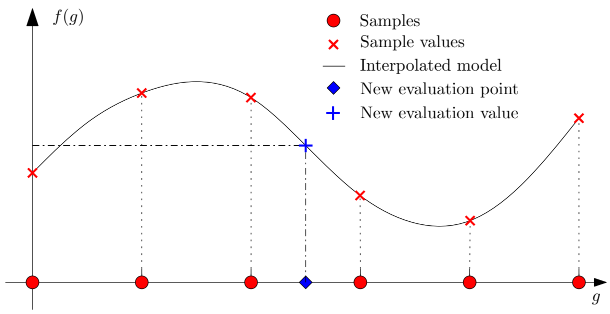

Fig. 2. Example of sampling design space grid.

the set of reduced matrices for the reduced system. Concerning the proposed PMOR algorithm, the block LSVD-MOR method is used to to generate the Krylov matrix $\mathbf{K}_q(\boldsymbol{g}_k)$ of the system (7) for each initial sample in the design space.

B. Interpolation models

Once the set of matrices $\{\mathbf{P}(\boldsymbol{g}_k), \mathbf{L}_p(\boldsymbol{g}_k), \mathbf{C}_d(\boldsymbol{g}_k), \mathbf{R}(\boldsymbol{g}_k), \mathbf{K}_q(\boldsymbol{g}_k)\}_{k=1}^{K_{tot}}$ is available, the corresponding interpolation models are built. Figure 2 shows an example for the case of one design parameter. Each interpolation model is built starting from a set of samples indicated with red dots ($\circ$) in Fig. 2. For each ($\circ$) sample in the design space, a set of PEEC matrices and a Krylov matrix are computed and the corresponding models, that cover the entire design space, are built by the means of an interpolation scheme. For interpolation purposes the multivariate cubic spline interpolation method [26], which is well-known for its stable and smooth characteristics, is used. The proposed interpolation scheme is continuous in the first and second order derivatives and can be used in the general case of an M-dimensional (M-D) design space.

First, the interpolation models $\left\{\overline{\mathbf{P}}(\boldsymbol{g}), \overline{\mathbf{L}}_p(\boldsymbol{g}), \overline{\mathbf{C}}_d(\boldsymbol{g}), \overline{\mathbf{R}}(\boldsymbol{g})\right\}$ are computed while guaranteeing positive definiteness and semidefiniteness matrix properties [19, 20]. At this step, according to Algorithm 2, it could be possible to compute a set of reduced matrices for each point of interest in the design space by using the block LSVD-MOR method previously described. However, to improve the efficiency of the proposed PMOR method, we choose to create an interpolation model for the $\mathbf{K}_q(\boldsymbol{g})$ matrix, starting from the corresponding data samples $\mathbf{K}_q(\boldsymbol{g}_k)$. From the model $\overline{\mathbf{K}}_q(\boldsymbol{g})$, the values of the projection matrices $\mathbf{V}_1(\boldsymbol{g})$ and $\mathbf{V}_2(\boldsymbol{g})$ can be computed for each point of interest in the design space.

Inspecting equation (19), only the interpolation models of the matrices $\{\mathbf{R}_1^{(i)}(\boldsymbol{g}_k)\}_{i=0}^{q-1}$ and $\{\mathbf{R}_2^{(i)}(\boldsymbol{g}_k)\}_{i=0}^{q-1}$ (namely $\{\overline{\mathbf{R}}_1^{(i)}(\boldsymbol{g})\}_{i=0}^{q-1}$ and $\{\overline{\mathbf{R}}_2^{(i)}(\boldsymbol{g})\}_{i=0}^{q-1}$) are sufficient to obtain the interpolation model $\overline{\mathbf{K}}_q(\boldsymbol{g})$. Furthermore, there is still one degree of freedom about how to compute the matrices $\{\mathbf{R}_2^{(i)}(\boldsymbol{g})\}_{i=0}^{q-1}$:

1. As described in Algorithm 2;
2. directly as derivative of $\{\overline{\mathbf{R}}_1^{(i)}(\boldsymbol{g})\}_{i=0}^{q-1}$ (see (13) and (18)).

The latter option is based on the interpolation model $\{\overline{\mathbf{R}}_1^{(i)}(\boldsymbol{g})\}_{i=0}^{q-1}$ that can provide derivatives with respect to $\boldsymbol{g}$. This choice is preferred since it allows storing only the model $\{\overline{\mathbf{R}}_1^{(i)}(\boldsymbol{g})\}_{i=0}^{q-1}$ and then saving memory resources, while keeping a similar accuracy.

Using the interpolation models $\left\{\overline{\mathbf{P}}(\boldsymbol{g}), \overline{\mathbf{L}}_p(\boldsymbol{g}), \overline{\mathbf{C}}_d(\boldsymbol{g}), \overline{\mathbf{R}}(\boldsymbol{g})\right\}$ and $\{\overline{\mathbf{R}}_1^{(i)}(\boldsymbol{g})\}_{i=0}^{q-1}$, it is possible to obtain a set of PEEC matrices and a set of projection matrices $\mathbf{V}_1(\boldsymbol{g})$ and $\mathbf{V}_2(\boldsymbol{g})$ for each point of the design space. Applying the congruence transformations, the sets of reduced matrices $\{\mathbf{C}_{r,i}(\boldsymbol{g}), \mathbf{G}_{r,i}(\boldsymbol{g}), \mathbf{B}_{r,i}(\boldsymbol{g}), \mathbf{L}_{r,i}(\boldsymbol{g})\}_{i=1,2}$ and $\left\{\widehat{\mathbf{C}}_{r,2}(\boldsymbol{g}), \widehat{\mathbf{G}}_{r,2}(\boldsymbol{g}), \widehat{\mathbf{B}}_{r,2}(\boldsymbol{g}), \widehat{\mathbf{L}}_{r,2}(\boldsymbol{g})\right\}$ are computed. The reduced version of (7) can be written as:

$$\begin{bmatrix}\mathbf{C}_{r,1}(\boldsymbol{g}) & 0\\ \widehat{\mathbf{C}}_{r,2}(\boldsymbol{g}) & \mathbf{C}_{r,2}(\boldsymbol{g})\end{bmatrix}\begin{bmatrix}\dot{\boldsymbol{x}}_r(t,\boldsymbol{g})\\ \dot{\widehat{\boldsymbol{x}}}_r(t,\boldsymbol{g})\end{bmatrix} = -\begin{bmatrix}\mathbf{G}_{r,1}(\boldsymbol{g}) & 0\\ \widehat{\mathbf{G}}_{r,2}(\boldsymbol{g}) & \mathbf{G}_{r,2}(\boldsymbol{g})\end{bmatrix}\begin{bmatrix}\boldsymbol{x}_r(t,\boldsymbol{g})\\ \widehat{\boldsymbol{x}}_r(t,\boldsymbol{g})\end{bmatrix} + \begin{bmatrix}\mathbf{B}_{r,1}(\boldsymbol{g}) & 0\\ \widehat{\mathbf{B}}_{r,2}(\boldsymbol{g}) & \mathbf{B}_{r,2}(\boldsymbol{g})\end{bmatrix}\begin{bmatrix}\boldsymbol{i}_p(t,\boldsymbol{g})\\ \widehat{\boldsymbol{i}}_p(t,\boldsymbol{g})\end{bmatrix}$$

$$\begin{bmatrix}\boldsymbol{v}_p(t,\boldsymbol{g})\\ \widehat{\boldsymbol{v}}_p(t,\boldsymbol{g})\end{bmatrix} = \begin{bmatrix}\mathbf{L}_{r,1}(\boldsymbol{g}) & \widehat{\mathbf{L}}_{r,2}(\boldsymbol{g})\\ 0 & \mathbf{L}_{r,2}(\boldsymbol{g})\end{bmatrix}^{\mathrm{T}}\begin{bmatrix}\boldsymbol{x}_r(t,\boldsymbol{g})\\ \widehat{\boldsymbol{x}}_r(t,\boldsymbol{g})\end{bmatrix}. \tag{25}$$

These reduced matrices are used to perform both time- and frequency-domain sensitivity analysis, with appropriate termination conditions.

IV. NUMERICAL EXAMPLES

Two numerical examples are proposed to validate the proposed PMOR technique for sensitivity analysis. Parameterized time- and frequency-domain sensitivity analyses are performed with the proposed PMOR technique and the results are compared with the approach proposed in [19] and with the perturbative approach (with respect to each parameter g_m) that in time- and frequency-domain reads:

$$\widehat{\boldsymbol{v}}_{p,g_m}(t,\boldsymbol{g}) = \frac{\boldsymbol{v}_p(t,g_1,..,g_m+\Delta g_m,..,g_M) - \boldsymbol{v}_p(t,\boldsymbol{g})}{\Delta g_m}, \tag{26}$$

$$\widehat{\mathbf{Z}}_{g_m}(s,\boldsymbol{g}) = \frac{\mathbf{Z}(s,g_1,..,g_m+\Delta g_m,..,g_M) - \mathbf{Z}(s,\boldsymbol{g})}{\Delta g_m}, \tag{27}$$

where $m = 1, \dots, M$, M and Δg_m represent the number of parameters and the increment, respectively. The accuracy of the perturbative approach depends on the choice of the increment Δg_m: if the increment is not small enough, the estimation of the derivative is not accurate, while if the perturbation is very small compared with the nominal value, numerical problems may occur due to numerical noise. This may lead to inaccurate computation of the system sensitivities. In contrast, thanks to the interpolation models, the methods presented in this paper and in [19] lead to more accuracy and numerical stability, since the derivatives are computed from continuously differentiable polynomials built by means of spline functions. The method [19] is denoted as Full Parameterized while the proposed method is denoted as Block PMOR in what follows.

In the numerical results (see Tables 1-2), for the Full Parameterized and Block PMOR models, the model evaluation CPU time indicates the average time needed to evaluate the corresponding parameterized models in a point of the validation grid in order to obtain a set of PEEC matrices. Moreover, for the Block PMOR model, the SVD operation is also part of the model evaluation. For the Perturbative Approach, the model evaluation CPU time refers to the average time needed to compute a set of PEEC matrices by a PEEC solver at and around a point in the validation grid, which are then used for a finite difference calculation. Once the parameterized models are evaluated, or PEEC matrices have been computed (perturbative approach), they can be used to carry out sensitivity analysis in frequency- and time-domain. For each of the three methods, the average time needed to perform the sensitivity analysis in a point of the validation grid is denoted as simulation CPU time.

Numerical simulations have been performed on a Linux platform on an AMD FX(tm)-6100 Six-Core Processor 3.3 GHz with 16 GB RAM.

A. Metallic enclosure coupled to a transmission line

In the first example a metallic enclosure coupled to a transmission line is studied. The cross section is shown in Fig. 3. The geometrical dimensions are $w_c = 1\,\text{mm}$, $d_c = 5\,\text{mm}$, $s_l = 1\,\text{mm}$, $d_l = 30\,\text{mm}$. A set of PEEC matrices is computed over a grid of 6×6 values of the conductor length $l_c \in [25 - 65]$ mm and $s_c \in [7 - 22]$ mm in order to build the aforementioned parameterized reduced order model. Furthermore, a parameterized full model has been built by means of the method [19] for the comparison. The order of the full models is 2870 while the reduced order is 471. Parameterized time- and frequency-domain sensitivities are performed over a validation grid of 5×5 values of $l_c \in [29 - 61]$ mm and $s_c \in [8.5 - 20.5]$ mm. The obtained results are then compared with the ones obtained by the perturbative model (26), (27). For the time-domain results, the bottom conductor is excited by a smooth pulse voltage source with amplitude 1V, rise/fall times $\tau_r = \tau_f = 1.5$ ns, width 6 ns and internal resistance $R_T = 50\ \Omega$. All the ports are terminated on 50 Ω resistances.

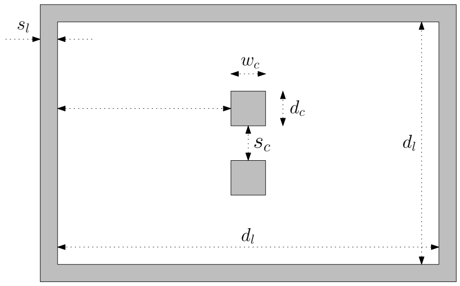

Fig. 3. Metallic enclosure coupled to a transmission line (example A).

Table 1: Simulation time comparison (Example A). The CPU time information related to time- and frequency-domain analysis refers to an average value of the CPU time needed to perform the sensitivity analysis in a point of the validation grid

		Block PMOR	Full Parameterized	Perturbative Approach
Time	*Model eval*	13 s	12 s	618 s
	Simulation	6 s	161 s	48 s
	Total	19 s	173 s	666 s
Freq	*Model eval*	13 s	12 s	618 s
	Simulation	37 s	639 s	944 s
	Total	50 s	651 s	1562 s

Figures 4-5 and 6-7 show time- and frequency-domain results that confirm the high accuracy of the proposed approach. Table 1 clearly shows the computational advantage of the proposed PMOR technique: the CPU time required to perform both time- and frequency-domain sensitivity simulations is considerably improved with respect to the two other compared approaches for a sensitivity analysis around a nominal design point and therefore also for a global sensitivity analysis. It is important to note that the Block PMOR and Full Parameterized methods require a one-time effort to build the corresponding parameterized models that then allow global sensitivity simulations. This CPU time for the Block PMOR method is equal to 8236 s and for the Full Parameterized method is equal to 7513 s.

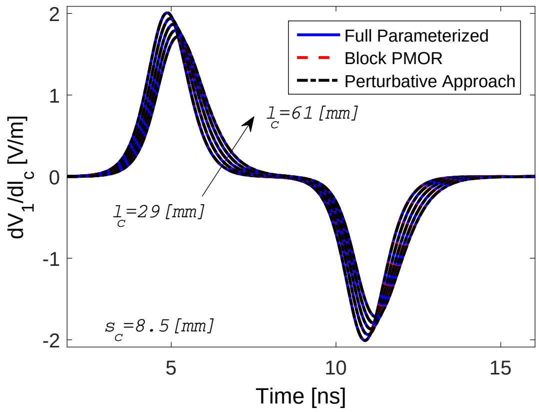

Fig. 4. Time-domain voltage sensitivity with respect to l_c at the port 1 (example A).

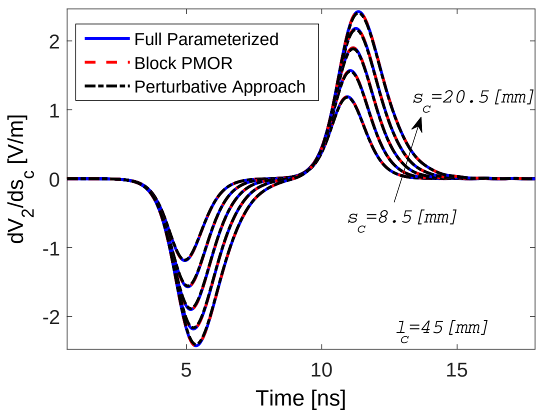

Fig. 5. Time-domain voltage sensitivity with respect to s_c at the port 2 (example A).

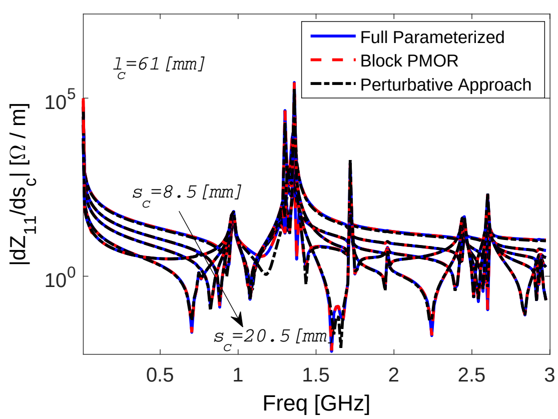

Fig. 6. Magnitude of the sensitivity of Z_{11} with respect to s_c (example A).

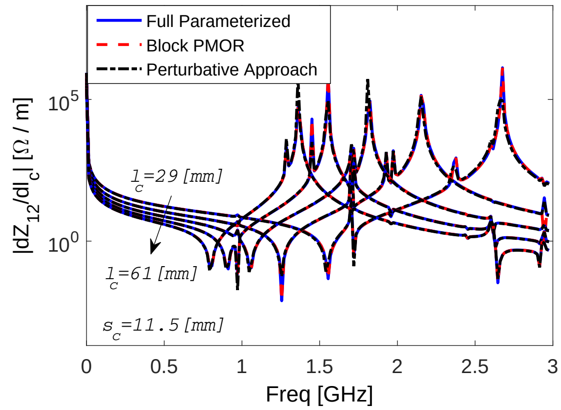

Fig. 7. Magnitude of the sensitivity of Z_{12} with respect to l_c (example A).

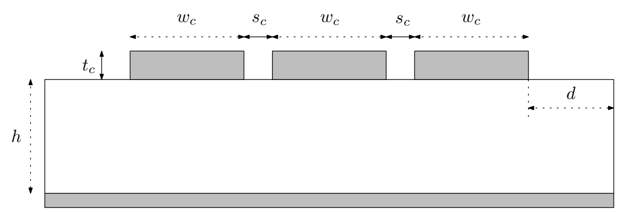

Fig. 8. Three conductors microstrip (example B).

B. Three conductors microstrip

Three coupled microstrips are modeled in this example and Fig. 8 shows the corresponding cross section. The geometrical dimensions are $w_c = 178\,\mu$m, $t_c = 35\,\mu$m, $d = 3$ mm and the length of the lines is $l = 40$ mm. The parameterized reduced order and parameterized full models have been built starting from a set of PEEC matrices computed over a grid of 6×6 values of $s_c \in [0.1 - 0.4]$ mm and $h \in [0.1 - 0.3]$ mm. The order of the full models is 3360 while the reduced order is 577. Parameterized time- and frequency-domain sensitivities are performed over a validation grid of 5×5 values of $s_c \in [0.13 - 0.37]$ mm and $h \in [0.12 - 0.28]$ mm. The obtained results are then compared with the perturbative approach (26), (27). For the time-domain results, a smooth pulse voltage source with amplitude 1V, rise/fall times $\tau_r = \tau_f = 1.5$ ns, width 6 ns and internal resistance $R_T = 50\ \Omega$ is applied on the first conductor. All the ports are terminated on 50 Ω resistances. Time-domain sensitivity results are shown in Figs. 9, 10 while frequency-domain sensitivity results are shown in Figs. 11, 12. As in the previous example, the results confirm the high accuracy of the proposed method. Table 2 shows the simulation time comparison that clearly confirms that the proposed PMOR method considerably reduces the CPU time

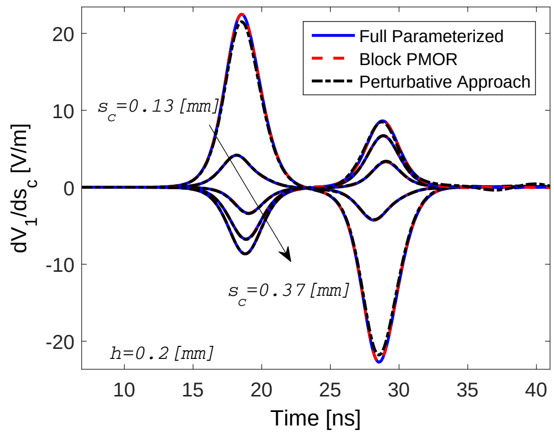

Fig. 9. Time-domain voltage sensitivity with respect to s_c at the port 1 (example B).

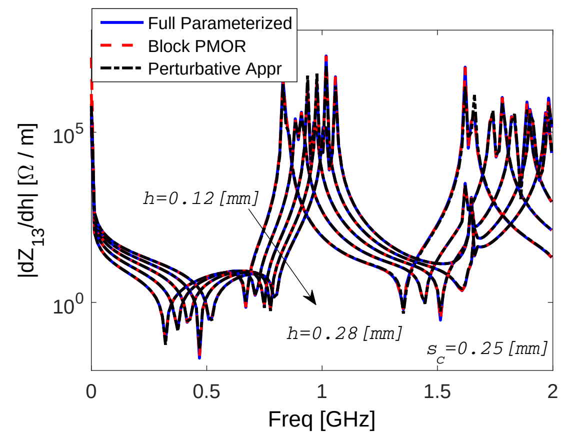

Fig. 11. Magnitude of the sensitivity of Z_{13} with respect to h (example B).

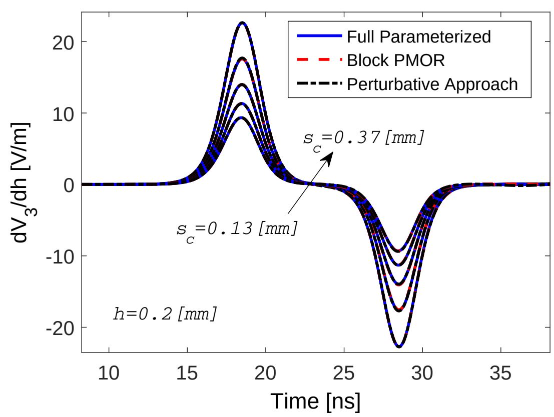

Fig. 10. Time-domain voltage sensitivity with respect to h at the port 3 (example B).

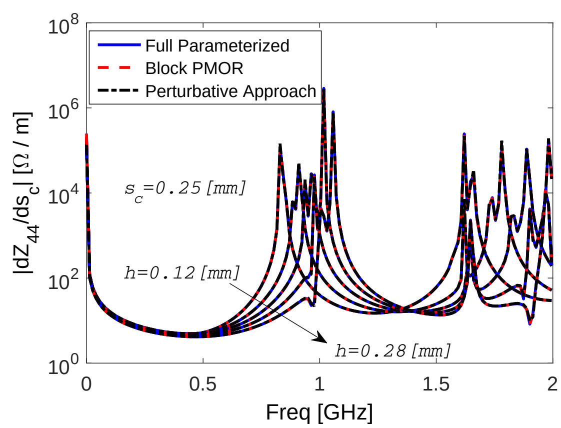

Fig. 12. Magnitude of the sensitivity of Z_{44} with respect to s_c (example B).

required for a sensitivity analysis with respect to the other two methods around a nominal design point and therefore for a global sensitivity analysis. As in the previous example, an initial computational effort is required to compute the Block PMOR and Full Parameterized models that is equal to 9306 s for the Block PMOR and to 8456 s for the Full Parameterized method.

V. CONCLUSIONS

In this paper we have presented a new PMOR technique to perform both time- and frequency-domain global sensitivity analysis of PEEC circuits. It is based on the PEEC method, the block Laguerre SVD model order reduction technique and interpolation schemes. Two numerical examples confirm the high modeling capability and the improved efficiency of the proposed approach with respect to existing sensitivity analysis methods.

Table 2: Simulation time comparison (Example B). The CPU time information related to time- and frequency-domain analysis refers to an average value of the CPU time needed to perform the sensitivity analysis in a point of the validation grid

		Block PMOR	Full Parameterized	Perturbative Approach
Time	*Model eval*	11 s	10 s	699 s
	Simulation	9 s	275 s	48 s
	Total	20 s	285 s	747 s
Freq	*Model eval*	11 s	10 s	699 s
	Simulation	52 s	591 s	857 s
	Total	63 s	601 s	1556 s

VI. APPENDIX

This appendix illustrates the pseudo-code of the Laguerre-SVD and the Block Laguerre-SVD algorithms.

Algorithm 1 Laguerre-SVD Algorithm

Select values for α and q
$\mathbf{R}^{(0)} \leftarrow (\mathbf{G}+\alpha\mathbf{C})\,\mathbf{R}^{(0)} = \mathbf{B}$
for $k = 1 \rightarrow q-1$ **do**
  $\mathbf{R}^{(k)} \leftarrow (\mathbf{G}+\alpha\mathbf{C})\,\mathbf{R}^{(k)} = (\mathbf{G}-\alpha\mathbf{C})\,\mathbf{R}^{(k-1)}$
end for
$\mathbf{K}_q = \left[\mathbf{R}^{(0)}, \mathbf{R}^{(1)}, \ldots, \mathbf{R}^{(q-1)}\right]$
$\mathbf{V}\Sigma\mathbf{U}^{\mathrm{T}} \leftarrow \mathrm{SVD}\left[\mathbf{K}_q\right]$
$\mathbf{C}_r \leftarrow \mathbf{V}^{\mathrm{T}}\mathbf{C}\mathbf{V}, \qquad \mathbf{G}_r \leftarrow \mathbf{V}^{\mathrm{T}}\mathbf{G}\mathbf{V}$
$\mathbf{B}_r \leftarrow \mathbf{V}^{\mathrm{T}}\mathbf{B}, \qquad \mathbf{L}_r \leftarrow \mathbf{V}^{\mathrm{T}}\mathbf{L}$

Algorithm 2 Block Laguerre-SVD Algorithm

Select values for α and q
$\mathbf{G}_N \leftarrow \mathbf{G}+\alpha\mathbf{C}, \quad \mathbf{G}_R \leftarrow \mathbf{G}-\alpha\mathbf{C}$
$\widehat{\mathbf{G}}_N \leftarrow \widehat{\mathbf{G}}+\alpha\widehat{\mathbf{C}}, \quad \widehat{\mathbf{G}}_R \leftarrow \widehat{\mathbf{G}}-\alpha\widehat{\mathbf{C}}$
$\mathbf{R}_1^{(0)} \leftarrow \mathbf{G}_N^{-1}\mathbf{B}$
$\mathbf{R}_2^{(0)} \leftarrow \widehat{\mathbf{G}}_N^{-1}\mathbf{B} + \mathbf{G}_N^{-1}\widehat{\mathbf{B}}$
for $k = 1 \rightarrow q-1$ **do**
  $\mathbf{R}_1^{(k)} \leftarrow \mathbf{G}_N^{-1}\mathbf{G}_R\mathbf{R}_1^{(k-1)}$
  $\mathbf{R}_2^{(k)} \leftarrow \left(\widehat{\mathbf{G}}_N^{-1}\mathbf{G}_R + \mathbf{G}_N^{-1}\widehat{\mathbf{G}}_R\right)\mathbf{R}_1^{(k-1)} + \mathbf{G}_N^{-1}\mathbf{G}_R\mathbf{R}_2^{(k-1)}$
end for
$\mathbf{K}_q = \left[\begin{array}{ccc|ccc} \mathbf{R}_1^{(0)} & \ldots & \mathbf{R}_1^{(q-1)} & 0 & \ldots & 0 \\ \hline \mathbf{R}_2^{(0)} & \ldots & \mathbf{R}_2^{(q-1)} & \mathbf{R}_1^{(0)} & \ldots & \mathbf{R}_1^{(q-1)} \end{array}\right]$
$n_r = q \cdot n_p$
$\mathbf{V} \leftarrow \mathbf{V}\,\Sigma\,\mathbf{U}^{\mathrm{T}} = \mathrm{SVD}\left(\mathbf{K}_q\right)$
$\mathbf{V} = \begin{bmatrix}\mathbf{V}_1 \\ \mathbf{V}_2\end{bmatrix}$
for $i = 1, 2$ **do**
  If rank $\mathbf{V}_i = r_{V_i} < n_r$ determine an $n_s \times r_{V_i}$ matrix $\widetilde{\mathbf{V}}_i$ with colspan $\widetilde{\mathbf{V}}_i$ = colspan $\mathbf{V}_i$ and rank $\widetilde{\mathbf{V}}_i = r_{V_i}$
end for
$\widetilde{\mathbf{V}} = \begin{bmatrix}\widetilde{\mathbf{V}}_1 & 0 \\ 0 & \widetilde{\mathbf{V}}_2\end{bmatrix}$
Apply congruence transformations (24)

ACKNOWLEDGMENT

This work was supported by the Research Foundation Flanders (FWO-Vlaanderen). Ferranti is currently a Post-Doctoral Research Fellow of FWO-Vlaanderen.

REFERENCES

[1] J. P. Webb, "Design sensitivity of frequency response in 3-D finite-element analysis of microwave devices," *IEEE Transactions on Magnetics*, vol. 35, pp. 1109–1112, Mar. 2002.

[2] S. Ali, N. N. Nikolova, and M. H. Bakr, "Sensitivity analysis with full-wave electromagnetic solvers based on structured grids," *IEEE Transactions on Magnetics*, vol. 40, no. 3, pp. 1521–1530, May 2004.

[3] N. K. Nikolova and M. H. Bakr, "An adjoint variable method for time-domain transmission-line modeling with fixed structured grids," *IEEE Transactions on Microwave Theory and Techniques*, vol. 52, no. 2, pp. 554–559, Feb. 2004.

[4] E. A. Soliman, M. H. Bakr, and N. K. Nikolova, "An adjoint variable method for sensitivity calculations of multiport devices," *IEEE Transactions on Microwave Theory and Techniques*, vol. 52, no. 2, Feb. 2004.

[5] N. K. Nikolova, J. W. Bandler, and M. H. Bakr, "Adjoint techniques for sensitivity analysis in high frequency structure CAD," *IEEE Transactions on Microwave Theory and Techniques*, vol. 52, no. 1, pp. 403–419, Jan. 2004.

[6] Y. Yang, T. Hallerod, D. Ericsson, A. Hellervik, A. Bondeson, and T. Rylander, "Gradient optimization of microwave devices using continuum design sensitivities from the adjoint problem," *IEEE Transactions on Magnetics*, vol. 41, no. 5, pp. 1780–1783, May 2005.

[7] N. K. Nikolova, J. Zhu, D. Li, M. H. Bakr, and J. W. Bandler, "Sensitivity analysis of network parameters with electromagnetic frequency-domain simulators," *IEEE Transactions on Microwave Theory and Techniques*, vol. 54, no. 2, pp. 670–681, Feb. 2006.

[8] N. Nikolova, X. Zhu, Y. Song, A. Hasib, and M. Bakrare, "S-Parameter sensitivities for electromagnetic optimization based on volume field solutions," *IEEE Transactions on Microwave Theory and Techniques*, vol. 57, no. 6, pp. 1526–1538, Jun. 2009.

[9] N. Nikolova, H. Tam, and M. Bakr, "Sensitivity analysis with the FDTD method on structured grids," *IEEE Transactions on Microwave Theory and Techniques*, vol. 52, no. 4, pp. 1207–1216, Apr. 2004.

[10] P. Basl, M. Bakr, and N. Nikolova, "Efficient estimation of sensitivities in TLM with dielectric discontinuities," *IEEE Microwave and Wireless Components Letters*, vol. 15, no. 2, pp. 89–91, Feb. 2005.

[11] A. E. Ruehli and P. A. Brennan, "Efficient capacitance calculations for three-dimensional multiconductor systems," *IEEE Transactions on Microwave Theory and Techniques*, vol. 21, no. 2, pp. 76–82, Feb. 1973.

[12] A. E. Ruehli, "Equivalent circuit models for three dimensional multiconductor systems," *IEEE Transactions on Microwave Theory and Techniques*, vol. MTT-22, no. 3, pp. 216–221, Mar. 1974.

[13] K. Coperich, A. Ruehli, and A. Cangellaris, "Enhanced skin effect for partial-element equivalent circuit (PEEC) models," *IEEE Transactions on Microwave Theory and Techniques*, vol. 48, no. 9, pp. 1435–1442, Sep. 2000.

[14] B. Archembeault and A. Ruehli, "Analysis of power/ground-plane EMI decoupling performance using the partial-element equivalent circuit technique," *IEEE Transactions on Electromagnetic Compatibility*, vol. 43, no. 4, pp. 437–445, Nov. 2001.

[15] P. J. Restle, A. Ruehli, S. G. Walker, and G. Papadopoulos, "Full-wave PEEC time-domain for the modeling of on-chip interconnects," *IEEE Transactions on Computer-Aided Design*, vol. 20, no. 7, pp. 877–887, Jul. 2001.

[16] G. Antonini, D. Deschrijver, and T. Dhaene, "Broadband macromodels for retarded Partial Element Equivalent Circuit (rPEEC) method," *IEEE Transactions on Electromagnetic Compatibility*, vol. 49, no. 1, pp. 34–48, Feb. 2007.

[17] C. Ho, A. Ruehli, and P. Brennan, "The modified nodal approach to network analysis," *IEEE Transactions on Circuits and Systems*, pp. 504–509, Jun. 1975.

[18] C. A. Balanis, *Advanced Engineering Electromagnetics*, John Wiley and Sons, New York, 1989.

[19] L. De Camillis, F. Ferranti, G. Antonini, D. Vande Ginste, and D. De Zutter, "Parameterized partial element equivalent circuit method for sensitivity analysis of multiport systems," *IEEE Transactions on Components, Packaging and Manufacturing Technology*, vol. 2, no. 2, pp. 248–255, Feb. 2012.

[20] F. Ferranti, G. Antonini, T. Dhaene, L. Knockaert, and A. Ruehli, "Physics-based passivity-preserving parameterized model order reduction for PEEC circuit analysis," *IEEE Transactions on Components, Packaging and Manufacturing Technology*, vol. 1, no. 3, pp. 399–409, Mar. 2011.

[21] M. Ahmadloo and A. Dounavis, "Sensitivity analysis of microwave circuits using parameterized model order reduction techniques," *IEEE Transactions on Components, Packaging and Manufacturing Technology*, vol. 1, no. 11, pp. 1795–1805, Nov. 2011.

[22] A. E. Ruehli and H. Heeb, "Circuit models for three-dimensional geometries including dielectrics," *IEEE Transactions on Microwave Theory and Techniques*, vol. 40, no. 7, pp. 1507–1516, Jul. 1992.

[23] H. Yu, L. He, and S. Tar, "Block structure preserving model order reduction," in *Behavioral Modeling and Simulation Workshop, 2005. BMAS 2005. Proceedings of the 2005 IEEE International*, pp. 1–6, Sep. 2005.

[24] R. W. Freund, "The SPRIM algorithm for structure-preserving order reduction of general RCL circuits," *Model Reduction for Circuit Simulation. Lecture Notes in Electrical Engineering*, vol. 74, pp. 25–52, 2011.

[25] L. Knockaert and D. De Zutter, "Laguerre-SVD reduced-order modeling," *IEEE Transactions on Microwave Theory and Techniques*, vol. 48, no. 9, pp. 1469–1475, Sep. 2000.

[26] C. De Boor, *A Practical Guide to Splines*, Springer-Verlag Berlin and Heidelberg GmbH & Co. K, 1978.

Luca De Camillis received the B.S. and M.S. degrees in Computer Science Engineering from Università degli Studi dell'Aquila, L'Aquila, Italy, in 2005 and 2007, respectively. He collaborated with the Electromagnetics Group, Department of Information Technology, Ghent University, Ghent, with the Department of Electrical Engineering, Università degli Studi dell'Aquila and with the ACE Laboratory, University of Washington, Seattle. His current research interests include parametric macromodeling and sensitivity analysis.

Giulio Antonini received the Laurea degree (*cum laude*) in Electrical Engineering from University of L'Aquila, L'Aquila, Italy, in 1994 and the Ph.D. degree in Electrical Engineering from University of Rome "La Sapienza" in 1998. Since 1998, he has been with the UAq EMC Laboratory, University of L'Aquila, where he is currently a Professor. His scientific interests are in the field of computational electromagnetics.

Francesco Ferranti received the B.S. degree in Electronic Engineering from the Università degli Studi di Palermo, Palermo, Italy, in 2005, the M.S. degree in Electronic Engineering from the Università degli Studi dell'Aquila, L'Aquila, Italy, in 2007, and the Ph.D. degree in Electrical Engineering from Ghent University, Ghent, Belgium, in 2011. He is currently an Assistant Professor at the Department of Fundamental Electricity and Instrumentation, Vrije Universiteit Brussel, Brussels, Belgium. His research interests include parameterized macromodeling and model order reduction, applied electromagnetics, behavioral modeling, adaptive sampling, system identification, microwave design and characterization, electro-thermal modeling, uncertainty quantification and optimization.

Finite Difference Analysis of an Open-Ended, Coaxial Sensor Made of Semi-Rigid Coaxial Cable for Determination of Moisture in *Tenera* Oil Palm Fruit

E. M. Cheng [1], Z. Abbas [2], MohamedFareq AbdulMalek [3], K. Y. Lee [4], K. Y. You [5], S. F. Khor [6], J. Hassan [2], and H. Zainuddin [2]

[1] School of Mechatronic Engineering,
Universiti Malaysia Perlis (UniMAP), Pauh Putra Campus, 02600 Arau, Perlis, Malaysia
emcheng@unimap.edu.my

[2] Physics Department, Faculty of Science
Universiti Putra Malaysia, 43400 Serdang, Selangor, Malaysia
za@upm.edu.my, jumiah@upm.edu.my, hishamuddin@upm.edu.my

[3] Faculty of Engineering and Information Sciences
University of Wollongong in Dubai, Al Sufouh Streetو Dubai Knowledge Village - إمارة دبيّ - United Arab Emirates
mohamedfareqmalek@uowdubai.ac.ae

[4] Department of Electrical and Electronic Engineering, Faculty of Engineering and Science
Tunku Abdul Rahman University, 53300 Setapak, Kuala Lumpur, Malaysia
kylee@utar.edu.my

[5] Radio Communication Engineering Department (RaCED), Faculty of Electrical Engineering
Universiti Teknologi Malaysia, Skudai, Johor 81310, Malaysia
kyyou@fke.utm.my

[6] School of Electrical Systems Engineering
Universiti Malaysia Perlis (UniMAP), Pauh Putra Campus, Arau, Perlis 02600, Malaysia
sfkhor@unimap.edu.my

Abstract **─** In this paper, the use of the Finite Difference Method (FDM) is proposed to determine the reflection coefficient of an open-ended coaxial sensor for determining the moisture content of oil palm fruit. Semi-rigid open-ended coaxial sensor is used in conjunction with Vector Network Analyzer for reflection coefficient measurement of oil palm fruit. Moisture content in oil palm fruit determine optimum harvest time of oil palm fruit. Finite difference method is then used to simulate measured reflection coefficient due to different moisture contents in oil palm fruit at various stages of ripeness. The FDM results were found to be in good agreement with measured data when compared with the quasi-static and capacitance model. Overall, the mean errors in magnitude and phase for the FDM were 0.03 and 3.70°, respectively.

Index Terms **─** Finite difference method, moisture content, oil palm fruit, open-ended coaxial sensor, reflection coefficient.

I. INTRODUCTION

A. Background of oil palm

The oil palm, *Elaeis guineensis Jacq*, is indigenous to West Africa where the cultivation area is from Sierra Leone, Liberia, the Ivory Coast, Ghana, Cameroon and extended to the equatorial regions of the Republics of Congo and Zaire [1].

The harvesting period begins around 24 to 30 months after planting [2] and each palm can produce between 8 to 15 fresh fruit bunches (FFB) per year. The weight of each bunch is about 15 to 25 kg each and this depends on the planting material and age of the palm. Each FFB contains about 1000 to 1300 fruit. Each fruit consists of 3 layers, which are the fibrous mesocarp layer, the endocarp (shell) and the kernel (Fig. 1).

Palm oil is obtained from the fleshy mesocarp, which is composed of 45-55 per cent oil by weight [3]. The *Tenera* has been the preference for the palm oil industry because of its thin shell and high oil content in the thick mesocarp structure.

Submitted On: July 22, 2015
Accepted On: July 4, 2016

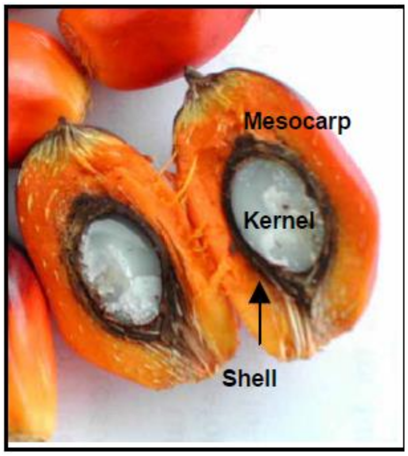

Fig. 1. Cross section of a fruitlet [2].

B. Conventional technique of determining the fruit ripeness

There are several techniques to gauge the oil palm fruit ripeness. The visible symptoms to determine fruit ripeness include the color change of the fruit [4]-[5], the percentage or number of detached fruit per bunch [6] and the fruit ability to float on water, or so called floatation technique [7]. However, they are unreliable due to their inconsistencies and inaccuracies.

C. The relationship between moisture content and ripeness of oil palm fruit

The current research in gauging the ripeness of oil palm fruit is via examination of the amount of moisture content in mesocarp of an oil palm fruit. Ariffin et al. [8] states that the moisture content in mesocarp of oil palm fruit can be used as an indicator to determine the fruit ripeness. It was found that the moisture content is higher in unripe oil palm fruit at the early stage of fruit development. The water in the mesocarp decreases gradually during fruit ripening which coincides with the oil accumulation approximately from week 12 to week 15 after anthesis (Fig. 2). The amount of water in fresh mesocarp decreases rapidly to 40% in the ripe fruit from week 16 to week 17 after anthesis. The water content will then decreases slowly from week 18 to week 24. The moisture content decrease is almost about the same time as the accumulation of oil in the mesocarp. Hence, there is a close relationship between the moisture content (mc) and oil content (oc) in mesocarp. This phenomenon is helpful to gauge the fruit ripeness. Hartley [1] states that the mass fraction of oil and mass fraction of water in the mesocarp can be expressed linearly. This relationship are visualize in Fig. 3.

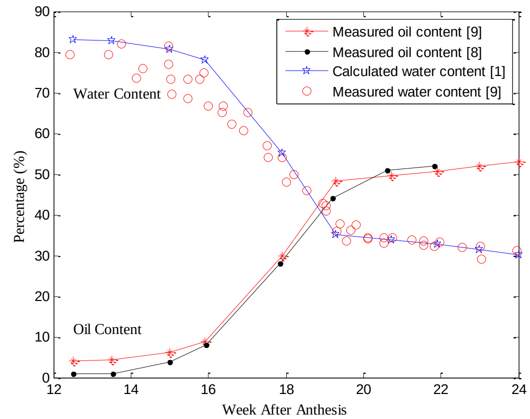

Fig. 2. Variation in moisture content and oil content after anthesis.

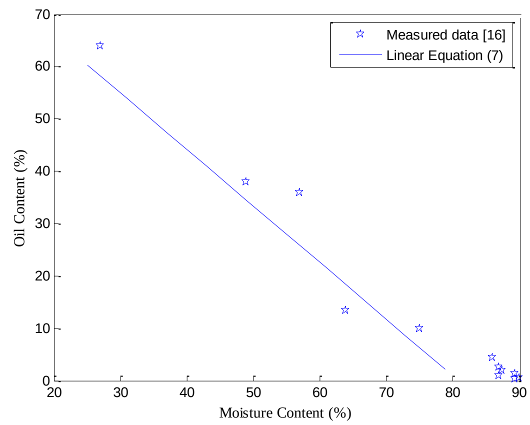

Fig. 3. The correlation of the water content (moisture content) against the oil content in mesocarp.

II. MATERIALS AND METHOD

A. Measurement of moisture content in oil palm fruit

For the sake of establishing the relationship between reflection coefficient and moisture content, the actual moisture content must first be determined by a reliable technique. Standard oven method was chosen to determine moisture content in palm oil fruit because it is the method proposed by Malaysia Palm Oil Board (MPOB). The relative moisture content of oil palm fruit, in percentage (wet basis) can be expressed as equation (1):

$$\text{m.c.} = \frac{m_{\text{before dry}} - m_{\text{after dry}}}{m_{\text{before dry}}} \times 100\% , \qquad (1)$$

where $m_{\text{before dry}}$ and $m_{\text{after dry}}$ are the weight of fruit sample before dried and after dried, respectively.

B. Simulation and measurement of open-ended coaxial sensor on oil palm fruit

Open-ended coaxial sensors have been used extensively to measure the reflection coefficient of oil palm fruit [10]-[12]. The probe associated with such a sensor is made of an RG-402 semi-rigid cable, normally operating at 2 GHz. The stage of fruit ripeness is determined by the percentage of moisture content. As the moisture content (or permittivity, ε_r^*) of the fruit changes, the values of reflection coefficient measured by the sensor also changed.

Unfortunately, both the quasi-static model (a.k.a. the admittance model) and the capacitance model assume that the thickness of the sample under consideration is infinite [13]. Therefore, these models are inappropriate for characterizing a thin sample or any sample with finite thickness, such as oil palm fruit. However, the dimensions of the sample must be taken into account in FDM calculation [14]-[15]. For instance, the length and thickness of the fruit are considered in FDM.

C. The moisture content and the dielectric properties in oil palm fruit

The moisture content of agricultural products is one of the most important parameters for determining the quality of the products. This information is required to determine the optimum time for harvesting and safe storage.

The standard oven-drying method is tedious and time-consuming, and they are not suitable for use in agro-production application. Hence, the development of a rapid test method, such as microwave method, is a pressing need in the industry. The complex dielectric permittivity, ε^* is often expressed by equation (2):

$$\varepsilon^* = \varepsilon' - j\varepsilon'', \tag{2}$$

where ε' is related to the ability of the material to store energy (dielectric constant) and ε'' is the loss factor which is the dissipation of energy in the material. The permittivity of oil palm fruit [17] can be expressed as:

$$\sqrt{\varepsilon^*} = v_w\sqrt{\varepsilon_w^*} + v_f\sqrt{\varepsilon_f^*} + v_0\sqrt{\varepsilon_0^*}, \tag{3}$$

where v_w, v_f, and v_0 are the volume fraction of water, fiber, and oil, respectively, and ε_w^*, ε_f^*, and ε_0^* are the corresponding complex permittivities. It has been shown that both ε_f^* and ε_0^* are essentially constant throughout the frequency range between DC and 10 GHz with $\varepsilon_f^* = 2.2 - 0.06j$ and $\varepsilon_0^* = 2.3 - 0.02j$. The values of ε_w^* are obtained from the Cole-Cole model [18]:

$$\varepsilon_w^* = \varepsilon_\infty + \frac{\varepsilon_s - \varepsilon_\infty}{1 + (j\omega\tau)^{1-\alpha'}}, \tag{4}$$

where α' is the distribution parameter, which is an empirical constant. Thus, the palm oil mixture consists of three main components, i.e., v_o, v_w, and v_f, and the relationship between them is:

$$v_0 = 1 - v_w - v_f. \tag{5}$$

Since $v_f = 0.16$ [1], v_w can be calculated as:

$$v_w = \frac{(m.c.)(\rho_f v_f + \rho_0 - \rho_0 v_f)}{\rho_w - (m.c.)\rho_w + (m.c.)\rho_0}, \tag{6}$$

where the densities ρ_w, ρ_f and ρ_0 are 1, 0.92 and 0.93 respectively and mc is the moisture content. The volume fraction of oil and water can be found by using Equation (5) and Equation (6), respectively. In Equation (7), the relative moisture content in the wet basis can be determined in terms of the mass of water, oil, and fiber, which are represented by m_w, m_0, and m_f, respectively [19]:

$$m.c. = \frac{m_w}{m_w + m_0 + m_f} \times 100\%. \tag{7}$$

Hence, the permittivity of the oil palm fruit can be calculated using the mixture model [12].

Figure 4 shows the permittivity of oil palm fruit for *mc* between 20% and 90%. The abnormal behavior of ε' with *mc* below 30% is due to bound water [20]-[21].

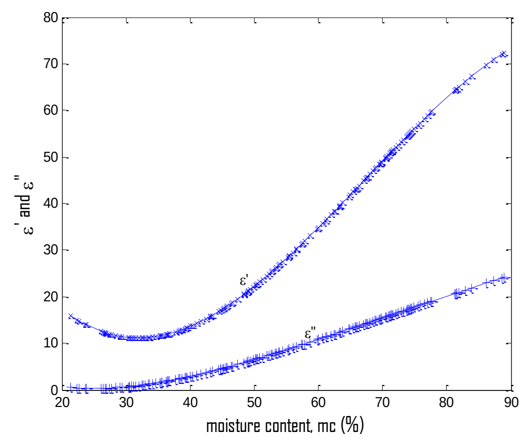

Fig. 4. Relationship of moisture content in oil palm fruit with ε' (dielectric constant) and ε'' (loss factor) at 2 GHz.

D. Admittance model (quasi-static model)

The relationship between normalized admittance and the reflection coefficient of an open-ended, coaxial sensor can be written as Equation (8):

$$\Gamma = \frac{Z_L - Z_0}{Z_L + Z_0} = \frac{1 - \tilde{Y}_L}{1 + \tilde{Y}_L}, \tag{8}$$

where Z_0 is the 50 Ω characteristic impedance of the coaxial sensor. The normalized admittance, $\tilde{Y}$ [12], [22], is established by two terms, i.e., normalized conductance, $G(0)/Y_0$, and susceptance $B(0)/Y_0$. $\tilde{Y}$ can be expressed as:

$$\tilde{Y} = \frac{G(0)}{Y_0} + j\frac{B(0)}{Y_0}, \tag{9}$$

where

$$\frac{G(0)}{Y_0} = \frac{\sqrt{\varepsilon_r}}{\ln\left(b/a\right)\sqrt{\varepsilon_c}} \int_0^{2\pi} \frac{1}{\sin\theta} \times \left[J_o\left(k_o\sqrt{\varepsilon}b\sin\theta\right) - J_o\left(k_o\sqrt{\varepsilon}a\sin\theta\right)\right]^2 d\theta, \tag{10}$$

$$\frac{B(0)}{Y_0} = \frac{\sqrt{\varepsilon}}{\pi\ln\left(b/a\right)\sqrt{\varepsilon_c}} \times \int_0^{\pi} \begin{bmatrix} 2\,\mathrm{Si}\left(k_o\sqrt{\varepsilon\left(a^2+b^2-2ab\cos\theta\right)}\right) \\ -\mathrm{Si}\left(2k_o\sqrt{\varepsilon}a\ \sin\left(\frac{\theta}{2}\right)\right) \\ -\mathrm{Si}\left(2k_o\sqrt{\varepsilon}b\ \sin\left(\frac{\theta}{2}\right)\right) \end{bmatrix} d\theta, \tag{11}$$

where ε_c is the dielectric constant of the material that fills the coaxial line, ε is the dielectric constant in the external medium, *a* and *b* are the inner and outer radii, respectively, k_o is the free space propagation constant, J_o is the zero-order Bessel function, and *Si* is the sine integral. Equations (10) and (11) can be approximated by the first term of the Taylor series expansion [22]. In this study, the aspect ratio, b/a was 3.2981.

E. Capacitance model

An open-ended coaxial sensor can be used to measure the dielectric constant of living tissue (*in vivo*), e.g., oil palm fruit. The expression that represents the aperture admittance in terms of the *in vivo* measurement of the relative permittivity of the external medium [13] is:

$$Y_L(\omega, \varepsilon_r^*) = j\omega(\varepsilon_r^* C_0) = j\omega C(\varepsilon_r^*), \tag{12}$$

in which

$$C(\varepsilon_r^*) = \varepsilon_r^* C_0, \tag{13}$$

$$C(\varepsilon_r^* = 1) = C_0, \tag{14}$$

$$C_0 = 2.38\varepsilon_0(b-a), \tag{15}$$

$$\varepsilon_0 = \frac{10^{-9}}{36\pi}\ \mathrm{F/m}, \tag{16}$$

where Y_L is the admittance at the end of the coaxial probe, ω is the angular frequency, ε_0 is the permittivity of free space, ε_r^* is the relative permittivity of the sample that occupies the space outside the coaxial line, and C_0 is the capacitance of the probe (in free space). The fringing capacitance, $C(\varepsilon_r^*)$ at the aperture of the probe consists of a part that is dependent on the relative permittivity of the sample and the filling of the coaxial line.

F. Iteration method in solving finite difference method (FDM)

The computation work of FDM involves large system of simultaneous equations, and iterative method was used to overcome these. Iterative method uses the approximation from previous computation to calculate the next approximation. This computation is carried out iteratively until its value converges.

Initial values of the potentials were set at the free nodes which equals to zero or to any reasonable value. For example, we set 1 V at the excitation plane and 0 V at the ground conductor or perfect electric conductor (PEC). These potential values are arranged to form a matrix. Maintaining the potentials at the fixed nodes constant at all times, then applying the equation:

$$V_{i,j} = \frac{1}{4}\left(V_{i+1,j} + V_{i-1,j} + V_{i,j+1} + V_{i,j-1}\right), \tag{17}$$

to every free node in turn until the potentials at all grid nodes (Fig. 5) are calculated. The potential in output matrix is fed to the input matrix to calculate the potential (element in matrix) in the next iteration. The potentials obtained at first iteration may only provide an approximate result because the first iteration may not able to converge the potential to a correct value. In order to enhance the accuracy of the potentials, the calculation was repeated at each free node using previously calculated potential. The iterative modification of the potential at each grid node or vertex points of meshes is repeated until desired degree of accuracies is obtained or until two successive values at each node are sufficiently equal.

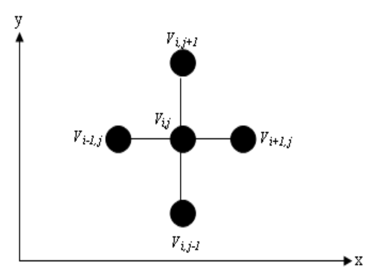

Fig. 5. Finite difference solution pattern: finite-difference, five-node molecule.

G. Application of the concept of finite-difference in the coaxial sensor and sample

Plane CD is the boundary between two different materials, i.e., the Teflon in the coaxial line and the sample. At the dielectric boundary (Fig. 6), the boundary condition,

$$D_{1n} = D_{2n}, \tag{18}$$

must be imposed where D_{1n} and D_{2n} are the normal components of the electric flux density at dielectric filler in coaxial line and in the sample being tested, respectively. This condition is based on Gauss' Law for electric fields, i.e.,

$$\oint D \cdot dl = \oint \varepsilon E \cdot dl = Q_{enc} = 0, \tag{19}$$

since no free charge is deliberately placed on the dielectric boundary. Substituting $E = -\nabla V$ in Equation (19) gives:

$$0 = \oint \varepsilon \nabla V \cdot dl = \oint \varepsilon \frac{\partial V}{\partial n} \cdot dl, \tag{20}$$

where $\frac{\partial V}{\partial n}$ denotes the derivative of V normal to the contour *l*. Applying Equation (20) to the interface in Fig. 6 yields:

$$V_0 = \frac{\varepsilon_1}{2(\varepsilon_1+\varepsilon_2)} V_1 + \frac{\varepsilon_2}{2(\varepsilon_1+\varepsilon_2)} V_3 + \frac{1}{4} V_2 + \frac{1}{4} V_4 . \tag{21}$$

The finite difference potential results on plane CD in Fig. 6 (circular ring potential in the area of the cross section of coaxial sensor, V_{ring}) were computed. The total potential, V_{area}, and the total charge, Q_{area}, at the area of the aperture of the probe can be determined easily by using Equations (22) and (23), respectively [23]:

$$V_{area} = \int_a^b V_{ring}\, d\rho, \tag{22}$$

$$Q_{area} = \varepsilon \int_a^b \int_0^{2\pi} \frac{V_{ring}}{\rho} \rho d\phi\, d\rho, \tag{23}$$

where ρ is the radius at aperture of the coaxial probe, *a* is the inner radius of the coaxial probe, and *b* is the outer radius of the coaxial probe. The normalized and characteristic admittance are expressed as:

$$\tilde{Y} = \frac{j\omega C}{Y_0}, \tag{24}$$

$$\tilde{Y}_0 = \frac{2\pi}{\sqrt{\frac{\mu_0}{\varepsilon_0 \varepsilon_c}} \cdot ln\left(\frac{b}{a}\right)}, \tag{25}$$

where ε_0 is the permittivity in free space, ε_c is the relative permittivity of the coaxial line (PTFE), and μ_0 is the free space of permeability. The reflection coefficient, Γ is obtained from Equation (8).

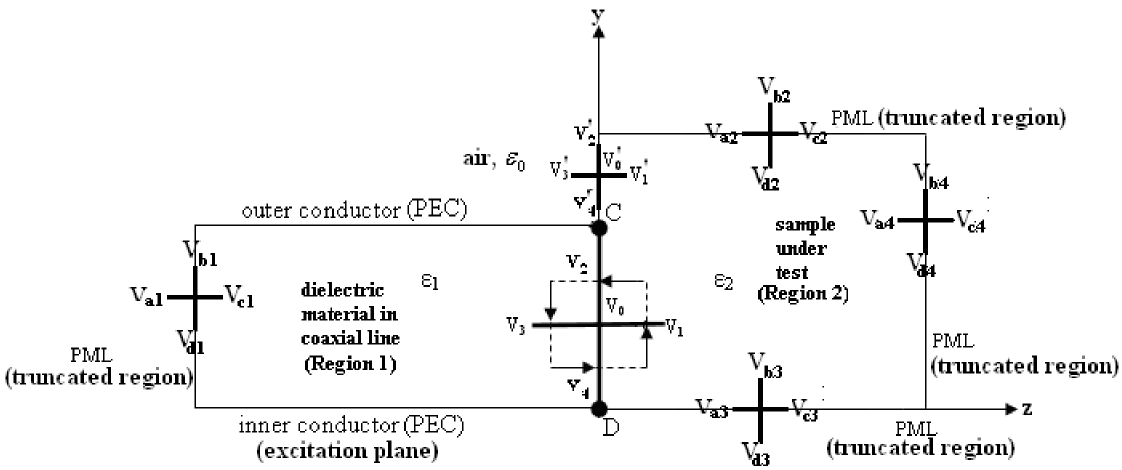

*PML=Perfect Matched Layer
PEC=Perfect Electric Conductor

Fig. 6. Interface between media of dielectric permittivities ε_1 (dielectric material in the coaxial line) and ε_2 (sample being tested).

III. RESULTS AND DISCUSSION

A. Magnitude of the reflection coefficient

The results comparison for the measured and calculated values of the reflection coefficient at various percentages of moisture content in oil palm fruit is shown in Fig. 7.

The whole results suggested that the magnitude of the reflection coefficient decreases as the moisture content of the fruit increased [24]. The results obtained using the mixture model indicated that complex permittivity, ε^* increased when the moisture content is high. This relationship, which is due to the high degree mismatch of impedance, is clearly shown in Fig. 8. Increases in ε^* could cause the sample's impedance, Z_L to decrease. The admittance model can be used to calculate this.

In summary, increasing the moisture content causes the complex permittivity to increase, as Fig. 4 shows. Hence, this condition results in the decrease of impedance, which, in turn, causes the magnitude of the reflection coefficient, $|\Gamma|$, to decrease. Figure 8 shows this relationship as a 3D line plot.

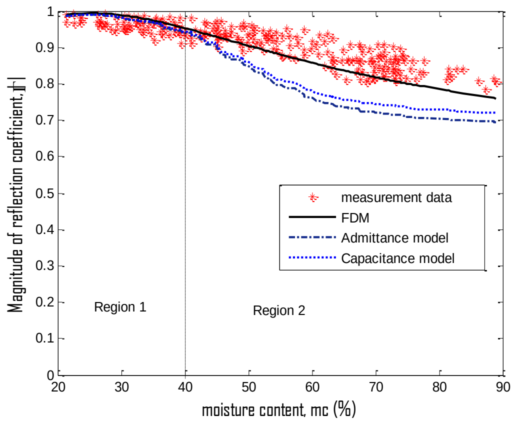

Fig. 7. The comparison between measured $|\Gamma|$ with calculated results obtained from finite difference method (FDM), admittance model and capacitance model at 2 GHz.

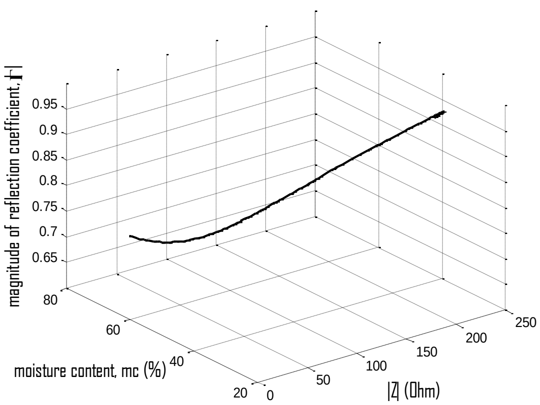

Fig. 8. The relationships between $|Z_L|$, $|\Gamma|$, and moisture content.

According to the admittance model, decreasing Z_L (as a result of a greater dielectric constant) results in a decrease in the magnitude of the reflection coefficient. The relationship between the normalized admittance, $\left(\tilde{Y}_L = \frac{Z_0}{Z_L}\right)$ and the reflection coefficient, Γ is shown by the Equation (25). Z_0 is the 50 Ω characteristic impedance of the coaxial sensor. Figure 8 shows the relationship between magnitude of reflection coefficient, magnitude of impedance, and moisture content.

The FDM, admittance model and capacitance model produced trends that were similar to the measurement results. The magnitudes that were acquired by FDM showed better agreement with the measured data than the admittance model or the capacitance model [19]. The FDM provided a mean error of 0.03 for the moisture content ranging from 20% to 90%. The mean errors produced by the admittance model and the capacitance model are 0.06 and 0.05, respectively. The poor accuracies of the admittance model and the capacitance model were due to the assumptions that were made in the models. In both models, it is assumed that the thickness of the sample is infinite [13]. Therefore, neither one of them is suitable for use in characterizing a thin sample or any sample with a finite thickness, such as the sample of oil palm fruit. However, the dimensions of the sample, i.e., its length and width, must be taken into account in the FDM calculation. The PML is necessary to truncate the computation region of the material, in order to retain the practicability of the computation.

Among the three models, the FDM approach had the best agreement with the measured values of the reflection coefficient, as shown in Fig. 7.

Figure 9 represents a portion of Fig. 7, which designated as region 1 in Fig. 7. Region 1 is in mc range from 20% to 40%. Meanwhile, the region where the mc range is from 40% to 90% is designated as region 2. These two mc ranges are important to study the period after anthesis. The relationship of water content in fruit and the period after anthesis can be referred to Fig. 2.

Measurement data shows $|\Gamma|$ decreases gradually when moisture content increases. Referring to Fig. 2, it can be observed that the mc in the range of 20% to 40% is within 18 weeks to 24 weeks after anthesis. During this period, the water content and oil content show insignificant change. The fruit accumulates maximum amount of oil content in this mc range. It can be used to determine the optimum of harvesting time of oil palm fruit. Therefore, the relationship of $|\Gamma|$ against moisture content can be used to predict moisture content upon the knowledge of $|\Gamma|$.

The trend line in Fig. 2 that represents water and oil content seems unchanged in this mc range. The fruit seems to be at constant water and oil level. The mean magnitude error of FDM, admittance model and capacitance model are similar, i.e., 0.01 when compared with Fig. 9. The similar values of mean magnitude error for these models are close to the mean magnitude error that is presented by the fitting line shown in Fig. 9, i.e., 0.01. The insignificant change in moisture content yield to the insignificant change in their magnitude of reflection coefficient as well. It can be proved by the sensitivity in Fig. 10. Figure 10 indicates the sensitivity of $\frac{d|\Gamma|}{d(mc)}$ in region 1. It can be noticed that the sensitivity is kept constant when the mc increases from 20% to 40%. It means that it is best represented as a linear relationship. It has been proved by the fitting linear equation in Fig. 9. The sensitivity value is -0.0017 and it is very small. This can be explained by Fig. 2. In Fig. 2, the range of water content which is between 20% to 40% shows the insignificant change when the fruit exceeds week 17 after anthesis.

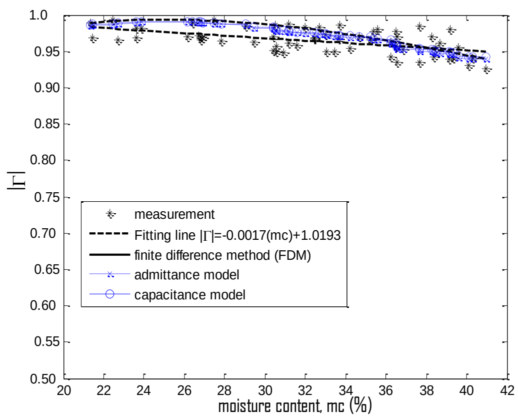

Fig. 9. Region 1 of Fig. 7.

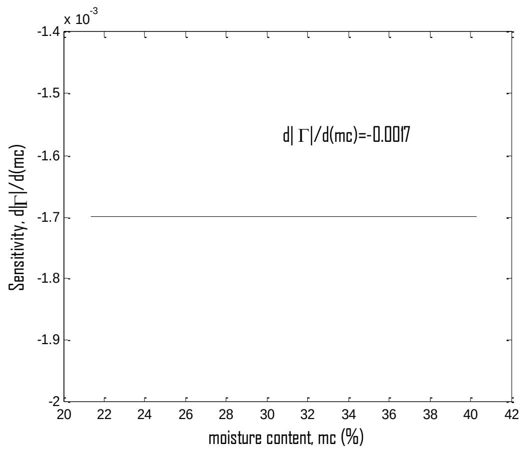

Fig 10. Sensitivity of $\frac{d|\Gamma|}{d(mc)}$ for the mc range between 20% to 40% (region 1).

Figure 11 represents region 2 in Fig. 7. The range 40% to 90% moisture content is within week 12 to week 16 after anthesis. It can be observed in Fig. 2 as well. The water content and oil content change drastically during week 16 to week 17. The water content starts to decrease, whereas oil content starts to rise on week 16 after anthesis. This is difficult to predict because the moisture content has an abrupt change. Hence, it can be observed that the error of FDM, admittance model and capacitance model are larger than the case in region 1 (Fig. 9), namely 0.06, 0.11 and 0.10. When FDM, admittance model and capacitance model are compared to each other, it can be found that FDM shows the best agreement with measured data with the smallest error, 0.06 during week 12 to 17 after anthesis. The fitted line of measure data is best represented as quadratic equation $|\Gamma| = (6\times10^{-6})(mc)^2 - 0.004(mc) + 1.111$. Hence, the sensitivity equation [25] can be represented by $\frac{d|\Gamma|}{d(mc)} = (1.2\times10^{-7})(mc) - 0.004$ and it is visualized in Fig. 12. Even though the sensitivity decreases when the moisture contents increases from 40% to 90%, however, the variation of sensitivity with mc is not drastic. Although the sensitivity decreases, it is still greater than the sensitivity in region 1 as shown in Fig. 10. Overall, the sensor has higher sensitivity $\frac{d|\Gamma|}{d(mc)}$ for moisture content greater than 40% (region 2) if compared with Fig. 10 and it is commendable as this coincides with the drastic change in moisture content from unripe fruits to the ripe stage.

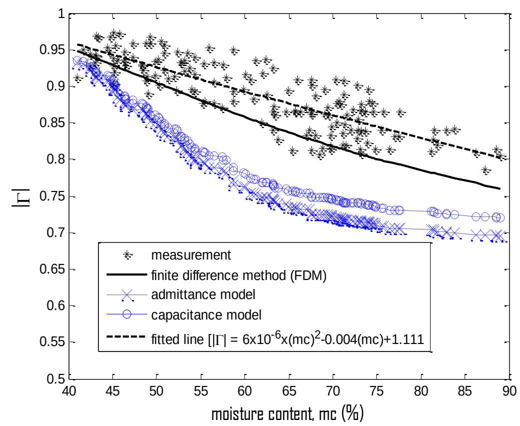

Fig. 11. Region 2 of Fig. 7.

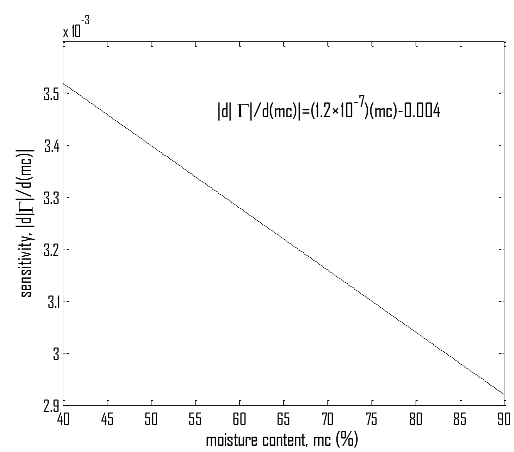

Fig. 12. Sensitivity of $d|\Gamma|/d(mc)$ for the mc range between 40% to 90% (region 2).

B. Phase of reflection coefficient

The variation of phase with moisture content, *mc*, is shown in Fig. 13. Phase is highly influenced by the complex permittivity, ε* and the thickness of the sample

[26]. In addition, the length of the coaxial line and the thickness of the fruit can cause a phase shift. The phase shift in Fig. 13 shows good agreement with the measured data when compared with the phase on plane AB. When the length of coaxial line varies from 0.5 cm to 10 cm, it can be observed that the error in FDM shows the smallest when the length is 6 cm as seen in Fig. 14. However, the measured length of coaxial sensor from the caliper shows 5.655 cm. This deviation may be due to the inhomogenity of the fruit in terms of permittivity. The FDM results deviated from the measured data because FDM only considers a homogeneous sample calculation. The phase of reflection coefficient from FDM still shows the best results for 6 cm coaxial sensor when compared to admittance model and capacitance model which have extended to plane AB as well by using technique of de-embedding of coaxial probe [27]. The effects of length of the open-ended, coaxial sensor towards reflection coefficient in reflection measurement had been reported [28]. Error shown by FDM is 45.6 degrees on the plane CD. After the plane is extended from plane CD to AB, the error is reduced to 7.80 degrees with similar condition. It is expected that the measurement plane must coincide with the calibration plane, since the calibration is done on plane AB. The mean phase error of admittance model (25.0 degrees of mean error) and capacitance model (27.1 degrees of mean error) are higher at plane CD if compared with the mean phase error at plane AB. After the plane CD is extended to plane AB, the error of admittance model is reduced to 17.3 degrees, while capacitance model is reduced to 15.0 degrees. After the comparison was done, the FDM on plane AB shows the best agreement with measured data. The poor accuracy in admittance model and capacitance model are due to the assumption made in both models. As mentioned previously, the admittance model and capacitance model assumed that the thickness of sample under consideration is infinite [13]. Therefore, they are not suitable to be used in characterizing a thin sample or any sample with finite thickness which is similar with oil palm fruit. This deviation of measured phase from the calculated phase using FDM may be due to the inhomogeneity of the oil palm fruit. The FDM results deviated from measured data because the FDM calculations only considered homogeneous samples. The FDM approach has better results for the phase of the reflection coefficient than the admittance model or the capacitance model. FDM has an error of only 3.70 degrees for similar conditions. The mean phase errors of the admittance model and the capacitance model were approximately 18 degrees and 15 degrees, respectively. When all the results were compared, it was apparent that the FDM provided the best agreement with the measured data. The poor accuracies in the admittance model and the capacitance model were due to the limiting assumptions that were made in both models. As mentioned previously, in both of these models, it was assumed that the thickness of sample of fruit was infinite. Therefore, neither of these two models is suitable for characterizing thin sample or any sample with finite thickness, such as the oil palm fruit. Figure 15 represents region 1 in Fig. 13. In Fig. 9, the magnitude of measured data, admittance model and capacitance model shows insignificant change with moisture content range 20% to 40%. The phase of admittance model and capacitance model for moisture content between 20% and 40% is almost constant as shown in Fig. 15. However, the measured phase decreases with equation $\phi = 0.0117(\mathrm{mc})^2 - 1.2846(\mathrm{mc}) - 30.665$. The mean phase error for FDM, admittance model and capacitance model on plane AB are 3.59 degrees, 4.27 degrees and 4.44s degree respectively. They have the mean phase error that is close to the fitting line which shows 3.13 degrees of mean error. Comparing FDM with admittance model and capacitance model, FDM has better agreement with the measured phase. The FDM, admittance model and capacitance model on plane CD (measurement plane) show a larger mean phase error if compared with the models on plane AB. It is due to the measured magnitude are collected on calibration plane but not the measurement plane. The differentiation of the fitting line equation with moisture content is:

$$\left|\frac{d\phi}{d(\mathrm{mc})}\right| = 0.0234(\mathrm{mc}) - 1.2846, \qquad (26)$$

or so-called sensitivity for moisture content range 20% to 40% as shown in Fig. 16. It is dissimilar to Fig. 10 because of the sensitivity in Fig. 16 decreases from 0.3 to 0.8 for moisture content range 20% to 40%, however, the sensitivity in Fig. 16 decreases insignificantly from 0.0035 to 0.0029. For this reason, the measured phase has higher sensitivity than the measured magnitude in region 1.

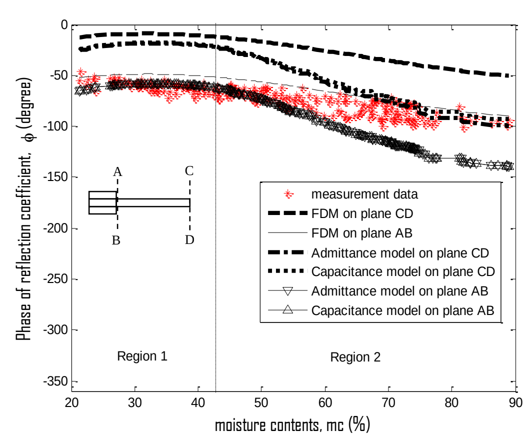

Fig. 13. Comparison of phase of reflection coefficient among measured data, FDM, admittance model and capacitance model.

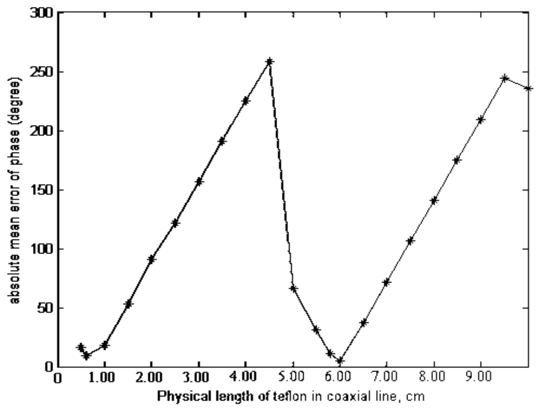

Fig. 14. Length of coaxial line with its phase error of reflection coefficient.

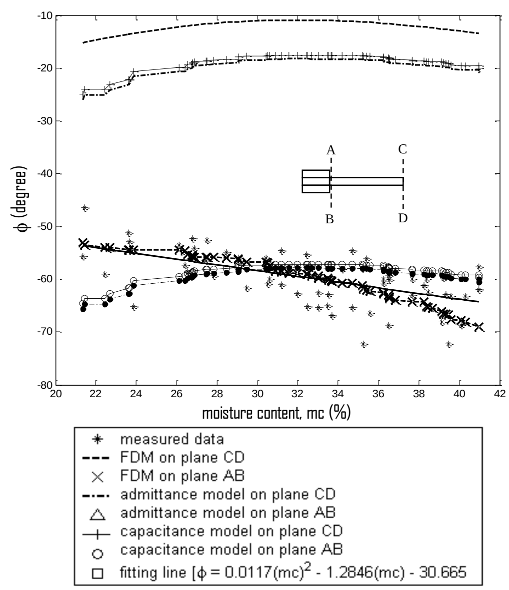

Fig. 15. Region 1 of Fig. 13.

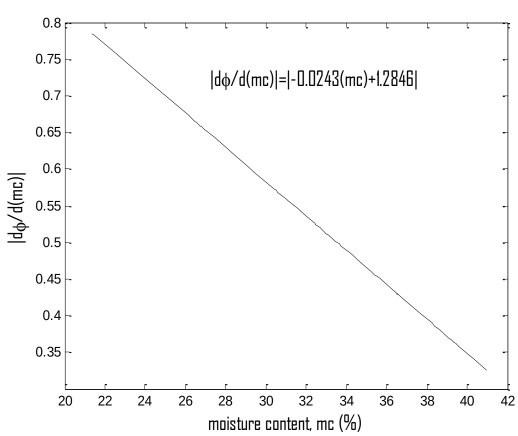

Fig. 16. Sensitivity, $|d\phi/d(mc)|$ for mc range between 20% to 40% (region 1).

Figure 17 represents region 2 in Fig. 13. The mc range 40% to 90% is within week 12 to week 16 after anthesis. During this period, the condition in Fig. 17 is similar to Fig. 11 because they show a similar trend. The water content starts to decrease, whereas oil content starts to rise in week 16 after anthesis. It can be observed that the error of FDM, admittance model and capacitance model are larger than the case in Fig. 15, namely 8.51 degrees, 22.29 degrees and 18.97 degrees. In Fig. 15, FDM still shows the best agreement with measured data. It has the smallest error compared with admittance model and capacitance model. Unlike the case in Fig. 15, the results of admittance model and capacitance model deviated from measured phase in mc range from 40% to 90%. The admittance model and capacitance model have larger mean phase error, namely 22.29 degrees and 18.97 degrees, respectively. The fitting equation that represents the trend of measured phase is $\phi = 0.0015(mc)^2 - 0.9145(mc) - 27.928$ as shown in Fig. 17, while the relationship between sensitivity and mc is $|d\varphi/d(mc)| = (0.0030)(mc) - 0.9145$.

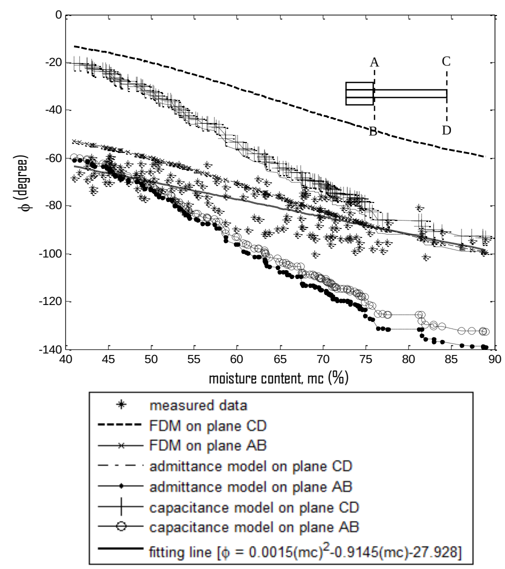

Fig. 17. Region 2 of Fig. 13.

For moisture content from 40% to 90%, the sensitivity decreases from 0.79 to 0.65. However, the range of sensitivity in Fig. 16 is from 0.3 to 0.8. The measured phase in the moisture content from 40% to 90% shows higher sensitivity than in Fig. 16. This can be explained by referring to Fig. 4. In Fig. 4, the ε' and ε" increase drastically when the moisture content is greater than 40%. The negative phase of reflection coefficient increases when the complex permittivity increases as well. The sensitivity of phase $\left(\left|\frac{d\phi}{d(mc)}\right|\right)$

shows higher than the magnitude in region 2 (Fig. 17). This implies that a small change in moisture content can be easily detected by the phase of reflection coefficient when compared with magnitude of reflection coefficient. This can help to estimate the moisture content accurately [23].

In region 2 where mc > 40%, the sensitivity is higher than region 1. The sensitivity can be expressed as $\left|\frac{d\phi}{d(mc)}\right| = \left|-0.0245(mc) + 2.25\right|$ (Fig. 18). It is in line with the response of moisture content to the weeks after anthesis as shown in Fig. 2, where the variation of mc becomes drastic when mc > 40%.

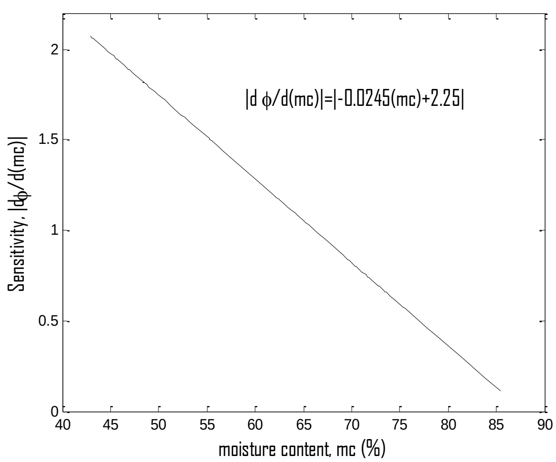

Fig. 18. Sensitivity, $\left|\frac{d\phi}{d(mc)}\right|$ for mc range that exceeds 40%.

IV. CONCLUSION

In this work, the complex reflection coefficient was analyzed computationally with FDM on an aperture coaxial sensor. The accuracy of this analysis was investigated by comparing calculated (FDM, the admittance model and the capacitance model) with measured reflection coefficients (measured using a Vector Network Analyzer). Figures 7 and 13 indicate that the FDM was more accurate than the admittance model and the capacitance model.

REFERENCES

[1] C. W. S. Hartley, *The Oil Palm*. 3rd ed., Longman, London, 1988.

[2] C. H. Teoh, "The Palm Oil Industry in Malaysia: From Seed to Frying Pan," *Report of WWF Malaysia*, pp. 5, 2002.

[3] A. Tola and T. B. Aishat, "Palm fruit in traditional African food culture," *Asia Pacific J. Clin. Nutr.*, vol. 12, no. 3, pp. 350-354, 2003.

[4] S. Y. Choong, S. Abbas, A. R. Shariff, R. Halim, M. H. S. Ismail, R. Yunus, S. Ali, and F. R. Ahmadun, "Digital image processing of oil palm fruits," *International Journal of Food Engineering*, vol. 2, iss. 2, Article 7, 2006.

[5] Z. May and M. H. Amaran, "Automated oil palm fruit grading system using artificial intelligence," *International Journal of Video & Image Processing and Network Security IJVIPNS-IJENS*, vol. 11, no. 03, pp. 30-35, 2011.

[6] A. Ariffin, "Fundamental aspects of oil and fats, *In Improving Oil Extraction Rates in Palm Oil Mills, Sabah: CEPP and UTM*, 2005.

[7] A. Ariffin, "Biochemical aspects of ripeness standard," *In Proceedings of the Symposium on Impact of Pollination Weevil on the Malaysian Oil Palm Industry, Kuala Lumpur: Palm Oil Research Institute of Malaysia*, 1984.

[8] A. Ariffin, S. R. Mat, M. Banjari, and O. W. E. Wan, "Morphological changes of the cellular component of the developing palm fruit (Tenera: Elaeis Guineesis)," *Palm Oil Research Institute of Malaysia Bulletin*, vol. 21, pp. 30-34, 1990.

[9] K. Khalid and Z. Abbas, "A microstrip sensor for determination of harvesting time for oil palm fruits (Tenera: Elaeis Guineesis)," *J. Microwave Power and Electromag. Energy*, vol. 27, pp. 3-10, 1992.

[10] Z. Abbas, Y. K. Yeow, A. H.Shaari, J. Hassan, E. Saion, K. B. Khalid, and A. Zakaria, "Fast and simple technique for determination of moisture content in oil palm fruits," *Jpn. J. Appl. Phys.*, vol. 44, no. 7A, pp. 5272-5274, 2005.

[11] K. Y. Lee, Z. Abbas, N. S. Mohamed Dan, and K. Y. You, "Portable microwave instrumentation system for determination of moisture content in oil palm fruits," *Jpn. J. Appl. Phys.*, vol. 48, 2009.

[12] Z. Abbas, K. Y. You, A. H. Shaari, K. Khalid, J. Hassan, and E. Saion, "Complex permittivity and moisture measurements of oil palm fruits using an open-ended coaxial sensor," *IEEE Sensor Journal*, vol. 5, no. 6, pp. 1281-1287, 2009.

[13] S. Khandige and D. Misra, **"**Characterization of the layered dielectrics using an open-ended coaxial line sensor," *In Proceeding of* Conference *on Precision Electromagnetic Measurements Digest*, pp. 65-66., 27th June-1st July, 1994.

[14] R. C. Rumpf, "Simple implementation of arbitrarily shaped total-field/scattered-field regions in finite-difference frequency-domain," *Progress in Electro-magnetics Research B*, vol. 36, pp. 221-248, 2012.

[15] V. Demir, "Graphics processor unit (GPU) acceleration of finite-difference frequency-domain (FDFD) method," *Progress in Electromagnetics Research M*, vol. 23, pp. 29-51, 2012.

[16] I. Karuppannan, O. Omar, and A. Ariffin, "Profiles of biochemical changes during the development of oil palm mesocarp (Elaesis Guineensis)," *Proc.*

Mal. Biochem. Soc. Conference, vol. 11, pp. 129-134, 1986.

[17] E. M. Cheng, M. F. B. A. Malek, M. Ahmed, K. Y. You, K. Y. Lee, and H. Nornikman, "The use of dielectric mixture equations to analyze the dielectric properties of a mixture of rubber tire dust and rice husks in a microwave absorber," *Progress in Electromagnetics Research*, *PIER*, vol. 129, pp. 559-578, 2012.

[18] A. Nyshadham, C. L. Sibbald, and S. S. Stuchly, "Permittivity measurements using open-ended sensors and reference liquid calibration – An uncertainty analysis," *IEEE Trans. Microwave Theory Tech*., vol. 43, pp. 1986-1989, 1992.

[19] K. Y. Lee, Z. Abbas, Y. K. Yeow, M. D. Nur Sharizan, and C. E. Meng, "In situ measurements of complex permittivity and moisture content in oil palm fruits," *Eur. Phys. J. Appl. Phys*., vol. 49, pp. 31201, 2010.

[20] M. A. Jusoh, Z. Abbas, J. Hassan, B. Z. Azmi, and A. F. Ahmad, "A simple procedure to determine complex permittivity of moist material using standard commercial coaxial sensor," *Meas. Sci. Review*, vol. 11, no. 1, pp. 19-22, 2011.

[21] V. M. Serdyuk, "Dielectric study of bound water in grain at radio and microwave frequencies," *Progress in Electromagnetics Research*, *PIER*, vol. 84, pp. 379-406, 2008.

[22] N. Marcuvtiz, *Waveguide Handbook*. Boston, MA: Boston Tech. Pub., pp. 213-216, 1964.

[23] K. Y. You, Z. Abbas, and K. Khalid, "Application of microwave moisture sensor for determination of oil palm fruit ripeness," *Meas. Sci. Review*, vol. 10, no. 1, pp. 7-14, 2010.

[24] A. Taflove, *Computational Electrodynamics: The Finite Difference Time Domain Method*. Boston, MA: Artech House, 1995.

[25] M. F. Zainuddin, Z. Abbas, M. H. M. Hafizi, M. A. Jusoh, and M. H. H. Razali, "Monopole antenna technique for determining moisture content in the Dioscorea hispida tuber," *Australian Journal of Crop Science*, *AJCS*, vol. 7, no. 1, pp. 1-6, 2013.

[26] A. H. Ali, Z. B. Abbas, J. B. Hassan, A. B. Jusoh, and R. B. M. Zahari, "Microwave antenna sensing technique for determination of moisture content in Hevea latex from Hevea Brasiliensis tree," *Australian Journal of Crop Science*, *AJCS*, vol. 5, no. 11, pp. 1326-1333, 2011.

[27] F. Ansarudin, Z. Abbas, J. Hassan, N. Z. Yahaya, and M. A. Ismail, "A simple insulated monopole sensor technique for determination of moisture content in *Hevea* rubber latex," *Meas. Sci. Review*, vol. 12, no. 6, pp. 249-254, 2012.

[28] K. Y. You, H. K. Mun, L. L. You, J. Salleh, and Z. Abbas, **"**A small and slim coaxial probe for single rice grain moisture sensing," *Sensors*, vol. 13, pp. 3652-3663, 2013.

Ee Meng Cheng was born in 1980. He obtained his B.Sc. (Honours) - Instrumentation Science in Universiti Putra Malaysia in 2004. He pursued his M.Sc. in Wave Propagation at the Institute for Mathematical Research in 2005 at Universiti Putra Malaysia and his Ph.D. in Microwave at the Faculty of Science in 2007 at Universiti Putra Malaysia. Recently, he is a Senior Lecturer in School of Mechatronic Engineering, Universiti Malaysia Perlis. His main personal research interest is in the computational electromagnetic modeling, microwave dielectric spectroscopy, wave propagation in RF & microwave and microwave sensors development for food and agricultural applications.

Zulkifly Abbas was born in Alor Setar, Malaysia, in 1962. He received the B.Sc. degree with honors in Physics from the University of Malaya, Kuala Lumpur, in 1986, the M.Sc. degree in Microwave Instrumentation from the Universiti Putra Malaysia (UPM), Serdang, in 1994, and the Ph.D. degree in Electronic and Electrical Engineering from the University of Leeds, Leeds, U.K., in 2000. He is currently an Associate Professor with the Department of Physics, UPM, where he has been a Faculty Member since 1987. His main personal research interest is in the theory, simulation, and instrumentation of electromagnetic wave propagation at microwave frequencies focusing on the development of microwave sensors for agricultural applications.

Mohd Fareq bin Abdul Malek obtained his B.Eng. (Honours) - Electronic and Communication Engineering in The University of Birmingham, United Kingdom in 1994. He pursued his M.Sc. (Eng.) in Microelectronic Systems and Telecommunications at The University of Liverpool, United Kingdom in 2003 and Ph.D. Electrical Engineering (Radio Frequency and Microwave) on 2005 in The University of Liverpool, United Kingdom. Recently, he is an Associate Professor in Faculty of Engineering and Information Sciences, University of Wollongong in Dubai. His main personal research interest is in electron maser, antenna design, embedded computing and microwave absorber development.

Kim Yee Lee was born in Muar, Johor, Malaysia. He received his B.Sc. Physics, M.Sc. (Microwaves), and Ph.D. (Microwaves) from Universiti Putra Malaysia in year 2002, 2004, and 2008 respectively. In December 2007, he joined Universiti Tunku Abdul Rahman as a Lecturer in Department of Electronics and Electrical Engineering. His areas of research include microwave measurement technique, microwave circuit and instrumentation, control and automation, material properties measurement, and instrumentation calibration.

Kok Yeow You was born in 1977. He obtained his B.Sc. Physics (Honours) degree in Universiti Kebangsaan Malaysia in 2001. He pursued his M.Sc. in Microwave at the Faculty of Science in 2003 and his Ph.D. in Wave Propagation at the Institute for Mathematical Research in 2006 at Universiti Putra Malaysia. Recently, he is a Senior Lecturer at Radio Communication Engineering Department, Universiti Teknologi Malaysia. His main personal research interest is in the theory, simulation, and instrumentation of electromagnetic wave propagation at microwave frequencies focusing on the development of microwave sensors for agricultural applications.

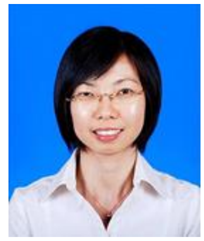

Shing Fhan Khor was born in 1982. She obtained her B.Sc. with Edu. (Honours) - Physics in Universiti Putra Malaysia in 2007. She pursued her Ph.D. in Materials Science at the Faculty of Science in 2011 at Universiti Putra Malaysia. Recently, she is a Senior Lecturer at School of Electrical Systems Engineering, Universiti Malaysia Perlis (UniMAP). Her main personal research interest is in the glass science and focusing on dielectric, optical, mechanical and thermal properties.

Jumiah Hassan is currently an Associate Professor with the Department of Physics, Faculty of Science, UPM. Her main research interests include dielectric physics, materials science, and condensed matter physics.

Hishammudin Zainuddin is currently an Associate Professor with the Department of Physics, Faculty of Science, UPM. His main research interests include Theoretical Physics, Quantum Physics, Geometry and Topology.

Design of PSR with Different Feed Configurations and Partition Lens System for Skin Cancer Treatment

Petrishia Arockiasamy and Sasikala Mohan

Department of ECE, Anna University, Chennai, Tamilnadu, India
petrishia7@yahoo.com, sasikala@annauniv.edu

Abstract ─ The Prolate Spheroidal Impulse Radiating Antenna (PSIRA) focuses pulsed radiation in the near field with a small beam width allowing the application of non-invasive skin cancer treatment. In this proposed work, SWB (Slanted Wire Bicone), EPH (Elliptical Profile Horn), TSVS (Tapered Slot Vivaldi Shape) and Tapered Arm Conical Plate (TACP) feed antenna configurations for Prolate Spheroidal Reflector (PSR) are explored to enhance the spatial resolution on biological target. The feed antenna is placed at the first focal point and the target is located at the second focal point of the PSR. Next, the resolution of focused electric field on the target is enhanced by using near field focusing lens. A 3 layer partition lens system is placed before the target to reduce the spot size of the focused field on the target. The delivery of subnanosecond pulses using reflector in conjunction with and without partition lens system on the biological target is compared for all feed antenna configurations. Tapered Arm Conical Plate (TACP) fed PSR with the 3 layer partition lens system greatly reduces the spot size to 0.5 cm along lateral direction and 1 cm along axial direction. The enhancement in spatial resolution is much favorable to reduce the damage of healthy tissues during cancer treatment.

Index Terms ─ Near field focusing lens, non-invasive cancer treatment, prolate spheroidal impulse radiating antenna, subnanosecond electric pulse, ultra wide band antenna.

I. INTRODUCTION

Recent research shows that fast, intense electromagnetic pulses can be used to kill melanoma cells [1, 2]. The conventional treatment for melanoma is an invasive method which delivers electric pulses in nanosecond range using electrodes into the skin. The non-invasive technique involves PSIRA to deliver an electric pulse. The non-invasive treatment limits surgery, reduces the pain, scarring and mortality of the patients while remaining cost effective and safe. From the past researches, it is observed that if an intense electric field is applied to cancer cells, it introduces a programmed cell death called apoptosis [3].

Xiao et al. showcased the high power electromagnetic pulses can treat melanoma cells [4, 5]. The intense pulses with subnanosecond range is preferred to obtain the higher probability of penetration into the interior of the cells. The preferred duration of subnanosecond pulse is in the range of 100-200 ps making it possible to focus the radiation on the target efficiently and produce small spot size on the target. Baum et al. designed PSIRA to deliver subnanosecond pulse. The PSIRA acts as a high power radiation source for melanoma treatment [6]. The PSIRA is based on the two foci of an ellipse. It radiates subnanosecond intense pulses from the first focus to the second focus. The feed of the PSIRA is an ultra-wideband antenna. The spatial resolution on the target is enhanced by placing lens system before the target. Kumar et al. designed a graded index lens system which is located before the dielectric slab ($\varepsilon_r = 9$). The spot diameter obtained from the numerical simulation is 1.187 cm [7].

In the proposed work, four types of PSIRA with partition lens are designed and their performance is compared in terms of spatial resolution on the target.

This paper is organized as follows. Section II presents the design of PSR. In Section III, the different feed configuration for PSR is discussed. Section IV discusses the partition lens system design .The skin model is presented in Section V. Section VI presents the comparative results of the numerical simulations of the PSIRA and focusing lens system.

II. PROLATE SPHEROIDAL REFLECTOR DESIGN

The Impulse Radiating Antenna (IRA) is a class of focused aperture antennas that have been used extensively for the generation and radiation of ultra wide band electromagnetic pulses [8, 9]. The IRA can effectively focus its radiation in the near field by using Prolate Spheroidal Reflector (PSR). A fast rising transient pulse is propagated from the first focus of the PSR. The wave is then refocused on the second focus of the PSR to obtain a very narrow impulsive waveform.

The PSIRA consists of two main parts, feed arms and a reflector. The schematic diagram of Prolate

Submitted On: July 17, 2015
Accepted On: May 22, 2016

Spheroidal Reflector is shown in Fig. 1. PSR is an elliptical reflector. It has two focal points. The feed antenna is placed at the first focal point .The target (skin) is placed at the second focal point. The radiated electromagnetic wave from the first focal point is concentrated at the second focal point where the target is placed. PSR is designed using the reflector geometry proposed by Xiao et al. [6]. The semi major axis (a) of the reflector is *29.8 cm*. The semi minor axis (b) is *25 cm*. It has two foci. The focal distance $z_0 = \sqrt{a^2 - b^2}$, i.e., 16.3 cm .The second focal point is closer to the near field region with focal distance less than $2D^2/\lambda$, where D is aperture diameter and λ is the wavelength. The distance between the two focal point is 32.6 cm.

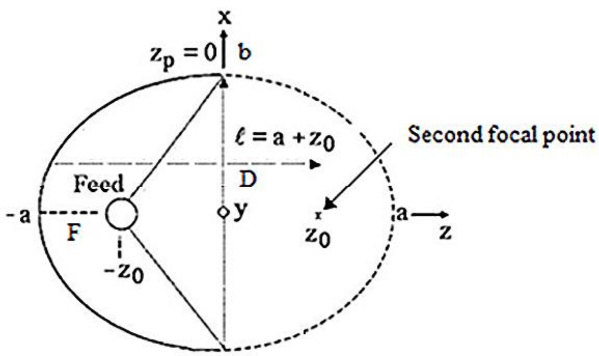

Fig. 1. Schematic diagram of prolate spheroidal reflector with geometrical parameter.

III. DESIGN OF FEED ANTENNA CONFIGURATIONS OF PSR

The radiation characteristics of IRA at high frequencies are very sensitive to the design of feeding structure. The design of different feed antenna structures for PSR is presented in this section.

A. Slanted Wire Bicone (SWB) fed PSR

The Slanted Wire Bicone (SWB) fed PSIRA design is presented. It is much suitable for ultra wide band application such as intense subnanosecond pulse radiation. The design of SWB is derived from bicone antenna [10].The radiation is focused in one direction by slanting the two cones in the desired direction by the angle of 30°, which is shown in Fig. 2 (a). In order to construct a light weight feed structure, the wire bicone is chosen instead of solid structure. The inner diameter of conical structure is 2 cm and the outer diameter is 22 cm. The excitation gap between the cone is optimized to 1 cm. The entire simulation setup is shown in Fig. 2 (b).

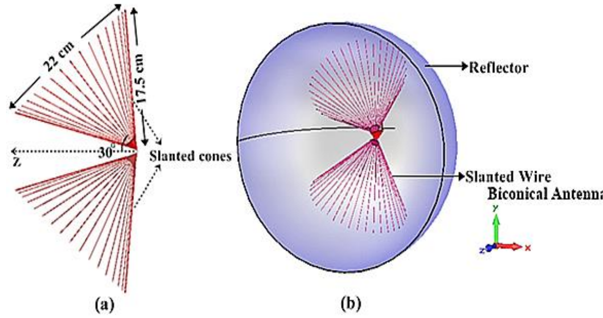

Fig. 2. SWB fed PSR: (a) geometry of SWB feed and (b) simulation model of SWB fed PSR.

B. Elliptical Profile Horn (EPH) fed PSR

The design of Elliptic Profile Horn (EPH) feed for PSR is presented. The EPH feed is simple and is designed from the single quadrant of the elliptical profile, which is shown in Fig. 3 (a). In this work the longitudinal section of the ellipse in the y-z plane is chosen, because it is easy to bend the surface smoothly at both the low impedance (driving point) as well as free space ends of the horn [11].

Two significant variables in the design of the elliptical profile horn are overall length a (semi major axis of the ellipse) and the height h (separation between the plate which is determined from the semi minor axis (b)).

The coordinates of the ellipse can be obtained from:

$$\frac{x^2}{a^2} + \frac{(y-h)^2}{b^2} = 1. \quad (1)$$

The parameter m is given by:

$$m = e^2 = 1 - b^2/a^2, \quad (2)$$

e-eccentricity of the ellipse.

The length of the arc described by the ellipse is given by E(m), the complete elliptic integral of the first kind,

$$E(m)=\int_0^{\pi/2} \sqrt{1 - m\, sin^2\theta d\theta}. \quad (3)$$

The simulation setup is shown in Fig. 3 (b). The semi major axis (a) of elliptic profile is 15 cm and semi minor axis (b) is 16 cm. At the excitation point the spacing between the plates is properly designed in order to avoid the higher order modes. For the design of horn structure the higher order modes are undesirable. So the feed gap has to be less than the wavelength at the highest operating frequency. The edges of the plates are tapered. The curvature of the tapering is optimized to completely remove the fluctuations in the main lobe at higher frequencies.

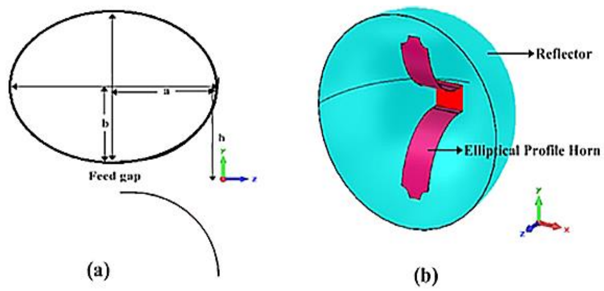

Fig. 3. EPH fed PSR: (a) geometry of elliptical profile and (b) simulation model of EPH fed PSR.

C. Tapered Slot Vivaldi Shaped (TSVS) fed PSR

The traditional Vivaldi feed arm structure for parabolic reflector has a low reflection loss in the entire frequency band but low radiation efficiency. The Tapered Slot Vivaldi Shaped (TSVS) feed arm shown in Fig. 4 (a) is designed in order to improve the radiation characteristics of the PSIRA. The Prolate Spheroidal Reflector with Tapered Slot Vivaldi Shaped feed arm is shown in Fig. 4 (b). It consists of two pairs of feed arms. The feed arms are separated by the arm angle φ=70° from the horizontal axis. The optimized arm angle (φ=70°) is used because the antenna has uniform aperture field distribution in the entire frequency band of interest [12].

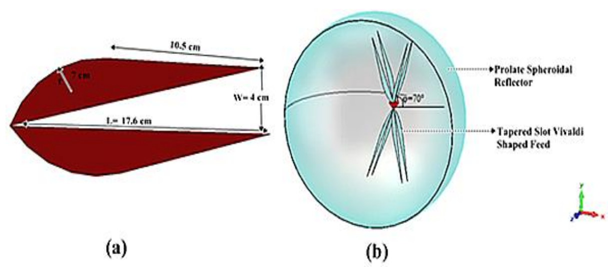

Fig. 4. TSVS fed PSR: (a) geometrical dimensions of TSVS feed and (b) simulation model of PSR with TSVS feed arms.

The TSVS feed is a combination of Vivaldi antenna and TEM coplanar transmission line. The Vivaldi shape is obtained by blending the edge of the coplanar transmission line with the radius(r) of *7* cm. The rounded portion of the TSVS feed is optimized to reduce the current reflection from the end of the antenna and to improve the radiation of low frequencies.

Two parts of the Vivaldi shape are joined at one end of the arm and the other end of the arm is arranged in such a way that it looks like a linearly tapered slot. The length of the slot, *L=17.6* cm. The width of the tapered slot, *W=4 cm*. The thickness of the arm is considered as 1 mm. The pair of two feed arms is placed at the first focal point of the PSR. The upper and lower feed arms are separated by the optimized feed gap of 1 cm.

D. Tapered Arm Conical Plate (TACP) fed PSR

The TACP fed PSR is constructed with a diameter of 50 cm and four tapered conical plate feed arm with separation angle of $\varphi_o = 60^o$. The design of a conical structure mainly depends on the three angles β_0, β_1, *and* β_2. The center angle is β_0, and β_1 and β_2 are the lower and upper side angle of the feed arm, which is shown in Fig. 5 (a). The conically symmetric TEM feeding structure parameters [β_0, β_1, β_2] are related to the equivalent longitudinally symmetric structure parameters (semi major axis a, semi minor axis b, diameter D, focal length F).

The center angle is specified as β_0:

$$\beta_0 = \arctan\left(1/\left(\frac{2F}{D} - \frac{D}{8F}\right)\right), \tag{4}$$

$$\beta_1 = 2\arctan\left(m^{1/4}\tan(\beta_0/2)\right), \tag{5}$$

$$\beta_2 = 2\arctan\left(m^{1/4}\tan(\beta_1/2)\right), \tag{6}$$

β_1 and β_2 are the lower and upper side angle of the feed arm.

Figure 5 (b) shows the PSIRA with TACP feed. These arms are terminated by 200 Ω load which are used as a low frequency matching circuit. Different termination loads have been tried [13] and it has been observed that there is no resistive termination load that can match the feeding arms with the reflector to remove the standing waves. It means that there is some stored energy around the arm-reflector junction. Because of that stored energy at the junction, the observed impedance is a complex value. It is not easy to match the feeding arms with the reflector for the entire frequency band. In order to reduce the energy stored around the junction of the arm-reflector and to improve the gain of the IRA, the end part of the feeding arms are tapered.

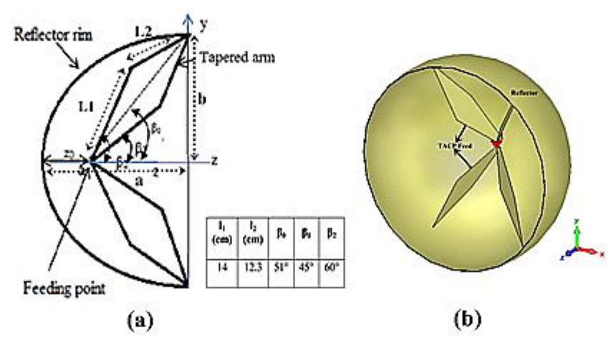

Fig. 5. TACP fed PSR: (a) configuration of TACP fed PSR and (b) simulation model of PSR with TACP feed arms.

E. Impedance and radiation characteristics of different feed configurations

The impedance and radiation characteristics of different feed configurations are presented. The spot size is one of the most important parameters to be considered for non-invasive cancer treatment. The spot is measured from the focal waveform at half power points.

The return loss and VSWR are calculated from Figs. 6 (a) and 7 (a) for SWB fed PSR. The return loss is -10 dB for the bandwidth of 600 MHz to 10 GHz. Within the band of 600 MHz to 10 GHz, the VSWR is lower than 2. The radiated pulse is focused to the second focal point where the target (skin) is placed. The focal waveform is shown in Fig. 8 (a). The maximum electric field measured is 49 V/m. The Full Width Half Maximum (FWHM) is 65ps.

The impedance characteristics of EPH fed PSIRA are shown in Figs. 6 (b) and 7 (b). The return loss is -10 dB for the bandwidth of 430 MHz to 15 GHz. The maximum electric field near second focus is measured as 100 V/m. The focal wave form is shifted towards the aperture of the reflector which is shown in Fig. 8 (b). The FWHM calculated from the focal waveform is 60 ps.

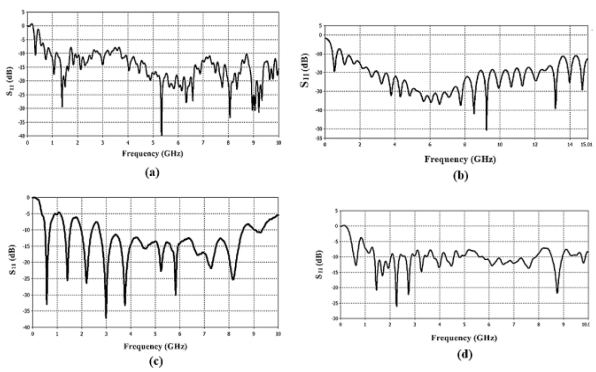

Fig. 6. Reflection parameter for: (a) SWB fed PSR, (b) EPH fed PSR, (c) TSVS fed PSR, and (d) TACP fed PSR.

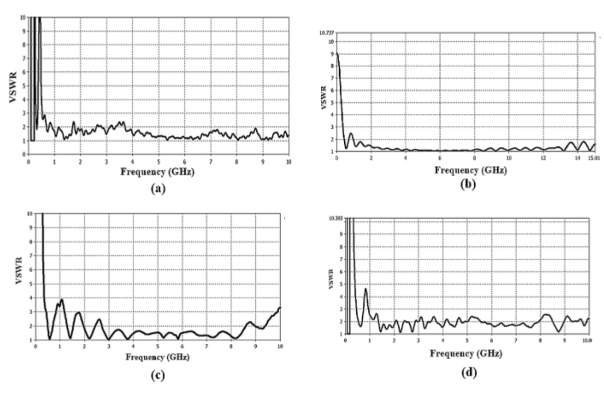

Fig. 7. VSWR for: (a) SWB fed PSR, (b) EPH fed PSR, (c) TSVS fed PSR, and (d) TACP fed PSR.

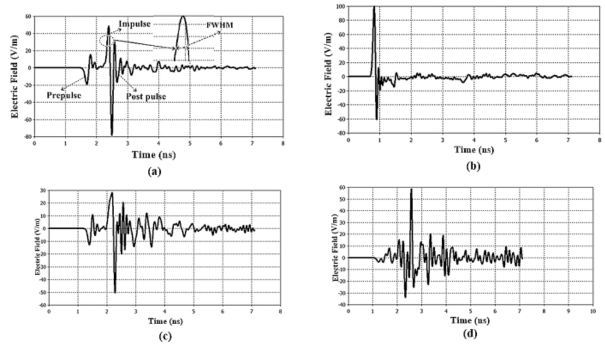

Fig. 8. Electric field at second focus in with an input Gaussian pulse. (a) SWB fed PSR, (b) EPH fed PSR, (c) TSVS fed PSR, and (d) TACP fed PSR.

In TSVS fed PSR, the return loss measured is -10 dB for the bandwidth of 500 MHz to 10 GHz from Fig. 6 (c). The return loss of -5 dB is obtained for the spectrum of 350 MHz to 10 GHz. Within the band of 500 MHz to 9.5 GHz, the VSWR is lower than 2 which is better than the case of traditional IRA, which is shown in Fig. 7 (c). The spot size measured from the focal wave form (Fig. 8 (c)) is 90ps.

The return loss and VSWR are measured from Figs. 6 (d) and 7 (d) for TACP fed PSR. The feed arm is well matched for the bandwidth of 1.5 GHz to 10 GHz. The FWHM measured from focal waveform Fig. 8 (d) is 100ps, which is the same as the rise time of the input signal.

IV. DESIGN OF PARTITION LENS

The design of the 3 layer partition lens is presented. The fast and intense electromagnetic pulse is illuminated to the target (skin) which is located at the second focal point. The major problem for concentrating the fields at the second focal point is the reflection. The dielectric property of the target medium and the medium though, which the incident wave propagates are different which causes reflections. The partition lens is used to focus the field at the second focal point. The addition of partition lens before the target leads to better match the wave to the target. The larger electric field and reduced spot size are obtained.

A. Partition lens design

The design of a partition dielectric lens is shown in Fig. 9. The partition lens is designed based on Fermat's Aplanatic principle and Fresnel law of refraction [14, 15]. The design contour of each layer is determined from the following equation:

$$y_i = f_i(x) = \sqrt{(n^2-1)x^2 - 2n(n-1)Fx + (n-1)^2F^2}, \quad (7)$$

where n is the refractive index of the lens, F is the focal length.

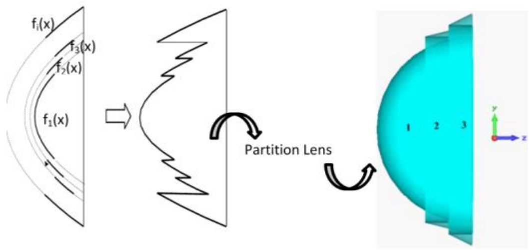

Fig. 9. Design of partition lens from hemisphere dielectric lens.

The thickness of the lens is varied from t_i to t_1. The relative dielectric constant $\varepsilon_r = 2$ for all three layers. In the lens design the phase difference between the electromagnetic waves plays an important role. The layers of the lens are designed with different focal length and different optical path. The electromagnetic waves through different parts of the lens have different phase. The partition lens is designed such that the phase difference between the electromagnetic waves through the different parts of the lens is an integer multiple of 2π till they arrive at the focal point.

L_i is the optical path of electromagnetic waves through the part of the lens,

$$\text{where} \quad L_i = F_i + n \times t_i, \tag{8}$$

$F_i + t_i$ = Constant, n is the refractive index of the lens, F_i is the focal length of the i^{th} layer, t_i = thickness of the i^{th} layer.

The appropriate focal length for each layer is chosen to make sure that the difference of optical length between each layer is an integer multiple of the wavelength (3 cm). The design parameters are shown in Table 1 for 3 layers. The inner and outer radius is used to decide the area of each layer. This will have an effect on the focusing ability of the partition lens. The area of the partition is optimised in order to obtain reduced spot size and enhanced electric field at the second focus. The intensity of the wave decreases from the reflector and increses at the geometric focus. Adding partition lens allows one to increase the field intensity near the geometric focus, but the strongest intensity is still found along the axis and increases as the wave penetrates deeper into the tissue.

The proposed lens is used to solve the thickness and volume problem of the short focus dielectric lens. The field at the second focus is higher because the phase difference between electromagnetic waves through the different part of the lens is chosen as integer multiples of 2π.

Table 1: Design parameter for partition lens

Parameter	Layer-1	Layer-2	Layer-3
Dielectric constant (ε_r)	2	2	2
Focal length (cm)	9	6	3
Outer radius (cm)	12	13.5	15
Inner radius (cm)	0	12	13.5

V. SKIN MODEL DESCRIPTION

A. Two layer skin model

The skin model chosen in this case has been simulated with a specific length and width. This is a two layer model which consists of the epidermis and dermis with the thickness of 0.15 mm and 3.85 mm respectively. The length and width of the model have been specified by 5 cm x 5 cm. The 100 ps pulse (microwave frequency) is radiated from the PSIRA to the skin. The dielectric constant chosen for the skin model is 38 for our simulation.

The skin model is kept at the distance of 48.6 cm from the antenna vertex. The skin is modeled according to the dielectric properties given in Table 2 [16-22].

Table 2: Dielectric properties of skin model

Properties	Skin
Dielectric constant	38
Conductivity (S/m)	0.2
Material density (Kg/m^2)	1100
Thermal conductivity (W/K/m)	0.5
Heat capacity (KJ/K/kg)	3.35

VI. NUMERICAL SIMULATIONS AND DISCUSSION

A. Electromagnetic simulation

The entire simulation setup is shown in Figs. 10-13. The CST Microwave Studio, 3-D Finite Integration Time Domain (FITD), commercially available software is used for simulation. The CST Microwave Studio is a module in CST which is dedicated to fast and very accurate electromagnetic simulations of high frequency problems. This module contains different solvers for simulations of structures, both in time and frequency domain. The CST transient solver is suitable for wide band antenna simulations and electrically large structures. The simulation code is computed using CST transient solver. The PSIRA with the partition lens system and skin model for four types of configuration is shown in Figs. 10-13. The three layer focusing lens has its center at the second focal point. The radius and focal length is obtained from Table 1. The two layer skin model is used as target medium. The reflector and feed arms are assumed to be perfect electric conductors, the focusing lens and skin model are assumed to be lossless and dispersion less. The PSIRA is fed with the input of 1 V, 100ps rise time Gaussian signal.

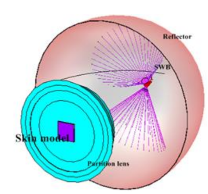

Fig. 10. Simulation design of SWB fed PSIRA with partition lens system and skin model.

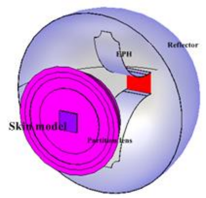

Fig. 11. Simulation structure of EPH fed PSIRA with partition lens system and skin model.

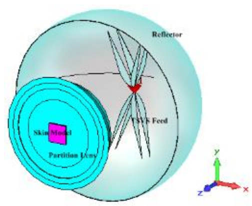

Fig. 12. Simulation setup of TSVS fed PSIRA with partition lens system and skin model.

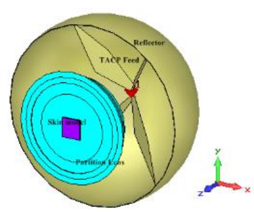

Fig. 13. Simulation design of TACP fed PSIRA with partition lens system and skin model.

B. Comparative spot size analysis

The spot size of the radiated pulse at the second focus plays a vital role in the treatment of skin cancer. The enhanced spatial resolution on the target reduces the damage of healthy tissue. The electric field component that contributes mostly to the electric field at the second focal point is the Y component. The amplitude of the electric field along X and Z directions are negligible. The electric field distribution is measured around the second focal point by placing the probe at regular spacing where the target is located.

This section presents the numerical simulation results of different feed antenna configurations for PSR with focusing lens. The electric field distribution is measured along lateral as well axial direction. The FWHM is obtained from the electric field distribution curve which is shown in Figs. 14-17 for all feed configurations. The beam width of the radiated electric field with and without lens is compared. The field intensity is maximum at the focal point and it is reduced to 50% with ± 1 *cm* near the focus for SWB, and TSVS fed PSR. In EPH fed PSR without lens configuration, the radiated impulse is not exactly focused on the second focal point. The peak of the impulse electric field on the z axis is shifted slightly from the geometric focus towards the reflector, which is observed in the modeled result (Fig. 15 (a)). This is because the impulse decreases inversely with the distance while it is focused in space. At the focal point, even though coherent combinations of waves are obtained, the impulse electric field is still smaller than the nearby locations toward the reflector due to a large impulse width, cδ (in spatial units). In order that the maximum impulse amplitude occurs at the geometric focus, the impulse width needs to be small compared to both $2z_0$ and 2b (similar discussion in the frequency domain can be seen in [23]). This shift of the impulse electric field is overcome by using partition lens. A pulse with faster rise time is allowed the shift of the focal spot towards the geometric focus. In TACP fed PSR maximum field intensity is obtained at the second focal point and it is reduced to 50% within ± 0.25 *cm* near the focal point.

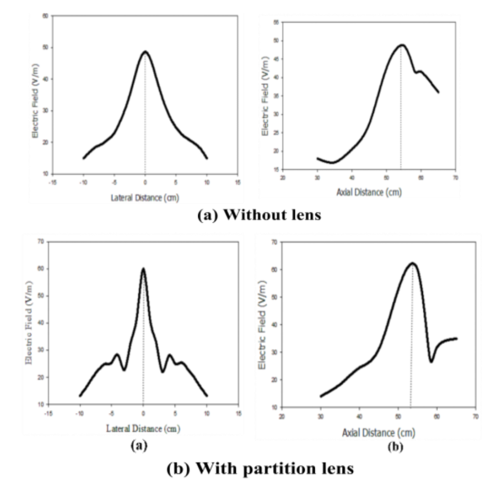

Fig. 14. Electric field distribution of SWB fed PSR at the second focal point: (a) without lens and (b) with partition lens.

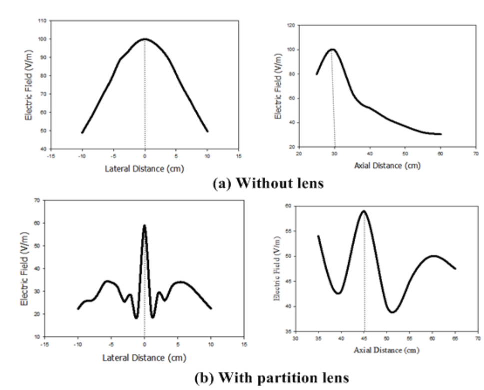

Fig. 15. Electric field distribution of EPH fed PSR at the second focal point: (a) without lens and (b) with partition lens.

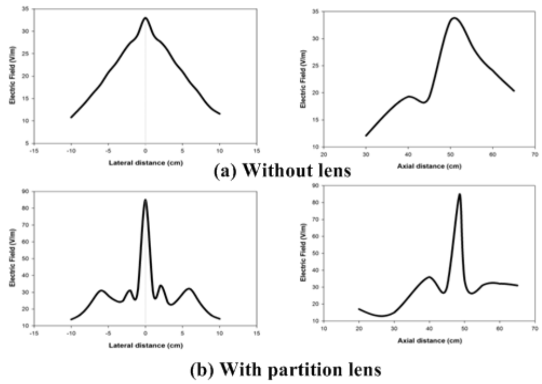

Fig. 16. Electric field distribution of TSVS fed PSR at the second focal point: (a) without lens and (b) with partition lens

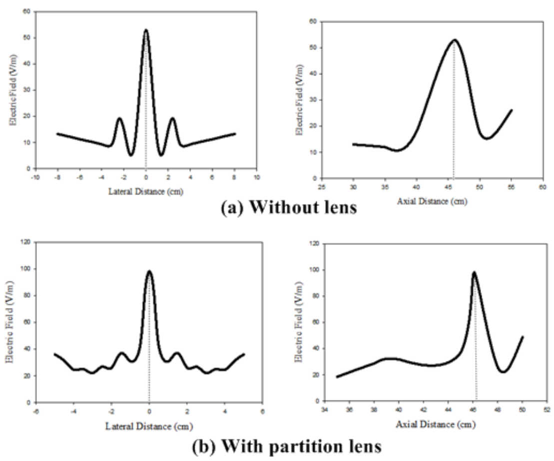

Fig. 17. Electric field distribution of TACP fed PSR at the second focal point: (a) without lens and (b) with partition lens.

Table 3 summarizes the radiation characteristics of all types of radiators. Their performance is compared in terms of electric field and spot size on the target.

The reflector dimension is the same for all configurations of PSIRA. The peak electric field for all feed configurations is compared. The TACP fed PSR provides the maximum electric field of 98 V/m. The spot diameter for TACP fed PSR with partition lens is less compared to the rest of the proposed PSIRAs. The spot size is measured from FWHM of electric field distribution around the second focal point along lateral and axial direction and shown in Figs. 18 (a) and 18 (b). It is observed that the spot size of TACP fed PSR is 1 cm along the lateral direction and 5 cm along the axial direction which is less compared to all configurations and it is further reduced to 0.5 cm along lateral direction and 1 cm along axial direction by using partition lens.

Table 3: Comparison of all types of PSIRA with and without partition lens system

Parameter	SWB Fed PSIRA	EPH Fed PSIRA	TSVS Fed PSIRA	TACP Fed PSIRA	SWB Fed PSIRA	EPH Fed PSIRA	TSVS Fed PSIRA	TACP Fed PSIRA
	Without Lens				With Partition Lens			
Reflector diameter (cm)	50	50	50	50	50	50	50	50
F/D	0.33	0.33	0.33	0.33	0.33	0.33	0.33	0.33
No. of arms	-	-	4	4	-	-	4	4
Separation between arms	-	-	70°	60°	-	-	70°	60°
Input Impedance (Ω)	100	100	200	200	100	100	200	200
Electric Field (V/m)	49	42	30	59.2	60	59	85	98
Spot size FWHA axial & FWHA lateral	Axial (cm)				Axial (cm)			
	10	13	14	5	8	7	2.5	1
	Lateral (cm)				Lateral (cm)			
	5	7.5	8	1	2	1	0.75	0.5

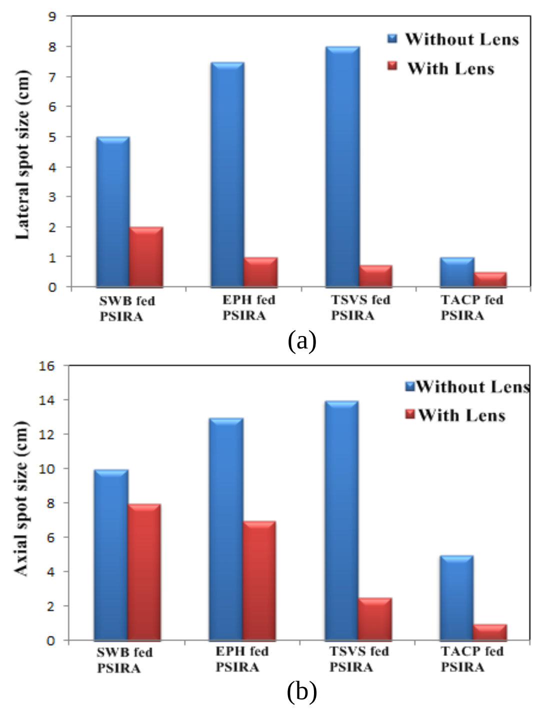

Fig. 18. (a) Spot size of all PSIRA with and without lens along lateral direction. (b) Spot size of all PSIRA with and without lens along axial direction.

VII. CONCLUSION

The Prolate Spheroidal Reflector (PSR) with different feed antenna configurations are designed to delivered subnanosecond pulses for non-invasive skin cancer treatment. The 100ps electric pulse is launched from the feed antenna and is focused at the second focal point where the target is placed. Further, deep near field focusing is obtained using partition lens. The lens modifies the electric field distribution on the target along lateral as well as axial direction. The radiation characteristics of all PSIRA configurations with and without lens system are compared. The TACP fed PSR with partition lens system produces narrow spot size of 0.5 cm along lateral direction and 1 cm along axial direction .The enhanced resolution is obtained on the target using TACP fed PSR with partition lens system. Adding a dielectric lens allows one to increase the field intensity near the geometric focus which is more beneficial to reduce the input voltage requirement to obtain high electric field and to enhance the spatial resolution for the treatment of skin cancer.

REFERENCES

[1] K. H. Schoenbach, B. Hargrave, R. P. Joshi, J. F. Kolb, R. Nuccitelli, C. Osgood, A. Pakhomov, M. Stacey, R. J. Swanson, J. A. White, S. Xiao, J. Zhang, S. J. Beebe, P. F. Blackmore, and E. S. Buescher, "Bioelectric effects of intense nanosecond pulses," *IEEE Trans. Dielectr. Electr. Insul*., vol. 14, no. 5, pp. 1088-1119, Oct. 2007.

[2] K. H. Schoenbach, S. Xiao, R. P. Joshi, J. T. Camp, T. Heeren, J. F. Kolb, and S. J. Beebe, "The effect of intense subnanaosecond electrical pulses on biological cells," *IEEE Trans. Plasma Sci.*, vol. 36, no. 2, pp. 414-422, Apr. 2008.

[3] R. Nuccitelli, U. Pliquett, X. Chen, W. Ford, J. Swanson, S. J. Beebe, J. F. Kolb, and K. H. Schoenbach, "Nanosecond pulsed electric fields cause melanomas to self-destruct,"*Biochem. Biophys. Res. Commun*., vol. 343, no. 2, pp. 351-360, May 2006.

[4] S. Xiao, S. Guo, V. Nesin, R. Heller, and K. H. Schoenbach, "Subnanosecond electric pulses cause membrane permeabilization and cell death," *IEEE Transactions on Biomedical Engineering*, vol. 58, no. 5, May 2011.

[5] S. Xiao, S. Guo, J. T. Camp, N. Vasyl, A. Pakhomov, R. Heller, and K. H. Schoenbach, "Biological cells response to high power electromagnetic Pplses," *Frank Reidy Research Center For Bioelectrics*.

[6] S. Xiao, S. Altunc, P. Kumar, C. E. Baum, and K. H.Schoenbach, "A reflector antenna for focusing in the near field," *IEEE Antennas Wireless Propag. Lett.*, vol. 9, pp. 12-15, 2010.

[7] P. Kumar, S. Altunc, C. E. Baum, C. G. Christodoulou, E. Schamiloglu, and C. J. Buchenauer, "Radially inhomogeneous spherical dielectric lens for matching 100ps pulses into biological targets," *IEEE Trans. Plasma Sci. (Special Issue)*, vol. 38, no. 8, pp. 1915-1927, Aug. 2010.

[8] K. H. Schonebach, S. Xiao, J. T. Camp, M. Migliaccio, S. J. Beebe, and C. E. Baum "Wideband, high-amplitude, pulsed antenna for medical therapies and medical imaging," *International Conference on Electromagnetics in Advanced Applications*, Torino, Sept. 14-18, 2009.

[9] P. Kumar, S. Altunc, C. E. Baum, C. G. Christodoulou, and E. Schamiloglu, "Launching a fast (100 ps), high-voltage (> 100 kV) pulse into a biological target," *International Conference on Electromagnetics in Advanced Applications (ICEAA)*, Sydney, Australia, Sept. 2010.

[10] N. Liu, Z. Zhang, G. Fu, Q. Liu, and L. Wang, "A compact biconical antenna for ultrawideband Aapplications," *IEEE 5th International Symposium on Microwave, Antenna, Propagation and EMC Technologies for Wireless Communications (MAPE)*, Chengdu, 2013.

[11] J. A. G Malherbe and N. Barnes, "Tem horn antenna with an elliptic profile," *Microwave and Optical Technology Letters*, vol. 49, no. 7, July 2007.

[12] M. Manteghi and Y. Rahmat Samii, "Improved feeding structures to enhance the performance of the reflector impulse radiating antenna (IRA)," *IEEE Transaction on Antenna and Propagation*, vol. 54, no. 3, pp. 823-834, Mar. 2006.

[13] J. S. Tyo, "Optimization of the TEM feed structure for four-arm reflector impulse radiating antennas," *IEEE Trans. Antennas Propag.*, vol. 49, no. 4, pp. 607-614, Apr. 2001.

[14] B. Nábělek, M. Malý, and V. Jirka, "Linear Fresnel lenses, their design and use," *Renewable Energy*, vol. 1, iss. 3-4, pp. 403-40, 1991.

[15] *Geometrical Optics: Lens, Snell's Law, Fresnel Equations, Fermat's Principle, Refraction, Total Internal Reflection, Depth of Field*, General Books.

[16] N. Chahat, M. Zhadobov, R. Sauleau, and S. I. Alekseev, "New method for determining dielectric properties of skin and phantoms at millimeter waves based on heating kinetics,"*IEEE Transactions on Microwave Theory and Techniques*, vol. 60, no. 3, Mar. 2012.

[17] J. T. Camp, Y. Jing, J. Zhuang, J. F. Kolb, S. J. Beebe, J. Song, R. P. Joshi, S. Xiao, and K. H. Schoenbach, "Cell death induced by subnanosecond pulsed electric fields at elevated temperatures," in *IEEE Transactions on Plasma Science*, vol. 40, no. 10, Oct. 2012.

[18] Italian National Research Council-Institute for Applied Physics-Online. http://niremf.ifac.cnr.it/tissprop/

[19] F. Gustrau and A. Bahr, "W-band investigation of material parameters, SAR distribution, and thermal

response in human tissue," *IEEE Transaction on Microwave Theory and Techniques*, vol. 50, no. 10, Oct. 2002.

[20] E. B. Garon, D. Saucer, P. T. Vernier, T. Tang, Y. Sun, L. Marcu, M. A. Gundersen, and H. P. Koeffler, "In vitro and in vivo evaluation and a case report of intense nanosecond pulsed electric field as a local therapy for human malignancies," *Int. J. Cancer*, vol. 121, no. 3, pp. 675-682, Aug. 2007.

[21] C. Gabriel, S. Gabriel, and E. Corthout, "The dielectric properties of biological tissues: I. Literature survey," *Physic. Med. Biol.*, vol. 41, pp. 2231-2249, 1996.

[22] A. Peyman, S. Holden, and C. Gabrial, "Dielectric properties at microwave frequencies," *RUM-3, 'Mobile Telecommunications and Health Research Programme'*, 2009.

[23] J. W. Sherman, III, "Properties of focused apertures in the Fresnel region," *IRE Trans. Antennas Propag.*, vol. AP-10, no. 4, pp. 399-408, July 1962.

Design, Simulation and Fabrication of a Wide Bandwidth Envelope Tracking Power Amplifier

I. Aryanian, A. Abdipour, and A. Mohammadi

Department of Electrical Engineering
Amirkabir University of Technology, Tehran, 15914, Iran
iman_aryanian@aut.ac.ir, abdipour@aut.ac.ir, abm125@aut.ac.ir

Abstract ─ In this paper an envelope tracking power amplifier is designed and implemented using MRF6S27015N MOTOROLA transistor in LDMOS technology. First, the amplifier is designed using load pull simulation and its parameters are optimized to increase the power added efficiency. Next, envelope detector and envelope amplifier are designed and simulated and finally ET is applied to the amplifier which results in more than 50% of PAE in a wide range of input power with bandwidth of 200 MHz. Envelope detector circuit is fabricated using schotkey diode and envelope amplifier is manufactured using a mosfet, an op amp, and a comparator.

Index Terms ─ Envelope amplifier, envelope elimination and restoration, power amplifier.

I. INTRODUCTION

Power amplifier is the most important part in a communication system because it uses the most amount of energy in the system. So, good efficiency of power amplifier can decrease amount of heat generated, and therefore boost performance of the total system. Back off may be used to maintain linearity of the power amplifier, but this may result in decreasing the efficiency. Some techniques are proposed to overcome this problem like LINC, $\Delta\Sigma$ modulation, Doherty, and EER Polar modulator. The first two techniques show high linearity with a moderate efficiency [1, 2] and the latter two techniques show high efficiency with a moderate linearity characteristic [3, 4]. However, applying the digital predistortion (DPD) technique to the latter two techniques can enhance the moderate linearity adequately. Envelope tracking power amplifiers are used to increase efficiency of the power amplifier [5-10]. ET uses a linear PA and a controlled supply voltage, which tracks the input envelope. When the supply voltage tracks the instantaneous envelope modulation signal, it is called Wide Bandwidth ET (WBET) [11]; when the supply voltage tracks the long-term average of the input envelope power, it is called Average ET (AET) [12]; when the supply voltage switches to different step levels according to the input envelope power, it is called Step ET (SET) [13]. EER (envelope elimination and restoration) uses a combination of a high efficiency switch-mode PA with an envelope re-modulation circuit [14]. To employ high efficiency operation of EER and at the same time reduce the strict necessities of bandwidth and time-alignment, the "hybrid" EER structure was proposed in [15]. Total system efficiency is determined by the product of the envelope amplifier efficiency and the RF transistor drain/collector efficiency. As a result, a high-efficiency envelope amplifier is vital for the EER/ET system. High efficiency envelope amplifier is usually realized by a DC/DC converter, where the switching frequency is required to be several times the signal bandwidth. For narrow bandwidth applications, most high efficiency switching mode DC/DC converters are realized by traditional delta modulation [16] or pulse width modulation (PWM) [17] modulators. Envelope amplifier block diagram is shown in Fig. 1, which consists of an OPAMP to realize the voltage source, and a MOSFET to realize the current source. This envelope amplifier consists of a voltage source and a current source. Although the current source has high efficiency, the voltage source has low efficiency. Therefore, we like to get most of the output current from the current source. To control the current of the voltage source, we use a hysteretic current feedback control to realize the soft power division between switch stage and linear stage amplification. The load voltage is controlled by the linear voltage source, and the load current is a mixture of the linear stage current and the switch stage current.

II. ET AMPLIFIER DESIGN

A. RF amplifier design

Si-LDMOS is a popular device choice for base-station high-power amplifiers, since LDMOS technology can provide reliable and cost effective solutions [18]. Envelope tracking techniques, in which a wideband envelope amplifier makes variable supply biasing to the RF stage, have established excellent performance using

Submitted On: March 31, 2015
Accepted On: August 1, 2016

a variety of device technologies including Si LDMOS and GaN FETs [19]. Nonetheless, the RF PA should have suitable characteristics to be appropriate for the envelope tracking operation and achieve the optimal performance such as low deviation of the output capacitance, since a large variation of the voltage dependent output capacitance will corrupt the average efficiency as the optimum impedance matching for the output of the PA changes with the supply voltage [17]. Besides, extra nonlinearity like AM-PM distortion from the nonlinear capacitance and AM-AM distortion from the envelope amplifier, and memory effects due to the limited bandwidth of the RF PA and the envelope amplifier is produced by the dynamic supply biasing. However, digital pre-distortion (DPD) techniques may be used to correct the nonlinearity of the dynamically biased amplifier. In this paper, the amplifier is designed and implemented using the MRF6S27015N MOTOROLA transistor in LDMOS technology and is simulated using ADS2008 software where nonlinear analysis is performed using harmonic balance method [20]. The design of the amplifier is at the central frequency of 2.1 GHz and the bandwidth of the RF amplifier is 200 MHz, which is high with respect to the other works. The amplifier is biased in class AB. Output current diagrams of the transistor is used to choose appropriate Vgs, which can be selected between 2.3 volt and 3.8 volt to work in class AB and is optimized to increase the efficiency.

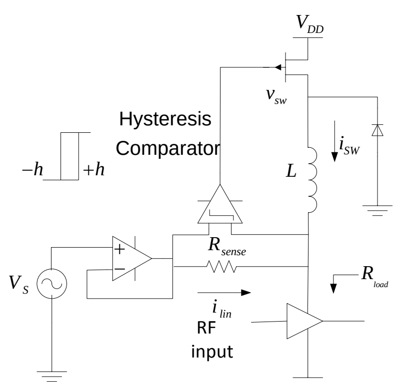

Fig. 1. Envelope amplifier block diagram.

Load pull simulation is used to select the optimum output impedance seen from the output of the transistor that increases the efficiency which is 5.7 + j12.6. Power added efficiency and gain of the transistor when it sees output impedance of 5.7 + j12.6, is shown in Fig. 2. Our aim in design of the power amplifier is to increase the efficiency. So, we optimized the amplifier to reach our goal and we changed Vgs, Vds, width and length of the matching transmission lines to reach to a good efficiency. Also, matching of the transistor is optimized in ADS software. Table 1 shows line width and line length of the optimized transmission lines. RO4003 substrate is used with $\varepsilon_r = 3.5$ and $\tan\delta = .0027$. Input matching and output matching schematics are shown in Fig. 3 and Fig. 4. Optimising the matching circuit in ADS software, input and output return losses are shown in Fig. 5 and Fig. 6.

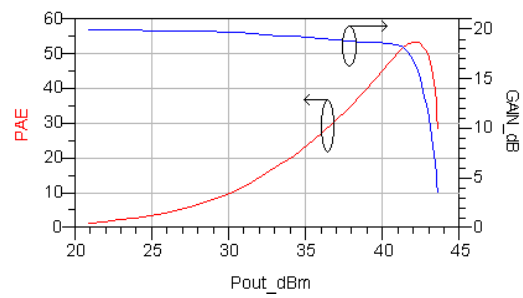

Fig. 2. Gain and power added efficiency versus output power for optimum output impedance.

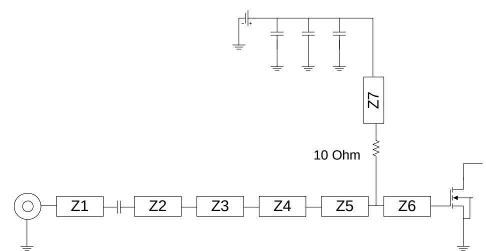

Fig. 3. Input matching circuit.

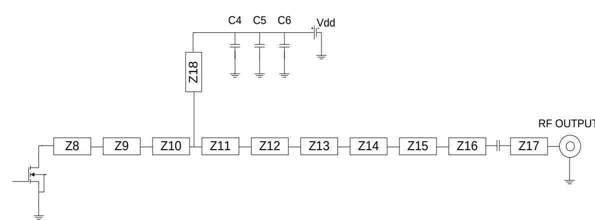

Fig. 4. Output matching circuit.

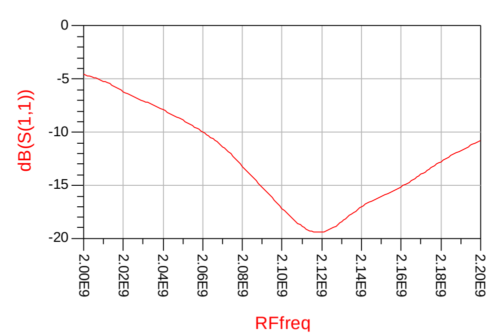

Fig. 5. Input matching

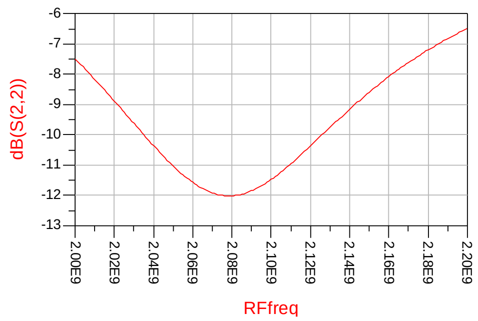

Fig. 6. Output matching.

Increasing the output power of the transistor will increase the PAE. However, our input signal has a high peak to average ratio and probability of the peak power is very low. Consequently, it is wise to design the matching for the case that happens most of the time, which is mean power. Therefore, because Vds changes with respect to the input power, we optimized the power amplifier for the Vds related to the mean power.

Table 1: Size of the matching transmission lines

Line Number	Line Length (mil)	Line Width (mil)
Z1	940	25
Z2	360	85
Z3	170	145
Z4	85	85
Z5	370	800
Z6	136	800
Z7	800	20
Z8	80	705
Z9	100	900
Z10	100	805
Z11	200	805
Z12	95	600
Z13	80	405
Z14	100	135
Z15	705	40
Z16	720	25
Z17	100	44
Z18	900	20

B. Changing V_{ds}

In the next step, we changed Vds of the power amplifier from 8v up to 28v by 4v to show the possibility of increase in PAE by envelope tracking. Power added efficiency and output power of the RF power versus input power at center frequency of 2.1 GHz by changing Vds from 8v up to 28v by 4v is shown in Fig. 7 and Fig. 8 respectively. When the input power is 10 dBm and Vds is 8v, this simulation shows about 17% of more PAE than the condition of Vds=28v.

Figure 7 shows that we can increase P1dB of the transistor when the input power is large by applying ET.

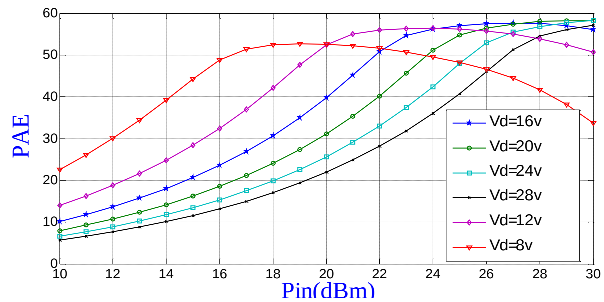

Fig. 7. PAE versus input power at center frequency by changing Vds.

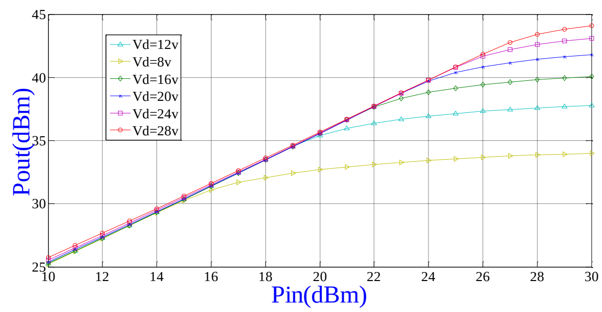

Fig. 8. Output power versus input power at center frequency by changing Vds.

C. Applying ET

When Vds is 8v, the PAE decreases in the peak power, and when Vds is 28v the PAE is low in low power. To overcome this problem, we can apply envelope tracking to our amplifier. By changing the Vds with respect to the input power, we can see that the PAE remains above 50% for a wide range of input power. Figure 9 shows PAE versus input power at center frequency by applying envelope tracking respectively.

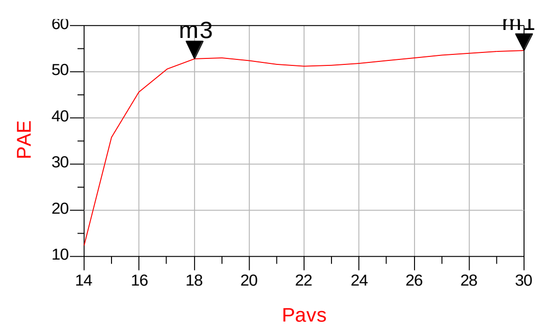

Fig. 9. PAE versus input power at center frequency by applying envelope tracking.

D. Envelope detector

Envelope detector is shown in Fig. 10, which consists of a Schottky diode and an LC circuit by L=190 (nH) and C=18 (pF). HSMS286K Schottky diode produced by Agilent is used. Envelope detector is simulated in ADS software by the signal shown in Fig. 11 and the output signal is obtained.

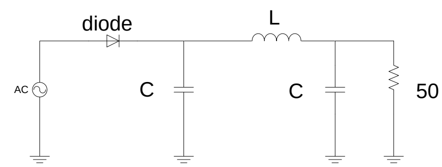

Fig. 10. Envelope detector.

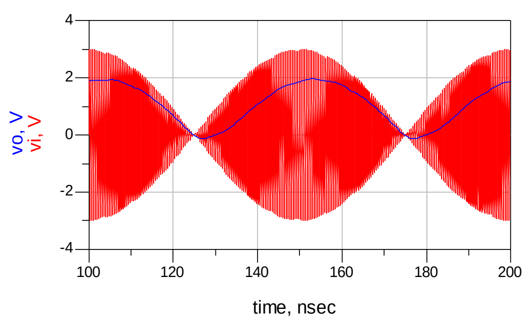

Fig. 11. Input and output signal of the envelope detector.

III. FABRICATION AND TEST

Manufactured circuit is shown in Fig. 12 which consists of 3 parts: 1) Wilkinson power divider, 2) envelope detector, and 3) transistor. In part 1 a Wilkinson power divider is used to divide the input signal to two equal parts. One part is fed to the transistor and one part is fed to an envelope detector circuit.

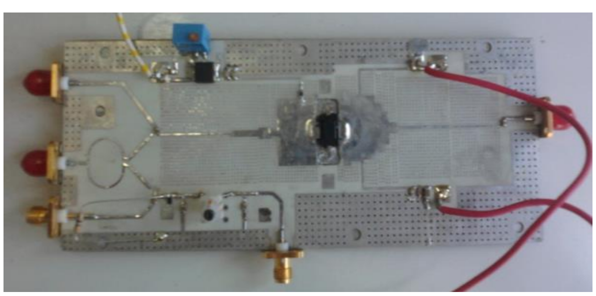

Fig. 12. Manufactured circuit.

Manufactured envelope amplifier circuit is shown in Fig. 13 and its block diagram is shown in Fig. 1, which consists of a mosfet, an op-amp, and a comparator where their part number is given in Table 2. Also, Table 3 compares previous works with this paper.

Gain versus input power at center frequency by changing Vds, output power versus input power at center frequency by changing Vds, and PAE versus input power at center frequency by changing Vds are shown in Fig. 14 up to Fig. 16.

Table 2: Envelope amplifier

Device	Number	Producer
OP-AMP	THS3095	TEXAS INSTRUMENT
MOSFET	FDFSP106A	FAIRCHILD
COMPARATOR	LM119J	NATIONAL

Fig. 13. Manufactured envelope amplifier circuit.

Table 3: Comparison to previous envelope amplifiers

	Power (dBm)	Envelope Amplifier BW (MHz)	Efficiency (%)
[4]	29.7	10	82
[5]	23.2	20	65
[6]	28.9	10	76
[7]	27	10	71
[8]	30.8	4	75.5
[9]	33	4	89
[10]	28	1.25	82
This work	40	1	65

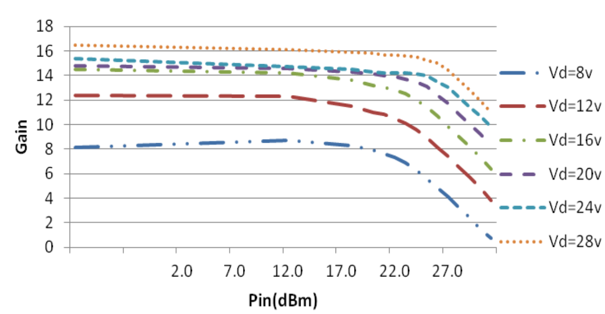

Fig. 14. Gain versus input power at center frequency by changing Vds.

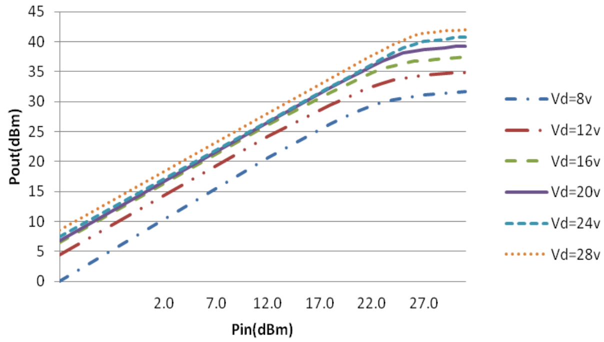

Fig. 15. Output power versus input power at center frequency by changing Vds.

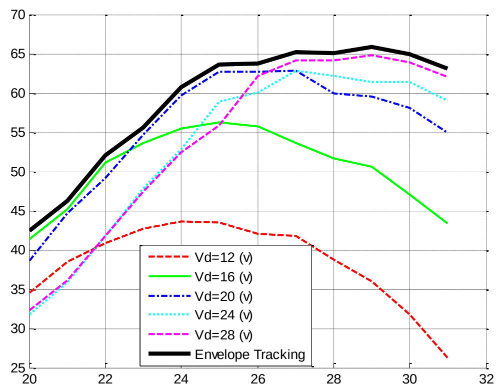

Fig. 16. PAE versus input power at center frequency by changing Vds.

IV. CONCLUSION

In this research an ET amplifier in the frequency range of 2 GHz to 2.2 GHz has been designed and fabricated using MRF6S27015N MOTOROLA transistor in LDMOS technology which has 10 watts output power. Also, implementation of the envelope amplifier and envelope detector has been described. It has been shown that the PAE remains above 50% for a wide range of input power for a bandwidth of 200 MHz.

REFERENCES

[1] Y. Y. Woo, J. Yi, Y. Yang, and B. Kim, "SDR transmitter based on LINC amplifier with bias control," in *Microwave Symposium Digest, 2003 IEEE MTT-S International*, pp. 1703-1706, 2003.

[2] M. Helaoui, S. Hatami, R. Negra, and F. M. Ghannouchi, "A novel architecture of delta-sigma modulator enabling all-digital multiband multistandard RF transmitters design," *IEEE Transactions on Circuits and Systems II: Express Briefs*, vol. 55, pp. 1129-1133, 2008.

[3] H. Golestaneh, F. A. Malekzadeh, and S. Boumaiza, "An extended-bandwidth three-way Doherty power amplifier," *IEEE Transactions on Microwave Theory and Techniques*, vol. 61, pp. 3318-3328, 2013.

[4] M. Hassan, L. E. Larson, V. W. Leung, and P. M. Asbeck, "A combined series-parallel hybrid envelope amplifier for envelope tracking mobile terminal RF power amplifier applications," *IEEE Journal of Solid-State Circuits*, vol. 47, pp. 1185-1198, 2012.

[5] F. Wang, D. F. Kimball, D. Y. Lie, P. M. Asbeck, and L. E. Larson, "A monolithic high-efficiency 2.4-GHz 20-dBm SiGe BiCMOS envelope-tracking OFDM power amplifier," *IEEE Journal of Solid-State Circuits*, vol. 42, pp. 1271-1281, 2007.

[6] D. Kim, D. Kang, J. Choi, J. Kim, Y. Cho, and B. Kim, "Optimization for envelope shaped operation of envelope tracking power amplifier," *IEEE Transactions on Microwave Theory and Techniques*, vol. 59, pp. 1787-1795, 2011.

[7] J. Choi, D. Kim, D. Kang, and B. Kim, "A new power management IC architecture for envelope tracking power amplifier," *IEEE Transactions on Microwave Theory and Techniques*, vol. 59, pp. 1796-1802, 2011.

[8] J. N. Kitchen, C. Chu, S. Kiaei, and B. Bakkaloglu, "Combined linear and-modulated switch-mode PA supply modulator for polar transmitters," *IEEE Journal of Solid-State Circuits*, vol. 44, pp. 404-413, 2009.

[9] D. Kang, D. Kim, J. Choi, J. Kim, Y. Cho, and B. Kim, "A multimode/multiband power amplifier with a boosted supply modulator," *IEEE Transactions on Microwave Theory and Techniques*, vol. 58, pp. 2598-2608, 2010.

[10] P. Y. Wu and P. K. Mok, "A two-phase switching hybrid supply modulator for RF power amplifiers with 9% efficiency improvement," *IEEE Journal of Solid-State Circuits*, vol. 45, pp. 2543-2556, 2010.

[11] F. Wang, A. H. Yang, D. F. Kimball, L. E. Larson, and P. M. Asbeck, "Design of wide-bandwidth envelope-tracking power amplifiers for OFDM applications," *IEEE Transactions on Microwave Theory and Techniques*, vol. 53, pp. 1244-1255, 2005.

[12] B. Sahu and G. A. Rincon-Mora, "A high-efficiency linear RF power amplifier with a power-tracking dynamically adaptive buck-boost supply," *IEEE Transactions on Microwave Theory and Techniques*, vol. 52, pp. 112-120, 2004.

[13] A. Khanifar, N. Maslennikov, R. Modina, and M. Gurvich, "Enhancement of power amplifier efficiency through dynamic bias switching," in *Microwave Symposium Digest, 2004 IEEE MTT-S International*, pp. 2047-2050, 2004.

[14] L. R. Kahn, "Single-sideband transmission by envelope elimination and restoration," *Proceedings of the IRE*, vol. 40, pp. 803-806, 1952.

[15] F. Wang, D. Kimball, J. Popp, A. Yang, D. Y. Lie, P. Asbeck, et al., "Wideband envelope elimination and restoration power amplifier with high efficiency wideband envelope amplifier for WLAN 802.11 g applications," in *IEEE MTT-S International Microwave Symposium Digest, 2005*, pp. 4, 2005.

[16] D. R. Anderson and W. H. Cantrell, "High-efficiency high-level modulator for use in dynamic envelope tracking CDMA RF power amplifiers," in *Microwave Symposium Digest, 2001 IEEE MTT-S International*, pp. 1509-1512, 2001.

[17] B. Sahu and G. A. Rincón-Mora, "A low voltage, dynamic, noninverting, synchronous buck-boost converter for portable applications," *IEEE Transactions on Power Electronics*, vol. 19, pp. 443-452, 2004.

[18] C. Wipf, R. Sorge, and J. Schmidt, "Evaluation of LDMOS transistors for 10 Gbps switched mode applications and X-band power amplifier," in *2016 IEEE 16th Topical Meeting on Silicon Monolithic Integrated Circuits in RF Systems (SiRF)*, pp. 57-59, 2016.

[19] J. J. M. Rubio, V. Camarchia, R. Quaglia, E. F. A. Malaver, and M. Pirola, "A 0.6–3.8 GHz GaN power amplifier designed through a simple strategy," 2016.

[20] I. Aryanian, A. Abdipour, and G. Moradi, "Nonlinear analysis of active aperture coupled reflectarray antenna containing varactor diode," *Applied Computational Electromagnetics Society Journal*, vol. 30, 2015.

Iman Aryanian was born in Iran in 1986. He obtained his B.Sc., M.Sc. and Ph.D. degree in Electrical Engineering from Amirkabir University of Technology, Tehran, Iran in 2008, 2010 and 2016 respectively. His research interests are in the areas of reflectarray antenna, computational electromagnetic, semiconductor RF modeling, electromagnetic theory, and computational electromagnetics.

Abdolali Abdipour was born in Alashtar, Iran, in 1966. He received his B.Sc. degree in Electrical Engineering from Tehran University, Tehran, Iran, in 1989, his M.Sc. degree in Electronics from Limoges University, Limoges, France, in 1992, and his Ph.D. degree in Electronic Engineering from Paris XI University, Paris, France, in 1996. He is currently a Professor with the Electrical Engineering Department, Amirkabir University of Technology (Tehran Polytechnic), Tehran, Iran.

Abbas Mohammadi received his B.Sc. degree in Electrical Engineering from Tehran University, Iran in 1988, and his M.Sc. and Ph.D. degrees in Electrical Engineering from the University of Saskatchewan, Canada, in 1995 and 1999, respectively. Since March 2000, he has been with the Electrical Engineering Department of Amirkabir University of Technology (Tehran Polytechnic), Tehran, Iran, where he is currently a Professor.

Analysis of Control Variables to Maximize Output Power for Switched Reluctance Generators in Single Pulse Mode Operation

Pairote Thongprasri and Supat Kittiratsatcha

Faculty of Engineering, King Mongkut's Institute of Technology Ladkrabang
Chalongkrung Road, Ladkrabang, Bangkok 10520, Thailand
sfengprt@src.ku.ac.th, kksupat@kmitl.ac.th

Abstract **─** This paper presents an analytical modeling method of optimal control variables to maximize the output power for switched reluctance generators (SRGs) in single pulse mode operation. A method to obtain the phase current equation used to determine the optimal control variables is proposed. The phase current equation is derived from the phase voltage equation in combination with the inductance model. The inductance model proposed in this paper is applied from the flux linkage function. The characteristics of the phase current and the energy conversion relations are analyzed to determine the optimal phase current shape. The analytical results indicate that the optimal shape can be generated when the SRG is controlled with the optimal control variables. The optimal shape is used for analysis based on the phase current equation to determine the optimal control variables. An 8/6 SRG experimental setup is used to validate the proposed method. The optimal control variables obtained from the proposed method are used to control the SRG. Based on the experimental results, the SRG can produce the maximum output power.

Index Terms **─** Control variables, optimal phase current shape, switched reluctance generator.

I. INTRODUCTION

A switched reluctance generator (SRG) is a potential candidate in various applications, such as an automotive starter/generator [1, 2] an engine starter/ generator [3, 4] and for variable speed wind energy [5] because it has a simple structure and low cost, is fault tolerant with a rugged structure, and involves easy starting/generating realization, high speed adaptability, with a high generation efficiency.

Its highly nonlinear nature is the main problem of the SRG, since the behavior of the SRG cannot be described by mathematical equations using conventional methods for a suitable controller design [6]. The SRG model is used for simulation to determine the relationship between output power and control variables since there is no analytical equation with which to determine the output power based on design parameters and control variables [7]. The dynamic model of an SRG using a cubic spline technique has been proposed to find the flux linkage, inductance, torque, and output power [8]. A model SRG based on the Finite Element Method (FEM) and power control methods for a small wind power generation system has been proposed in [9]. The SRG model is used to find the output power curve versus the shaft speed. This curve is analyzed to determine the optimal switching on-off angle for maximum efficiency in the system.

The output power of the SRG in single pulse mode can be controlled by adjusting the excitation angles, with the turn-on/off angle being fixed while the turn-off/on angle is adjusted, or by adjusting both the turn-on and turn-off angles. Constant output power control of the SRG has been proposed by controlling the turn-on angle with a fuzzy logic algorithm while the turn-off angle is fixed [10]. The optimal excitation angles for output power control using automatic closed loop control have been proposed so that the optimal turn-off angle in terms of power and speed is determined from an analytical fit curve [11], while the optimal turn-on angle is automatically adjusted based on the closed loop power control to regulate the output power. The optimal excitation angles have been proposed for maximum system efficiency calculated using the ratio of the two flux linkages [12]. The minimum torque ripple occurs in this case. With two flux linkages, one is the position at which the stator and rotor pole corners begin overlap and the other is the position at maximum value. A Modified Angle Position Control (MAPC) method has been proposed to determine the optimal shape of the phase current [13]. The optimal turn-on angle is fixed and the optimal turn-off angle can be determined by the analytical model of the SRG for the maximum energy conversion [14, 15].

A mathematical model for analyzing control variables and describing the behavior of the SRG and the flux linkage versus current characteristics calculation is essential. There are at least two methods to obtain flux linkage versus current characteristics—an analytical approach based on the FEM and an experimental

Submitted On: November 28, 2015
Accepted On: July 17, 2016

approach based on direct measurements. The flux linkage model based on the FEM has well known reliability, however it requires intensive computation and many details of the machine geometry and structure [16]. Analytical nonlinear models of flux linkage have been described in [17-20] that are accurate and reliable. The model based on machine geometry introduced in [17] is complicated and depends on flux linkage at aligned and unaligned positions, and a position-dependent function. The position-dependent term has a physical significance in that its coefficient needs to be related to the machine geometry. The model proposed in [18] is a little complex because the flux linkage curve is divided into 2 parts, namely, linear and nonlinear. However, it only requires the flux linkage versus current characteristics at the aligned and unaligned positions. The model described in [19] based on a Fourier series with a limited number of terms is complex since it is necessary to know the flux linkage versus current characteristics at the aligned, unaligned, and midway positions. The coefficients in terms of the Fourier series depend on the flux linkage positions at aligned, unaligned, and midway positions so that the flux linkage at the aligned and midway positions can be calculated via curve fitting based on an arc-tangent function. The Stiebler model proposed [20] is simple in that it is composed of an angular function and aligned and unaligned flux linkage. However, it is proposed in a per-unit system.

An analytical modeling method of the optimal control variables to maximize the output power of the SRGs in single pulse mode operation is presented in this paper. The control variables comprise a dc bus voltage, a shaft speed or angular velocity, and excitation angles. This paper proposes a method to obtain the phase current equation used to determine the optimal control variables. The phase current equation is derived from the phase voltage equation in combination with the inductance model. The proposed inductance model in a real system is applied from the flux linkage function in a per-unit system introduced by Stiebler. It requires the geometrical parameters of an SRG at the aligned and unaligned rotor positions. These parameters are easily quantified using the FEM. The optimal phase current shape depending on the control variables is investigated to determine the optimal shape. Finally, the optimal shape of the phase current is used to determine the optimal control variables. An 8/6 SRG experimental setup is used to verify the proposed method.

II. PRINCIPLE OF SRG IN SINGLE PULSE MODE OPERATION

A 4-phase 8/6 SRG is used in this paper which is driven by a 4-phase asymmetrical bridge converter as shown in Fig. 1. When S_A and $S_{A'}$ are both on, the phase A voltage is u. If S_A and $S_{A'}$ are both off, the phase A voltage is $-u$.

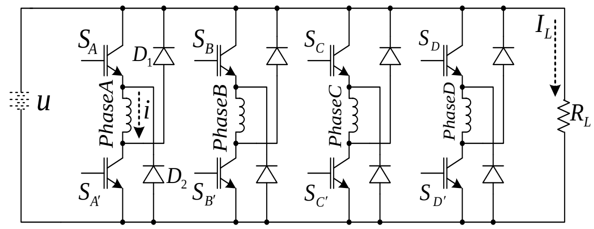

Fig. 1. 4-phase asymmetrical bridge converter.

The mutual inductance between individual phases of the SRG is usually neglected. Therefore, the equation of voltage for each phase of SRG is expressed as:

$$u = Ri + \frac{d\lambda(i,\theta)}{dt}. \tag{1}$$

The voltage equation at constant speed is given by:

$$u = Ri + L(\theta)\frac{di}{dt} + e\,, \tag{2}$$

where u represents the dc bus voltage, i is the phase current, R and L are the phase of resistance and inductance, respectively, ω is the angular velocity, and the back emf is defined as:

$$e = i\omega\frac{\partial L(i,\theta)}{\partial\theta}. \tag{3}$$

The energy converted is the area enclosed by the loci which is expressed as:

$$W = \oint \lambda di = \oint i d\lambda\,. \tag{4}$$

The SRG requires an excitation source in order to generate electrical energy. The SRG (phase A) is excited by the asymmetrical bridge converter as shown in Fig. 2. This converter is used as the dc source [21] for the exciting phase A of the SRG through two switches as shown in Fig. 2 (bottom) and demagnetizing the same phase through two diodes as shown in Fig. 2 (top).

In Fig. 2, the current builds in the SRG phase winding when the controllable switches are closed and no energy is supplied to the load. When the controllable switches are opened, the stored energy is supplied to the load through the two diodes. The average load current can be defined as:

$$I_L = \frac{1}{2\pi/N_r}\left(\int_{\theta_{off}}^{\theta_e} id\theta - \int_{\theta_{on}}^{\theta_{off}} id\theta\right), \tag{5}$$

where turn-on θ_{on} and turn-off θ_{off} angles represent the controllable switches which are closed and opened, respectively, θ_e is the angle at which the phase current is depleted and it is given as $2\theta_{off} - \theta_{on}$, θ is the rotor position and N_r is the number of rotor poles.

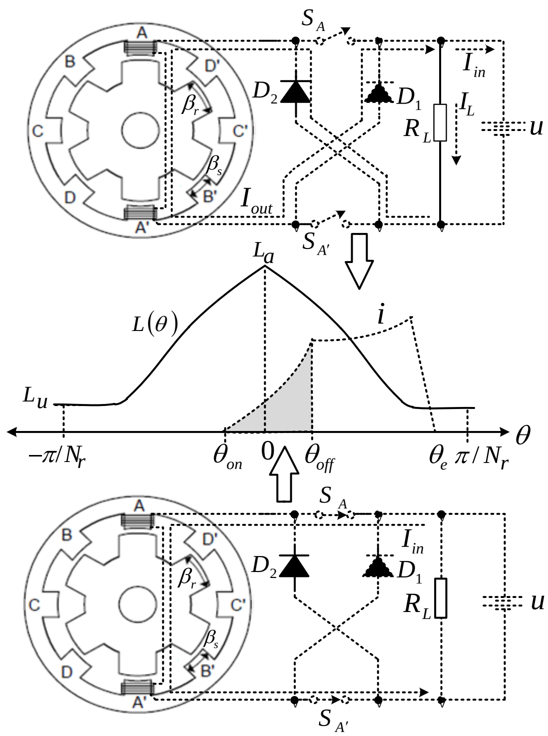

Fig. 2. Power generation process for the SRG in single pulse mode.

The average electric power of the SRG is the summation of the output power of each phase in one revolution which is given by:

$$P_{out} = I_L u . \tag{6}$$

The main electrical losses of an SRG are copper loss and iron loss. The copper loss P_{Cu} depends on the rms phase current I_{rms} on the range $\theta_{off} \le \theta \le \theta_e$ [22] which is expressed as:

$$P_{Cu} = N_{ph} I_{rms}^2 R , \tag{7}$$

and

$$I_{rms}^2 = \frac{1}{2\pi / N_r} \int_{\theta_{off}}^{\theta_e} i^2 d\theta . \tag{8}$$

The iron loss is in proportion to the excitation magnetic motive force and the stroke frequency. It is not uniformly distributed in the core since the flux shape is non-sinusoidal and the flux harmonic spectrum differs in various parts of the magnetic spectrum. The iron loss [23] can be approximately calculated as:

$$P_C = K_h f B_m^{a+bB_m} + K_e f^2 B_m^2 , \tag{9}$$

where f is the stroke frequency, K_h and K_e are the hysteresis and eddy-current loss coefficients, respectively, a and b are the constants of the exponent, and B_m is the amplitude of flux density for sinusoidal variation.

III. ANGLE POSITION CONTROL METHOD

The control variables of the SRG are the dc bus voltage u, the angular velocity ω, the phase current i, and turn-on/off angle $\theta_{on} / \theta_{off}$. The Angle Position Control (APC) method can control the phase current shape by adjusting θ_{on} and θ_{off} while u and ω are constant. The output power can be adjusted by the phase current. The advantages of the APC method [13] are that the optimal θ_{on} and θ_{off} can improve efficiency, the multiple phases can be conducted at the same time, and the torque adjustment range is wide.

The effect of θ_{on} and θ_{off} on the phase current shape using the APC method is illustrated in Fig. 3, where θ_{on} is fixed and θ_{off} is adjusted as shown in Fig. 3 (a) and θ_{off} is fixed and θ_{on} is adjusted as shown in Fig. 3 (b).

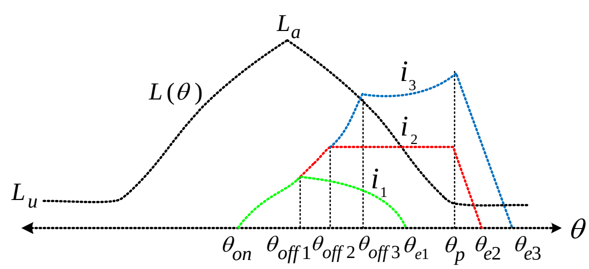

(a) θ_{on} is fixed and θ_{off} is adjusted

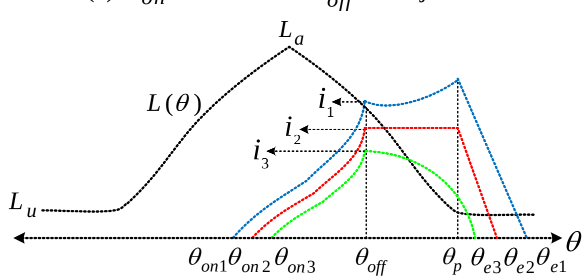

(b) θ_{off} is fixed and θ_{on} is adjusted

Fig. 3. Phase current shapes using the angle position control method.

When the resistance of the phase windings and the voltage drops of the main switches and diodes are neglected, the voltage Equation in (2) can be expressed as:

$$u = \omega L(\theta) \frac{di}{d\theta} + \omega i \frac{\partial L(i,\theta)}{\partial \theta} . \tag{10}$$

The maximum value of the phase current in Fig.

4 is in the range $\theta_{off} \le \theta \le \theta_p$ and θ_p equals $(\beta_r + \beta_s)/2$, where β_r is the rotor pole arc and β_s is the stator pole arc. Considering (10), if the back emf is smaller than the dc bus voltage, then $di/d\theta < 0$. The phase current shape in this case is shown in Fig. 4 (a). If the back emf is equal to the dc bus voltage, then $di/d\theta = 0$. In this case, the phase current shape is shown in Fig. 4 (b). If the back emf is bigger than the dc bus voltage, then $di/d\theta > 0$ and the phase current shape is shown in Fig. 4 (c).

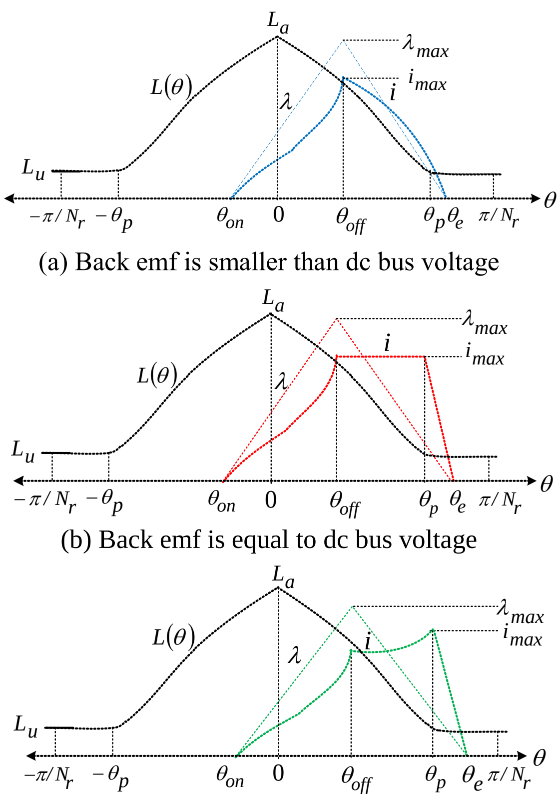

(a) Back emf is smaller than dc bus voltage

(b) Back emf is equal to dc bus voltage

(c) Back emf is bigger than dc bus voltage

Fig. 4. Three kinds of phase current and flux linkage at different turn-on and turn-off angles with the same maximum value of the phase current.

From (9), the iron loss depends on the maximum flux linkage. The maximum value of the flux linkage in Fig. 4 occurs for θ_{off}. The copper loss depends on the rms phase current which can be quantified by (7).

The energy conversion loops for 3 kinds of i and λ by the loci are shown in Fig. 5. The maximum output power can be produced when the phase current is controlled in the shape of a flat top (Fig. 4 (b)). This result has been confirmed by [24].

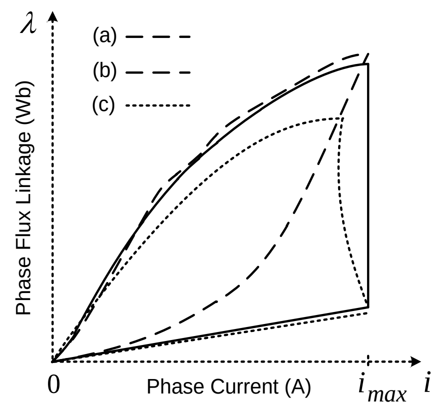

Fig. 5. Energy conversion loops by the loci with the same maximum value of the phase current.

IV. PROPOSED METHOD FOR ANALYZING THE OPTIMAL CONTROL VARIABLES

An analytical modeling method of the optimal control variables to maximize output power of the SRGs in single pulse mode operation is presented in this paper. This paper proposes a method to obtain the phase current equation used to determine the optimal control variables. The phase current equation will be derived from the phase voltage equation in combination with the inductance model. The inductance model is applied from the flux linkage function. Finally, the optimal shape of the phase current is used to determine the optimal control variables.

A. Flux linkage model

The flux linkage model in a real system as shown in Fig. 6 has been developed from the flux linkage function in a per-unit system introduced by Stiebler [20]. It requires the geometrical parameters of an SRG at the aligned and unaligned rotor positions. These parameters are easily determined using an experiment or the FEM. The parameters comprise inductance at positions of aligned L_a and unaligned L_u, and flux linkage at points s and m as shown in Fig. 6.

The flux linkage function in Fig. 6 is composed of the linear and saturated regions. The saturated region begins at point s and finishes at point m. The flux linkage of the saturated region can be determined using a Froelich function [25] $\lambda = (i/(a+b))$, where a and b are constants as the slope and intercept, respectively. The constants a and b can be determined by substituting the λ_{as}, i_s of the point s and λ_{am}, i_m of the point m into the Froelich function.

The proposed model of the flux linkage can be expressed as:

$$\lambda(i,\theta) = L_u i + (L_a - L_u)\frac{i}{a+bi} f(\theta), \qquad (11)$$

where θ_k is the effective overlap position of the stator and rotor poles, and the angular function is given by:

$$f(\theta) = \begin{cases} 0.5 + 0.5\cos\left(\theta\dfrac{\pi}{\theta_k}\right) & , -\theta_k \le \theta \le \theta_k \\ 0 & , else \end{cases} . \qquad (12)$$

To verify the proposed method, an 8/6 SRG is used to determine its geometrical parameters using the FEM with its specifications as shown in Table 1.

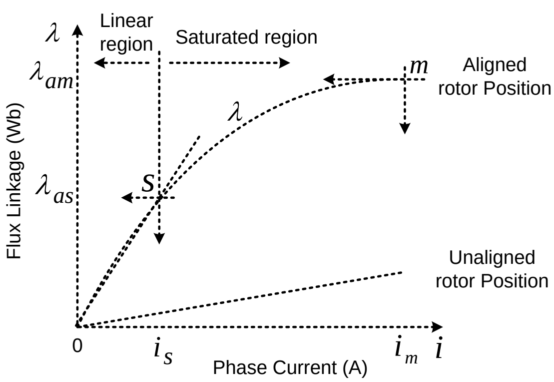

Fig. 6. Magnetization curve of an SRG.

Table1: Specifications of the candidate SRG

Parameter	Value
Outer diameter of stator	150 mm
Inner diameter of stator	70 mm
Stack length	72 mm
Length of air gap	0.5 mm
Number of phases	4
Stator/Rotor pole arc	23°/23.5°
Number of stator poles/rotor poles	8/6
Rated voltage/power/speed	48 V/2.3 kW/ 6000 rpm

The relationship between the flux linkage and current at rotor positions 0°, 15°, and 30° is obtained using the FEM and are shown in Table 2.

The parameters obtained using the FEM for calculation in this paper consist of L_a = 470 μH, L_u = 42 μH, θ_k = 27°, a = 0.65, and b = 0.155.

Figure 7 shows the resultant magnetization curve at rotor positions 0°, 15°, and 30° obtained from the analytical model (11) compared with the FEM which demonstrates the validity of the proposed model.

Table 2: Analytical results obtained using the FEM

Current (A)	Rotor Position (Mech. Degree)		
	0°	15°	30°
50	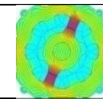	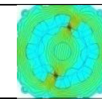	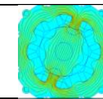
40	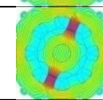	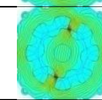	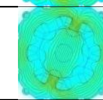
30	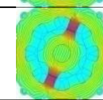	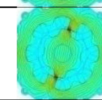	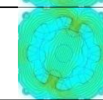
20	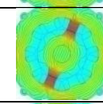	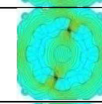	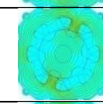
10	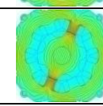	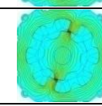	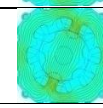

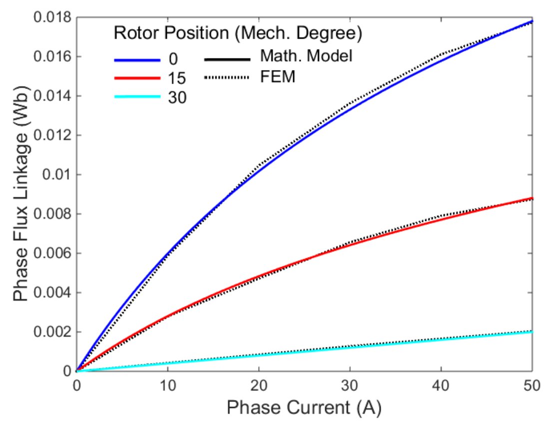

Fig. 7. Magnetization curves of the candidate SRG at rotor positions 0°, 15°, and 30° obtained using the analytical model (solid lines) and the FEM (dotted lines).

B. Proposed model of phase current

The phase inductance involves much more than a comparison with the mutual inductance, as the mutual inductance is neglected [26, 27]. It is known by $L(i,\theta) = \lambda(i,\theta)/i$. Therefore, based on (11) and (12), the phase inductance is;

$$L(i,\theta) = L_u + \frac{L_a - L_u}{a+bi} f(\theta), \qquad (13)$$

where the angular function $f(\theta)$ is in the range $-\theta_k \le \theta \le \theta_k$.

The inductance profile is a periodic function with period of $2\pi/N_r$ or the rage from $-\pi/N_r$ to π/N_r. Consequently, the phase inductance model proposed in this paper is divided into three regions depending on the phase current and rotor position as shown in Fig. 8. It can be expressed as:

$$L(i,\theta)=\begin{cases} L_u & ,-\dfrac{\pi}{N_r}\le\theta<-\theta_k \\ L_u+\dfrac{L_a-L_u}{a+bi}f(\theta) & ,-\theta_k\le\theta\le\theta_k \\ L_u & ,\theta_k<\theta\le\dfrac{\pi}{N_r} \end{cases}. \quad (14)$$

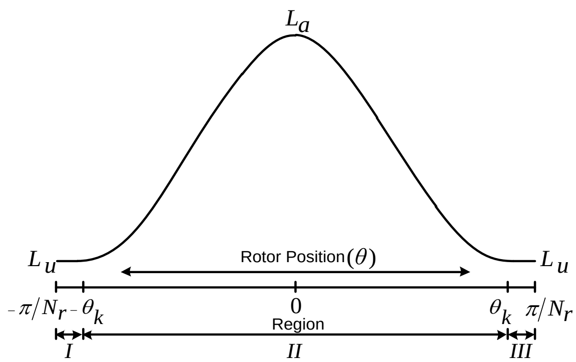

Fig. 8. Phase inductance profile is divided into three regions.

Figure 9 depicts the phase inductance of the candidate SRG obtained using the proposed analytical model (14) and the FEM so that the characteristics of the phase inductance versus the current and rotor position closely match each other.

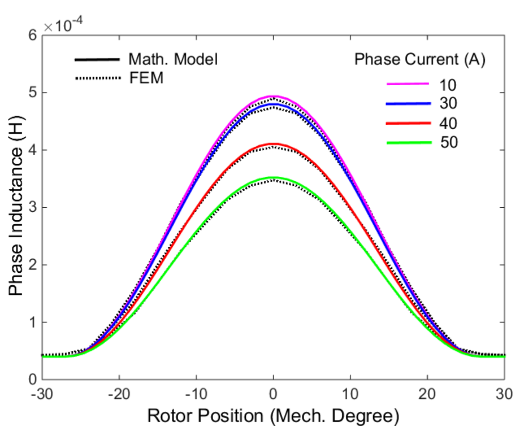

Fig. 9. Phase inductance of the candidate SRG obtained using the mathematical model and the FEM.

The expression of the phase current is obtained by substituting the inductance model (14) into the phase voltage Equation (10). It can be expressed as:

$$i=\begin{cases} \dfrac{u(\theta-\theta_{on})}{\omega\left[L_u+\left(\dfrac{L_a-L_u}{a+bi}\right)f(\theta)\right]} & ,\theta_{on}\le\theta<\theta_{off} \\ \dfrac{u(\theta_e-\theta)}{\omega\left[L_u+\left(\dfrac{L_a-L_u}{a+bi}\right)f(\theta)\right]} & ,\theta_{off}\le\theta\le\theta_e \\ 0 & ,else \end{cases}. \quad (15)$$

The phase torque is given by:

$$T(i,\theta)=\frac{1}{2}i^2\frac{\partial L(i,\theta)}{\partial\theta}$$

$$=\left(\frac{(a+bi)f'(\theta)+bf(\theta)\left((L_a-L_u)f(\theta)i+\dfrac{u}{\omega}b\right)+c}{(2bL_u+d)(a+bi)^2}\right)$$

$$\times(L_a-L_u)i^2, \quad (16)$$

where

$$c=u\begin{cases} -a & ,\theta_{on}\le\theta<\theta_{off} \\ a & ,\theta_{off}\le\theta\le\theta_e \\ 0 & ,else \end{cases},$$

$$d=aL_u+(L_a-L_u)f(\theta)-\frac{b}{\omega}h,$$

$$h=\frac{u}{\omega}\begin{cases} u(\theta-\theta_{on}) & ,\theta_{on}\le\theta<\theta_{off} \\ u(\theta_e-\theta) & ,\theta_{off}\le\theta\le\theta_e \\ 0 & ,else \end{cases}.$$

C. Analysis of optimal control variables

To obtain the maximum output power, the optimal control variables are required from Equation (15) as mentioned in the previous topic. The maximum value of the phase current in Fig. 4 can occur when θ is in the range $\theta_{off}\le\theta\le\theta_p$. Therefore, the maximum value of the phase current based on (15) can be given as:

$$i_{\max}=\frac{u(\theta_e-\theta)}{\omega\left[L_u+\left(\dfrac{L_a-L_u}{a+bi_{\max}}\right)f(\theta)\right]}. \quad (17)$$

The maximum output power can be produced when the phase current is controlled in the shape of a flat top as shown in Fig. 4 (b). This result has been confirmed by [24]. Therefore, the shape of the phase current in Fig. 4 (b) is used to determine the optimal control variables so that the maximum value exists in the interval θ_{off} to θ_p.

The maximum value of the phase current at $\theta = \theta_{off}$ or $i_{\max 1}$ can be known by substituting $\theta = \theta_{off}$ into (17) which is given by:

$$i_{\max 1} = \frac{u(\theta_{off} - \theta_{on})}{\omega\left[L_u + \left(\frac{L_a - L_u}{a + bi_{\max 1}}\right)\left(\frac{1}{2} + \frac{1}{2}\cos\left(\theta_{off}\frac{\pi}{\theta_k}\right)\right)\right]}. \tag{18}$$

Furthermore, the maximum value of the phase current at $\theta = \theta_p$ or $i_{\max 2}$ can be determined by substituting $\theta = \theta_p$ into (17) which is expressed as:

$$i_{\max 2} = \frac{u(2\theta_{off} - \theta_{on} - \theta_p)}{\omega\left[L_u + \left(\frac{L_a - L_u}{a + bi_{\max 2}}\right)\left(\frac{1}{2} + \frac{1}{2}\cos\left(\theta_p\frac{\pi}{\theta_k}\right)\right)\right]}. \tag{19}$$

Now $i_{\max 1}$ is equal to the $i_{\max 2}$ since the shape of phase current is flat topped. The optimal turn-on angle can be calculated by substituting $i_{\max 1}$ into $i_{\max 2}$.

Consequently,

$$\theta_{on}^{opt} = \frac{\theta_{off}^{opt}(L_u + 2qf_1(\theta) - qf_2(\theta)) - \theta_3(L_u + qf_1(\theta))}{q(f_1(\theta) - f_2(\theta))}, \tag{20}$$

where

$$q = \frac{L_a - L_u}{a + bi_{\max}},$$

$$f_1(\theta) = 0.5 + 0.5\cos\left(\theta_{off}^{opt}\frac{\pi}{\theta_k}\right),$$

$$f_2(\theta) = 0.5 + 0.5\cos\left(\theta_p\frac{\pi}{\theta_k}\right).$$

Based on (15) in the range $\theta_{off} \le \theta \le \theta_p$, the position of θ at the maximum current point can be determined by $\frac{di}{d\theta} = 0$:

$$\pi(L_a - L_u)\sin\left(\theta\frac{\pi}{\theta_k}\right) = 2\left(\frac{u}{\omega}\right)\theta_k(a + bi_{\max}). \tag{21}$$

Then, the optimal turn-off angle can be found by substituting θ_{off} into θ:

$$\theta_{off}^{opt} = \frac{\theta_k}{\pi}\sin^{-1}\left(\frac{2u\theta_k}{\omega\pi(L_a - L_u)}(a + bi_{\max})\right). \tag{22}$$

Ultimately, as θ_p, u, and $i_{\max}$ are defined, the control variables of the SRG for maximum output power can be calculated as follows:

i. The angular velocity ω can be determined by substituting values of u, $i_{\max}$, and $\theta = \theta_p$ into (21).
ii. The value of θ_{off}^{opt} can be found by applying the values of θ_p, u, $i_{\max}$, and ω into (22).
iii. The value of θ_{on}^{opt} can be determined from (20).

V. ANALYTICAL AND EXPERIMENTAL RESULTS

To verify the proposed method, an 8/6 SRG system is set up as shown in Fig. 10. A 3-phase induction motor is used as the prime mover so that its speed is controlled by an inverter. The parameters of the SRG are shown in Table 1. A battery rated at 12 V and 120A is used as the constant dc bus voltage u. The average torque T_m of the prime mover is measured by a rotational torque transducer which is connected between the prime mover and the SRG. The shaft speed or angular velocity ω and aligned position θ_a are detected by a resolver mounted on the SRG. The SRG is driven by a 4-phase asymmetrical bridge converter so that excitation angles are created by a TMS320F28027. The R_L equals 1.25 Ω and is used as the resistive load.

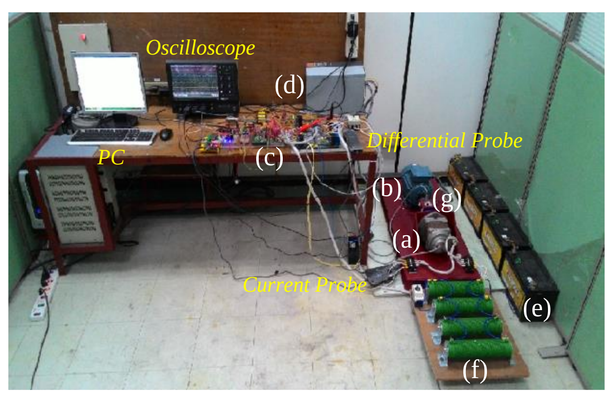

Fig. 10. Experimental setup: (a) 8/6 SRG with a resolver, (b) prime mover, (c) asymmetrical bridge converter and TMS320F28027 DSP controller, (d) variable speed inverter, (e) 12 V, 120 A battery, (f) resistive load, and (g) torque meter.

Figure 11 shows the schematic layout of the experimental setup so that the mechanical input power can be calculated by:

$$P_{in} = T_m \omega \,. \qquad (23)$$

The efficiency of the system is defined as:

$$\eta = \frac{P_{out}}{P_{in}}, \qquad (24)$$

where P_{out} is the electrical output power and P_{in} is the mechanical input power.

In this paper, the parameters used for analysis comprise L_u = 42 μH, L_a = 470 μH, β_s = 23°, β_r = 23.5°, a = 0.65, and b = 0.155.

The relationship between the system efficiency of the SRG and the 3 kinds of phase current are investigated, if the P_{out}, u, and θ_{off} are defined as 1000 W, 36 V, and 9°, respectively, the I_L equals to 27.78 A obtained from (6). Analytical results based on the mathematical models (5), (8), (11), and (15) and Figs. 12-14 show the power generation waveforms when the turn-on angle and angular velocity have been adjusted to control I_L = 27.78 A. The values of θ_{on}, θ_{off}, ω, $i_{\max}$, λ_{max}, and I_{rms} are summarized in Table 3.

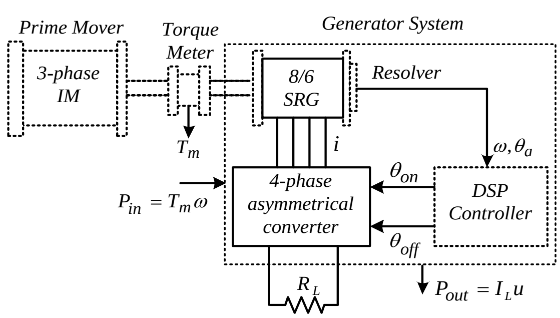

Fig. 11. Schematic layout of the experimental setup.

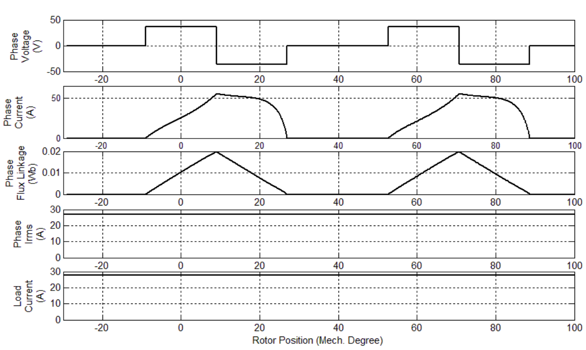

Fig. 12. Case 1: θ_{on} and θ_{off} are -9.20° and 9°.

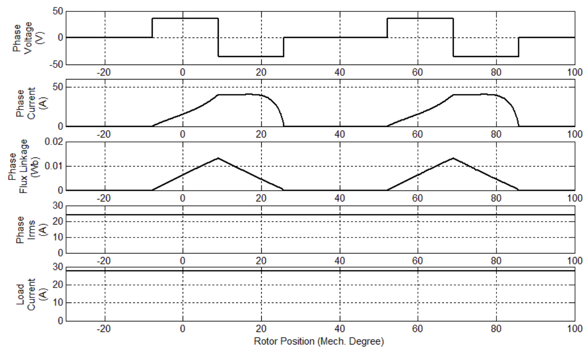

Fig. 13. Case 2: θ_{on} and θ_{off} are -7.80° and 9°.

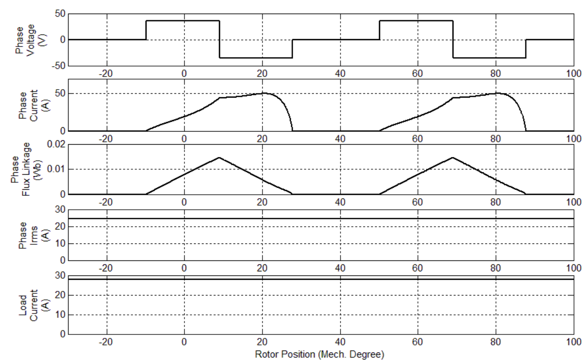

Fig. 14. Case 3: θ_{on} and θ_{off} are -8.15° and 9°.

Table 3: Results obtained from analytical model

Case	θ_{on} (°)	θ_{off} (°)	ω (rad/s)	$i_{\max}$ (A)	$\lambda_{\max}$ (Wb)	I_{rms} (A)
1	-9.20	9	524	55	0.0193	26.81
2	-7.80	9	586	40	0.0132	23.85
3	-8.15	9	605	50	0.0145	24.54

Based on (7) and (9), the copper loss and iron loss depend on I_{rms} and λ_{max}, respectively. In Table 3, the maximum efficiency of the system occurs in case 2 since the copper loss and iron loss are lowest.

The experimental results in Figs. 15-17 show the waveforms of the average torque of the prime mover, phase current, dc bus voltage, and load current. Their values are summarized in Table 4.

The efficiency of the system can be determined using (24). In Table 4, the maximum efficiency of the system occurs in case 2 where the shape of the phase current is flat topped. This result corresponds with the result obtained from the proposed analytical model.

The relationship between the output power of the SRG and the 3 kinds of phase current is investigated where the maximum value of the 3 kinds of the phase current is controlled at 40 A by adjusting the control variables. The analytical results, the shapes of the phase inductance, phase flux linkage, phase current, phase torque, and load current obtained from analytical models (14), (11), (15), and (16), respectively, are shown in Figs. 18 (a)-(c). The energy conversion loops are shown in Fig. 18 (d) with the maximum output power occurring in case b. In this case, the phase current shape is flat topped. The control variables are summarized in Table 5.

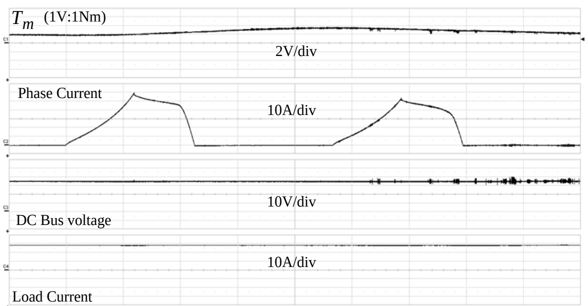

Fig. 15. Case 1: i_{max} = 55 A, θ_{on} and θ_{off} are -9.20° and 9°.

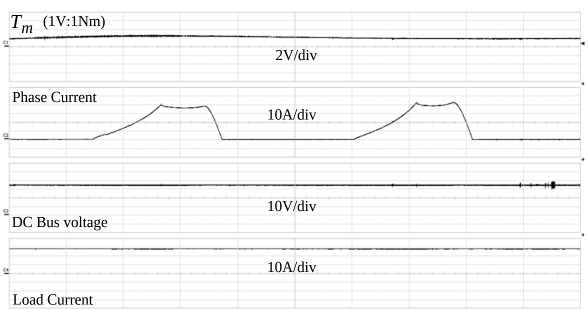

Fig. 16. Case 2: i_{max} = 40 A, θ_{on} and θ_{off} are -7.80° and 9°.

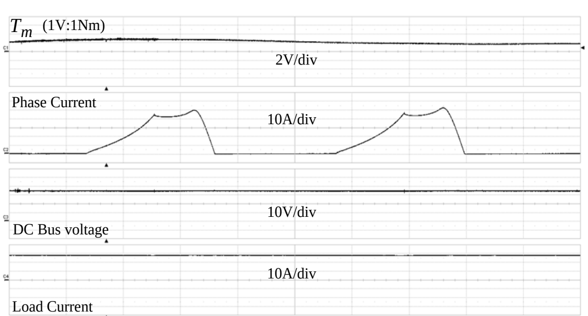

Fig. 17. Case 3: i_{max} = 50 A, θ_{on} and θ_{off} are -8.15° and 9°.

Table 4: System efficiency obtained by 3 kinds of i

Case	ω (rad/s)	T_m (Nm)	P_{in} (W)	u (V)	I_L (A)	P_{out} (W)	η (%)
1	524	2.58	1351.9	36.2	26.7	965.5	71.4
2	586	2.04	1195.4	36.1	26.8	967.5	80.9
3	605	2.11	1276.6	36.3	26.6	965.6	75.6

Table 5: Three cases of control variables

Case	u (V)	ω (rad/s)	i_{max} (A)	θ_{on} (°)	θ_{off} (°)	I_L (A)	P_{out} (W)
a	36	513	40	-7.8	5.5	16.70	601.2
b	36	586	40	-7.8	9	27.80	1000.8
c	36	648	40	-7.8	9.5	24.68	888.5

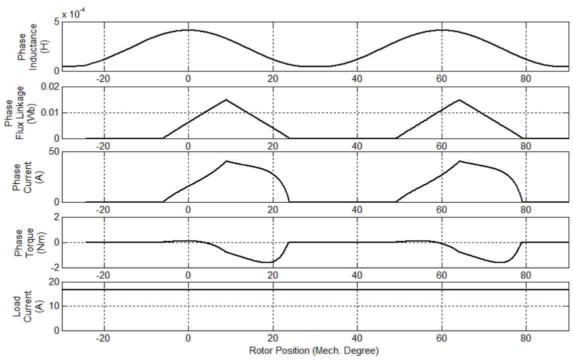

(a) Case a: θ_{on} = -7.8° and θ_{off} = 5.5°

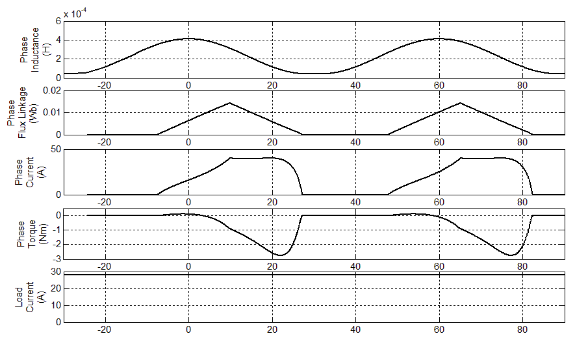

(b) Case b: θ_{on} = -7.8° and θ_{off} = 9°

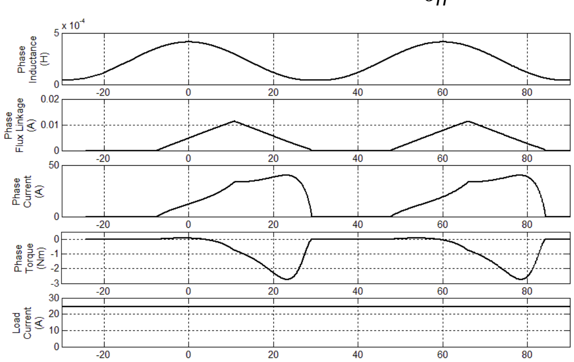

(c) Case c: θ_{on} = -7.8° and θ_{off} = 9.5°

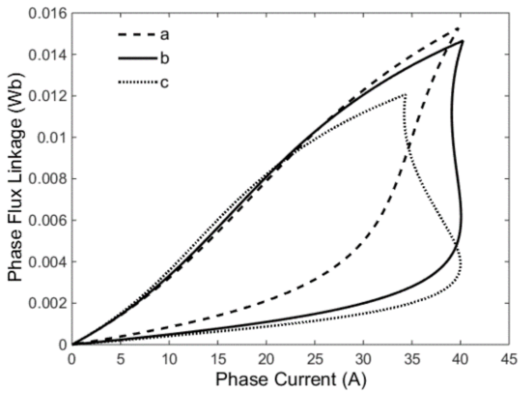

(d) Three cases of energy conversion loop

Fig. 18. Relationship between P_{out} and 3 kinds of i .

The experimental results in Fig. 19 show the waveforms of the phase voltage, phase current, dc bus voltage, and load current. The 3 cases of output power are: case a = 582.8 W, case b = 967.5 W, and case c = 857.9 W. The output power obtained from the measurement is less than the output power obtained from the analytical model since the resistance of the phase windings in the analytical model is neglected. The SRG can produce the maximum output power in case b so that this result corresponds with the analytical result.

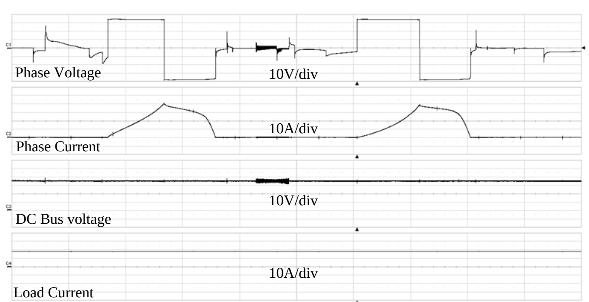

(a) Case a: $i_{\max}$ = 40 A, θ_{on} = -7.8°, θ_{off} = 5.5°, I_L = 16.1 A, and u = 36.2 V

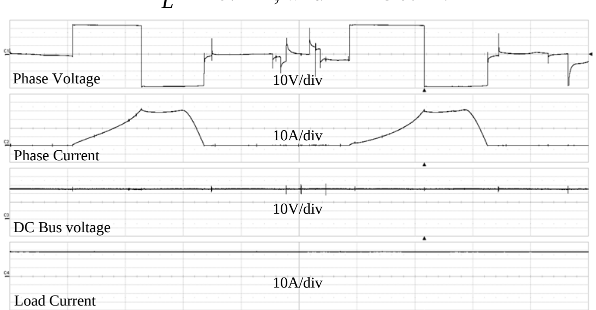

(b) Case b: $i_{\max}$ = 40 A, θ_{on} = -7.8°, θ_{off} = 9°, I_L = 26.8 A, and u = 36.1 V

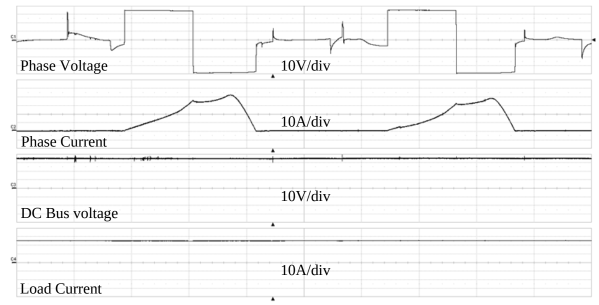

(c) Case c: $i_{\max}$ = 40 A, θ_{on} = -7.8°, θ_{off} = 9.5°, I_L = 23.7 A, and u = 36.2 V

Fig. 19. Relationship between P_{out} and 3 kinds of i at the same maximum value based on measurement.

To maximize the output power, the optimal control variables ω, θ_{off}^{opt} , and θ_{on}^{opt} can be calculated as follows:

i. The angular velocity ω can be determined by substituting u , $i_{\max}$, and $\theta = \theta_p$ into (21).
ii. The value of θ_{off}^{opt} can be found by using the values of θ_p , u , $i_{\max}$, and ω in (22).
iii. The value of θ_{on}^{opt} can be determined from (20).

Table 6 shows the control variables obtained by the proposed model where θ_p , u , and $i_{\max}$ are defined as: θ_p = 23.25°, u = 24 V, 36 V, and 48 V, and $i_{\max}$ = 30 A, 40 A, and 50 A.

Table 6: Control variables using the proposed model

Case	θ_p (°)	u (V)	$i_{\max}$ (A)	ω (rad/s)	θ_{on} (°)	θ_{off} (°)	I_L (A)
i	23.25	24	30	547	-7.2	8.8	19.59
ii	23.25	36	40	586	-7.8	9	27.8
iii	23.25	48	50	628	-8.4	9.2	39.76

The analytical results for the three cases, the shapes of the phase A voltage, phase A current, phase B current, and the load current obtained from analytical model are shown in Fig. 20. The shape of the phase current in all cases is flat-topped because the SRG is controlled using the optimal variable controls.

The experimental results in Fig. 21 show the waveforms of the phase A voltage, phase A current, Phase B current, and load current. The 3 cases of output power are: case i = 454.9 W, case ii = 967.5 W, and case iii = 1841.2 W.

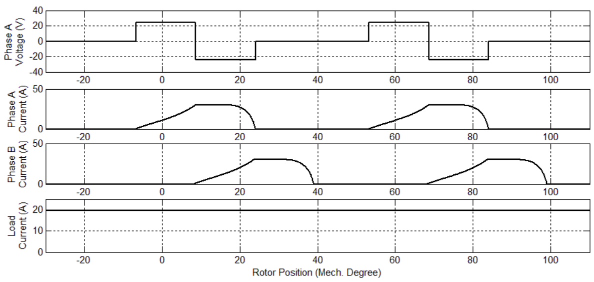

(a) Case i: θ_{on} = -7.2°, θ_{off} = 8.8°, and I_L = 19.59 A

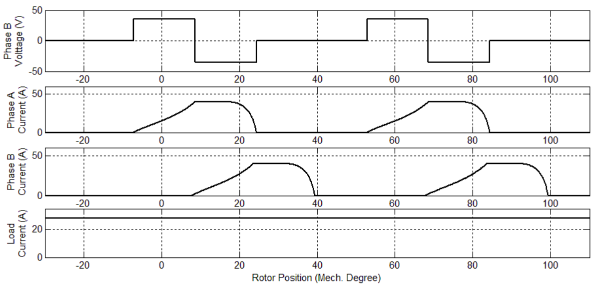

(b) Case ii: θ_{on} = -7.8°, θ_{off} = 9°, and I_L = 27.8 A

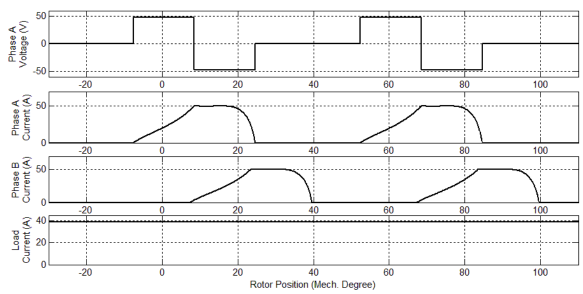

(c) Case iii: θ_{on} = -8.4°, θ_{off} = 9.2°, and I_L = 39.76 A

Fig. 20. Three cases for waveforms of the phase current, when the SRG is controlled with the control variables obtained from the analytical model.

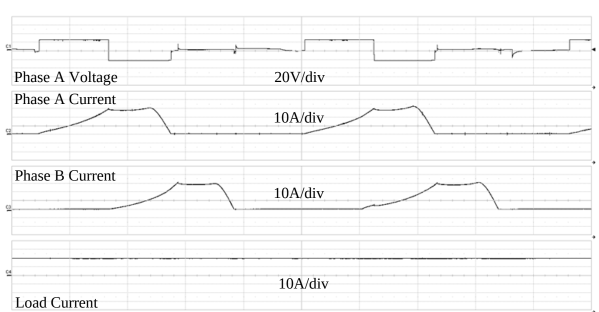

(a) Case i: i_{max} = 30 A, θ_{on} = -7.2°, θ_{off} = 8.8°, and I_L = 18.8 A, and u = 24.2 V

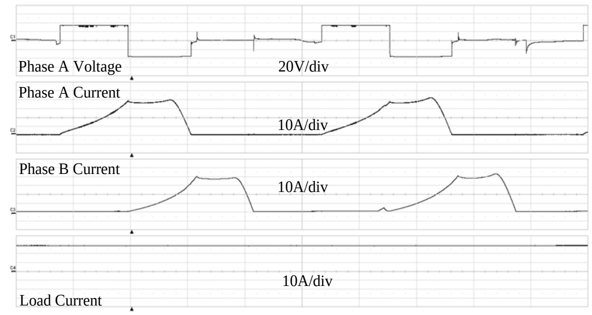

(b) Case ii: i_{max} = 40 A, θ_{on} = -7.8°, θ_{off} = 9°, and I_L = 26.8 A, and u = 36.1 V

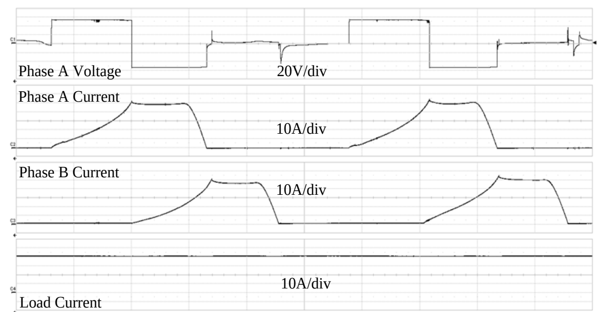

(c) Case iii: i_{max} = 50 A, θ_{on} = -8.4°, θ_{off} = 9.2°, and I_L = 38.2 A, and u = 48.2 V

Fig. 21. Three cases of waveform of phase current, when the SRG is controlled using the control variables obtained by measurement.

The phase current shape in all cases is flat-topped and the maximum output power is produced because the SRG is controlled using the optimal control variables. These results confirm the validity of the proposed analytical model.

The values of the dc bus voltage, load current, and output power for all three cases are summarized in Table 7. The output power obtained from the analytical model is different from the measurements by an average of 3.49%.

Table 7: Output power obtained from analytical model and by measurement

Case	Mathematical Model			Measurement		
	u (V)	I_L (A)	P_{out} (W)	u (V)	I_L (A)	P_{out} (W)
i	24	19.59	470.2	24.2	18.8	454.9
ii	36	27.8	1000.8	36.1	26.8	967.5
iii	48	39.76	1908.5	48.2	38.2	1841.2

The value of the current obtained from the analytical model is more than the value of the current obtained from the measurement. Since the resistance of the phase windings in the analytical model is neglected. Considering the output power based on (6), the key factor used to calculate is the current. Consequently, the output power obtained from the measurement is slightly less than the output power obtained from the analytical model. The efficiency of the system depends on the system's losses. The main losses of the system are copper loss and iron loss. The copper loss based on (7), the significant factor used to calculate is the current. The iron loss based on (9) depending on the flux linkage, the key factor used to calculate the flux linkage is the current. Therefore, the result obtained from the analytical model is different from the measurements.

VI. CONCLUSION

In this paper, the proposed inductance model applied from the flux linkage function is divided into three regions depending on the phase current and rotor position. It requires the geometrical parameters of an SRG at aligned and unaligned rotor positions. The parameters are easily quantified using the FEM. The characteristics of the inductance curve obtained using the proposed model compared with the FEM are closely matched. This result confirms the validity of the proposed model. The phase current model proposed in this paper is derived from the phase voltage equation in combination with the proposed inductance model. The shape of phase current obtained from the analytical model is also corresponding with the measurements. The optimal shape of phase current is investigated. Finally, a method to obtain the optimal control variables to maximize the output power for SRGs in single pulse mode operation is proposed. The optimal shape of the phase current is used to determine the optimal control variables. An 8/6 SRG experimental setup is used to verify the proposed method. Regarding to the results, the SRG can generate the maximum output power when the proposed optimal control variables are applied. The output power obtained from the analytical model is slightly different from the measurements. Therefore, the proposed method is accurate and reliable.

REFERENCES

[1] B. Fahimi, A. Emadi, and R. B. Sepe, "A switched reluctance machine-based starter/alternator for more electric cars," *IEEE Trans. Energy Conversion*, vol. 19, no. 1, pp. 116-124, Mar. 2004.

[2] N. Schofield and S. Long, "Generator operation of a switched reluctance starter/generator at extended speeds," *IEEE Trans. Vehicular Technology*, vol. 58, no. 1, pp. 48-56, Jan. 2009.

[3] S. R. Macminn and W. D. Jones, "A very high speed switched-reluctance starter-generator for aircraft engine applications," *in Proc. Conf. Aerospace and Electronics*, pp. 1758-1764, 1989.

[4] C. A. Ferreira, S. R. Jones, W. S. Heglund, and W. D. Jones, "Detailed design of a 30-kW switched reluctance starter/generators system for a gas turbine engine application," *IEEE Trans. Industry Applications*, vol. 31, no. 3, pp. 553-561, May 1995.

[5] R. Cardenas, W. F. Ray, and G. M. Asher, "Switched reluctance generators for wind energy applications," *in Proc. Conf. Power Electronics Specialists*, pp. 559-564, 1995.

[6] M. Ziapour, E. Afjei, and M. Yousefi, "Optimum commutation angles for voltage regulation of a high speed switched reluctance generator," *in Proc. Conf. Power Electronics, Drive Systems and Technology*, pp. 271-276, 2013.

[7] P. Asadi and B. Fahimi, "Design and control characterization of switched reluctance generator for maximum output power," *in Proc. Conf. Applied Power Electronics*, pp. 1639-1644, 2006.

[8] P. Kerdtuad and S. Kittiratsatcha "Modeling of a switched reluctance generator using cubic spline coefficients on the phase flux linkage, inductance and torque equations," *Advances in Electrical and Computer Engineering*, vol. 15, no. 1, pp. 41-48, 2015.

[9] D. W. Choi, S. I. Byun, and Y. H. Cho, "A study on the maximum power control method of switched reluctance generator for wind turbine," *IEEE Trans. Magnetics*, vol. 50, no. 1, article: 4003004, Jan. 2014.

[10] H. Chen and Z. Shao, "Turn-on angle control for switched reluctance wind power generator system," *in Proc. Conf. Industrial Electronics Society*, pp. 2367-2370, 2004.

[11] S. Yilmaz and D. A. Torrey, "Closed loop control of excitation parameters for high speed switched-reluctance generators," *IEEE Trans. Power Electronics*, vol. 19, no. 2, pp. 335-362, Mar. 2004.

[12] I. Kioskeridis and C. Mademlis, "Optimal efficiency control of switched reluctance generators," *IEEE Trans. Power Electronics*, vol. 21, no. 4, pp. 1062-1072, July 2006.

[13] S. Yu, F. Zhang, D. H. Lee, and J. W. Ahn, "High efficiency operation of a switched reluctance generator over a wide speed range," *Journal of Power Electronics*, vol. 15, no. 1, pp. 123-130, 2015.

[14] S. Wongguokoon and S. Kittiratsatcha, "Analysis of a switched-reluctance generator for maximum energy conversion," *in Proc. Conf. Sustainable Energy Technologies*, pp. 125-129, 2008.

[15] P. Thongprasri and S. Kittitratsatcha, "Optimal excitation angles of a switched reluctance generator for maximum output power," *Journal of Electrical*

Engineering and Technology, vol. 9, no. 5, pp. 1527-1536, 2014.

[16] K. N. Srinivas and R. Arumugam, “Dynamic characterization of switched reluctance motor by computer-aided design and electromagnetic transient simulation,” *IEEE Trans. Magnetics*, vol. 39, no. 3, pp. 1806-1812, May 2003.

[17] S. A. Hossain and I. Husain, “A geometry based simplified analytical model of switched reluctance machines for real-time controller implementation,” *IEEE Trans. Power Electronics*, vol. 18, no. 6, pp. 1384-1389, Nov. 2003.

[18] C. Roux and M. M. Morcos, “On the use of a simplified model for switched reluctance motors,” *IEEE Trans. Energy Conversion*, vol. 17, no. 3, pp. 400-405, Sep. 2002.

[19] H. P. Chi, R. L. Lin, and J. F. Chen, “Simplified flux-linkage model for switched-reluctance motors,” *in Proc. Electric Power Applications*, pp. 577-583, 2005.

[20] M. Stiebler and K. Liu, “An analytical model of switched reluctance machines,” *IEEE Trans. Energy Conversion*, vol. 14, no. 4, pp. 1100-1107, Dec. 1999.

[21] D. A. Torrey, “Switched reluctance generators and their control,” *IEEE Trans. Industrial Electronics*, vol. 49, no. 1, pp. 3-14, Feb. 2002.

[22] P. N. Materu and R. Krishan, “Estimation of switched reluctance motor loses,” *IEEE Trans. Industry Applications*, vol. 28, no. 3, pp. 668-679, June 1992.

[23] P. Rafajdus, V. Hrabovcova, and P. Hudak, “Investigation of losses and efficiency in switched reluctance motor,” *in Proc. Conf. Power Electronics and Motion Control*, pp. 296-301, 2006.

[24] S. Yu, D. H. Lee, and J. W. Ahn, “Efficiency analysis of switched reluctance generator according to current shape under rated speed,” *Journal of International Conference on Electrical Machines and Systems*, vol. 2, no. 4, pp. 491-497, Nov. 2013.

[25] R. L. Lin, J. F. Chen, and H. P. Chi, “Spice-based flux-linkage model for switched reluctance motors,” *in Proc. Conf. Electric Power Applications*, pp. 1468-1476, 2005.

[26] M. Krishnamurthy, B. Fahimi, and C. S. Edrington, “On the measurement of mutual Inductance for a switched reluctance machine,” *in Proc. Conf. Power Electronics Specialists*, pp. 1-7, 2006.

[27] H. K. Bae and R. Krishnan, “A novel approach to control of switched reluctance motors considering mutual inductance,” *in Proc. Conf. Industrial Electronics Society*, pp. 369-374, 2000.

Pairote Thongprasri He received his M.Eng. degree in Electrical Engineering from KMITL. He is studying in D.Eng. program (Electrical Engineering) at KMITL. His research interests are switched reluctance machine and power electronics.

Supat Kittiratsatcha received his M.S. and Ph.D. degrees in Electric Power Engineering from Rensselaer Polytechnic Institute, Troy, NY. He is an Associate Professor with the Department of Electrical Engineering at KMITL. His research interests include switched reluctance machine design and solid state lighting.

Electromagnetic Coupling Analysis of Transient Excitations of Rectangular Cavity through Slot using TD-EFIE with Laguerre Polynomials as Temporal Basis Functions

D. Omri and T. Aguili

Syscom Laboratory
National Engineering School of Tunis, BP 37, Belvédère, 1002, Tunis, Tunisia
omridorsaf@yahoo.fr

Abstract **─** This paper presents an electromagnetic coupling analysis of transient waves excited a rectangular cavity containing an interior scatterer coupled to an external scatterer through a slot. Based on the equivalence principle, time domain integral equations are established by enforcing the boundary conditions on the internal and external scatterers, the slot and the cavity walls. The method of moments is applied in space and time domains to solve the developed system of integral equations. The unknown coefficients of the electric and magnetic currents are approximated by the triangular piecewise functions associated with Dirac function as space basis. To obtain accurate and stable solutions, the Laguerre functions are used as temporal basis. Numerical results involving the coupling effects between the cavity components are investigated. The numerical results are found to be in good agreement with EM theory and literature.

Index Terms **─** Coupling effect, equivalence principle, Laguerre functions, MoM, piecewise triangular functions, slot, TD-EFIE, transient electric and magnetic currents.

I. INTRODUCTION

In electromagnetic compatibility, it is interesting to model the coupling through a slot-aperture backed by a rectangular cavity. When the cavity is excited by internal field source, it acts as an aperture antenna that radiates in external region. The problem of coupling between this radiation element and some components close to the cavity can influence the integrity of communication system. Another typical problem is the evaluation of the current induced by incident electromagnetic fields through an aperture because this current may damage some critical components in the system. Also the response of the cavity through the slot can damage the equipments at the side of cavity.

In order to tackle the two problems, many researchers have developed a lot of frequency domain methods for many cavity designs [1]-[5]. But, for the defense and security reasons, the transient response of these problems can be depicted easily in time domain.

The transient response of the cavity through an aperture is obtained primarily by Inverse Fourier Transforms (IFT) [6]. An exact solution using this method cannot be found. Reference [7] solves the transient problem by using the singularity expansion method (SEM). Recently, the integral equations are formulated and solved in time domain using a time stepping technique [8]-[11]. That later suffers from the late-time instabilities.

In this paper, we consider a communication system composed on a rectangular cavity backed slot containing an internal (probe) and external (thin wire antenna) scatterers. The latters are coupled through the slot.

The aim of this work is to develop a general system of Time Domain Electric Field Integral Equations (TD-EFIE) based on the equivalence principle and the appropriate boundary conditions. In fact, when the cavity is excited through the slot by internal and/or external transient electromagnetic waves, we can apply the developed integral equations system to predict the transient responses of the structure and to study the physical coupling effects between the component of the designed system.

In order to solve the proposed TD-EFIE by applying the Method of Moments (MoM) [12], we introduce a spatial and temporal testing procedures. The piecewise triangular functions [13] associated with Dirac functions are used as spatial basis functions. The present paper sets out to present an accurate technique to obtain stable solutions of the obtained TD-EFIE system using Laguerre polynomials as temporal basis functions [14]-[18]. The transient responses of the structure are compared to the results obtained by applying the B-Spline functions as a temporal basis [22]. In fact, an accurate comparison of the two time approaches (Laguerre scheme and B-Spline scheme) in terms of complexity, accuracy and stability was presented in [22].

Submitted On: January 31, 2015
Accepted On:January 9, 2016

In this work and based on the results stemming from this comparison, a coupling between the thin wire antenna and the probe through the slot is studied using Laguerre functions. The space distributions of the currents are presented.

The paper is divided in four sections. Section II presents the integral equations formulation in the time domain and the method of solving these equations. Numerical results are given in Section III. Section IV concludes the paper.

II. TD-EFIE FORMULATION

The geometry of the analyzed problem is depicted in Fig. 1, which consists of a cavity with a slot on its wall, located in the X-Y plan. A linear electric probe of the length l_p at the position (x_P, y_P) is located inside the cavity at the distance D of the slot. Outside the cavity, we consider a thin wire antenna of the length l_A vertically placed at the distance d from the cavity and located in parallel to the slot at the position (x_A, y_A).

To investigate the radiation characteristics of the structure, we assume that:

- The cavity walls, the antenna and the probe are considered as perfect conductors and very thin.
- The antenna is excited by $\vec{E}_{01} = E_{01}\vec{y}$.
- The probe is excited by $\vec{E}_{02} = E_{02}\vec{y}$.

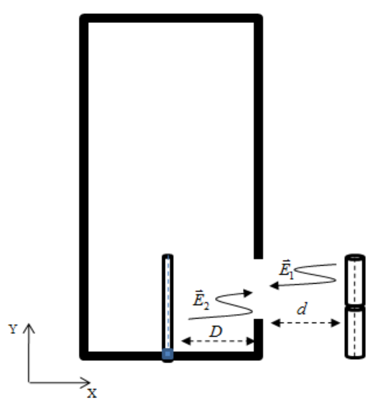

Fig. 1. The geometry of the problem.

By involving the equivalence principle [19], an equivalent surface replaces the physical structure with equivalent magnetic current density radiating in free space over the slot. References [20]-[21] have demonstrated that the magnetic current density is moving an infinitesimal distance away from equivalent surface. Mathematical analysis of this step shows that the slot can be short-circuited. Therefore, two coupled-equivalent problems are established (Fig. 2). In both the external and internal equivalent problems, we retain the sources in the region of interest. In Fig. 3, we represent the different domains:

- $D = \Omega_1 \cup \Omega_3 \cup \Omega_4$ the external analyzed domain.
- $D = \Omega_2 \cup \Omega_3 \cup \Omega_4$ the internal analyzed domain.

Where Ω_1 is the surface of the antenna; Ω_2 is the surface of the probe; Ω_3 is the equivalent domain replacing the slot; Ω_4 is equivalent surface replacing the cavity walls. In fact, the domain Ω_3 is the sub-domain infinitesimally close to, but not coincident with Ω_4. Over it remains not null the equivalent magnetic current.

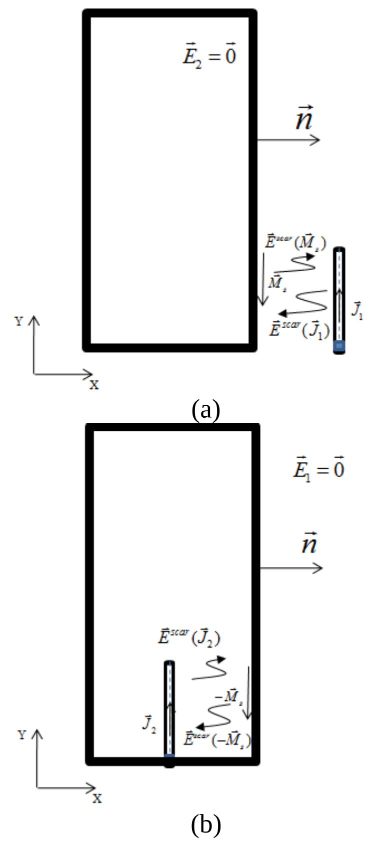

Fig. 2. The equivalent problem: (a) equivalent external problem, and (b) equivalent internal problem.

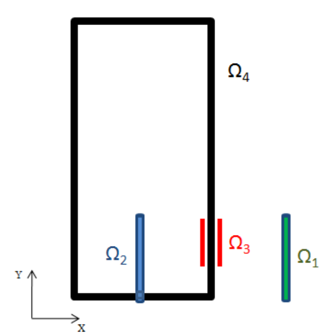

Fig. 3. The different domains: cavity walls, slot, antenna and probe.

The external problem contains the equivalent magnetic current density $\vec{M}_s$ and the unknown electric current $\vec{J}_1$ (Fig. 2 (a)). The fields inside Ω_4 are zero and outside are equal to the radiation produced by the incident field $\vec{E}_{01}$ and scattered fields induced by $\vec{M}_s$ and $\vec{J}_1$. These fields must satisfy the following boundary condition:

$$\vec{M}_s = -\vec{n} \times \vec{E}_1, \tag{1}$$

where

$$\vec{E}_1 = \vec{E}_{01} + \vec{E}^{scar}(\vec{M}_s) + \vec{E}^{scar}(\vec{J}_1). \tag{2}$$

For the internal problem, as shown in Fig. 2 (b), the equivalent magnetic current density $\vec{M}_s$ and the unknown electric current $\vec{J}_2$ are selected so that the fields outside equivalent surface Ω_4 are zero and inside are equal to the radiation produced by $\vec{E}_{02}$ and the scattered fields $\vec{E}^{scar}(\vec{J}_2)$ and $\vec{E}^{scar}(-\vec{M}_s)$. These fields must satisfy the boundary condition (1), where,

$$\vec{E}_2 = \vec{E}_{02} + \vec{E}^{scar}(\vec{J}_2) + \vec{E}^{scar}(-\vec{M}_s). \tag{3}$$

An alternate formulation of the TD-EFIE is applied in this paper to describe unknown equivalent magnetic current sheet over the slot and the unknown electric currents at the probe and the antenna. This formulation is based on the equivalence principle in addition to enforce the following boundary conditions:

- The tangential magnetic fields are contentious through the slot aperture both inside and outside the cavity.
- The source is considered at the bottom of the probe inside the cavity.
- The source is considered at the center of the antenna outside the cavity.

Taking into account the interaction between the probe, the antenna and slot we obtain the following system:

$$\begin{cases} \left[\vec{E}_{01} + \vec{E}^{scar}(\vec{J}_1) + \vec{E}^{scar}(\vec{M}_s)\right]_{\tan} = \vec{0} \;\; over\; \Omega_1 \\ \left[\vec{E}_{02} + \vec{E}^{scar}(\vec{J}_2) + \vec{E}^{scar}(-\vec{M}_s)\right]_{\tan} = \vec{0} \;\; over\; \Omega_2 \\ \left[\vec{E}^{scar}(\vec{J}_1) + \vec{E}^{scar}(\vec{M}_s)\right]_{\tan} \\ \qquad = \left[\vec{E}^{scar}(\vec{J}_2) + \vec{E}^{scar}(-\vec{M}_s)\right]_{\tan} \;\; over\; \Omega_3 \\ \left[\vec{E}^{scar}(\vec{J}_1) + \vec{E}^{scar}(\vec{M}_s)\right]_{\tan} = \vec{0} \;\; over\; \Omega_4 \\ \left[\vec{E}^{scar}(\vec{J}_2) + \vec{E}^{scar}(-\vec{M}_s)\right]_{\tan} = \vec{0} \;\; over\; \Omega_4 \end{cases}, \tag{4}$$

where

$$\vec{E}^{scar}\left(\vec{M}_s\right) = -\frac{1}{\varepsilon}\nabla \times \vec{F}, \tag{5}$$

$$\vec{E}^{scar}(\vec{J}_i) = -\frac{\partial}{\partial t}\vec{A}_i - \nabla \varphi_i. \tag{6}$$

The magnetic vector and electric scalar potentials, $\vec{A}_i$ and φ_i, are expressed on the antenna (i=1) or the probe (i=2) which are mathematically given by:

$$\vec{A}_i(x,y,t) = \frac{\mu}{4\pi}\iint_{\Omega_i} \frac{\vec{J}_i(x',y',t-{R_{ij}}/{C})}{R_{ij}(x,y,x',y')}ds', \;(x,y)\in\Omega_j, \tag{7}$$

$$\varphi_i(x,y,t) = \frac{1}{4\pi\varepsilon}\iint_{\Omega_i} \frac{q_i(x',y',t-{R_{ij}}/{C})}{R_{ij}(x,y,x',y')}ds', \;(x,y)\in\Omega_j, \tag{8}$$

where μ is the permeability and C is the velocity of propagation of the electromagnetic wave in free space.

The potential electric vector $\vec{F}$ is given by the time retarded integral equation involving the magnetic current $\vec{M}_s$. It is mathematically obtained by application of the concept of electromagnetic duality for Maxwell theories:

$$\vec{F}(x,y,t) = \frac{\varepsilon}{4\pi}\iint_{\Omega_3} \frac{\vec{M}_s(x',y',t-{R_{3j}}/{C})}{R_{3j}(x,y,x',y')}ds', \;(x,y)\in\Omega_j, \tag{9}$$

where $\vec{M}_s$ is the equivalent density current vector along Ω_3 and ε is permittivity of free space. The retarded time is expressed by $t-{R_{ij}}/{C}$. The distance $R_{ij}=\sqrt{(x-x')^2+(y-y')^2}$ represents the interaction between the observation point $(x,y)\in\Omega_j$ and the source point $(x',y')\in\Omega_i$, as shown in Fig. 4.

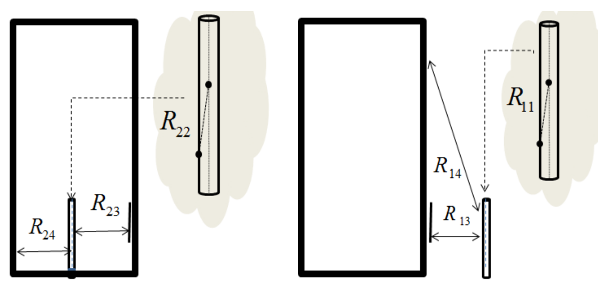

Fig. 4. The different distances between the observation and source points for the internal and external equivalent problems.

For convenience of numerical computation [13], it is useful to derive the scalar and vector potentials from the sources terms by means of the Hertz vectors which does not have a time integral term. Hence, the electric current and the charge density can be expressed in terms of the single Hertz vector $\vec{G}_i$:

$$\vec{J}_i(x,y,t) = \frac{d}{dt}\vec{G}_i(x,y,t), \tag{10}$$

$$q_i(x,y,t) = -\nabla.\vec{G}_i(x,y,t). \tag{11}$$

The magnetic current is also expressed by means of the Hertz vector $\vec{L}$:

$$M_s(x,y,t) = \frac{d}{dt}\vec{L}(x,y,t). \tag{12}$$

By substituting (5)-(12) in (4), we obtain the following time domain integral equations system:

$$\begin{bmatrix} -\frac{\mu}{4\pi}\frac{\partial^2}{\partial t^2}\iint_{\Omega_1}\frac{\vec{G}_1(x',y',t-R_{11}/C)}{R_{11}(x,y,x',y')}ds' \\ +\frac{1}{4\pi\varepsilon}\nabla\iint_{\Omega_1}\frac{\nabla.\vec{G}_1(x',y',t-R_{11}/C)}{R_{11}(x,y,x',y')} \\ -\frac{1}{4\pi}\nabla\times\iint_{\Omega_3}\frac{1}{R_{31}(x,y,x',y')}\frac{d}{dt}\vec{L}(x',y',t-R_{31}/C)ds' \end{bmatrix} = -\vec{E}_{01}(x,y,t) \tag{13}$$

$$\begin{bmatrix} -\frac{\mu}{4\pi}\frac{\partial^2}{\partial t^2}\iint_{\Omega_2}\frac{\vec{G}_2(x',y',t-R_{22}/C)}{R_{22}(x,y,x',y')}ds' \\ +\frac{1}{4\pi\varepsilon}\nabla\iint_{\Omega_2}\frac{\nabla.\vec{G}_2(x',y',t-R_{22}/C)}{R_{22}(x,y,x',y')} \\ +\frac{1}{4\pi}\nabla\times\iint_{\Omega_3}\frac{1}{R_{32}(x,y,x',y')}\frac{d}{dt}\vec{L}(x',y',t-R_{32}/C)ds' \end{bmatrix} = -\vec{E}_{02}(x,y,t) \tag{14}$$

$$\begin{bmatrix} -\frac{\mu}{4\pi}\frac{\partial^2}{\partial t^2}\iint_{\Omega_1}\frac{\vec{G}_1(x',y',t-R_{13}/C)}{R_{13}(x,y,x',y')}ds' \\ +\frac{1}{4\pi\varepsilon}\nabla\iint_{\Omega_1}\frac{\nabla.\vec{G}_1(x',y',t-R_{13}/C)}{R_{13}(x,y,x',y')} \\ -\frac{1}{4\pi}\nabla\times\iint_{\Omega_3}\frac{1}{R_{33}(x,y,x',y')}\frac{d}{dt}\vec{L}(x',y',t-R_{33}/C)ds' \end{bmatrix} = \begin{bmatrix} -\frac{\mu}{4\pi}\frac{\partial^2}{\partial t^2}\iint_{\Omega_2}\frac{\vec{G}_2(x',y',t-R_{23}/C)}{R_{23}(x,y,x',y')}ds' \\ +\frac{1}{4\pi\varepsilon}\nabla\iint_{\Omega_2}\frac{\nabla.\vec{G}_2(x',y',t-R_{23}/C)}{R_{23}(x,y,x',y')} \\ +\frac{1}{4\pi}\nabla\times\iint_{\Omega_3}\frac{1}{R_{33}(x,y,x',y')}\frac{d}{dt}\vec{L}(x',y',t-R_{33}/C)ds' \end{bmatrix}, \tag{15}$$

$$\begin{bmatrix} -\frac{\mu}{4\pi}\frac{\partial^2}{\partial t^2}\iint_{\Omega_1}\frac{\vec{G}_1(x',y',t-R_{14}/C)}{R_{14}(x,y,x',y')}ds' \\ +\frac{1}{4\pi\varepsilon}\nabla\iint_{\Omega_1}\frac{\nabla.\vec{G}_1(x',y',t-R_{14}/C)}{R_{14}(x,y,x',y')} \\ -\frac{1}{4\pi}\nabla\times\iint_{\Omega_3}\frac{1}{R_{34}(x,y,x',y')}\frac{d}{dt}\vec{L}(x',y',t-R_{34}/C)ds' \end{bmatrix} = \vec{0}, \tag{16}$$

$$\begin{bmatrix} -\frac{\mu}{4\pi}\frac{\partial^2}{\partial t^2}\iint_{\Omega_2}\frac{\vec{G}_2(x',y',t-R_{24}/C)}{R_{24}(x,y,x',y')}ds' \\ +\frac{1}{4\pi\varepsilon}\nabla\iint_{\Omega_2}\frac{\nabla.\vec{G}_2(y',t-R_{24}/C)}{R_{24}(x,y,x',y')} \\ +\frac{1}{4\pi}\nabla\times\iint_{\Omega_3}\frac{1}{R_{34}(x,y,x',y')}\frac{d}{dt}\vec{L}(x',y',t-R_{34}/C)ds' \end{bmatrix} = \vec{0}. \tag{17}$$

The TD-EFIE are solved in space and time domains by applying the Method of Moments (MoM) [12]. Firstly, the problem is converted to a discrete one by employing a system of appropriate space-time bases functions. Secondly, a testing procedure is applied to convert the discrete vector functional equation into a linear scalar system of equations.

We start the space numerical procedure by the choice of suitable space basis functions in order to approximate the unknown Hertz vectors $\vec{G}_1$, $\vec{G}_2$ and $\vec{L}$. Indeed, the choice of the basis function strongly influences the properties of the MoM approximation of the unknowns. We define the spatial basis functions as the piecewise triangular functions [13] associated with Dirac function $\vec{f}_n = H_n^{(\Omega_i)}.\Lambda_{\chi_j}^{(\Omega_i)}\vec{u}$, where,

$$H_k^{(\Omega_i)}(h) = \begin{cases} \frac{h-h_{k-1}}{h_k-h_{k-1}}, & h\in[h_{k-1},h_k] \\ \frac{h_{k+1}-h}{h_{k+1}-h_k}, & h\in[h_k,h_{k+1}] \\ 0, & otherwise \end{cases}. \tag{18}$$

$$\Lambda_{\chi_j}^{(\Omega_i)}(\chi) = \begin{cases} 1, & \chi=\chi_j \\ 0, & otherwise \end{cases}$$

The choice of the piecewise triangular function has the following advantages: it minimized the required computational and it leads to an accurate evaluation of the unknowns with few expansion functions.

The goal of the association between the Dirac function and the piecewise triangular function is metalized the domains Ω_i only.

Now, we express the Hertz vectors $\vec{G}_i$ and $\vec{L}$ in terms of vector basis functions $\vec{f}_n$ and $\vec{h}_n = \vec{n}\times\vec{f}_n$, respectively:

$$\begin{cases} \vec{G}_1(x,y,t) = \sum_{n=1}^{N_1} g_n^1(t)\vec{f}_n^{\,1}(x,y) \\ \vec{f}_n^{\,1}(x,y) = H_n^{(\Omega_1)}(y).\Lambda_{x_A}^{(\Omega_1)}(x)\vec{y} \end{cases}, \tag{19}$$

$$\begin{cases} \vec{G}_2(x,y,t) = \sum_{n=1}^{N_2} g_n^2(t)\vec{f}_n^{\,2}(x,y) \\ \vec{f}_n^{\,2}(x,y) = H_n^{(\Omega_{21})}(y).\Lambda_{x_p}^{(\Omega_2)}(x)\vec{y} \end{cases}, \tag{20}$$

$$\begin{cases} \vec{L}(x,y,t) = \sum_{n=1}^{N_3} l_n(t)\vec{h}_n(x,y) \\ \vec{h}_n = \vec{n}\times\vec{f}_n \\ \vec{f}_n(x,y) = H_n^{(\Omega_3)}(y).\Lambda_{x_S}^{(\Omega_3)}(x)\vec{y} \end{cases}. \tag{21}$$

Note that the axis of the antenna, the probe and the slot are divided into N_1, N_2 and N_3 equal sub-domains of which the space step is Δy.

In order to discretize Ω_4, we divide the cavity walls in $N_4 = N_{4x}\times N_{4y}$ equal sub-domains whose the lengths are Δx and Δy along x-y directions, respectively. The functions $\vec{f}_n^{\,4}$ illustrated in Fig. 5 is given by:

$$\begin{cases} f_{n,y}^4(x,y) = H_n^{(\Omega_4)}(y).\Lambda_{x_{\{1,N_{4x}\}}}^{(\Omega_4)}(x) \\ f_{n,x}^4(x,y) = H_{\{1,N_{4y}\}}^{(\Omega_4)}(y).\Lambda_{x_n}^{(\Omega_4)}(x) \end{cases}. \tag{22}$$

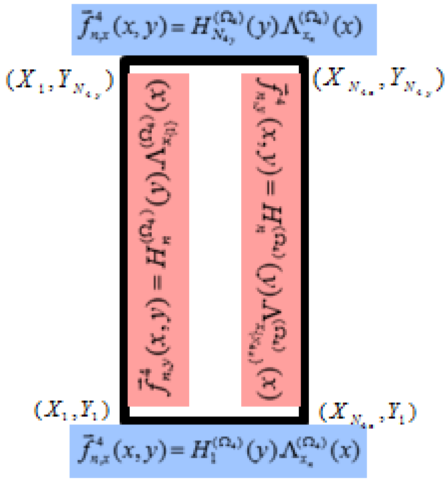

Fig. 5. Testing function $\vec{f}^{\,4}_n$.

We substitute (19)-(21) into (13)-(17), then we apply the spatial testing procedure, we obtain:

$$\left[\begin{array}{l}\sum_{n=1}^{N_1}\left[-\mu a_{mn}^{11}\dfrac{d^2 g_n^1(t-R_{mn}^{11}/C)}{dt^2}+\dfrac{b_{mn}^{11}}{\varepsilon}g_n^1(t-R_{mn}^{11}/C)\right]\\ +\sum_{n=1}^{N_3}-c_{mn}^{31}\dfrac{dl_n(t-R_{mn}^{31}/C)}{dt}\end{array}\right]=-E_m^1(t)\,, \tag{23}$$

$$\left[\begin{array}{l}\sum_{n=1}^{N_2}\left[-\mu a_{mn}^{22}\dfrac{d^2 g_n^2(t-R_{mn}^{22}/C)}{dt^2}+\dfrac{b_{mn}^{22}}{\varepsilon}g_n^2(t-R_{mn}^{22}/C)\right]\\ +\sum_{n=1}^{N_3}c_{mn}^{32}\dfrac{dl_n(t-R_{mn}^{32}/C)}{dt}\end{array}\right]=-E_m^2(t)\,, \tag{24}$$

$$\left[\begin{array}{l}\sum_{n=1}^{N_1}\left[-\mu a_{mn}^{13}\dfrac{d^2 g_n^1(t-R_{mn}^{13}/C)}{dt^2}+\dfrac{b_{mn}^{13}}{\varepsilon}g_n^1(t-R_{mn}^{13}/C)\right]\\ -\sum_{n=1}^{N_2}\left[-\mu a_{mn}^{23}\dfrac{d^2 g_n^2(t-R_{mn}^{23}/C)}{dt^2}+\dfrac{b_{mn}^{23}}{\varepsilon}g_n^2(t-R_{mn}^{23}/C)\right]\\ +2\sum_{n=1}^{N_3}-c_{mn}^{33}\dfrac{dl_n(t-R_{mn}^{33}/C)}{dt}\end{array}\right]=0\,, \tag{25}$$

$$\left[\begin{array}{l}\sum_{n=1}^{N_1}\left[-\mu a_{mn}^{14}\dfrac{d^2 g_n^1(t-R_{mn}^{14}/C)}{dt^2}+\dfrac{b_{mn}^{14}}{\varepsilon}g_n^1(t-R_{mn}^{14}/C)\right]\\ +\sum_{n=1}^{N_3}-c_{mn}^{34}\dfrac{dl_n(t-R_{mn}^{34}/C)}{dt}\end{array}\right]=0\,, \tag{26}$$

$$\left[\begin{array}{l}\sum_{n=1}^{N_2}\left[-\mu a_{mn}^{24}\dfrac{d^2 g_n^2(t-R_{mn}^{24}/C)}{dt^2}+\dfrac{b_{mn}^{24}}{\varepsilon}g_n^2(t-R_{mn}^{24}/C)\right]\\ +\sum_{n=1}^{N_3}c_{mn}^{34}\dfrac{dl_n(t-R_{mn}^{34}/C)}{dt}\end{array}\right]=0\,. \tag{27}$$

We assume that the unknown transient quantities $\{g_n^i, l_n\}$ does not change appreciably within the segment Δy so that $\tau^{ij}=t-R^{ij}/C \to \tau_{mn}^{ij}=t-R_{mn}^{ij}/C$:

$$\begin{aligned}E_m^j(t)&=\left\langle \vec{f}_m^{\,j}(x,y),\vec{n}\times\vec{E}_{0j}(x,y,t)\right\rangle\\ &=\iint_{\Omega_j}\vec{f}_m^{\,j}(x,y).\left[\vec{n}\times\vec{E}_{0j}(x,y,t)\right]ds\end{aligned}\,, \tag{28}$$

$$\left\{\begin{array}{l}a_{mn}^{ij}=\left\langle f_m^{\,j}(x,y),\dfrac{1}{4\pi}\iint_{\Omega_i}\dfrac{f_n^{\,i}(x',y')}{R_{ij}(x,y,x',y')}ds\right\rangle\\ b_{mn}^{ij}=\left\langle f_m^{\,j}(x,y),\dfrac{1}{4\pi}\nabla\iint_{\Omega_i}\dfrac{\nabla f_n^{\,i}(x',y')}{R_{ij}(x,y,x',y')}\right\rangle\\ c_{mn}^{3j}=\left\langle f_m^{\,j}(x,y),\dfrac{1}{4\pi}\nabla\times\iint_{\Omega_3}\dfrac{\vec{h}_m(x',y')}{R_{3j}(x,y,x',y')}ds'\right\rangle\end{array}\right.\,. \tag{29}$$

On the other hand, we consider the temporal procedure. In order to obtain stable and accurate solutions, a temporal basis functions derived from the Laguerre polynomials [14] is applied. The transient electric and magnetic coefficients introduced in (19) and (20) are expanded by:

$$g_n^i(t)\approx\sum_{a=0}^{\infty}g_{n,a}^i\varphi_a(st)\,, \tag{30}$$

$$l_n(t)\approx\sum_{a=0}^{\infty}l_{n,a}\varphi_a(st)\,, \tag{31}$$

where $\{g_{n,a}^i, l_{n,a}\}$ are the unknown coefficients; $\{\varphi_a(st), a=0..\infty\}$ is the temporal basis functions derived from the Laguerre function $\left(\varphi_a(st)=e^{-st/2}L_a(st)\right)$. So, the term $L_a(st)$ represents the Laguerre polynomial of order "a" and "s" is a time scaling factor [17]. The mathematical properties of these functions, the first and the second derivatives are introduced in [14]-[15].

In order to apply the Galerkin's Method [12] in time domain, we substitute (30)-(33) into (23)-(27) and we apply the temporal testing procedure with $\varphi_b(st)$, we obtain the following system:

$$\left\{\begin{array}{l}
\left[\begin{array}{l}\sum_{n=1}^{N_1}\left[-s^2\mu a_{mn}^{11}\sum_{a=0}^{b}\left[\frac{1}{4}g_{n,a}^1+\sum_{k=0}^{a-1}(a-k)g_{n,k}^1\right]I_{ba}\left(s\left(R_{mn}^{11}/C\right)\right)+\frac{b_{mn}^{11}}{\varepsilon}\sum_{a=0}^{b}g_{n,a}^1 I_{ba}\left(s\left(R_{mn}^{11}/C\right)\right)\right]\\ +\sum_{n=1}^{N_3}-sc_{mn}^{31}\sum_{a=0}^{b}\left[\frac{1}{2}l_{n,a}+\sum_{k=0}^{a-1}l_{n,k}\right]I_{ba}\left(s\left(R_{mn}^{31}/C\right)\right)\end{array}\right]=-E_{m,b}^1(t)\\[2ex]
\left[\begin{array}{l}\sum_{n=1}^{N_2}\left[-s^2\mu a_{mn}^{22}\sum_{a=0}^{b}\left[\frac{1}{4}g_{n,a}^2+\sum_{k=0}^{a-1}(a-k)g_{n,k}^2\right]I_{ba}\left(s\left(R_{mn}^{22}/C\right)\right)+\frac{b_{mn}^{22}}{\varepsilon}\sum_{a=0}^{b}g_{n,a}^2 I_{ba}\left(s\left(R_{mn}^{22}/C\right)\right)\right]\\ +\sum_{n=1}^{N_3}sc_{mn}^{32}\sum_{a=0}^{b}\left[\frac{1}{2}l_{n,a}+\sum_{k=0}^{a-1}l_{n,k}\right]I_{ba}\left(s\left(R_{mn}^{32}/C\right)\right)\end{array}\right]=-E_{m,b}^2(t)\\[2ex]
\left[\begin{array}{l}\left[\sum_{n=1}^{N_1}\left[-s^2\mu a_{mn}^{13}\sum_{a=0}^{b}\left[\frac{1}{4}g_{n,a}^1+\sum_{k=0}^{a-1}(a-k)g_{n,k}^1\right]I_{ba}\left(s\left(R_{mn}^{13}/C\right)\right)+\frac{b_{mn}^{13}}{\varepsilon}\sum_{a=0}^{b}g_{n,a}^1 I_{ba}\left(s\left(R_{mn}^{13}/C\right)\right)\right]\right]\\ \left[-\sum_{n=1}^{N_2}\left[-s^2\mu a_{mn}^{23}\sum_{a=0}^{b}\left[\frac{1}{4}g_{n,a}^2+\sum_{k=0}^{a-1}(a-k)g_{n,k}^2\right]I_{ba}\left(s\left(R_{mn}^{23}/C\right)\right)+\frac{b_{mn}^{23}}{\varepsilon}\sum_{a=0}^{b}g_{n,ab}^2 I_{ba}\left(s\left(R_{mn}^{23}/C\right)\right)\right]\right]\\ \left[+2\sum_{n=1}^{N_3}-sc_{mn}^{33}\sum_{a=0}^{b}\left[\frac{1}{2}l_{n,a}+\sum_{k=0}^{a-1}l_{n,k}\right]I_{ba}\left(s\left(R_{mn}^{33}/C\right)\right)\right]\end{array}\right]=0\\[2ex]
\left[\begin{array}{l}\sum_{n=1}^{N_1}\left[-s^2\mu a_{mn}^{14}\sum_{a=0}^{b}\left[\frac{1}{4}g_{n,a}^1+\sum_{k=0}^{a-1}(a-k)g_{n,k}^1\right]I_{ba}\left(s\left(R_{mn}^{14}/C\right)\right)+\frac{b_{mn}^{14}}{\varepsilon}\sum_{a=0}^{b}g_{n,a}^1 I_{ba}\left(s\left(R_{mn}^{14}/C\right)\right)\right]\\ +\sum_{n=1}^{N_3}-sc_{mn}^{34}\sum_{a=0}^{b}\left[\frac{1}{2}l_{n,a}+\sum_{k=0}^{a-1}l_{n,k}\right]I_{ba}\left(s\left(R_{mn}^{34}/C\right)\right)\end{array}\right]=0\\[2ex]
\left[\begin{array}{l}\sum_{n=1}^{N_2}\left[-s^2\mu a_{mn}^{24}\sum_{a=0}^{b}\left[\frac{1}{4}g_{n,a}^2+\sum_{k=0}^{a-1}(a-k)g_{n,k}^2\right]I_{ba}\left(s\left(R_{mn}^{24}/C\right)\right)+\frac{b_{mn}^{24}}{\varepsilon}\sum_{a=0}^{b}g_{n,a}^2 I_{ba}\left(s\left(R_{mn}^{24}/C\right)\right)\right]\\ +\sum_{n=1}^{N_3}sc_{mn}^{34}\sum_{a=0}^{b}\left[\frac{1}{2}l_{n,a}+\sum_{k=0}^{a-1}l_{n,k}\right]I_{ba}\left(s\left(R_{mn}^{34}/C\right)\right)\end{array}\right]=0
\end{array}\right.\,. \tag{32}$$

We note that, we can change the upper limit of the sum (30) and (31) form ∞ to “b” based on the orthogonality condition detailed in [14]:

$$I_{ba}(s\frac{R_{mn}^{ij}}{C}) = \left\langle \varphi_b(st), \varphi_a(s(t-\frac{R_{mn}^{ij}}{C})) \right\rangle$$
$$= \int_0^\infty \varphi_b(st)\varphi_a(s(t-\frac{R_{mn}^{ij}}{C}))d(st)$$
$$= \begin{cases} e^{-\frac{sR_{mn}}{2C}}\left[L_{b-a}(s\frac{R_{mn}}{C}) - L_{b-a-1}(s\frac{R_{mn}}{C})\right], \ a \le b \\ 0, \ a > b \end{cases} .$$

The scalar product of the field E_m^v (28) by the Laguerre function of order « b » is given by:

$$E_{b,m}^v = \int_0^\infty \varphi_b(st)E_m^v(t)d(st) . \tag{33}$$

In the system (32), we move the terms including $g_{n,b}^1$, $g_{n,b}^2$ and $l_{n,b}$, which is known for a<b to the right-hand side. Rewriting the resulting equations in a simple form, we have:

$$\sum_{n=1}^{N_1} A_{mn}^{11} g_{n,b}^1 + \sum_{n=1}^{N_3} B_{mn}^{31} l_{n,b} = E_{m,b}^1 + S_{m,b}^1 , \tag{34}$$

$$\sum_{n=1}^{N_2} A_{mn}^{22} g_{n,b}^2 + \sum_{n=1}^{N_3} B_{mn}^{32} l_{n,b} = E_{m,b}^2 + S_{m,b}^2 , \tag{35}$$

$$\sum_{n=1}^{N_1} A_{mn}^{13} g_{n,b}^1 + \sum_{n=1}^{N_2} A_{mn}^{23} g_{n,b}^2 + \sum_{n=1}^{N_3} B_{mn}^{33} l_{n,b} = S_{m,b}^3 , \tag{36}$$

$$\sum_{n=1}^{N_1} A_{mn}^{14} g_{n,b}^1 + \sum_{n=1}^{N_3} B_{mn}^{34} l_{n,b} = K_{m,b}^4 , \tag{37}$$

$$\sum_{n=1}^{N_2} A_{mn}^{24} g_{n,b}^2 + \sum_{n=1}^{N_3} B_{mn}^{34} l_{n,b} = H_{m,b}^4 . \tag{38}$$

The spatial matrices $\left(A^{ij}, B^{ij}\right)$ and the retarded terms $S_{m,b}^1$, $S_{m,b}^2$, $S_{m,b}^3$, $K_{m,b}^4$ and $H_{m,b}^4$ are presented in appendix.

Now, we write (34)-(38) in a matrix form:

$$\begin{bmatrix} [A^{11}] & [0] & [B^{31}] \\ [0] & [A^{22}] & [B^{32}] \\ [A^{13}] & [A^{23}] & [B^{33}] \\ [A^{14}] & [0] & [B^{34}] \\ [0] & [A^{24}] & [B^{34}] \end{bmatrix} \begin{bmatrix} g_b^1 \\ g_b^2 \\ l_b \end{bmatrix} = \begin{bmatrix} E_b^1 + S_b^1 \\ E_b^2 + S_b^2 \\ S_b^3 \\ K_b^4 \\ H_b^4 \end{bmatrix} . \tag{39}$$
$$\Leftrightarrow A * X = B$$

It is important to note that the matrix A is not a function of the degree of the temporal testing function “b”. Therefore, we obtain the unknown coefficients by solving (39) as increasing the degree of temporal testing functions. Consequently, we solve the problem only in space for each degree of the Laguerre function. Finally, the transient currents are calculated by:

$$J_i^j(t) = \frac{d}{dt}G_i^j(t) = s\sum_{a=0}^{A}\left[\frac{1}{2}g_{i,a}^j + \sum_{k=0}^{a-1} g_{i,k}^j\right]\varphi_a(st) , \tag{40}$$

$$M_i(t) = \frac{d}{dt}L_i(t) = s\sum_{a=0}^{A}\left[\frac{1}{2}l_{i,a} + \sum_{k=0}^{a-1} l_{i,k}\right]\varphi_a(st) , \tag{41}$$

where A is the maximum order of the Laguerre function [16].

III. NUMERICAL RESULTS

In this section, we present the different numerical results by applying the proposed formulation and we compared the latters with the results obtained by the B-Spline scheme, developed in [22]. Thus, we consider the structure shown in Fig. 6. Their related parameters are presented in Table 1. The space parameters N_i , $1 \le i \le 4$ are described in Table 2.

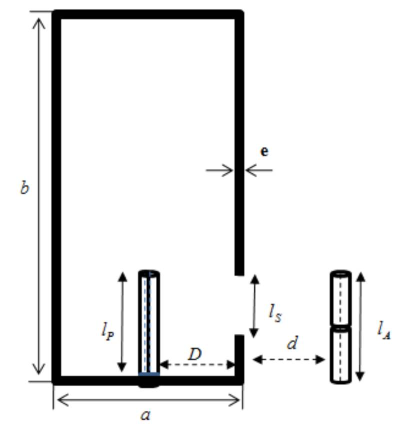

Fig. 6. Structure of the problem.

Table 1: Cavity parameters

Symbol	Quantity	Value
a	Cavity width	0.346λ m
b	Cavity length	0.692λ m
l_s	Slot length	0.048λ m
(x_s,y_s)	Center of slot	(0.346λ, 0.173λ)
l_P	Probe length	0.25λ m
(x_p,y_p)	Probe center	(0.172λ, 0)
l_A	Antenna length	0.25λ m
(x_A,y_A)	Position of antenna	(a+0. 172λ,0)
e	Thickness	10^{-5}

In this table, we used same parameters of the cavity presented in [2] at the resonance frequency of 1.9 GHz.

Table 2: Space parameters

Symbol	Quantity	Value
Δx	Space step	$2.73\ 10^{-4}$ m
Δy	Space step	$5.46\ 10^{-4}$ m
N_1	Number of antenna sub-domains	$l_A/\Delta y$
N_2	Number of probe sub-domains	$L_p/\Delta y$
N_3	Number of slot sub-domains	$L_s/\Delta y$
N_4	Number of cavity walls sub-domains	$(N_{4x},N_{4y})=(a/\Delta x,b/\Delta y)$

We assume that the probe (inside the cavity) is excited by the Gaussian pulse voltage generator $V(t)$ at the bottom. The antenna is also excited by $V(t)$ at its center. The source $V(t)$ is expressed by:

$$V(t) = V_0 e^{\left(-g^2(t-t_0)\right)}, \tag{42}$$

with parameters $V_0 = 1V$, $g = 10^8 s^{-1}$ and $t_0 = 10^{-8} s$. We suppose that the antenna and the probe have same length $\left(l_A = l_p\right)$ and same radius e.

The value of the time scale factor s is 2.10^9 and the number of Laguerre functions A is fixed at 80. The values of s and A are sufficient to get accurate solutions. In fact, the terms s and A are the Laguerre function parameters.

In order to verify the results, we apply the B-Spline scheme developed in [22]. In fact, for the two schemes (Laguerre and B-Spline), we consider the case when the two antennas are excited by (42). The transient responses of the structure are depicted in Fig. 7 and Fig. 8. Thus, we clearly observe the good agreement between the results obtained by the two schemes.

Consequently, we apply the Laguerre scheme developed in this paper to study the coupling between the components of the designed communication system. This scheme is unconditionally stable. The space and the time steps are not related as the most temporal techniques (FDTD, TLM, MOT). We obtain stable and accurate solutions.

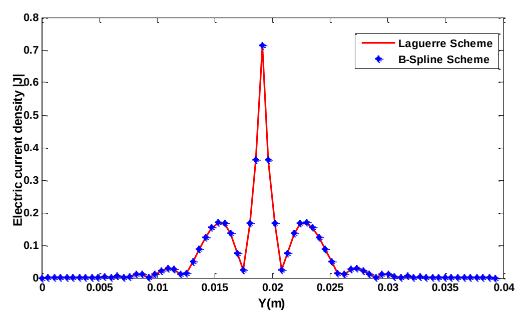

(a)

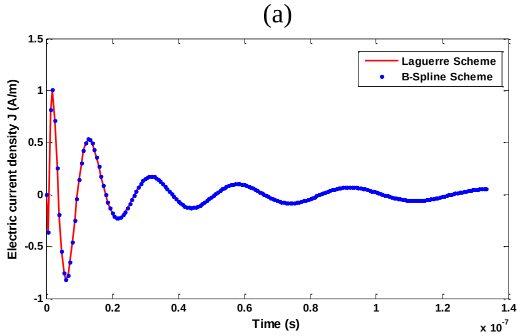

(b)

Fig. 7. The transient response of the antenna: (a) the normalized electric current density at the instant t=1.33*10^{-9} s, and (b) transient electric current density at the center of antenna.

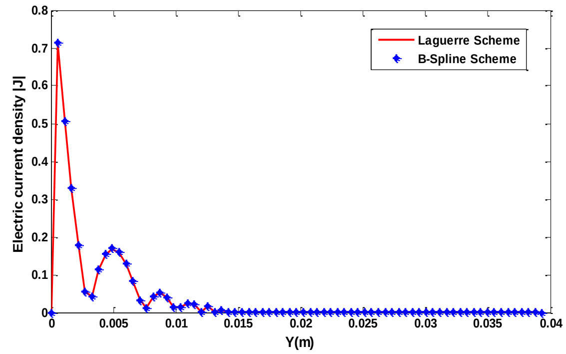

(a)

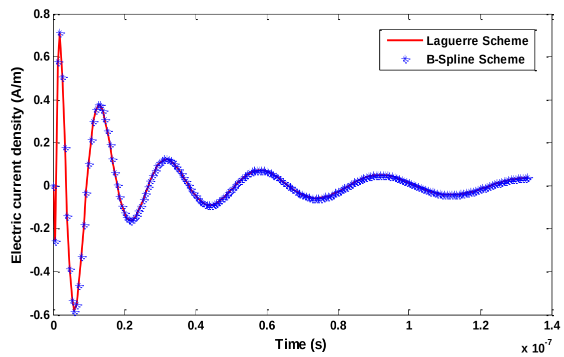

(b)

Fig. 8. The transient response of the probe: (a) the normalized electric current density at the instant t=1.33*10^{-9} s, and (b) transient electric current density at the top of the probe.

A. Electric and magnetic currents distributions

In order to describe the transient behaviors of the structure, three cases are considered:

- The antenna and the probe are both excited.
- Only the antenna is excited.
- Only the probe is excited.

The transient responses are determined at the center of antenna, at the bottom of probe and the center of slot.

Figure 9 shows the space distribution of electric current density of the antenna. It is obvious that the peak of the electric current occurred at the center point as expected for the case when the antenna is excited. But when the antenna is unexcited, the current vanish. The transient response plotted, in Fig. 10, at the center of the antenna confirms the latter interpretation.

The transient response of the probe is shown in Fig. 11 and Fig. 12; we should note that the peak of electric current occurred at the feed point and the amplitude vanish when the probe is unexcited. The miniature curve in Fig. 11 presents the coupling effect when the probe is unexcited and the antenna is excited.

The magnetic current density is presented in space and time when the antenna and the probe are both excited in Fig. 13.

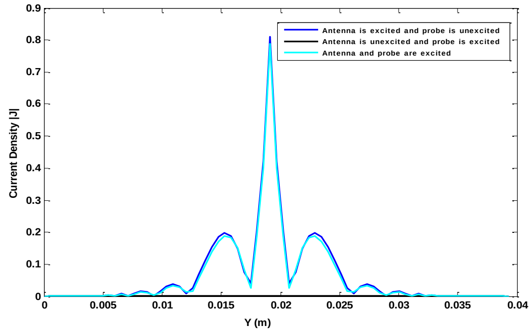

Fig. 9. The normalized electric current density of the antenna at the instant t=1.33*10^{-9} s.

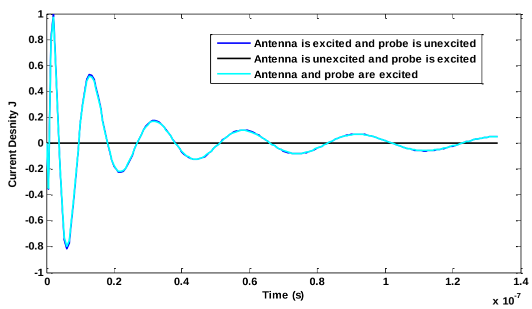

Fig. 10. Transient electric current density at the center of antenna.

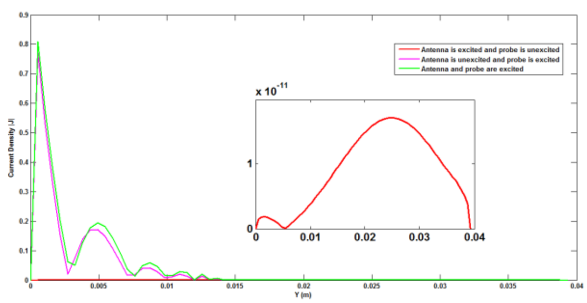

Fig. 11. The normalized electric current density of the probe at the instant t=1.33*10^{-9} s.

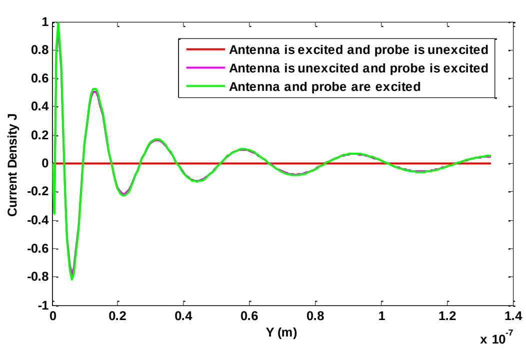

Fig. 12. Transient electric current density at the top of the probe.

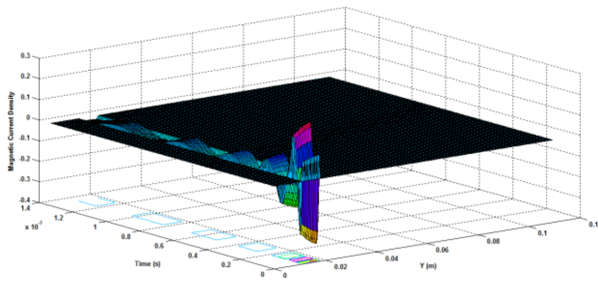

Fig. 13. The normalized magnetic current density at the slot when the antenna and the probe are excited.

B. Study of coupling through the slot depending on separate distances d and D

In order to study the Antenna-Slot coupling and Probe-Slot coupling, we consider four separate distances:

$$d = D = d_1 = 0.018 \times \mathrm{a}, \quad d = D = d_2 = 0.146 \times \mathrm{a},$$

$$d = D = d_3 = 0.274 \times \mathrm{a}, \quad d = D = d_4 = 0.875 \times \mathrm{a}.$$

Starting by the study of the coupling effect of antenna and cavity as function of different distances d (the value of D is fixed in Table 1).

Figure 14 represents the theoretical coupling between the antenna and the slot calculated via the matrix Aij. It is clearly that the coupling vanish from $d_c = 0.005\,\mathrm{m}$. The transient magnetic current plotted in Fig. 15 for different separated distances d confirms the theoretical results. We note that, if $d > d_c$, the magnetic current does not change.

To study the coupling between the cavity and the probe, we vary the separate distances D and we fix the distance d (Table 1).

The coupling vanishes from $d_c = 0.008\,\mathrm{m}$ as presented in Fig. 16. This result is detailed in Fig. 17; but for the distance d_4, the current amplitude is non-zero and a low variation is detected. This variation is due to the effect of the cavity walls which amplified the currents inside the cavity.

Also, lower values of the electric current at the probe and the magnetic current at the slot are observed when the cavity size becomes larger (Fig. 18).

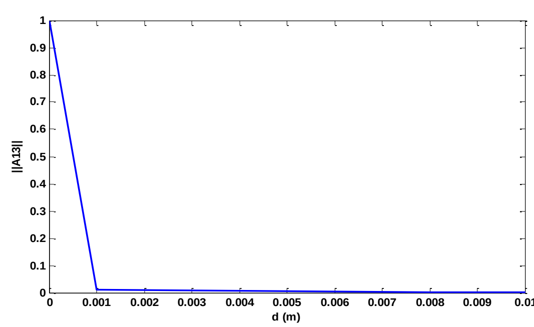

Fig. 14. Matrix coupling antenna-slot.

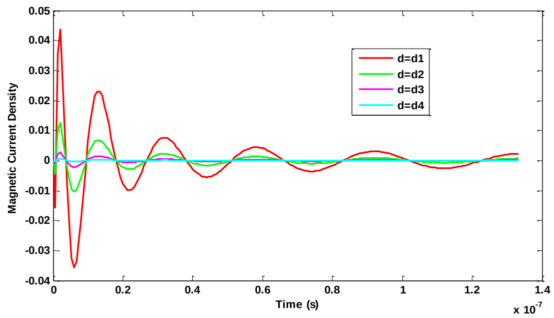

Fig. 15. Transient magnetic current at the center of the slot for various distances d.

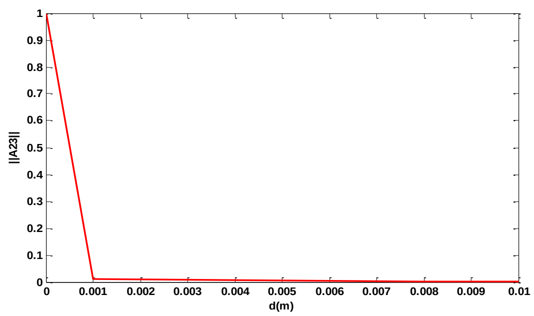

Fig. 16. Matrix coupling between probe-slot.

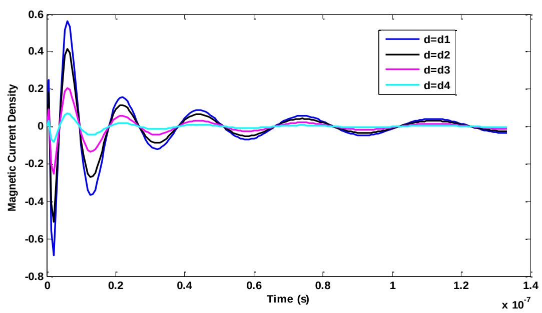

Fig. 17. Transient magnetic current at the center of the slot for various distances D.

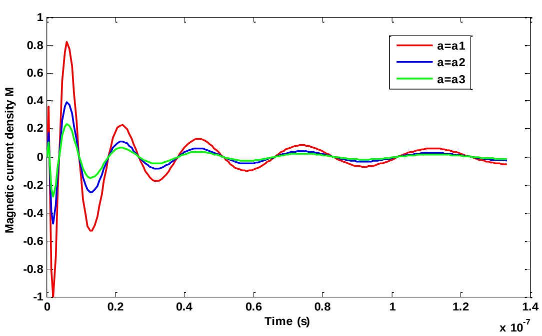

Fig. 18. Transient magnetic current at the center of slot for various cavity widths a=a1=0.55*λ, a=a2=0.69*λ and a=a3=0.75*λ.

C. Study of coupling through the slot depending on slot length

It is very important to study the coupling taking into account the length of the slot. Therefore, we vary the latter parameter and two cases can be defined. One hand, when only the probe is excited, the transient current density at the top of the antenna as shown in Fig. 19. The amplitude becomes more important when the length of the slot is increased. This result is confirmed by this shown in Fig. 10.

On the other hand, when only the antenna is excited, the transient current density at the top of probe for the shorter slot is lower than the longer ones, as depicted in Fig. 20.

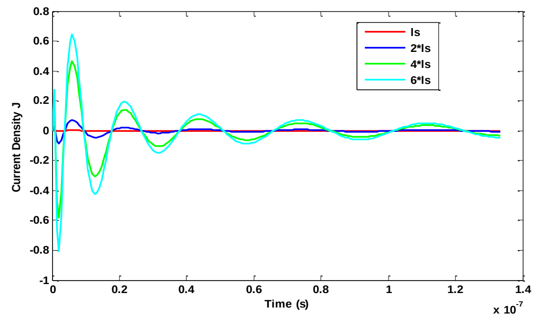

Fig. 19. Transient current at the top of the antenna when the probe is excited and for various lengths of slot.

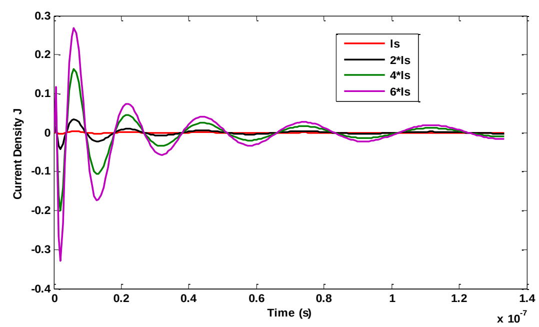

Fig. 20. Transient current at the top of the probe when the antenna is excited and for various lengths of slot.

IV. CONCLUSIONS

The transient behaviors of communication system composed on rectangular cavity containing an interior scatterer coupled to an external scatterer through a slot were studied. A 2-D numerical time domain formulation based on the combination of the equivalence principle and the MoM has been successfully developed and applied to the designed system.

The physical coupling effects between the components of the system through the slot have been provided depending on the separate distances and the lengths of the slot. Stable and accurate results have been found mainly with electric and magnetic currents responses.

This formulation can be extended to 3-D and applied for many complex structures.

APPENDIX

The spatial matrices A^{ij}_{mn} and B^{ij}_{mn} can be defined as:

$$A^{ij}_{mn}=\left[-s^2\frac{\mu a^{ij}_{mn}}{4}+\frac{b^{ij}_{mn}}{\varepsilon}\right]I_{bb}\left(s\left(R^{ij}_{mn}/C\right)\right),$$

$$B^{ij}_{mn}=\pm s\,\frac{c^{ij}_{mn}}{2}\,I_{bb}\left(s\left(R^{ij}_{mn}/C\right)\right),$$

where

$$I_{bb}\left(s\left(R^{ij}_{mn}/C\right)\right)=e^{-\frac{s}{2}\left(R^{ij}_{mn}/C\right)}.$$

The retarded terms takes the following forms:

$$S^{1}_{m,b}=-\begin{bmatrix}-s^2\mu\sum_{n=1}^{N_1}a^{11}_{mn}\sum_{k=0}^{b-1}(b-k)g^{1}_{n,k}\,I_{bb}(s(R^{11}_{mn}/C))\\-s^2\mu\sum_{n=1}^{N_1}a^{11}_{mn}\sum_{a=0}^{b-1}\left[\frac{1}{4}g^{1}_{n,a}+\sum_{k=0}^{a-1}(a-k)g^{1}_{n,k}\right]I_{ba}(s(R^{11}_{mn}/C))\\+\frac{1}{\varepsilon}\sum_{n=1}^{N_1}b^{11}_{mn}\sum_{a=0}^{b-1}g^{1}_{n,a}\,I_{ba}(s(R^{11}_{mn}/C))\\-\sum_{n=1}^{N_3}sc^{13}_{mn}\sum_{k=0}^{b-1}l_{n,k}I_{bb}(s(R^{13}_{mn}/C))\\-\sum_{n=1}^{N_3}sc^{13}_{mn}\sum_{a=0}^{b-1}\left[\frac{1}{2}l_{n,a}+\sum_{k=0}^{a-1}l_{n,k}\right]I_{ba}(s(R^{13}_{mn}/C))\end{bmatrix},$$

$$S^{2}_{m,b}=-\begin{bmatrix}-s^2\mu\sum_{n=1}^{N_2}a^{22}_{mn}\sum_{k=0}^{b-1}(b-k)g^{2}_{n,k}\,I_{bb}(s(R^{22}_{mn}/C))\\-s^2\mu\sum_{n=1}^{N_2}a^{22}_{mn}\sum_{a=0}^{b-1}\left[\frac{1}{4}g^{2}_{n,a}+\sum_{k=0}^{a-1}(a-k)g^{2}_{n,k}\right]I_{ba}(s(R^{22}_{mn}/C))\\+\frac{1}{\varepsilon}\sum_{n=1}^{N_2}b^{22}_{mn}\sum_{a=0}^{b-1}g^{2}_{n,a}\,I_{ba}(s(R^{22}_{mn}/C))\\+\sum_{n=1}^{N_3}sc^{23}_{mn}\sum_{k=0}^{b-1}l_{n,k}I_{bb}(s(R^{23}_{mn}/C))\\+\sum_{n=1}^{N_3}sc^{23}_{mn}\sum_{a=0}^{b-1}\left[\frac{1}{2}l_{n,a}+\sum_{k=0}^{a-1}l_{n,k}\right]I_{ba}(s(R^{23}_{mn}/C))\end{bmatrix},$$

$$S^{3}_{m,b}=-\begin{bmatrix}\begin{bmatrix}-s^2\mu\sum_{n=1}^{N_1}a^{13}_{mn}\sum_{k=0}^{b-1}(b-k)g^{1}_{n,k}\,I_{bb}(s(R^{13}_{mn}/C))\\-s^2\mu\sum_{n=1}^{N_1}a^{13}_{mn}\sum_{a=0}^{b-1}\left[\frac{1}{4}g^{1}_{n,a}+\sum_{k=0}^{a-1}(a-k)g^{1}_{n,k}\right]I_{ba}(s(R^{13}_{mn}/C))\\+\frac{1}{\varepsilon}\sum_{n=1}^{N_1}b^{13}_{mn}\sum_{a=0}^{b-1}g^{1}_{n,a}\,I_{ba}(s(R^{13}_{mn}/C))\end{bmatrix}\\+\begin{bmatrix}-s^2\mu\sum_{n=1}^{N_2}a^{23}_{mn}\sum_{k=0}^{b-1}(b-k)g^{2}_{n,k}\,I_{bb}(s(R^{23}_{mn}/C))\\-s^2\mu\sum_{n=1}^{N_2}a^{23}_{mn}\sum_{a=0}^{b-1}\left[\frac{1}{4}g^{2}_{n,a}+\sum_{k=0}^{a-1}(a-k)g^{2}_{n,k}\right]I_{ba}(s(R^{23}_{mn}/C))\\+\frac{1}{\varepsilon}\sum_{n=1}^{N_2}b^{23}_{mn}\sum_{a=0}^{b-1}g^{2}_{n,a}\,I_{ba}(s(R^{23}_{mn}/C))\end{bmatrix}\\-2\begin{bmatrix}\sum_{n=1}^{N_3}sc^{33}_{mn}\sum_{k=0}^{b-1}l_{n,k}I_{bb}(s(R^{33}_{mn}/C))\\+\sum_{n=1}^{N_3}sc^{33}_{mn}\sum_{a=0}^{b-1}\left[\frac{1}{2}l_{n,a}+\sum_{k=0}^{a-1}l_{n,k}\right]I_{ba}(s(R^{33}_{mn}/C))\end{bmatrix}\end{bmatrix},$$

$$K^{4}_{m,b}=-\begin{bmatrix}-s^2\mu\sum_{n=1}^{N_1}a^{14}_{mn}\sum_{k=0}^{b-1}(b-k)g^{1}_{n,k}\,I_{bb}(s(R^{14}_{mn}/C))\\-s^2\mu\sum_{n=1}^{N_1}a^{14}_{mn}\sum_{a=0}^{b-1}\left[\frac{1}{4}g^{1}_{n,a}+\sum_{k=0}^{a-1}(a-k)g^{1}_{n,k}\right]I_{ba}(s(R^{14}_{mn}/C))\\+\frac{1}{\varepsilon}\sum_{n=1}^{N_1}b^{14}_{mn}\sum_{a=0}^{b-1}g^{1}_{n,a}\,I_{ba}(s(R^{14}_{mn}/C))\\-\sum_{n=1}^{N_3}sc^{34}_{mn}\sum_{k=0}^{b-1}l_{n,k}I_{bb}(s(R^{34}_{mn}/C))\\-\sum_{n=1}^{N_3}sc^{34}_{mn}\sum_{a=0}^{b-1}\left[\frac{1}{2}l_{n,a}+\sum_{k=0}^{a-1}l_{n,k}\right]I_{ba}(s(R^{34}_{mn}/C))\end{bmatrix},$$

$$H^{4}_{m,b}=-\begin{bmatrix}-s^2\mu\sum_{n=1}^{N_2}a^{24}_{mn}\sum_{k=0}^{b-1}(b-k)g^{2}_{n,k}\,I_{bb}(s(R^{24}_{mn}/C))\\-s^2\mu\sum_{n=1}^{N_2}a^{24}_{mn}\sum_{a=0}^{b-1}\left[\frac{1}{4}g^{2}_{n,a}+\sum_{k=0}^{a-1}(a-k)g^{2}_{n,k}\right]I_{ba}(s(R^{24}_{mn}/C))\\+\frac{1}{\varepsilon}\sum_{n=1}^{N_2}b^{24}_{mn}\sum_{a=0}^{b-1}g^{2}_{n,a}\,I_{ba}(s(R^{24}_{mn}/C))\\+\sum_{n=1}^{N_3}sc^{34}_{mn}\sum_{k=0}^{b-1}l_{n,k}I_{bb}(s(R^{34}_{mn}/C))\\+\sum_{n=1}^{N_3}sc^{34}_{mn}\sum_{a=0}^{b-1}\left[\frac{1}{2}l_{n,a}+\sum_{k=0}^{a-1}l_{n,k}\right]I_{ba}(s(R^{34}_{mn}/C))\end{bmatrix}.$$

REFERENCES

[1] J. Hirokawa, A. Hiroyuki, and G. Naohisa, "Cavity-backed wide slot antenna," *IEE Proceedings H (Microwaves, Antennas and Propagation), IET Digital Library*, vol. 136, no. 1, pp. 29-33, February 1989.

[2] T. Lertwiriyaprapa, C. Phongcharoenpanich, S. Kosulvit, and M. Krairiksh, "Analysis of impedance characteristics of a probe fed rectangular cavity-backed slot antenna," *IEEE Antennas and Propagation Society International Symposium, IEEE; 1999*, vol. 1, pp. 576-579, July 2001.

[3] A. Hadidi and M. Hamid, "Aperture field and circuit parameters of cavity-backed slot radiator," *IEE Proceedings H (Microwaves, Antennas and Propagation), IET Digital Library*, vol. 136, no. 2, pp. 139-146, April 1989.

[4] S. Eardprab and C. Phongcharoenpanich, "Diffraction on a rectangular aperture antenna mounted on an open-ended cavity excited by a probe," *Communications and Information Technologies, 2006, ISCIT'06, International Symposium on IEEE*, pp. 779-782, October 2006.

[5] M. V. Nesterenko, V. A. Katrich, D. Y. Penkin, S. L. Berdnik, and V. I. Kijko, "Electromagnetic waves scattering and radiation by vibrator-slot structure in a rectangular waveguide," *Progress In Electromagnetics Research M*, vol. 24, pp. 69-84, 2012.

[6] D. B. Wright, R. Lee, and D. G. Dudley, "Transient current on a wire penetrating a cavity-backed circular aperture in an infinite screen," *Electromagnetic Compatibility, IEEE Transactions on*, vol. 32, no. 3, pp. 197-204, August 1990.

[7] M. Bailin and D. K. Cheng, "Transient electromagnetic fields coupled into a conducting cavity through a slot aperture," *Scientia Sinica Series Mathematical Physical Technical Sciences*, vol. 27, pp. 775-784, July 1984.

[8] N. J. Šekeljić, A. Manić, B. M. Notaroš, and M. M. Ilić, "Transient analysis of 3D waveguides using double-higher-order time-domain finite element method," *AP-S*, 2013.

[9] Y. Zhang and M. H. Bakr, "Transient adjoint sensitivity analysis exploiting FDTD," *Microwave Symposium Digest (MTT), 2012 IEEE MTT-S*

International, IEEE, pp. 1-3, June 2012.
[10] M. Omiya, T. Hikage, N. Ohno, K. Horiguchi, and K. Itoh, "Design of cavity-backed slot antennas using the finite-difference time-domain technique," *Antennas and Propagation, IEEE Transactions on*, vol. 46, no. 12, pp. 1853-1858, December 1998.
[11] Z. Chen and S. Luo, "Generalization of the finite-difference-based time-domain methods using the method of moments," *Antennas and Propagation, IEEE Transactions on*, vol. 54, no. 9, pp. 2515-2524, September 2006.
[12] W. C. Gibson, *The Method of Moments in Electromagnetic*. CRC Press, US, 2008.
[13] M. Coghetto and C. Offelli, "A procedure for the evaluation of radiated emissions from polygonal wires with the method of moments," *Electromagnetic Compatibility, 1999 IEEE International Symposium on*, vol. 1, pp. 334-339, 1999.
[14] B. H. Jung, Y. S. Chung, and T. K. Sarkar, "Time-domain EFIE, MFIE, and CFIE formulations using Laguerre polynomials as temporal basis functions for the analysis of transient scattering from arbitrary shaped conducting structures," *Progress In Electromagnetics Research*, vol. 39, pp. 1-45, 2003.
[15] B. H. Jung, T. K. Sarkar, Y. S. Chung, M. Salazar-Palma, Z. Ji, S. Jang, and K. Kim, "Transient electromagnetic scattering from dielectric objects using the electric field integral equation with Laguerre polynomials as temporal basis functions," *Antennas and Propagation, IEEE Transactions on*, vol. 52, no. 9, pp. 2329-2340, 2004.
[16] J. Láčík and Z. Raida, "Modeling microwave structure in time domain using Laguerre polynomials," *Radioengineering*, vol. 15, no. 3, pp. 1-9, September 2006.
[17] Z. Mei, Y. Zhang, X. Zhao, B. H. Jung, T. K. Sarkar, and M. Salazar-Palma, "Choice of the scaling factor in a marching-on-in-degree time domain technique based on the associated Laguerre functions," *Antennas and Propagation, IEEE Transactions on*, vol. 60, no. 9, pp. 4463-4467, September 2012.
[18] X. Guan, S. Wang, Y. Su, and J. Mao, "A method to reduce the oscillations of solution of time domain integral equation using Laguerre polynomials," *PIERS Online*, vol. 3, no. 6, 2007.
[19] K. M. Chen, "A mathematical formulation of the equivalence principle," *IEEE Transactions on Microwave Theory and Techniques*, vol. 37, no. 10, pp. 1576-1581, October 1989.
[20] A. J. Booysen, "Aperture theory and the equivalence principle," *Antennas and Propagation Magazine, IEEE*, vol. 45, no. 3, pp. 29-40, 2003.
[21] A. J. Booysen, "Aperture theory and the equivalence theorem," *Antennas and Propagation Society International Symposium, 1999, IEEE*, vol. 2, pp. 1258-1261, July 1999.
[22] D. Omri and T. Aguili, "Time-domain techniques for electromagnetic coupling analysis of transient excitations of rectangular cavity through slot," *Journal of Electromagnetic Waves and Applications, 2015, IEEE*, vol. 29, pp. 1297-1316, April 2015.

Dorsaf Omri received the Master degree in Mathematics from Faculty of Mathematical, Physical and Natural Sciences of Tunis and the M.Sc. degree in Communication Technologies from the National Engineering School of Tunis. In 2010, she received the Ph.D. degree in Information and Communication Technologies and Sciences from the National Engineering School of Tunis. Her research interest is in the field of electromagnetic modeling and time domain numerical methods.

Taoufik Aguili received his Engineering degree in Electrical Engineering and his Ph.D. degree in Telecommunications from INSA, France. He is working as Professor at the National Engineering School of Tunis (ENIT). His research activities include electromagnetic microwave circuits modeling and analysis of scattering and propagation phenomena in free space.

Ultra-Wideband Balanced Bandpass Filters Based on Transversal Signal-Interference Concepts

Chaoying Zhao [1], Wenjie Feng [1*], Yuanchuan Li [2,3], and Wenquan Che [1]

[1] Department of Communication Engineering, Nanjing University of Science & Technology, Nanjing, China
[2] School of Electronic and Information Engineering, South China University of Technology, Guangzhou, China
[3] State Key Laboratory of Millimeter Waves, Southeast University, Nanjing, China
fengwenjie1985@163.com

Abstract **─** Two ultra-wideband balanced bandpass filters based on transversal signal-interference concepts are proposed in this paper. By employing the two structures: microstrip/slotline transition, and quarter-wavelength shorted coupler lines, 180° phase shift can be easily implemented for each design. In addition, due to the different transmission paths, wideband common mode rejection and differential mode transmission bandwidth can be achieved. Two balanced filters centered at 3 GHz are calculated, fabricated and measured successfully. For the differential mode, the 3-dB fractional bandwidths are 102% from 1.47 GHz to 4.53 GHz and 103% from 1.52 GHz to 4.61 GHz, respectively, and the return loss are both greater than 20 dB. For the common mode, signals are suppressed below -20 dB and -15 dB over the whole frequency band.

Index Terms **─** Balanced filter, differential/common mode, shorted stubs, Ultra-wideband.

I. INTRODUCTION

RF circuits and systems are becoming a complicated closer space with more functions. So, the electromagnetic interference between nodes at different dielectric layers and mutual link in communication systems to be eliminated is indispensable. Compared to single-ended technology, balanced circuits have advantages of wideband common mode rejection capability which is beneficial to immunity to the environmental noise and dynamic range.

As a high performance balanced circuit, only the differential mode signals pass through in the desired frequency band, while the common mode signals must be all-stop. In the past few years, different balanced filters for single-band, dual-band and wideband were proposed using different ways [1-8]. Chen et al. designed differential filter firstly with wideband common-mode suppression exploiting microstrip and CPW transition [1]-[3]. However, the differential-mode width increase difficulty and the insertion loss is a little big. Cascaded branch-line was used to design wideband balanced filters as well [4]-[5]. However, these filters implied larger circuit size, and their out-of-band common mode suppression is not so good. Another way to get wideband balanced filter is using T-shaped structures [6]. Their main advantage is the high selectivity of the passband, but the suppression of common mode is always unsatisfactory. As a very convenient balanced transmission line for balanced circuits, DSPSL can be used to design ideal phase shifter for balanced filters [7]-[8]. They show good performance for the differential mode and common mode, but the problem of heat dissipation remained unsolved. In [9], a low profile balanced tunable BPF using λ/2 resonator has been presented. The common mode suppression can be kept at a high level by adding a varactor. In [10], it is a balanced SIW BPF which is simplified though designing a 2-port filter with high performance. But [9] and [10] both have the defect of differential-mode bandwidth.

II. ANALYSIS OF PROPOSED BALANCED FILTERS

In this part, the proposed two balanced filters based on transversal signal-interference concepts are illustrated detailedly. Firstly, we use the differential mode and common mode equivalent circuits to analyze their performance. And then, in *Part C*, simulated results of the two balanced filters are presented.

A. Balanced filter analysis with microstrip/slotline transition

The ideal circuit of the balanced filter with two ideal 180^o phase shifter is shown in Fig. 1 (a). The transformer works as a phase shifter. We see that it is a central symmetric structure of all components. Specifically, there are two shunted $\lambda/4$ shorted lines loaded at four arms each, and the characteristic impedances of the input ports and output ports microstrip lines are all Z_0 = 50 Ω. For the purpose of elaborate description, the equivalent circuits of the differential mode and common mode are

Submitted On: July 11, 2016
Accepted On: August 22, 2016

illustrated in Figs. 1 (b) and (c).

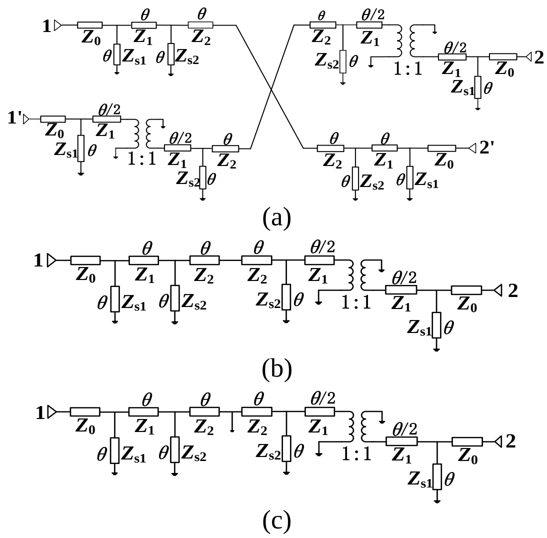

Fig. 1. (a) The ideal circuit of the balanced filter with microstrip/slotline transition, (b) equivalent circuit for the differential mode, and (c) equivalent circuit for the common mode.

When ports 1 and 1′ are excited by differential mode signals, out-phase signals will be changed into in-phase signals after one kind phase of the signals pass through the phase converter. We can obtain θ_{12} (f_0) = 360°, $\theta_{1'2}$ (f_0) = 360° (θ = 90° at the center frequency f_0), then they are combined at the center point and propagate to output ports. The differential-mode circuit illustrated in Fig. 1 (b) shows that it is half of the circuit in Fig. 1 (a) due to the symmetrical structure. Besides, a virtual open appears at the joint of four arms. This means that the differential-mode circuit comes out a typical bandpass filter. The *ABCD* matrix of the transmission lines and the shorted lines are:

$$M_{s1} = \begin{bmatrix} 1 & 0 \\ 1/jZ_{s1}\tan\theta & 1 \end{bmatrix}, \quad (1)$$

$$M_{s2} = \begin{bmatrix} 1 & 0 \\ 1/jZ_{s2}\tan\theta & 1 \end{bmatrix}, \quad (2)$$

$$M_1 = \begin{bmatrix} \cos\theta & jZ_1\sin\theta \\ j\sin\theta/Z_1 & \cos\theta \end{bmatrix}, \quad (3)$$

$$M_2 = \begin{bmatrix} \cos 2\theta & jZ_2\sin 2\theta \\ j\sin 2\theta/Z_2 & \cos 2\theta \end{bmatrix}, \quad (4)$$

$$M_{1/2} = \begin{bmatrix} \cos(\theta/2) & jZ_1\sin(\theta/2) \\ j\sin(\theta/2)/Z_1 & \cos(\theta/2) \end{bmatrix}, \quad (5)$$

$$M_t = \begin{bmatrix} -1 & 0 \\ 0 & -1 \end{bmatrix}. \quad (6)$$

From port 1 to port 2, the *ABCD* parameter matrix can be defined as $M_{s1}\times M_1\times M_{s2}\times M_2\times M_{s2}\times M_{1/2}\times M_t\times M_{1/2}\times M_{s1}$ derived from Equations (1) to (6). Then we can get the frequency response form *ABCD*- to *Y*-parameter conversions. The poles, the insertion loss and bandwidth can be controlled by changing the transmission line impedances.

The simulated frequency responses of Fig. 1 (b) are shown in Fig. 2 (Simulated with ANSYS Designer v3.0). We can find that the transmission zero at both sides of the passband will not change with the characteristic impedance Z_{s1} and Z_{s2}. But Z_{s1} increased can improve performance of $|S_{dd11}|$ obviously in the passband. Without the two shorted lines of Z_{s1}, transmission poles decrease to three. As to Z_{s2}, it influences the bandwidth deeply, bigger Z_{s2} and bandwidth wider. But when it comes to the return loss in-band, the performance shows better first and then becomes worse with Z_{s2} increased. Although the bandwidth is much bigger, $|S_{dd11}|$ will down to 10 dB.

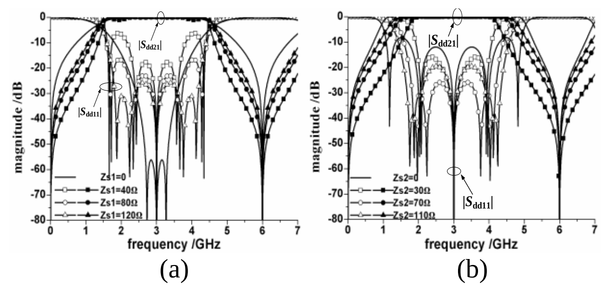

Fig. 2. Simulated frequency responses of Fig. 1 (b): (a) $|S_{cc11}|$&$|S_{cc21}|$, Z_1 = 50 Ω, Z_2 = 70 Ω, Z_{s2} = 70 Ω, and (b) $|S_{cc11}|$&$|S_{cc21}|$, Z_1 = 50 Ω, Z_2 = 70 Ω, Z_{s1} = 120 Ω.

When ports 1 and 1′ are excited by common mode signals, similarly, in-phase signals will be changed into out-phase signals after one kind phase of the signals pass through the phase converter. That means input signals will be cancelled out at the center point, due to θ_{12} (f_0) = 180° and $\theta_{1'2}$ (f_0) = 360° (θ = 90° at the center frequency f_0). In this case, the common mode circuit in Fig. 1 (c) is generated and there is a virtual short appears at the joint of four arms. Because common mode signals canceled at the joint, the circuit presents a stopband filter over the whole frequency band. So common mode signals suppression in/out-of-band for the differential mode is easy to achieve.

Figures 3 (a)-(b) plot the simulated frequency responses of Fig. 1 (c). As the two plots show that $|S_{cc11}|$ is almost steady over whole frequency band despite the characteristic impedance Z_{s1} and Z_{s2} change. But $|S_{cc21}|$ increased follows Z_{s1} or Z_{s2} increased. The performance becomes worse. Moreover, without the two shorted lines of Z_{s1} or Z_{s2}, $|S_{cc11}|$ and $|S_{cc21}|$ becomes worse than they existed.

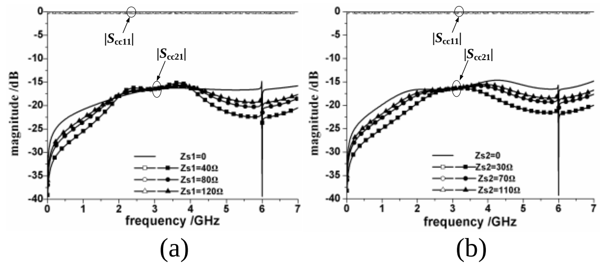

Fig. 3. Simulated frequency responses of Fig. 1 (c): (a) $|S_{cc11}|$&$|S_{cc21}|$, $Z_1 = 50\ \Omega$, $Z_2 = 70\ \Omega$, $Z_{s2} = 70\ \Omega$, and (b) $|S_{cc11}|$&$|S_{cc21}|$, $Z_1 = 50\ \Omega$, $Z_2 = 70\ \Omega$, $Z_{s1} = 120$.

B. Balanced filter analysis with λ/4 shorted coupled line

Figure 4 (a) shows ideal circuit of the balanced filter, which is a central symmetric structure of all components. Figures 4 (b) and (c) are the equivalent differential/ common mode circuits to be analyzed accordingly. We use $\lambda/4$ shorted coupled line in this circuit and its equivalent circuit model gives in Fig. 5. The *ABCD* matrix can be written as follow:

$$\begin{bmatrix} A & B \\ C & D \end{bmatrix} = \begin{bmatrix} 1 & 0 \\ Y_{11}+Y_{12} & 1 \end{bmatrix} \begin{bmatrix} 1 & -Y_{12} \\ 0 & 1 \end{bmatrix} \begin{bmatrix} 1 & 0 \\ Y_{22}+Y_{12} & 1 \end{bmatrix} = \begin{bmatrix} -1 & 0 \\ 0 & -1 \end{bmatrix} \begin{bmatrix} Y_{11}/Y_{12} & 1/Y_{12} \\ (Y_{11}^2-Y_{12}^2)/Y_{12} & Y_{11}/Y_{12} \end{bmatrix}, \quad (7)$$

$$\begin{bmatrix} -1 & 0 \\ 0 & -1 \end{bmatrix} = \begin{bmatrix} \cos(180^0) & jZ\sin(180^0) \\ jY\sin(180^0) & \cos(180^0) \end{bmatrix}, \quad (8)$$

$$Y_{11} = Y_{22} = -j(Y_{oo}+Y_{oe})/(2\cdot\tan\theta_1), \quad (9)$$

$$Y_{12} = -j(Y_{oo}-Y_{oe})/(2\cdot\sin\theta_1). \quad (10)$$

From the upper Equations from (7) to (10), we can draw a conclusion that the two $\lambda/4$ shorted coupled lines are acted as 180° phase shifter and will not change with frequency. The characteristic impedances of the input ports and output ports microstrip lines are all $Z_0 = 50\ \Omega$.

As discussed in *Part A*, a virtual open appears at the joint of four arms for differential-mode circuit in Fig. 4 (b). Due to the signals combined at the center point, it comes out a typical bandpass filter when ports 1 and 1′ are excited by differential mode signals. Furthermore, a virtual short appears at the joint of four arms for common-mode circuit in Fig. 4 (c). Due to the signals canceled at the center point, it comes out a stopband filter when ports 1 and 1′ are excited by common mode signals.

Figures 6 (a) and (b) are the simulation results at different value of k. k is coupling coefficient of the two shorted coupler line. It is apparent that the differential mode and common mode performance show better with k increases. But there is a problem that big coupling coefficient is hard to realize in monolayer PCB microstrip line structure. In order to get tight coupling, we introduce a slot under the coupled lines [12]. For a simple coupled line, even-mode impedance is mainly depend on capacitance of metal strips to ground, while odd-mode impedance is depend on capacitance of metal strips and coupled lines to ground. So even-mode and odd-mode capacitance will decrease with the slot at the same time. In addition, placing a rectangular conductor inside the slot can make sure that odd-mode decrease in company with even-mode.

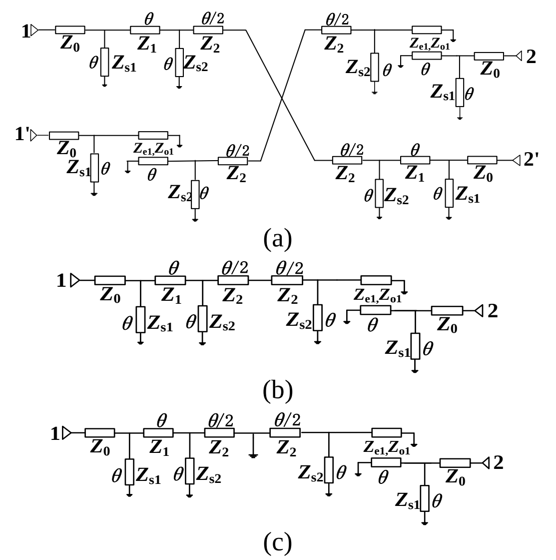

Fig. 4. (a) The ideal circuit of the balanced filter with $\lambda/4$ shorted coupled line, (b) equivalent circuit for the differential mode, and (c) equivalent circuit for the common mode.

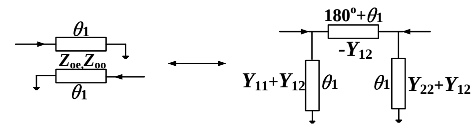

Fig. 5. Equivalent circuit model of the $\lambda/4$ shorted coupled line.

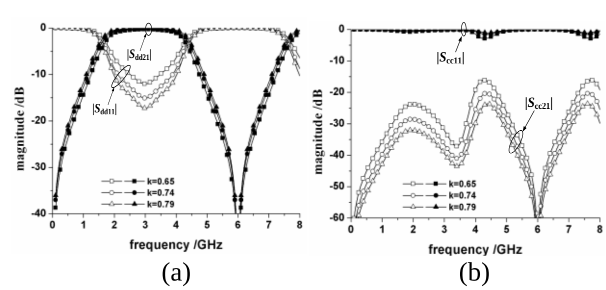

Fig. 6. Simulated frequency responses of Figs. 4 (b) and (c): (a) $|S_{dd21}|$&$|S_{dd11}|$, $Z_1 = 55\ \Omega$, $Z_2 = 65\ \Omega$, $Z_{s1} = 120\ \Omega$, $Z_{s2} = 120\ \Omega$, and (b) $S_{cc21}|$&$|S_{cc11}|$, $Z_1 = 55\ \Omega$, $Z_2 = 65\ \Omega$, $Z_{s1} = 120\ \Omega$, $Z_{s2} = 120\ \Omega$.

C. Proposed to balanced bandpass filters

Based on the above discussions and the simulated results in *Part A and B* of *Section II*, the 3-dB bandwidths of the two balanced filters are chosen as 102% and 103%, and the final parameters in Figs. 1, 4 are: Z_0 = 50 Ω, Z_1 = 50 Ω, Z_2 = 90 Ω, Z_{s1} = 114 Ω, Z_{s2} = 104 Ω; Z_0 = 50 Ω, Z_1 = 45 Ω, Z_2 = 60 Ω, Z_{s1} = 112 Ω, Z_{s2} = 112 Ω, Z_{e1} = 200 Ω, Z_{o1} = 30 Ω. Figure 7 presents the geometries of the two balanced filters (78.94 mm × 56.83 mm, 66.2 mm × 37.28 mm) are: l_1 = 16.85 mm, l_2 = 17.08 mm, l_3 = 9.93 mm, s_1 = 17.65 mm, s_2 = 18.42 mm, g_1 = 0.3 mm, lg = 7 mm, a = 9.5 mm, b = 2 mm, w_0 = 1.36 mm, w_1 = 1.36 mm, w_2 = 0.23 mm, w_3 = 0. 3 mm, w_4 = 0.44 mm, d_1 = 0.6 mm, d_2 = 1 mm, d_3 = 10 mm; l_1 = 16.7 mm, l_2 = 17.7 mm, l_3 = 8.05 mm, s = 0.15 mm, s_1 = 16.7 mm, s_2 = 16.7 mm, q_1 = 7.95 mm, q_2 = 14.7 mm, w_0 = 1.36 mm, w_1 = 2.1 mm, w_2 = 0.24 mm, w_3 = 1 mm, w_4 = 0. 26 mm, g_1 = 1.6 mm, g_2 = 0.3 mm, d_1 = 0.6 mm, d_2 = 0.8 mm.

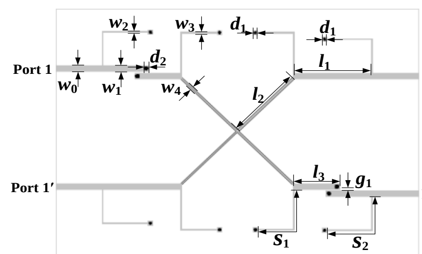

(a)

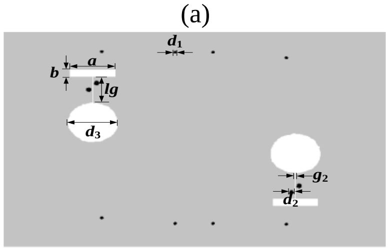

(b)

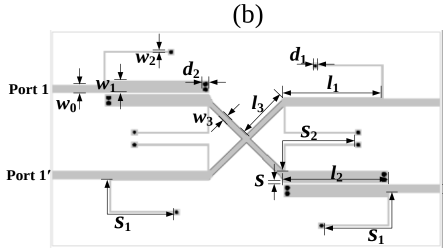

(c)

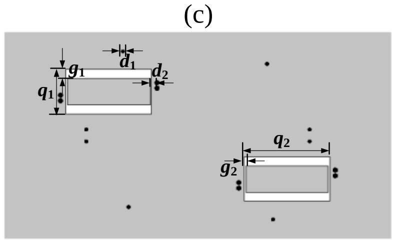

(d)

Fig. 7. Geometries of two proposed balanced filters. (a) Top view of structure I, (b) bottom view of structure I, (c) top view of structure II, and (d) bottom view of structure II.

The simulated results and photographs of the two balanced filters with two different 180° phase shifter are shown in Figs. 8 and 9 (Simulated with ANSYS HFSS v.11.0). As to the balanced filter with microstrip/slotline transition, the in-band insertion loss of differential mode is less than 1 dB with 3-dB bandwidth approximately 102% from 1.47 GHz to 4.53 GHz. And insertion loss of common mode is greater than 23 dB (0-5.7 GHz, 1.9f_0), which manifested good wideband suppression. Furthermore, for the balanced filter with λ/4 shorted coupled line, 3-dB bandwidth is about 103% from 1.52 GHz to 4.61 GHz, meanwhile, the in-band insertion loss of differential mode is less than 1.3 dB. And insertion loss of common mode is greater than 15 dB (0-7.5 GHz, 2.5f_0).

III. RESULTS AND DISCUSSION

Figures 8 and 9 present the measured results and photographs of the two balanced filters. We can see from Fig. 8 (a), 3-dB bandwidth is approximately 100% (1.47-4.48 GHz), the passband return loss is greater than 12.5 dB and insertion loss is less than 1.1 dB of the differential mode; for the common mode in Fig. 8 (b), a broadband rejection (0-7.5 GHz, 2.5f_0) is achieved which up to 20 dB. The results of the second balanced filter are shown in Fig. 9, 3-dB bandwidth is approximately 100% (1.48-4.48 GHz), the passband return loss is greater than 11 dB and insertion loss is less than 1.3 dB of the differential mode; for the common mode in Fig. 9 (b), a broadband rejection (0-7.4 GHz, 2.46f_0) is achieved which up to 15 dB. Aforementioned two structures, the in-band performance of differential mode has a bit discrepancy is mainly caused by the fabrication inaccuracy and errors of measurement.

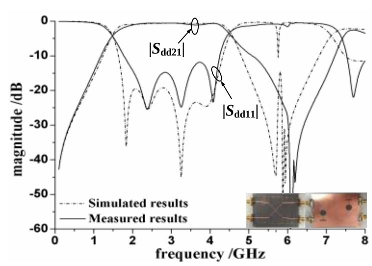

(a)

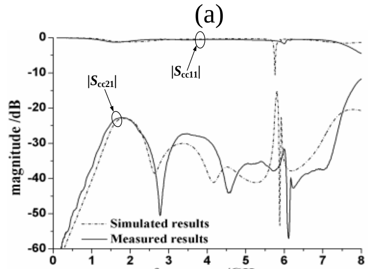

(b)

Fig. 8. Measured and simulated results of the balanced filter with microstrip/slotline transition. (a) Differential mode and (b) common mode.

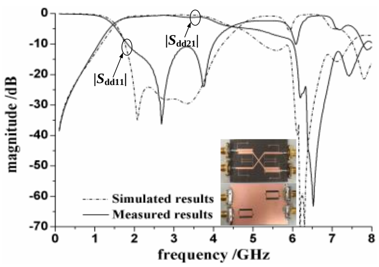

(a)

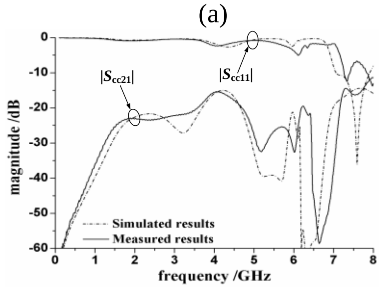

(b)

Fig. 9. Measured and simulated results of the balanced filter with λ/4 shorted coupled line. (a) Differential mode and (b) common mode.

IV. CONCLUSION

Two ultra-wideband balanced filters based on transversal signal-interference concepts are proposed in this paper. Wideband common mode signals suppression can be implemented conveniently for the filters with two structures, microstrip/slotline transition and quarter-wavelength shorted coupler lines. Then 180^o phase shift realized therefore. It shows good performance for common mode suppression and little insertion loss of differential mode.

ACKNOWLEDGEMENT

This work is supported by the 2012 Distinguished Young Scientist awarded by the National Natural Science Foundation Committee of China (61225001), and by National Natural Science Foundation of China (6140010914, 61571231), Natural Science Foundation of Jiangsu Province (BK20140791) and the 2014 Zijin Intelligent Program of Nanjing University of Science and Technology.

REFERENCES

[1] Y.-S. Lin and C. H. Chen, "Novel balanced microstrip coupled-line bandpass filters," *in Proc. URSI Int. Electromagn. Theory Symp*., pp. 567-569, 2004.

[2] C. H. Wu, C. H. Wang, and C. H. Chen, "Novel balanced coupled-line bandpass filters with common-mode noise suppression," *IEEE Trans. Microw. Theory Tech*., vol. 55, no. 2, pp. 287-295, Feb. 2007.

[3] C. H. Wu, C. H. Wang, and C. H. Chen, "Stopband-extended balanced bandpass filter using coupled stepped-impedance resonators," *IEEE Microw. Wireless Compon. Lett*., vol. 17, no. 7, pp. 507-509, July 2007.

[4] T. B. Lim and L. Zhu, "A differential-mode wideband bandpass filter on microstrip line for UWB application," *IEEE Microwave Wireless Compon. Lett*., vol. 19, no. 10, pp. 632-634, Oct. 2009.

[5] T. B. Lim and L. Zhu, "Differential-mode ultra-wideband bandpass filter on microstrip line," *IET Electron. Lett*., vol. 45, no. 22, pp. 1124-1125, Oct. 2009.

[6] J. Shi and Q. Xue, "Balanced bandpass filters using center-loaded half-wavelength resonators," *IEEE Trans. Microw. Theory Techn.*, vol. 58, no. 4, pp. 970-977, Apr. 2010.

[7] X. H. Wang, Q. Xue, and W. W. Chio, "A novel ultra-wideband differential filter based on double-sided parallel-strip line," *IEEE Microw. Wirel. Compon. Lett*., vol. 20, no. 8, pp. 471-473, 2010.

[8] J. Shi, J.-X. Chen, and Q. Xue, "A novel differential bandpass filter based on double-sided parallel-strip line dual-mode resonator," *Microw. Opt. Tech. Lett*., vol. 50, no. 7, pp. 1733-1735, July 2008.

[9] Q.-Y. Lu, J.-X. Chen, L.-H. Zhou, and H. Tang, "Novel varactor-tuned balanced bandpass filter with continuously high common-mode suppression," *ACES Jour*., vol. 28, no. 7, pp. 628-632, July 2013.

[10] Q. Xiao and C. X. Zhou, "Design of balanced SIW filter with transmission zeroes and linear phase," *ACES Jour*., vol. 30, no. 9, pp. 1019-1023, Sep. 2015.

[11] W. R. Eisenstant, B. Stengel, and B. M. Thompson, *Microwave Differential Circuit Design Using Mixed-Mode S-Parameters*. Boston, MA: Artech House, 2006.

[12] Y. X. Guo, Z. Y. Zhang, and L. C. Ong, "Improved wide-band Schiffman phase shifter," *IEEE Trans. Microw. Theory Techn.*, vol. 54, no. 3, pp. 2412-2418, Mar. 2006.

Chaoying Zhao was born in Wuhu, Anhui Province, China, in 1992. She received the B.E. degree from the Shandong University, Weihai, China, in 2014. From October 2014, she went to Nanjing University of Science and Technology (NUST), Nanjing, China, for further study as a postgraduate.

Her research interests include ultra-wideband (UWB) circuits and technologies, power dividers and planar microstrip filters.

Wenjie Feng was born in Shangqiu, Henan Province, China, in 1985. He received the B.Sc. degree from the First Aeronautic College of the Airforce, Xinyang, China, in 2008, the M.Sc. and Ph.D. degrees from the Nanjing University of Science and Technology (NUST), Nanjing, China, in 2010, 2013.

From November 2009 to February 2010, March 2013 to September 2013, he was a Research Assistant with the City University of Hong Kong. From October 2010 to March 2011, he was an exchange student with the Institute of High-Frequency Engineering, Technische Universität München, Munich, Germany. He is currently an Associate Professor with the Nanjing University of Science and Technology, Nanjing, China. He has authored or co-authored over 100 internationally referred journal and conference papers. His research interests include ultra-wideband (UWB) circuits and technologies, substrate integrated components and systems, planar microstrip filters and power dividers, LTCC circuits.

Feng is a Reviewer for over ten internationally referred journal and conference papers, including eight IEEE Transactions and Letters. He serves as an Associate Editor for the International Journal of Electronics from 2015.

Yuan Chun Li was born in Anhui Province, China. She received the B.S. degree in Electronic Engineering from Anhui University, Hefei, China, in 2006, the M.S. degree in Electronic Engineering from University of Science and Technology of China, Hefei, China, in 2009, and the Ph.D. degree in Electronic Engineering from the City University of Hong Kong, Kowloon, Hong Kong.

From Oct 2012 to Jun 2015, she was a Research Fellow with the City University of Hong Kong. She is currently an Associate Professor with the School of Electronic and Information Engineering, South China University of Technology. Her research interests include RF and microwave passive and active circuits, and monolithic microwave integrated circuits.

Wenquan Che received the B.Sc. degree from the East China Institute of Science and Technology, Nanjing, China, in 1990, the M.Sc. degree from the Nanjing University of Science and Technology (NUST), Nanjing, China, in 1995, and the Ph.D. degree from the City University of Hong Kong (CITYU), Kowloon, Hong Kong, in 2003.

In 1999, she was a Research Assistant with the City University of Hong Kong. From March 2002 to September 2002, she was a Visiting Scholar with the Polytechnique de Montréal, Montréal, QC, Canada. She is currently a Professor with the Nanjing University of Science and Technology, Nanjing, China. From 2007 to 2008, she conducted academic research with the Institute of High Frequency Technology, Technische Universität München. During the summers of 2005–2006 and 2009–2012, she was with the City University of Hong Kong, as Research Fellow and Visiting Professor. She has authored or co-authored over 110 internationally referred journal papers and over 60 international conference papers. She has been a Reviewer for *IET Microwaves, Antennas and Propagation*. Her research interests include electromagnetic computation, planar/coplanar circuits and subsystems in RF/microwave frequency, microwave monolithic integrated circuits (MMICs) and medical application of microwave technology.

Che is a Reviewer for the IEEE Transactions on Microwave Theory and Techniques, IEEE Transactions on Antennas and Propagation, IEEE Transactions on Industrial Electronics, and IEEE Microwave and Wireless Components Letters. She was the recipient of the 2007 Humboldt Research Fellowship presented by the Alexander von Humboldt Foundation of Germany, the 5th China Young Female Scientists Award in 2008 and the recipient of Distinguished Young Scientist awarded by the National Natural Science Foundation Committee (NSFC) of China in 2012.

Novel Pentagonal Dual-Mode Filters with Adjustable Transmission Zeros

Zhaojun Zhu, Shuo Liang, and Chaolei Wei

Institute of Applied Physics
University of Electronic Science and Technology of China, Chengdu, 610054, China
uestc98@163.com, uestcliangshuo@163.com, uestcweichaolei@163.com

Abstract ─ Novel compact pentagonal dual-mode filters with open stub is presented. The field patterns of this type of resonators are investigated using full-wave electromagnetic simulations. The technique of utilizing capacitive and inductive source-load coupling to improve the performance of filters is explored. Advantages of using this type of filter are not only its compact size, but also its transmission zeros that can be independently controlled. Then, two dual-mode bandpass filters are designed, fabricated and tested to validate the design concept. Both simulated and measured results are presented.

Index Terms ─ Bandpass filter, dual-mode, transmission zero.

I. INTRODUCTION

Bandpass filter (BPF) is one of the most important components in microwave circuits. To meet the requirement of modern microwave communication systems, microwave BPFs with compact size and high performance are in demand. The dual-mode resonators are attractive because each resonator can be used as a doubly tuned circuit, and therefore, the number of resonators is reduced by half, resulting in a compact size. Wolff first demonstrated a microstrip dual-mode filter in 1972 [1]. Since then, dual-mode microstrip filters have been widely used in communications systems [2-3]. Among them, E-shaped microstrip resonators and filters have been originally reported in [4]. More recently, the E-shaped resonator was modeled as a dual-mode resonator in [5]. However, it was difficult to control the location of the transmission zeros. Circular dual-mode filter based on source-load coupling was proposed in [6]. By introducing a capacitive cross-coupling between the input and output ports so that additional zero can be generated, but transmission zeros cannot be independently controlled. The open stub dual-mode filter with adjustable transmission zeros by inductive source-load coupling (S-L coupling) was firstly proposed in [8]. Two novel bandpass filters with multiple transmission zeros using only four open/ shorted stubs was proposed in [9]. The out-of-band transmission zeros can be adjusted easily by only changing the electrical length of the four open/shorted stub. But the resonator occupied a large circuit area, size reduction is becoming a major design consideration for practical applications.

In this paper, two compact bandpass filters with a pentagonal dual-mode resonator and S-L coupling are introduced. The reduction of the size is achieved by using a pentagonal dual-mode resonator. Furthermore, with a cross-coupling between the input and output feed lines, two tunable transmission zeros are obtained that can be controlled independently by the amount of the capacitive or inductive S-L coupling. The proposed bandpass filter shows a good stopband rejection because of the two tunable transmission zeros. Two exemplary filters verify the feasibility of the technique.

II. DUAL-MODE PENTAGONAL RESONATOR

Figure 1 shows the geometry of proposed dual-mode filters with the pentagonal open-loop resonator by open stub loaded. The filter comprises an improved pentagonal half-wavelength resonator and a hexagonal open loaded stub. The S-L coupling include two types, i.e., capacitive and inductive S-L coupling.

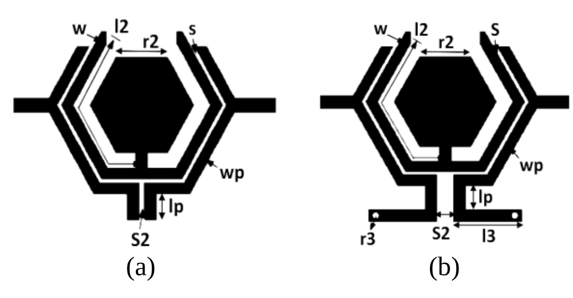

Fig. 1. Layout of the proposed pentagonal dual-mode bandpass filter: (a) capacitive S-L coupling, and (b) inductive S-L coupling.

Figure 2 shows a T-shaped resonator model with a half-wavelength resonator and a shunt open stub, where z_1 is the characteristic impedance of the half-

Submitted On: August 15, 2014
Accepted On: August 11, 2016

wavelength resonator with the electrical length $\theta_1 = 90^\circ$, and z_2 the characteristic impedance of the open stub with electrical length θ_2. C_1 is the coupling capacitance between resonator and feed line. As θ_2 increases, the odd resonant frequencies are fixed, while the even resonant frequencies and the transmission zero frequency keeps decreasing. When θ_2 is slightly smaller/larger than 90°, the even resonant frequency is slightly beyond/below fundamental frequency of the half-wavelength resonator, respectively. The proposed resonator then becomes a dual-mode resonator with a transmission zero close to the resonant frequency [7]. If the S-L coupling is introduced, an additional transmission zero is presented. Then, the proposed filter will show two transmission zeros.

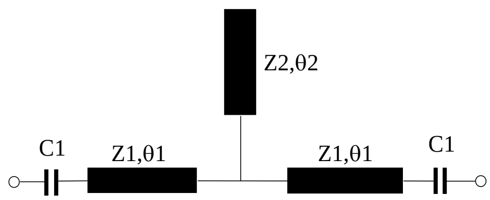

Fig. 2. Schematic of a half-wavelength resonator with an open stub.

For a compact size, the half-wavelength length line is bent to a pentagon, and the uniform shunt open stub is also replaced by a hexagonal stepped-impedance open stub. The open hexagonal stub at the centre of the half-wavelength resonator introduces another transmission pole near the fundamental frequency. This new pole and the fundamental frequency pole of the half-wavelength resonator make the proposed structure a dual-mode resonator. So this symmetric structure can support two modes, i.e., an even mode and odd mode.

The commercially available full-wave electromagnetic simulators (HFSS) were used to characterize the electric field patterns for a dual-mode open-loop resonator. HFSS uses the finite element method (FEM) to analyze the electromagnetic characteristics of 3D objects. The basic process of solving the problem by FEM includes three parts, which are the mesh discretization of the object, the solution of the simultaneous matrix equations related the mesh and the postprocessing calculation of the problem.

It can be seen that the whole structure is symmetrical with the center point, so the center point is modeled as the origin point and the mirror operation is applied. The physical excitation of the filter is by the coaxial line with the TEM wave. In order to use the wave-guide port in the simulation code, the port surface must cover more than ninety-five percent of the TEM field. It is assumed that the width of the excitation microstrip is w and the thickness of the dielectric layer is h. The height of the wave port is generally set to 6~10h. When w>h, the width of the wave port is set to about 10w; when w<h, the width of the wave port is set to about 5w. Finally, the height and width of the wave port of are 10h and 10w in this paper.

According to the standard which is set up by user, HFSS simulation code uses adaptive mesh generation technology. The solution frequency of the meshing is generally set at the center frequency of the filter. After each new mesh subdivision, HFSS will compare the results of the S parameters with the old one. If the error is less than the set criterion, it is shown that the result is convergent and the adaptive process will end. The dimensions are optimized by a full-wave simulation to take all the discontinuities into consideration.

Figure 3 depicts the simulated electric field vector between the metal strip and ground plane at the resonance frequency. The electric field pattern of the odd mode is illustrated in Fig. 3 (a), where the maxima of the field are located along the left and right arms. The field distribution is similar to that of a half-wavelength single-mode resonator. As a consequence, the open stub does not affect the resonant frequency of the odd mode. Figure 3 (b) shows the electric field pattern of the even-mode, where the maxima of the field are moved to the open stub and both side of the arms. Moreover, it is observed from the direction of the electric field vector that the field is symmetric with respect to the symmetry axis. Hence, changing the dimension of the open stub makes the resonant frequency of the even mode shift.

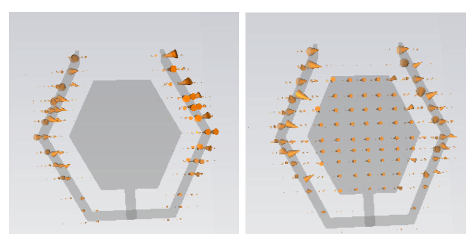

(a) (b)

Fig. 3. Simulated electric field patterns for a dual-mode pentagonal open-loop resonator: (a) odd mode and (b) even mode.

To observe the mode splitting, the dual-mode pentagonal loop resonators have been simulated with different loaded element size. The resonant frequencies of the two modes are plotted in Fig. 4 as a function of the size l_2 and r_2. As shown in Fig. 4 (a), when l_2 increases from 10 to 20 mm, the resonant frequency of the odd mode decreases from 4.45 to 2.8 GHz, while that of the even mode decreases from 3.85 to 3.1 GHz. As shown in Fig. 4 (b), when r_2 increases from 3 to 5 mm, the resonant frequency of the even mode decreases from 3.58 to 3.45 GHz, while that of the odd mode hardly change.

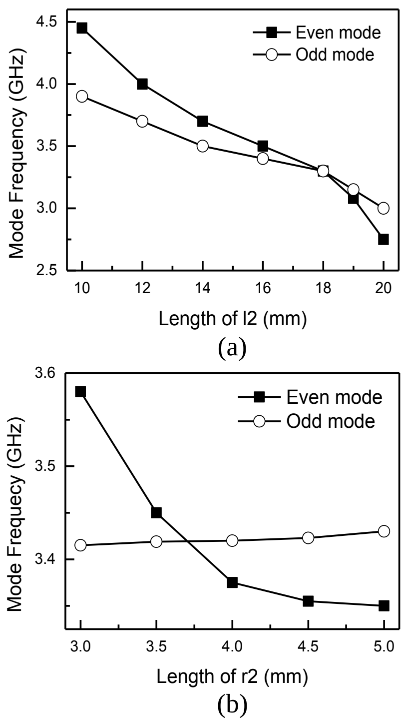

Fig. 4. Simulated resonance frequencies of the two modes against: (a) l_2, where r_2 = 5 mm, and (b) r_2, where l_2 = 15 mm.

III. BANDPASS FILTERS USING DUAL-MODE PENTAGONAL RESONATOR

Figure 1 shows the layout of the pentagonal dual-mode open loop BPF. It consists of the capacitive S-L coupling and inductive S-L coupling filter. The gap between the resonator and coupling arms was selected in consideration of strong coupling and etching tolerance. The characteristic impedance of the input/output microstrip is taken as 50 ohm. The length of the S-L coupling line is l_p. The gap of the S-L coupling line is s_2.

As illustrated in [6], the open stub dual-model filter has an interesting property. There is an inherent finite-frequency transmission zero when the two modes split. If $f_{even} < f_0 < f_{odd}$, the inherent transmission zero would be in the lower stopband. If $f_{odd} < f_0 < f_{even}$, the inherent transmission zero would be in the upper stopband. f_0 is the center frequency.

For further improving the filters' performance, S-L coupling is introduced to generate an additional zero. Using capacitive and inductive S-L coupling technique, the response with two adjustable zeros can be obtained for the proposed dual-mode filters. The locations of these two transmission zeros can be controlled by transforming the type and amount of the source-load cross-coupling. For the capacitive S-L coupling, an additional transmission zero shows in the upper stopband. For the inductive S-L coupling, an additional transmission zero shows in the lower stopband. Two exemplary filters verify the feasibility of the new technique. We take $f_{odd} < f_0 < f_{even}$ for instance.

A. Dual-mode filter with capacitive S-L coupling

Filter A exhibits both the inherent transmission zero and the additional zero in the upper stopband. Here, the capacitive S-L coupling is introduced to generate the additional zero. The locations of the additional zero may be controlled by adjusting the values of the s_2 and l_p. As shown in Fig. 5, when s_2 decreases from 1.1 to 0.7 mm, the inner transmission zero almost doesn't change, and the outer transmission zero moves toward the passband edge. As shown in Fig. 6, when l_p increases from 1 to 2.4 mm, the inner transmission zero almost doesn't change, while the outer transmission zero moves toward the passband edge. Therefore, the s_2 and l_p can be selected to meet the required filter selectivity.

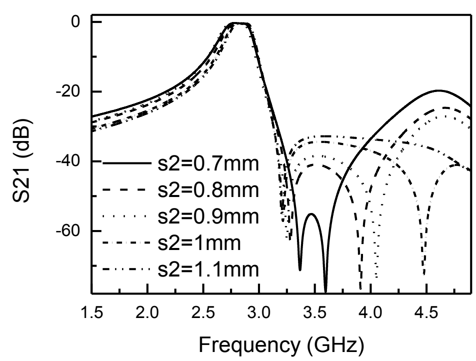

Fig. 5. Simulated scattering parameters of the filter A for five values of s_2.

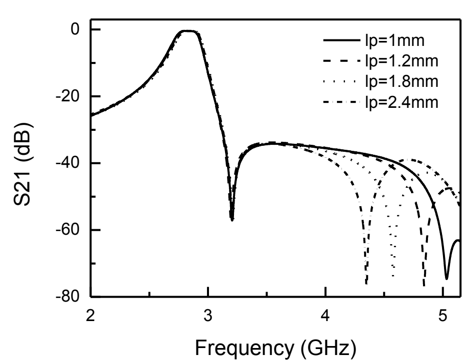

Fig. 6. Simulated scattering parameters of the filter A for four values of l_p.

The dimensions are optimized by a full-wave simulator to take all the discontinuities into consideration. The designed filter is fabricated on the substrate Rogers RO4003, which relative dielectric constant is 3.38 and the thickness is 0.508 mm. Figure 7 shows the photograph of the fabricated filter A. Both measured and simulated results are plotted in Fig. 8. As seen from the measured results, at the center frequency of 2.75 GHz, the 3 dB fractional bandwidth is about 8%. Two transmission zeros are realized at 3.2 and 4.75 GHz. The insertion loss is less than 2 dB in passband, and the minimum of insertion loss is 1.5 dB. The return loss is greater than 20 dB in passband. Simulation results almost agree with the measured results.

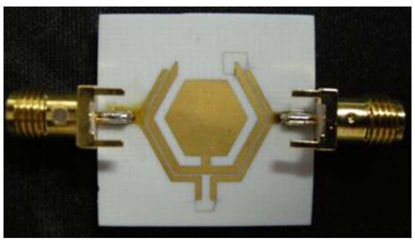

Fig. 7. Photograph of the fabricated filter A. Geometric parameters of the filters are w =1, r_2 = 5, l_2 = 11.55, l_p = 2, s_2 = 1 and s = 0.22. All are in mm.

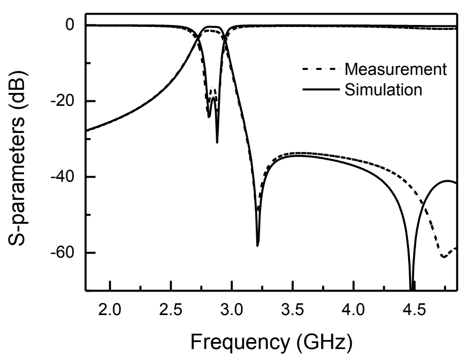

Fig. 8. Simulated and measured frequency responses of the filter A.

B. Dual-mode filter with inductive S-L coupling

Filter B demonstrates a filter characteristic with the inherent finite frequency zero located at the upper side of the passband, while the additional zero at the lower side. This is because $f_{odd} < f_0 < f_{even}$ for the proposed filter. As it has been noted, the inherent zero is at upper side of passband. The inductive S-L coupling is introduced to generate an additional zero at lower side of passband. As shown in Fig. 9 and Fig. 10, when s_2 decreases from 3.5 to 0.5 mm, the inherent transmission zero changed little, while the additional transmission zeros increases from 0.85 to 1.9 GHz. When l_p increases from 1 to 7 mm, the inherent transmission zero also changed little, while the additional transmission zeros increases from 0.85 to 1.65 GHz. Thus, a sharper fall-off at both lower and upper passband edge may be achieved by adjusting the s_2 and l_p.

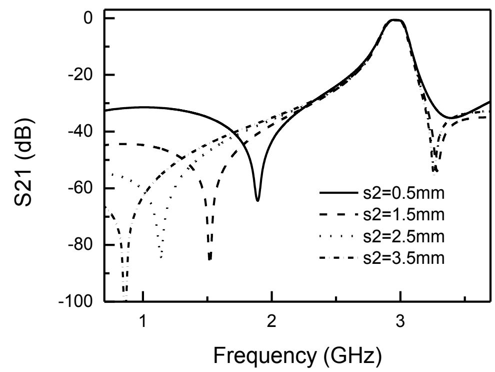

Fig. 9. Simulated scattering parameters of the filter B for four values of s_2.

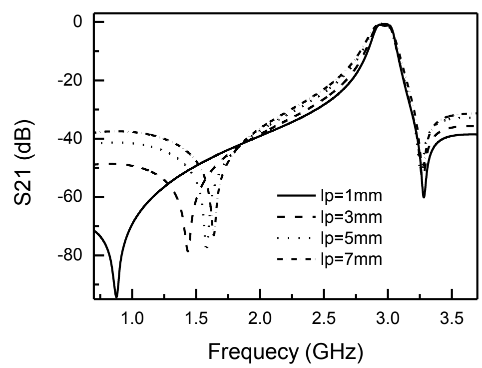

Fig. 10. Simulated scattering parameters of the filter B for four values of l_p.

Figure 11 shows the photograph of the fabricated filter B. The simulated and measured frequency responses are shown in Fig. 12. The simulated results show that the filter B operated at 3 GHz and a 3 dB fractional bandwidth of 5.3%. Two transmission zeros are located at 1.55 GHz and 3.3 GHz respectively. The minimum insertion loss is about 0.6 dB, and the return loss is greater than 20 dB in passband. The measured minimum insertion loss is about 2 dB, and the return loss is greater than 16 dB in passband. The measured results meet the simulation results well.

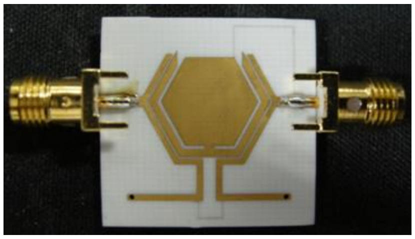

Fig. 11. Photograph of the fabricated filter B. Geometric parameters of the filters are w =1, r_2 = 5, r_3 = 8, l_2 = 11.55, l_3 = 8, l_p = 4, s_2 = 1.5 and s = 0.18. All are in mm.

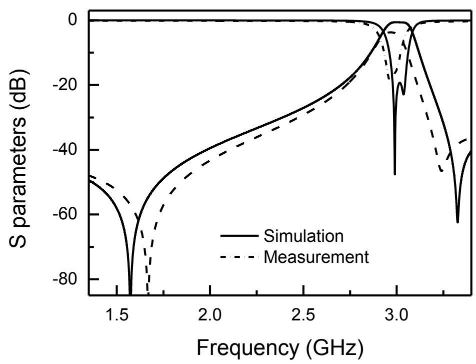

Fig. 12. Simulated and measured frequency responses of the filter B.

IV. CONCLUSION

The application of capacitive and inductive S-L coupling has been studied intensively in this paper. The novel pentagonal dual-mode filter loaded by hexagonal open stub is presented. By S-L coupling, the proposed filters exhibits two transmission zeros. It reveals that a quasi-elliptic response with two adjustable transmission zeros can be obtained easily. The proposed structure and design method is verified by two exemplary filters.

ACKNOWLEDGMENT

This work is supported by “National Natural Science Foundation of China (Grant No. 61101042)”.

REFERENCES

[1] I. Wolff, “Microstrip bandpass filter using degenerate modes of a microstrip ring resonator,” *Electron. Lett.*, vol. 8, pp. 302-303, June 1972.

[2] B. F. Ganji and M. Samadbeik, “Simple configuration low-pass filter with very wide stop band,” *ACES Express Journal*, vol. 1, no. 1, pp. 4-7, 2016.

[3] X. Deng and K. D. Xu, “Novel microstrip ultra-wideband bandpass filter using radial-stub-loaded structure,” *ACES Express Journal*, vol. 1, no. 1, pp. 20-23, 2016.

[4] J. R. Lee and J. H. Cho, “New compact bandpass filter using microstrip λ/4 resonator with open stub inverter,” *IEEE Microw. Guided Wave Lett.*, vol. 10, no. 12, pp. 526-527, Dec. 2000.

[5] T. Yan, X. H. Tang, and J. Wang, “A novel quad-band bandpass filter using short stub loaded E-shaped resonators,” *IEEE Microwave & Wireless Components Letters*, vol. 25, no. 8, pp. 508-510, Aug. 2015.

[6] W.-H. Wu, “Compact double-mode cross-coupled microstrip bandpass filter with tunable transmission zeros,” *IET Microw. Antennas Propag.*, vol. 2, no. 4, pp. 373-377, Dec. 2008.

[7] L. Gao and X. Y. Zhang, “High-selectivity dual-band bandpass filter using a quad-mode resonator with source-load coupling,” *IEEE Microwave & Wireless Components Letters*, vol. 23, no. 9, pp. 474-476, Sept. 2013.

[8] J.-S. Hong and H. Shaman, “Dual-mode microstrip open-loop resonators and filters,” *IEEE Trans. Microw. Theory Tech.*, vol. 55, no. 8, pp. 1764-1770, Aug. 2007.

[9] W. Feng, X. Gao, and W. Che, “Bandpass filters with multiple transmission zeros using open/ shorted stubs,” *IET Microw., Antennas Propag.*, vol. 9, no. 8, pp. 769-774, June 2015.

[10] B. Yu, B. Jia, and Z. Zhu, “Compact tri-band bandpass filter with stub-loaded stepped-impedance resonator,” *Electron. Lett.*, vol. 51, no. 9, pp. 701-703, Apr. 2015.

Zhaojun Zhu was born in Sichuan, China, in 1978. He received the B.S. degree and the Ph.D. degree in Physical Electronics in UESTC, Chengdu, in 2002 and 2007 respectively. Since 2012, he has been an Associate Professor with the UESTC. His research interests include the design of microwave and millimeter-wave circuits.

Shuo Liang was born in SiChuan Province, China, in 1990. He received the B.S. degree in School of Electronic Engineering from HUAT, Hubei, in 2014, and is currently working toward the M.D. degree in UESTC. His research interests include the design of microwave and millimeter-wave circuits.

Chaolei Wei was born in Shandong Province, China, in 1981. He received the B.S. degree in Physics from the Liaocheng University, in 2006, and the M.D. degree in Nuclear Energy Engineering from the Institute of Southwest Physics, in 2009, respectively, and is currently working toward the Ph.D. degree in UESTC. His research interests include the design of microwave and millimeter-wave circuits.

Miniaturized Microstrip Suppressing Cell with Wide Stopband

M. Hayati [1,2], F. Shama [2], and M. Ekhteraei [3]

[1] Department of Electronics, Kermanshah Branch, Islamic Azad University, Kermanshah, Iran
Mohsen_hayati@yahoo.com

[2] Department of Electronics, Razi University, Tagh-E-Bostan, Kermanshah-67149, Iran
f.shama@aut.ac.ir

[3] Young Researchers and Elite Club, Kermanshah Branch, Islamic Azad University, Kermanshah, Iran
m.ekhteraei.ir@ieee.org

Abstract **─** In this paper, based on simple stepped impedance structures a methodology is followed to design a very compact size lowpass filter (LPF) as a suppressing cell. The proposed suppressing cell consists of stepped impedance ladder-type resonators, which provides a wide stopband by creating the transmission zeros to its frequency response. The proposed suppressing cell has clear advantages like low insertion loss in the passband and suitable roll-off. The designed LPF is fabricated on a microstrip layout and tested. The measured results highlight the efficiency of the filter and have a good agreement with the simulated results. With mentioned expression, the fabricated LPF can be a powerful block as a suppressing cell to implement in the distributed high frequency circuits.

Index Terms **─** Lowpass filter, microstrip, miniaturized, stepped impedance structure, suppressing cell.

I. INTRODUCTION

Design of the high frequency circuits are highly extended and demanded, in the modern technologies. Handset devices and wireless communications depend on the high frequency circuits and the suppression of the spurious signals is an important requirement in this field [1]. The position of the lowpass filters is undeniable in order to block and suppress the unwanted harmonics. From the introducing of microstrip technology until now, many microstrip structures and many methods have been presented to design the high efficient LPFs [1-14]. Planar structures are widely used for their simple fabrication and design in [1-13], which have sharp transition band and wide stopband, but these LPFs suffers from the big size, which makes them inappropriate as the suppressing cells to use in hybrid high frequency circuits, in addition to their almost low attenuation levels in their stopbands.

A miniaturized LPF with very sharp roll-off has been designed to eliminate the unwanted harmonics for a Wilkinson power divider in [14], which has a so narrow stopband bandwidth. In [15], using defected ground structures (DGS), an Elliptic-function LPF has been fabricated with sharp roll-off, this technique design not only is not easy to implement but also has disadvantages such as large circuit size and narrow stopband width. A lowpass filter has been designed in [16] with sharp roll-off as a miniaturized LPF, but it is not so compact and has a very narrow rejection bandwidth. In [17], the fabricated LPF has a compact structure, although the stopband region is not wide enough. A wide stopband LPF has been presented in [18], but this filter suffers from its high insertion loss in the passband and its large circuit size. In [19-24], the low value of maximum variation of the group delay in the passband has been introduced as an effective factor in LPF designs, which it tried to be improved in the proposed work. Also, the simple geometry and topology of the designed filter is a significant specification, which can be effective in fabrication and implementation. Therefore the design of a simple structure and high efficient LPF is the main objective of this paper.

In this paper, using stepped impedance microstrip stubs and ladder-type structures, a miniaturized LPF with good rejection bandwidth is designed. The LPF has - 3 dB cut-off frequency at 4 GHz. The rejection band is achieved from 5 to 23.3 GHz. A simple methodology is used to design this filter that follows in the next session. All the simulations are done using Agilent Advanced Design System (ADS) software, and all of the microstrip layouts are designed and fabricated on RT/Duriod5880 substrate with dielectric constant (ε_r) of 2.22, the thickness of 0.508 mm and the loss tangent of 0.0009.

Submitted On: May 26, 2016
Accepted On: August 9, 2016

II. SUPPRESSING CELL DESIGN

At the first step, Elliptic function resonator layout has been selected and expanded using high and low impedance lines, as shown in Fig. 1. The physical lengths of the low-impedance and high-impedance lines are calculated using below equations [10]:

$$L_i = \frac{g_i Z_0}{2\pi f_c g_0}, \quad (1)$$

$$C_i = \frac{g_i g_0}{2\pi f_c Z_0}, \quad (2)$$

$$d_{L_i} = \frac{\lambda g_{L_i}}{2\pi} sin^{-1}\left(\frac{2\pi f_c L_i}{Z_{0L}}\right), \quad (3)$$

$$d_{c_i} = \frac{\lambda g_{c_i}}{2\pi} sin^{-1}(2\pi f_c C_i Z_{0c}), \quad (4)$$

where, Z_{0Ci} and Z_{0Li} are corresponded to the impedance transmission lines with low and high impedance, respectively. g_i and go are the element values of each part of the prototype layout, λ_{gLi} and λ_{gCi} are the guided wavelengths of high and low impedance lines, respectively. With considering the Fig. 1, the ABCD matrix for the proposed resonator can be written as:

$$\begin{bmatrix}A & B\\ C & D\end{bmatrix} = \begin{bmatrix}1 & \frac{Z_{oc3}}{2}\\ 0 & 1\end{bmatrix} \times \begin{bmatrix}1 & 0\\ Y_{oc1}+Y_{oc2}+Y_{oL1}+Y_{oL2} & 1\end{bmatrix} \times \begin{bmatrix}1 & \frac{Z_{oc3}}{2}\\ 0 & 1\end{bmatrix}, \quad (5)$$

where, $Y_{oc1}, Y_{oc2}, Y_{oL1}$ and Y_{oL2} are the admittances of the high and low impedance transmission lines, which are indicted in Fig. 1.With calculation, the Equation (5) can be simplified in:

$$\begin{bmatrix}A & B\\ C & D\end{bmatrix} = \begin{bmatrix}1 & Z_{oc3}\\ 0 & 1\end{bmatrix} \times \begin{bmatrix}1 & 0\\ Y_T & 1\end{bmatrix} = \begin{bmatrix}1+Z_{oc3}Y_T & Z_{oc3}\\ Y_T & 1\end{bmatrix}, \quad (6)$$

where, $Y_T = Y_{oc1} + Y_{oc2} + Y_{oL1} + Y_{oL2}$.

The proposed resonator has a symmetric shape as illustrated in Fig. 1; so clearly, it is expected that the resonator must have a reciprocal response. Therefore, the determinant of the ABCD matrix must be equal to 1. The determinant of the ABCD matrix can be calculated from Equation 6 as:

$$\Delta \begin{bmatrix}A & B\\ C & D\end{bmatrix} = 1 + Z_{oc3}Y_T - Z_{oc3}Y_T = 1. \quad (7)$$

Then, the Equation (7) validates the achieved ABCD matrix of the proposed resonator. The simulated S-parameters of the proposed resonator are shown in Fig. 2. As considered, in the passband the resonator has a transmission pole at 2.87 GHz with attenuation level of -15.6 dB and in the stopband the resonator has a transmission zero at 8.5 GHz with attenuation level of -64.3 dB with -3 dB cut-off frequency at 5.6 GHz. The resonator has a smooth passband region; although it has a narrow rejection bandwidth and gradual response in the transition band.

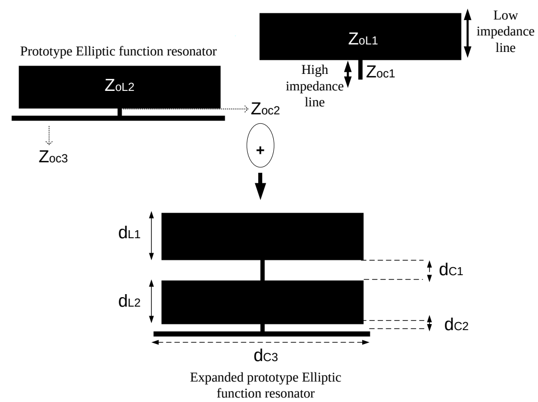

Fig. 1. The layout implementation procedure for the proposed expanded prototype Elliptic function resonator.

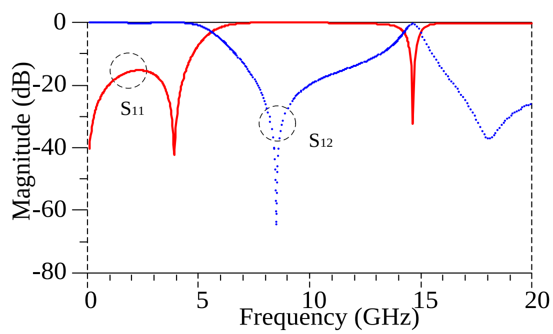

Fig. 2. Simulated S-parameters of the proposed expanded prototype Elliptic function resonator.

For this structure, the LC model for the proposed resonator is extracted as shown in Fig. 3. In this model, C represents the overall capacitance of low impedance stubs (Z_{0L1}, Z_{0L2}) respect to ground; L1 represents the overall inductance of high impedance lines (Z_{0C1}, Z_{0C2}); L represents the inductance of high impedance line of Z_{0C3}.

A comparison of the S21 parameters of this model and layout is shown in Fig. 4. The values of the lumped elements are illustrated in this figure, which are the conventional values of an Elliptic function 3 order resonator with -3 dB cut off frequency at 5.6 GHz. Transfer function for the calculation of the first transmission zero has been extracted using the proposed LC model as below:

$$T(s) = \frac{(9.793\times10^{9})S^2+2.789\times10^{31}}{S^3+(3.398\times10^{10})S^2+(1.539\times10^{21})S+2.789\times10^{31}}. \quad (8)$$

In this equation, the coefficients of the polynomials of the numerator and denominator depends on the capacitances and inductances values of the LC model and the location of transmission zero can be adjusted by changing these values. For example, as seen in Fig. 5, by increasing the lengths of d_{L1} and d_{L2} from 1 mm to 1.5 mm, due to increment of the capacitance of C, which is the total capacitance of Z_{OL1} and Z_{OL2}, first transmission zero moves from 8.4 GHz to 7.2 GHz. Also, by decreasing the lengths of d_{L1} and d_{L2} from 1mm to 0.5 mm, due to decrement of the capacitance of C, first transmission zero moves to 11.4 GHz.

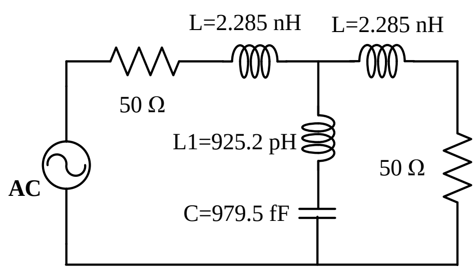

Fig. 3. The LC model for the proposed resonator.

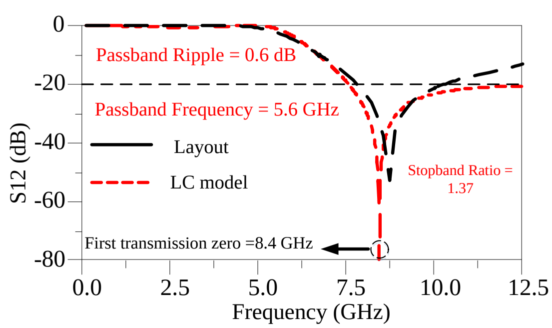

Fig. 4. A comparison of the S21 parameters of LC model and layout of the proposed resonator.

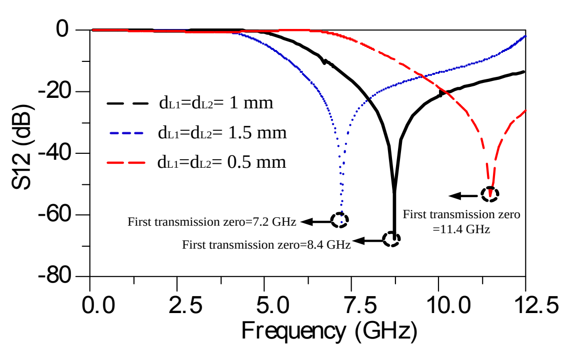

Fig. 5. Simulated S21 parameter of the proposed resonator as a function of d_{L1} and d_{L2}.

To modify the frequency response, another resonator can be cascaded to the previous one with the same dimensions as shown in Fig. 6. These dimensions are as follows: W = 1 mm, W1 = 1.1 mm, d = 4.8 mm, d2 = 0.5 mm and d3 = 11 mm. Using Equation (7), the ABCD matrix for the proposed cascaded resonator can be written as:

$$\begin{bmatrix} A & B \\ C & D \end{bmatrix} = \begin{bmatrix} 1 + Z_{oc3}Y_T & Z_{oc3} \\ Y_T & 1 \end{bmatrix} \times \begin{bmatrix} 1 + Z_{oc3}Y_T & Z_{oc3} \\ Y_T & 1 \end{bmatrix}. \tag{9}$$

The simulated S12-parameter of the proposed cascaded resonator is shown in Fig. 7. As seen, by moving the existence transmission zero to the lower frequency at 6.8 GHz and creating a new transmission zero at 10.7 GHz; the -3 dB cut-off frequency moves to 5 GHz with sharper transition band. Also, wider rejection band can be obtained. It has a stopband bandwidth from 5.9 GHz to 13 GHz for the attenuation level of -20 dB. But, the rejection band is so narrow yet. To extend the stopband width enough, the proposed cascaded resonator can be improved by adding another resonator, symmetrically with same dimensions as the proposed filter, as shown in Fig. 8. Thus, the stopband bandwidth has been improved up to 157% of the previous rejection band. Also, two stubs are added to the feeding lines at input and output to match the proposed filter to 50 Ω coaxial line. The ABCD matrix for the proposed cascaded symmetric resonator can be written using symmetric rules for impedances and with considering Equation 9 as:

$$\begin{bmatrix} A & B \\ C & D \end{bmatrix} = \begin{bmatrix} 1 + 2Z_{oc3}Y_{Ts} & 2Z_{oc3} \\ Y_{Ts} & 1 \end{bmatrix} \begin{bmatrix} 1 + 2Z_{oc3}Y_{Ts} & 2Z_{oc3} \\ Y_{Ts} & 1 \end{bmatrix}, \tag{10}$$

where, $Y_{Ts} = {}^{1}/_{2}\,(Y_{oc1} + Y_{oc2}) + 2(Y_{oL1} + Y_{oL2})$.

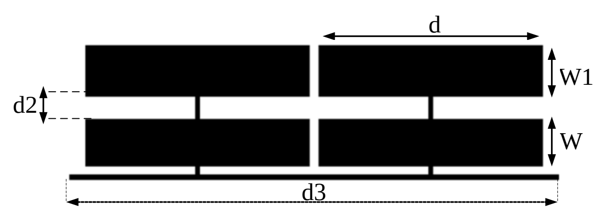

Fig. 6. The proposed cascaded resonator.

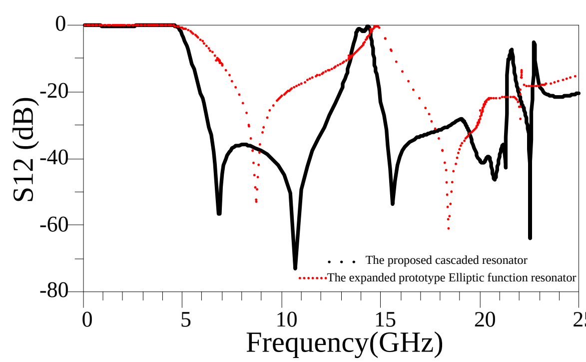

Fig. 7. The simulated S12-parameter of the proposed cascaded resonator.

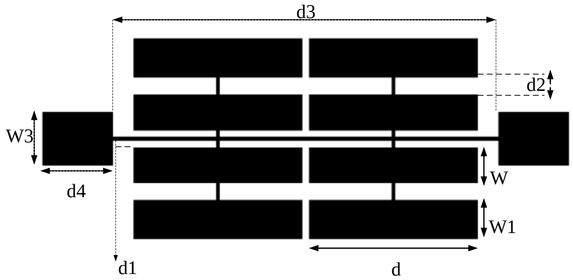

Fig. 8. The layout of the proposed LPF.

III. RESULTS

The designed LPF has been fabricated on RT/Duriod5880 substrate with dielectric constant (ε_r) of 2.22, the thickness of 0.508 mm and the loss tangent of 0.0009 and is illustrated in Fig. 9. The mentioned dimensions in the Fig. 8 are determined using equations (1-10) and tuned using ADS as a tuning tool. These dimensions are as follows: W = 1 mm, W1 = 1.1 mm, W2 = 0.1 mm, W3 = 1.5 mm, d = 4.8 mm, d1 = 0.2 mm, d2 = 0.5 mm, d3 = 11 mm and d4 = 2 mm. The measurements are done using HP8757A network analyzer. The simulated and measured S-parameters of the fabricated LPF are shown in Fig. 10. As seen, the -3 dB cut-off frequency is placed at 4 GHz. The rejection band is extended from 5 to 23.3 GHz with corresponding attenuation level of 16.6 dB. Also, the return loss is about 0 dB in the more space of the rejection band. The maximum insertion loss in the 90% of the passband region is 0.1 dB, where the maximum return loss is 15.6 dB. The physical size of the fabricated circuit, which occupies very small area, is only 11 mm × 5.5 mm = 60.5 mm^2 ($0.197\lambda_g \times 0.098\lambda_g$), where λ_g is the guided wave length at -3 dB cut-off frequency. A comparison between the characteristics of the proposed LPF and some referred works are shown in Table 1. In this table, RL (dB) and IL (dB) are the maximum return loss and insertion loss in the passband region, respectively.

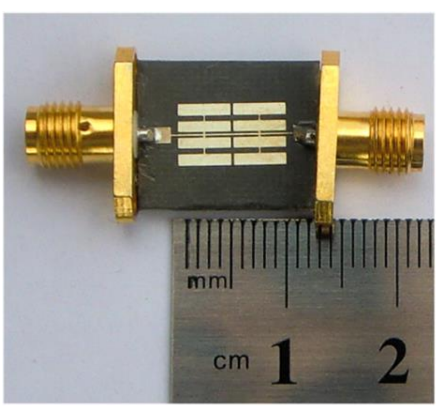

Fig. 9. Photograph of the fabricated LPF.

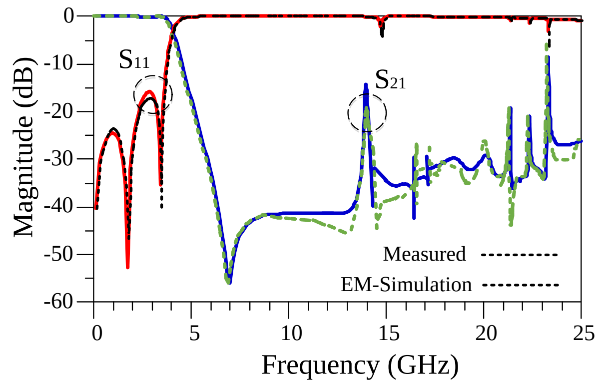

Fig. 10. The simulated and measured S-parameters of the fabricated LPF.

As can be seen in Table 1, the proposed LPF has the smallest size (60.3 mm) and the best insertion loss (0.1) among the referred filters. The good specifications of the rejection band and the small size are the important factors, which show that the proposed filter can be used in compact modern high frequency circuits as a suppressing cell in order to suppress the unwanted harmonics and interferences. The group delay of a microwave filter has a relationship to the insertion loss of a filter and design of a filter with flat group delay in the passband region is desirable [18-24]. As seen in Fig. 11, maximum variation of the measured group delay in the passband has not a significant variation and has a dispensable value and is only 0.23 ns. Table 2 shows a comparison between the maximum variation of the measured group delay in the passband for the proposed LPF and some referred works with reported group delay. As illustrated, the proposed filter has the best performance in the case of group delay.

Table 1: Performance comparisons between the proposed LPF and some referred works

Ref.	f_c (GHz)	SF	SBW/ f_c	Size (mm^2)	RL dB	IL (dB)
2	5.45	2	5.7	221	15	0.12
3	2	1	8.4	482	10	1.00
4	1.78	2	2.8	643.7	~10	0.30
5	1.67	1	5.9	100	12	0.50
6	1	2	4.1	638.4	20	0.40
12	1.18	1.5	5.9	174.2	-	-
13	1.5	2	12.1	364	20	0.13
14	3.6	2	1.9	59.8	~15	0.11
15	2.4	2	2.2	284	17	0.30
16	1.5	1.5	0.9	269	10	-
17	4.16	2	3	83.7	11	0.11
18	2.3	2	9.5	169.1	~10	1.80
This work	4	1.6	4.6	60.5	~15	0.10

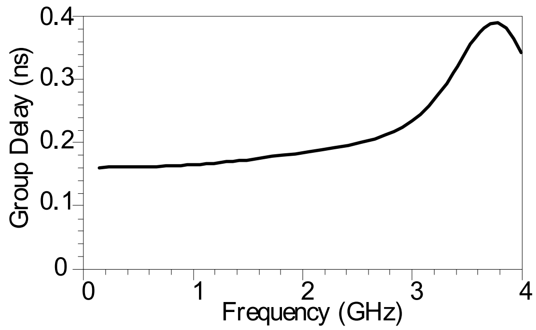

Fig. 11. The measured group delay in the passband for the proposed LPF.

Table 2: A comparison between the maximum variations of the measured group delay between some referred works with reported group delay

Ref	*f*c (GHz)	Maximum Variation of the Group Delay in the Passband (ns)	Resonator Structure
19	1.1	0.5	Tapered
20	1.74	0.5	Butterfly-shaped
21	1.55	0.5	Semi-circle stepped impedance
22	3.55	0.4	Spiral
23	2.37	0.44	Stub loaded semi-circle stepped-impedance
24	4	0.27	T-Shaped, patch and stepped impedance
This work	4	0.23	Stepped impedance

IV. CONCLUSION

A miniaturized LPF has been proposed with wide rejection band as a small size and efficient suppressing cell. The proposed LPF rejects the spurious signals from 5 GHz to 23.3 GHz with attenuation level of 16.6 dB. The maximum variation of the measured group delay in the passband region is only 0.23 ns, which is the less value in comparison with some reported works. The measurement results clear the accuracy of the simulations.

REFERENCES

[1] S. Majidifar, "High performance microstrip LPFs using dual taper loaded resonator," *Optik-International Journal for Light and Electron Optics*, vol. 127 no. 6, pp. 3484-3488, Mar. 2016.

[2] M. Hayati and F. Shama, "Compact microstrip low-pass filter with wide stopband using symmetrical U-shaped resonator," *IEICE Electronics Express*, vol. 9, no. 3, pp. 127-132, Feb. 2012.

[3] F. Wei, L. Chen, and X. Shi, "Compact lowpass filter based on coupled-line hairpin unit," *Electronics Letters*, vol. 48, no. 7, pp. 1, Mar. 2012.

[4] M. Hayati and A. Lotfi, "Elliptic-function lowpass filter with sharp cutoff frequency using slit-loaded tapered compact microstrip resonator cell," *Electronics Letters*, vol. 46, no. 2, pp. 143-144, Jan. 2010.

[5] X. B. Wei, et al., "Compact wide-stopband lowpass filter using stepped impedance hairpin resonator with radial stubs," *Electronics Letters*, vol. 47, no. 15, pp. 1, July 2011.

[6] L. Lin, Z. Li, and J. Mao, "Compact lowpass filters with sharp and expanded stopband using stepped impedance hairpin units," Microwave and *Wireless Components Letters IEEE*, vol. 206, pp. 310-312, June 2010.

[7] W. Jiacheng, "Compact quasi-elliptic .microstrip lowpass filter with wide stopband," *Electronics Letters*, vol. 46, no. 20, pp. 1384-1385, Sep. 2010.

[8] J. Wang and G. Zhang, "Design of microstrip lowpass filter with compact size and ultra-wide stopband," *Electronics Letters*, vol. 48, no. 14, pp. 856-857, July 2012.

[9] G. Lefei, J. P. Wang, and Y. Guo, "Compact microstrip lowpass filter with ultra-wide stopband," *Electronics Letters*, vol. 46, no. 10, pp. 689-691, May 2010.

[10] M. Hayati, F. Shama, and H. Abbasi. "Compact microstrip lowpass filter with wide stopband and sharp roll-off using tapered resonator," *International Journal of Electronics*, vol. 100, no. 12, pp. 1751-1759, Dec. 2013.

[11] V. Vamsi Krishna and S. Sanyal, "Sharp roll-off lowpass filter with wide stopband using stub-loaded coupled-line hairpin unit," *Microwave and Wireless Components Letters, IEEE*, vol. 21, no. 6, pp. 301-303, June 2011.

[12] M. Hayati, H. Asadbeigi, and A. Sheikhi, "Microstrip lowpass filter with high and wide rejection band," *Electronics Letters*, vol. 48, no. 19, pp. 1217-1219, Sep. 2011.

[13] M. Hayati, H. Abbasi, and F. Shama, "Microstrip lowpass filter with ultrawide stopband and sharp roll-off," *Arabian Journal for Science and Engineering*, vol. 39, no. 8, pp. 6249-53, Aug. 2014.

[14] M. Hayati, S. Roshani, S. Roshani, and F. Shama, "A novel miniaturized Wilkinson power divider with n th harmonic suppression," *Journal of Electromagnetic Waves and Applications*, vol. 27, no. 6, pp. 726-735, Apr. 2013.

[15] J. Yang and W. Wu. "Compact elliptic-function low-pass filter using defected ground structure," *Microwave and Wireless Components Letters IEEE*, vol. 18, no. 9, pp. 578-580, Sep. 2008.

[16] J. P. Wang, L. Ge, Y. X. Guo, and W. Wu, "Miniaturized microstrip lowpass filter with broad

stopband and sharp roll-off," *Electronics Letters*, vol. 46, no. 8, pp. 573-575, Apr. 2010.
[17] M. Hayati and A. Lotfi, "Compact lowpass filter with high and wide rejection in stopband using front coupled tapered CMRC," *Electronics Letters*, vol. 46, no. 12, pp. 846-848, June 2010.
[18] G. Karimi, et al., "Design of modified Z-shaped and T-shaped microstrip filter based on transfer function analysis," *Wireless Personal Communications*, vol. 82, no. 4, pp. 2005-2016, 2015.
[19] M. Hayati, F. Shama, and H. Abbasi, "Compact microstrip lowpass filter with wide stopband and sharp roll-off using tapered resonator," *International Journal of Electronics*, vol. 100, no. 12, pp. 1751-1759, Dec. 2013.
[20] M. Hayati, G. Hajian, F. Shama, and M. Shahbazitabar, "A novel microstrip lowpass filter with ultra-wide stopband using butterfly-shaped resonator," *Caspian Journal of Applied Sciences Research*, vol. 1, no. 13, Dec. 2012.
[21] M. Hayati and A. Sheikhi, "Design of wide stopband lowpass filter with sharp roll-off," *IEICE Electronics Express*, vol. 8, no. 16, pp. 1348-1353, Aug. 2011.
[22] M. Hayati and A. Sheikhi, "Compact lowpass filter with ultra-wide stopband using novel spiral compact microstrip resonant cell," *IEICE Electronics Express*, vol. 8, no. 13, pp. 1028-1033, July 2011.
[23] M. Hayati and A. Sheikhi, "Microstrip lowpass filter with very sharp transition band and wide stopband," *ETRI Journal*, vol. 33, no. 6. pp. 981-984, Dec. 2011.
[24] M. Hayati and A. Sheikhi, "Microstrip lowpass filter with very sharp transition band using T-shaped, patch and stepped impedance resonators," *ETRI Journal*, vol. 35, no. 3, pp. 538-41, June 2013.

Mohsen Hayati received the Ph.D. degrees in Electronics Engineering from Delhi University, Delhi, India, in 1992. He is currently a Professor in the Electrical Engineering Department, Razi University, Kermanshah, Iran. He has authored or co-authored over 165 papers published in international, domestic journals and conference proceedings. His current research interests include microwave and millimeter-wave devices and circuits, application of computational intelligence, artificial neural networks, fuzzy systems, neurofuzzy systems, electronic circuit synthesis, and modeling and simulations.

Farzin Shama is currently working toward the Ph.D. degree in Electrical Engineering in Razi University, Kermanshah, Iran. His research interests include the microwave engineering, and passive and active circuits design. He has been selected as top student of Iran, awarded by First Vice President of Iran in 2015.

Milad Ekhteraei is currently working toward the Ph.D. degree in Electrical Engineering in Azad University, Kermanshah, Iran. His research interests include design and analysis of the microstrip filters, and antennas.

A Low-pass Filter with Sharp Transition and Wide Stop-band Designed based on New Metamaterial Transmission Line

L. Peng [1,2], Y. J. Qiu [1], X. Jiang [1], and C. L. Ruan [3]

[1] Guangxi Key Laboratory of Wireless Wideband Communication and Signal Processing
Guilin University of Electronic Technology, Guilin, Guangxi, 541004, China
penglin528@hotmail.com, 524852836@qq.com, jiang_x@guet.edu.cn

[2] Guangxi Experiment Center of Information Science, Guilin, 541004, Guangxi, China
penglin528@hotmail.com

[3] Institute of Applied Physics
University of Electronic Science and Technology of China, Chengdu, Sichuan, 610054, China
rcl@uestc.edu.cn

Abstract ─A low-pass filter (LPF) with sharp and wide stop-band was designed based on new metamaterial transmission line. Its characteristics were investigated, and found to have good low-pass performances with only one cell. The simulated results of the LPF are in good agreements with the measured results. Two measured transmission poles were observed at 1.35 GHz and 2.13 GHz. The measured 3 dB cut-off frequency is 2.38 GHz and the transmission attenuate to -20 dB at 2.62 GHz, thus, a 240 MHz width sharp transition was achieved. The measured attenuation of the stop-band is larger than 25 dB with two transmission zeros at 2.79 GHz and 5.19 GHz. A wide stop-band over 10 GHz was observed. Therefore, the proposed LPF is a good candidate for RF systems.

Index Terms ─ Low-pass filter, metamaterial transmission line, sharp transition, wide stop-band.

I. INTRODUCTION

Compact and high-performance low-pass filters (LPFs) are highly desired in many communication systems as they can be used to suppress undesired harmonics and spurious signals of the mixing products in RF front-ends [1-4]. These designs are based on several design units of defected ground structure (DGS) [1], stepped-impedance resonator (SIR) [2], lumped elements [3], and finite-ground microstrip line [4]. On the other hand, there has been a growing interest for the use of metamaterial transmission lines (TL) in the development of compact microwave components [5-6] and band-pass filters [7-8]. The concept of metamaterial has been successfully utilized to design complementary split ring resonator (CSRR) based band-pass filters (BPF) [9-11] and LPF [12]; however, these filters need multiple units to obtain sharp transition and wide stop-band, which is not suitable for compactness.

In our previous work [13], a novel metamaterial TL with right-hand (RH) property at low and high-frequency bands and left-hand (LH) property at middle-frequency band was analyzed. The TL exhibits low-pass function with/without notches. As discussed in [13], the high RH band can be designed as stop-band through using large grounded capacitance, and the middle LH band can be designed to be impedance mismatch to have a good low-pass response. It is seen that the LH band is the transition between the low-pass and high-stop bands. Thus, narrower LH band means sharper skirt. Besides LH cell is much smaller than the wavelength. Therefore, compact low-pass filter with sharp and wide stop-band can be designed based on such metamaterial TL.

In this work, the designing of LPF based on our previous studied metamaterial TL [13] is proposed. In [13], an implementation of the metamaterial TL was achieved by cross stubs-loaded square DGS and microstrip line-connected equilateral triangle stubs. It is found that the high RH band of the implementation is transmission forbidden due to the large grounded capacitance produced by the equilateral triangle stubs. Its attenuation is up to 30 dB even for a single cell. However, impedance mismatch happens at the upper part of the low RH band and the middle LH band matches well. Thus, a notch was observed for the low-pass response.

To solve this problem, characteristics of the upper part of the low RH band and the middle LH band must be disturbed. Therefore, dimension of the triangle stubs, which correspond to RH characteristics, were adjusted to impedance match the low RH band. Then, parallel

Submitted On: September 2, 2014
Accepted On: August 11, 2016

stubs connected to the cross stubs were utilized to enhanced LH property. The introduced parallel stubs increase the capacitance C_{h1}, the capacitance C_{v2} and the inductance L_{v2}. Thus, LPF's upper edge is greatly decreased, and the transition width between the pass-band and stop-band is improved. Therefore, the proposed design enables a steep attenuation transition from pass- to stop-band and wide stop-band with only one element, while a large number of components are needed in [1-4, 12]. Thereafter, a LPF was designed successfully. As the fabrication of the proposed LPF is based on printed circuit board (PCB) technique, its manufacture is very easy and extremely low cost, as well as facilitating for integrates into integrated circuit (IC).

II. METAMATERIAL LPF DESIGN AND ANALYSIS

A. Metamaterial LPF design

Configuration of the proposed LPF was shown in Fig. 1 (a). The LPF was fabricated on RT/Duroid 5880 substrate with relative permittivity ε_r = 2.2 and thickness 0.508 mm. Two triangle stubs with length of a side L_t were connected to a 50 Ω microstrip line, and one of their peaks locate at the center of the microstrip line. On the other side of the substrate, a square defected pattern was etched in the ground plane with width L. Four cross stubs with width W_1 were placed in the square defected pattern. To enhance LH property, four parallel stubs were introduced by connecting to the four cross stubs, respectively. Then, the LH capacitance C_{h1}, and the capacitance C_{v2} and inductance L_{v2} are increased, which lead to the decreasing of LH frequency and the obtaining of a desired low-pass function. In simulations, the proposed LPF was excited by two wave ports at the ends of the microstrip line. The wave port is used to imitate infinite length of the microstrip line. Typical parameters of the LPF are L = 16 mm, L_t = 10 mm, W_0 = 1.52 mm, W_1 = 1.8 mm, W_2 = 2.15 mm, g = 0.2 mm, and d = 1.5 mm. In many researches, LH properties were obtained by periodic structures, however, according CRLH theory, CRLH property can be achieved by single cell [5, 13]. Then, to obtained compact size, only one cell was used in this design.

The equivalent circuit model of the structure was derived and shown in Fig. 1 (b). The capacitances and inductances are related to certain parts of the LPF structure. The capacitance C_{v2} is owing to the voltage gradients between the triangular stubs and the cross/ parallel stubs. The inductance L_{v2} is generated by the current flowing along the stubs, while the capacitance C_{v3} is engendered by the voltage gradients between the triangular stubs and the ground plane. Then, the shunt resonant tank (Y_2) that forms by C_{v2}, L_{v2} and C_{v3} was obtained. The gap g_0 between the four parallel stubs are used to produce capacitance C_{h1}, while the etched pattern in the ground plane provides inductance L_{h1}. Then, series resonant tank (Z_1) was achieved. The reactance Z_3 (L_{h3}) is due to the current flowing along the microstrip line. Therefore, it is easily understand that the introduction of parallel stubs greatly increase the LH capacitance C_{h1} and the capacitance C_{v2}. The equivalent circuit model is similar to the basic type 1 of the proposed metamaterial TL in [13]. We must point out that this circuit model is rough as some of the distributed effects may not be considered. However, it offers us a way to perceive insight into the structure.

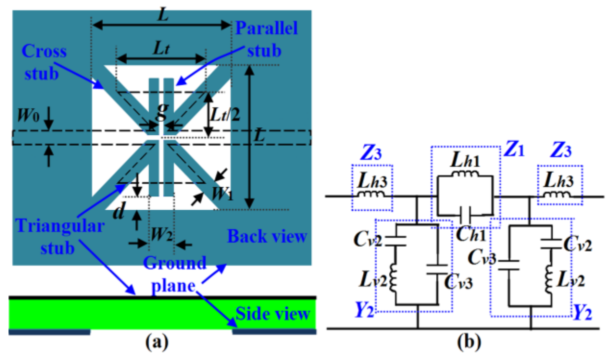

Fig. 1. The proposed LPF: (a) configuration and (b) equivalent-circuit model.

As the S-parameters are utilized for T type network parameters, effective permittivity and permeability extraction, then, simulated results of the proposed LPF were illustrated in Fig. 2 for further analysis. For comparison, results of a structure without parallel stubs (the inset of Fig. 2) were also demonstrated. It is found from the figure that the proposed LPF exhibits excellent low-pass function, wide stop-band and sharp transition. Its -3 dB upper edge is 2.39 GHz, and its transmission attenuation decrease to -20 dB at 2.65 GHz. Therefore, the transition width is 260 MHz. A wide stop-band with attenuation more than 20 dB was obtained over 10 GHz. The results of the structure without parallel stubs show a -3 dB upper edge at 3.15 GHz. Its transmission attenuation decreases to -20 dB at 3.70 GHz. The transition width is 550 MHz. Though the LPFs with and without parallel stubs have the same size, the one with parallel stubs is much superior in better low-pass impedance matching, lower cut-off frequency and sharper transition between pass-band and stop-band.

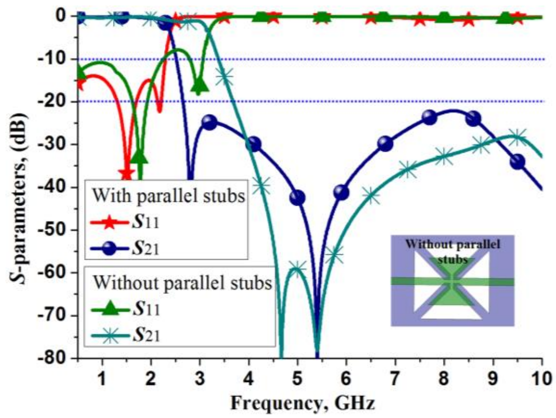

Fig. 2. S-parameters with/without stubs.

B. T type network parameters

The derived lumped-circuit model offers us a way to perceive insight into the structure. However, the calculating of the values of the capacitors and inductors is a burdensome and difficult task. Besides, the equivalent circuit model is a rough one with some distribute parameters not considered. Therefore, equivalent T type network would be a helpful substitution. Extract the parameters of the equivalent T type network is convenient thanks to the microwave network theory and fast developed computer technology. Importantly, T type network enable us conveniently and directly cognize the nature of the structure. As the structure is symmetrical, we assumed its T type network has horizontal branch Z_1 and vertical branch Z_2 as shown in Fig. 3. Typical T type network is derived by solving $ABCD$ matrix according to S parameters of full wave simulation [14]. Then, we have:

$$Z_1 = (A-1)/C \qquad Z_2 = 1/C. \tag{1}$$

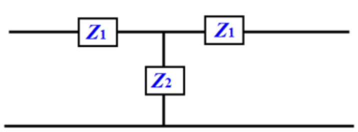

Fig. 3. T type network.

The reactance curves of Z_1 and Z_2 of the two LPFs with and without parallel stubs were calculated by formula (1) and illustrated in Fig. 4. Their corresponding S_{21} curves were also plotted in the figure for comparison. It is found that both the structures with/without parallel stubs exhibit LH property (Imag(Z_1) < 0 and Imag(Z_2) > 0) at middle-frequency band and RH property (Imag(Z_1) > 0 and Imag(Z_2) < 0, Imag(Z_2) is close to zero for the high-frequency band) at low- and high-frequency bands. Balanced conditions are met at the transitions between the low-frequency RH band and middle-frequency LH band, while ENG bands [15] (epsilon-negative, Imag(Z_1) > 0 and Imag(Z_2) > 0) were observed between the middle-frequency LH band and the high-frequency RH band. It is found that the introduction of parallel stubs moves the lower edge of LH band from 2.61 GHz to 2.07 GHz and the width of the LH band is reduced from 570 MHz to 380 MHz, consequently, LPF with more compact size and sharper transition is achieved.

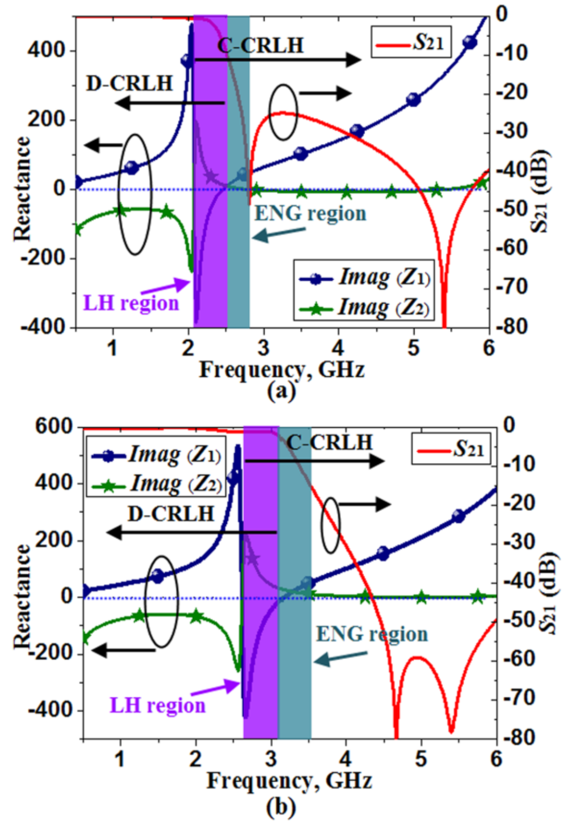

Fig. 4. T type parameters and S_{21} parameter: (a) the proposed LPF with parallel stubs, and (b) the LPF without parallel stubs.

C. Effective permittivity and permeability

As the dimension of the unit cell is much less than the operational wavelength, the structure can be characterized by quasi-TEM model and effective medium theory. Thereby, effective permittivity $\varepsilon_{\mathrm{eff}}$ and effective permeability μ_{eff} will be extracted to further validate our conclusion. An improved Nicolson-Ross-Weir (NRW) approach was adopted for the effective constitutive parameters extraction [16]. First, we list the formula in the following:

$$\mu_{eff} = \frac{2}{jk_0 d}\frac{1-(S_{21}-S_{11})}{1+(S_{21}-S_{11})} \qquad \varepsilon_{eff} = \mu_{eff} + j\frac{2S_{11}}{k_0 d}, \tag{2}$$

where k_0 is the wave number of free space, d is the length of the unit-cell, S_{11} and S_{21} are the scattering parameters. The transmission factor can be described as $\tau = \exp(-jkd)$.

The extracted effective permittivity and permeability for the structures with/without parallel stubs were illustrated in Fig. 5, and their S_{21} parameters were also presented for comparison. Their effective permittivity and permeability are positive for the low- and high-frequency RH bands, and negative for the middle-frequency LH band. The ENG regions have negative permittivity and positive permeability. The constitutive parameters have good agreement with the *T* type network parameters, then, validity of these extract approaches on our structures were verified.

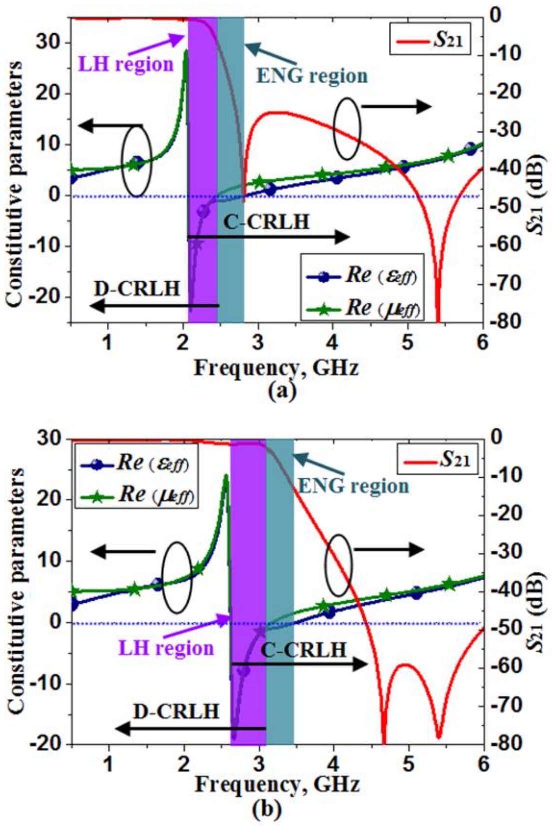

Fig. 5. Constitutive parameters and S_{21} parameter: (a) the proposed LPF with parallel stubs, and (b) the LPF without parallel stubs.

III. RESULTS AND DISCUSSION

We have investigated the LPF by means of equivalent circuit model, *T* type network, and constitutive parameters in Section II. Then, the operational mechanism of the LPF was revealed. To better understand the LPF's characteristics, and utilize it for further design in practical applications, more discussion and results were illustrated in this Section.

A. Parametric study

In Section II A, we found the derived equivalent circuit model elements have certain connection with certain parts of the LPF, therefore, the adjusting of certain parameters of the structure will tune their corresponding capacitances or inductances, consequently LPF performances. Therefore, the proposed LPF with parallel stubs were studied by sweeping its three key parameters (g, d, and L_t) as shown in Fig. 6. The simulated *S*-parameters for the three parameters were demonstrated in Figs. 6 (a), (b) and (c), respectively, while their extracted constitutive parameters were illustrated in Figs. 6 (d), (e) and (f) correspondingly. Note that, when one parameter is changed, others are fixed.

According to the capacitance calculation formulation $C = \varepsilon S/d_0$ of parallel-plate conductors with area S and distance d_0, if the parameter g is increased from 0.2 mm to 0.6 mm, it is equivalent to enlarge the distance d_0. Therefore, the coupling between the parallel stubs is minimized and LH capacitance C_{h1} is decreased. Subsequently, the LH frequency increase as demonstrated in Fig. 6 (d). The ascending of the LH band results in increasing of the cut-off frequency as shown in Fig. 6 (a). While the parameter d increased from 1.5 mm to 5.5 mm, the lengths of the parallel stubs are shortened. Thus, it is equivalent to reduce area S of a parallel-plate, consequently, both the LH capacitance C_{h1} and inductance L_{v2} are decreased. Therefore, both the cut-off frequency and LH band is ascended as exhibited in Figs. 6 (b) and (e). It is found from Figs. 6 (a) and (b) that the decreasing of C_{h1} (LH feature weakened) also leads to a more broadened transition. For example, when g increased from 0.2 mm to 0.6 mm, the width of the transition for -3 dB to -20 dB increased from 260 MHz to 390 MHz, while d increased from 1.5 mm to 5.5 mm, the width transition for -3 dB to -20 dB increased from 260 MHz to 480 MHz. While parameter L_t is increased, the couplings between the triangular stubs and cross/parallel stubs/ground plane are increased. Therefore, both the capacitances C_{v2} and C_{v3} are enhanced. Then, the parameter L_t mainly affects RH characteristics of the proposed LPF. Therefore, the high RH stop-band presents better attenuation and the middle LH band is almost unmoved with L_t increasing as shown in Figs. 6 (c) and (f). However, enhanced RH feature results in difficulty for impedance matching of upper part of low RH band. At last, we can conclude from Fig. 6 that, LH enhancement lead to sharper transition and lower cut-off frequency, while RH enhancement means better high RH stop-band attenuation. However, by considering impedance matching of the pass-band (especially upper part of low RH band), trade-off among impedance matching, transition width and high stop-band must be considered by its LH and RH properties.

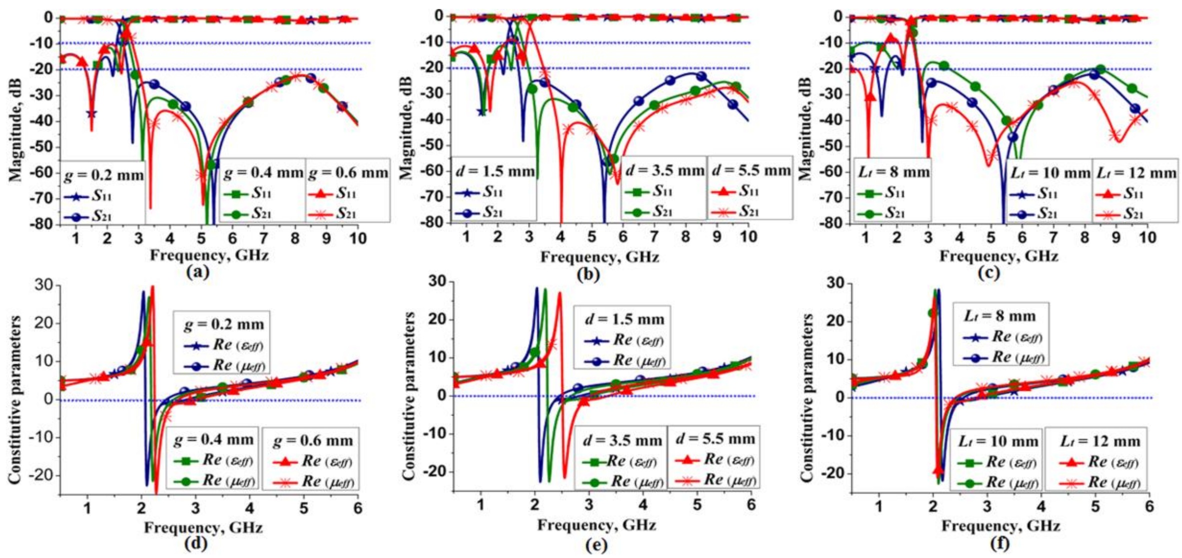

Fig. 6. Frequency responses of the filter: (a) *S*-parameters in terms of g (C_{h1}), (b) *S*-parameters in terms of d (C_{h1} and L_{v2}), (c) *S*-parameters in terms of L_t (C_{v2} and C_{v3}), (d) constitutive parameters in terms of g (C_{h1}), (e) constitutive parameters in terms of d (C_{h1} and L_{v2}), and (f) constitutive parameters in terms of L_t (C_{v2} and C_{v3}).

B. Fabrication and measurement

To further validate the properties of the proposed LPF, it was fabricated as illustrated in Fig. 7. Based on printed circuit board (PCB) technique, the manufacture of the proposed LPF is very easy and extremely low cost, as well as facilitating for integrates into integrated circuit (IC). Two SMA connectors were soldered at the ends of the microstrip fed line for measurement as presented in the figure. Note that, the measurements were performed by an Agilent E5071C ENA series network analyzer with the highest measurable frequency at 8.5 GHz. The simulated and measured *S*-parameters of the proposed LPF are demonstrated in Fig. 8 with good agreements between them observed. The measured 3 dB cut-off frequency is 2.38 GHz with two transmission poles at 1.35 GHz and 2.13 GHz, and two transmission zeros at 2.79 GHz and 5.19 GHz. The transmission attenuation decreased to -20 dB at 2.62 GHz. Therefore, the measured transition width is 240 MHz. Besides, the measured attenuation of the stop-band is larger than 25 dB.

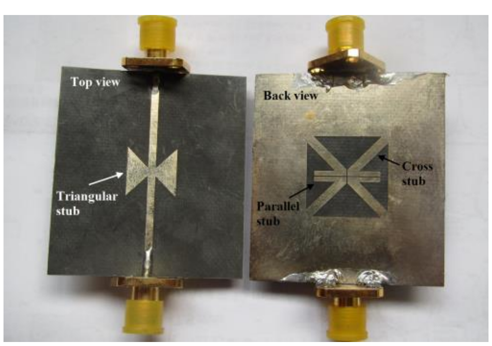

Fig. 7. Photograph of the proposed LPF.

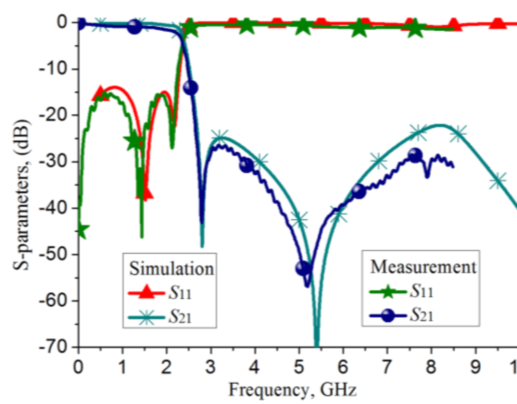

Fig. 8. Simulated and measured *S*-parameters.

IV. CONCLUSION

This paper provides a new approach for LPF designing by applying metamaterial TL technology. Equivalent circuit model of the proposed LPF was derived, and comparison of LPFs with/without parallel stubs was conducted by *S*-parameters, *T* type network parameters and constitutive parameters. Parametric study was performed to reveal the relations between LH/RH characteristics and LPF performances (*S* parameters). Research found the effects of LH and RH features on the cut-off frequency, transition width and high-stop band, which in turn could be used to guide the designing of LPF. The proposed LPF has sharp transition and wide stop-band that turn out to be good candidate for RF front-end circuits.

ACKNOWLEDGMENT

This work is supported in part by National Natural Science Foundation of China (61401110 & 61371056), in part by Natural Science Foundation of Guangxi (2015GXNSFBA139244), in part by Dean Project of Guangxi Key Laboratory of Wireless Wideband Communication and Signal Processing (GXKL06160109), in part by Guangxi Experiment Center of Information Science (YB1405), and in part by Program for Innovative Research Team of GUET.

REFERENCES

[1] M. A. Aziz, A. M. E. Safwat, F. Podevin, and A. Vilcot, "Coplanar waveguide filters based on multibehavior etched-ground stubs," *IEEE Trans. Comp. Packaging Tech.*, vol. 32, no. 4, pp. 816-824, 2009.

[2] L. Wang, H. C. Yang, and Y. Li, "Design of compact microstrip low-pass filter with ultra-wide stopband using SIRs," *Progress Electromag. Res. Lett.*, vol. 18, pp. 179-186, 2010.

[3] D. Kaddour, E. Pistono, J. Duchamp, J. D. Arnould, H. Eusèbe, P. Ferrari, and R. G. Harrison, "A compact and selective low-pass filter with reduced spurious responses, based on CPW tapered periodic structures," *IEEE Trans. Microw. Theory Tech.*, vol. 54, no. 6, pp. 2367-2375, 2006.

[4] S. Sun and L. Zhu, "Stopband-enhanced and size-miniaturized low-pass filters using high-impedance property of offset finite-ground microstrip line," *IEEE Trans. Microw. Theory Tech.*, vol. 53, no. 9, pp. 2844-2850, 2005.

[5] C. Caloz and T. Itho, *Electromagnetic Metamaterials: Transmission line Theory and Microwave Applications (The Engineering Approach)*. Wiley & Sons, Hoboken, New Jersey, 2006.

[6] R. Marques, F. Martin, and M. Sorolla, *Metamaterials with Negative Parameters: Theory, Design, and Microwave Applications*. John Wiley & Sons, New York, 2008.

[7] M. Oliaei, M. Tayarani, and M. Karami, "Compact microstrip bandpass filter improved by DMS and ring resonator," *Progress Electromag. Res. Lett.*, vol. 45, pp. 7-12, 2014.

[8] M. Gil, J. Bonache, and F. Martín, "Metamaterial filters: A review," *Metamaterials*, vol. 2, no. 4, pp. 186-197, 2008.

[9] J. Bonache, F. Martin, J. García-García, I. Gil, R. Marques, and M. Sorolla, "Ultra wide band pass filters (UWBPF) based on complementary split rings resonators," *Microw. Optical Tech. Lett.*, vol. 46, no. 3, pp. 283-286, 2005.

[10] J. Bonache, I. Gil, J. Garcia-Garcia, and F. Martin, "Novel microstrip bandpass filters based on complementary split-ring resonators," *IEEE Trans. Microw. Theory Tech.*, vol. 54, no. 1, pp. 265-271, 2006.

[11] M. Gil, J. Bonache, J. Garcia-Garcia, J. Martel, and F. Martin, "Composite right/left-handed metamaterial transmission lines based on complementary split-rings resonators and their applications to very wideband and compact filter design," *IEEE Trans. Microw. Theory Tech.*, vol. 55, no. 6, pp. 1296-1304, 2007.

[12] A. Ali and Z. Hu, "Negative permittivity metamaterial microstrip binomial low-pass filter with sharper cut-off and reduced size," *IET Microw. Antennas & Propag.*, vol. 2, no. 1, pp. 15-18, 2008.

[13] L. Peng and C. L. Ruan, "Design, analysis and implementation of novel metamaterial transmission line with dual composite right/left-handed and conventional composite right/left-handed properties," *IET Microw. Antennas & Propag.*, vol. 6, no. 15, pp. 1687-1695, 2012.

[14] D. M. Pozar, *Microwave Engineerng. 3rd ed*, J. Wiley, Hoboken, N. J., 2005.

[15] A. Alù and N. Engheta, "Pairing an epsilon-negative slab with a mu-negative slab: resonance, tunneling and transparency," *IEEE Trans. Antennas Propagat.*, vol. 51, no. 10, pp. 2558-2571, 2003.

[16] R. W. Ziolkowski, "Design, fabrication, and testing of double negative metamaterials," *IEEE Trans. Antennas Propagat.*, vol. 51, no. 7, pp. 1516-1529, 2003.

Lin Peng was born in Guangxi Province, China, in 1981. He received the B.E. degree in Science and Technology of Electronic Information, Master and Doctor's degree in Radio Physics from University of Electronic Science and Technology of China (UESTC), Chengdu, China, in 2005, 2008 and 2013, respectively. From 2011 to 2013, he was sponsored by the China Scholarship Council (CSC) to study at the University of Houston (UH) as joint Ph.D. student. From 2013, he joined Guilin University of Electronic Technology (GUET), and became an Associate Professor from Jan. 2016.

Peng has published over 20 papers as first and corresponding author. He is also co-author with over 20 papers. In recent years, he is sponsored by several funds, such as Fundamental Research Funds for the Central Universities, National Natural Science Foundation of China, Program for Innovative Research Team of Guilin University of Electronic Technology, and Guangxi Wireless Broadband Communication and Signal Processing Key Laboratory, etc. Peng serves as Reviewer for *IEEE TMTT*, *IEEE MWCL*, *IEEE AWPL*, *ACES*, *EL*, *Wireless Personal Communications*, *Progress* *in Electromagnetics Research*, *IET Microwave, Antennas & Propagation*, and *Journal of Electromagnetic Waves and Applications*.

Peng's research interests include Antenna/Filter design (For example: communication antennas, Zeroth-order resonator (ZOR) antenna, circular-polarized antenna, UWB antenna, Microstrip antenna and WLAN antenna), Electromagnetic bandgap (EBG) structure design and its application in antenna, Composite right/left-handed (CRLH) transmission line and its applications, and Conformal antenna array.

Yu-Jie Qiu was born in Jiangsu Province, China, in 1990. He received the B.E. degree in Communication Engineering from Tongda College of Nanjing University of Posts and Telecommunications, Jiangsu, China, in 2012, and the Master's degree in Electronic and Communication Engineering from Guilin University of Electronic Technology (GUET), Guangxi, China, in 2015. He is currently a Research Assistant at the GUET. His research interests include antennas and metamaterials.

Xing Jiang received the Master's degree in Electromagnetic Field and Microwave Technology from Beijing Institute of Technology (BIT), in 1986. From 2000, she joined Guilin University of Electronic Technology (GUET) as Professor. Jiang has published over 30 papers. She also sponsored by National Natural Science Foundation of China and Natural Science Foundation of Guangxi. Jiang is a Senior Member of China Communications Society, a Member of Chinese Institute of Electronics (CIE). Jiang's research interests include Smart communication system design, Conformal antenna array, and Bio-electromagnetics.

Cheng-Li Ruan received the Ph.D. degree in Electromagnetic Field and Microwave Technology from the University of Electronic Science and Technology of China (UESTC), Chengdu, China, in 1983. From 1985 to 1988, he was an Associate Professor at UESTC. Since 1988, he has been a Professor in the Institute of Applied Physics at UESTC. His current research interests include millimeter wave techniques, electromagnetic scattering, antenna theory, electromagnetic missiles and UWB electromagnetic. He has published over 90 papers on these subjects.

Ruan is a Member of the Chinese Institute of Electronics and the Chinese Electricity Society.

High Selectivity Balanced Filters Based on Transversal Signal-interaction Concepts

Wenjie Feng, Meiling Hong, and Wenquan Che

Department of Communication Engineering
Nanjing University of Science and Technology, Nanjing, 210094, China
fengwenjie1985@163.com

Abstract ─ Two novel high selectivity balanced filters based on transversal signal-interaction concepts with wideband common mode suppression are proposed in this paper. Four and six transmission zeros near each passband are realized to improve the selectivity for the differential mode. In addition, the common mode can be suppressed with insertion loss greater than 15 dB over a wide frequency band. Two prototypes (ε_r = 2.65, h = 0.5 mm, tan δ = 0.003) with 3-dB fractional bandwidths of 31.3% and 32% for the differential mode with upper stopband greater than 18 dB are designed and fabricated. Good agreements can be observed between measured results and theoretical expectations.

Index Terms ─ Balanced filter, differential/common mode, open/shorted coupled lines, transmission zeros, transversal signal-interaction concepts.

I. INTRODUCTION

Balanced circuits have recently attracted special attention in communication systems for their higher immunity to the environmental noises, better dynamic range, and lower electromagnetic interference [1]. Many different balanced filters with selective filtering of differential mode (DM) signal and suppression for common-mode (CM) response are illustrated in [2]-[12]. In [2], the multi-stage branch-line topologies on a single-layer microstrip line were utilized to design a class of wideband balanced filters, but these filters have disadvantages of large overall circuit area. Some differential ultra-wideband (UWB) balanced bandpass filters based on double-sided parallel-strip line (DSPSL) are illustrated in [3], however, the upper stopbands for the differential mode are a little narrow. In [4], wideband differential filters employing the transversal signal-interaction concept are used to improve the common mode suppression, as well as the simple design theory with large insertion loss. In [5], the low-loss balanced filter with wideband common mode suppression using microstrip-slotline coupling are realized, but the numbers of transmission zeros near the differential mode passband are difficult to increase. In addition, the T-shaped resonator in [6] and ring resonator in [7]-[8] were applied to design balanced filters. In [9], the common-mode suppression of the balanced bandpass filter can be kept at a high level by adding a varactor to the center of the resonator. In [10], a balanced SIW filter using source-load coupling is proposed. To further improve the selectivity of the balanced filters, coupled lines and quarter/half-wavelength open/shorted stubs have been widely used [11-12].

In this paper, two novel balanced filter circuits based on transversal signal-interaction concepts with multiple transmission zeros for the differential/common mode are proposed. Four and six transmission zeros near the differential mode passband can be easily realized using the transversal signal interference concept, and five and seven transmission zeros can be also used to realize wideband common mode suppression. Two prototypes of the balanced filters operating at 3.0 GHz are constructed on the dielectric substrate with ε_r = 2.65, h = 0.5 mm, and tan δ = 0.003.

II. ANALYSIS OF PROPOSED BALANCED FILTERS

In this section, two balanced filters based on transversal signal-interaction concepts are analyzed in detail. The differential mode and common mode circuit are used to analyze the transmission characteristics of the two balanced filters in *Part A* and *Part B*, the simulated results of the two balanced filters are given in *Part C*.

A. Balanced filter analysis (Structure I)

Figure 1 (a) shows the ideal circuit of the proposed balanced filter structure with four transmission zeros. Four open/shorted coupled lines (even/odd-mode characteristic impedance Z_{oe2} and Z_{oo2}, electrical length θ) with two quarter-wavelength transmission lines (characteristic impedance Z_1, electrical length θ) on each side are shunted connected in the input/output ports 1, 1', 2, 2'. Four open coupled lines (even/odd-mode characteristic impedance Z_{oe1} and Z_{oo1}, electrical length θ) are located in the center of the equivalent circuit with two shorted stubs (characteristic impedance Z_1, electrical

Submitted On: April 5, 2016
Accepted On: July 15, 2016

length θ) and an open stub (characteristic impedance Z_1, electrical length 2θ). The characteristic impedances of the microstrip lines at the input/output ports are Z_0 = 50 Ω.

When the differential mode signals are excited from ports 1 and 1' in Fig. 1 (a), a virtual short appears along the symmetric lines, as shown in Fig. 1 (b). The odd-mode equivalent circuits for the differential mode are shown in Fig. 2 (a), and the even/odd-mode input admittances for the differential mode are:

$$Y_{o1-DM} = -j\frac{2\cos\theta\left[2Z_{oe1}Z_{oo1}\cos^2\theta - Z_1(Z_{oe1}+Z_{oo1})\sin^2\theta\right]}{2Z_{oe1}Z_{oo1}(Z_{oe1}+Z_{oo1})\sin\theta\cos^2\theta + Z_1\sin\theta\left[(Z_{oe1}+Z_{oo1})^2\cos^2\theta-(Z_{oe1}-Z_{oo1})^2\right]} + j\frac{-(Y_{oe2}+Y_{oo2})^2Z_2\cos^2\theta+(Y_{oo2}-Y_{oe2})^2Z_2+2(Y_{oe2}+Y_{oo2})\sin^2\theta}{(Y_{oe2}+Y_{oo2})^2Z_2^2\sin\theta\cos\theta-(Y_{oo2}-Y_{oe2})^2Z_2^2\tan\theta+(Y_{oe2}+Y_{oo2})Z_2\sin 2\theta}, \tag{1}$$

$$Y_{e1-DM} = \frac{j[4Z_1\tan^2\theta-2(Z_{oe1}+Z_{oo1})]}{(Z_{oe1}+Z_{oo1})(2Z_1+Z_{oe1}+Z_{oo1})\tan\theta} + \frac{j[Z_2(Z_{oe2}+Z_{oo2})+2Z_{oe2}Z_{oo2}]}{2Z_{oe2}Z_{oo2}\cot\theta-Z_2^2(Z_{oe2}+Z_{oo2})\tan\theta}, \tag{2}$$

$$Y_{o2-DM} = -j\frac{2\cos\theta\left[2Z_{oe1}Z_{oo1}\cos^2\theta - Z_1(Z_{oe1}+Z_{oo1})\sin^2\theta\right]}{2Z_{oe1}Z_{oo1}(Z_{oe1}+Z_{oo1})\sin\theta\cos^2\theta + Z_1\sin\theta\left[(Z_{oe1}+Z_{oo1})^2\cos^2\theta-(Z_{oe1}-Z_{oo1})^2\right]} + j\frac{Z_2(Z_{oe2}+Z_{oo2})+2Z_{oe2}Z_{oo2}}{2Z_2Z_{oe2}Z_{oo2}\cot\theta-Z_2^2(Z_{oe2}+Z_{oo2})\tan\theta}, \tag{3}$$

$$Y_{e2-DM} = Y_{e1-DM}. \tag{4}$$

When $Y_{e/o\text{-}DM}$=0, the resonator frequencies in the passband for the odd-mode for the differential mode can be calculated as:

$$\theta_{o1} = \arccos\sqrt{\frac{-B\pm\sqrt{B^2-4AC}}{2A}},\quad \theta_{o2} = \pi - \arccos\sqrt{\frac{-B\pm\sqrt{B^2-4AC}}{2A}},$$
$$A = a_1^2a_2Z_1(a_2Z_2+2)+2a_1a_2^2Z_2(Z_1Z_2+Z_{oe1}Z_{oo1})+4a_1a_2(Z_1Z_2+Z_{oe1}Z_{oo1}) + 4a_2Z_2Z_{oe1}Z_{oo1}(a_2Z_2+2),$$
$$B = -[a_1^2Z_1(b_2^2Z_2+2a_2)+2a_1a_2(a_2Z_1Z_2^2+2Z_1Z_2+2Z_{oe1}Z_{oo1})+2a_1b_2^2Z_1Z_2^2 + 2a_1b_2^2Z_2Z_{oe1}Z_{oo1}+a_2b_1^2Z_1(a_2Z_2+2)+4b_2^2Z_2^2Z_{oe1}Z_{oo1}],$$
$$C = 2a_1b_2^2Z_1Z_2^2+b_1^2b_2^2Z_1Z_2+2a_2b_1^2Z_1,$$
$$a_1 = Z_{oe1}+Z_{oo1},\quad b_1 = Z_{oe1}-Z_{oo1},$$
$$a_2 = Y_{oe2}+Y_{oo2},\quad b_2 = Y_{oo2}-Y_{oe2}. \tag{5}$$

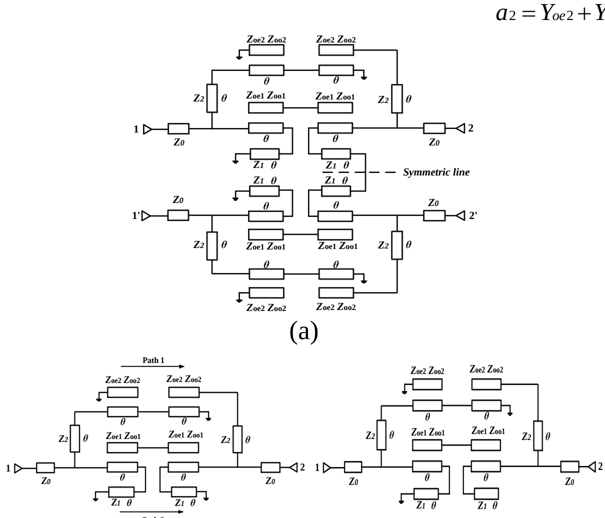

(a)

(b) (c)

Fig. 1. (a) The ideal circuit of the balanced filter, (b) equivalent circuit for the differential mode, and (c) equivalent circuit for the common mode. (*Structure I*).

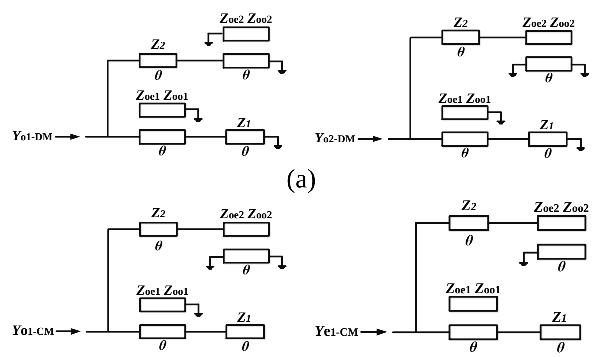

(a)

(b)

Fig. 2. (a) Odd-mode equivalent circuit of differential mode circuit, and (b) even/odd-mode equivalent circuit of common mode circuit. (*Structure I*).

Figures 3 (a)-(d) plot the odd-mode resonant frequencies versus θ and the simulated results of the circuit in Figs. 1 (b)-(c). Due to the superposition of signals for Paths 1 and 2, four transmission zeros (f_{tz1},

f_{tz2}, f_{tz3}, f_{tz4}) can be easily achieved for the proposed balanced filter [13]. The 3-dB bandwidth of the differential mode is mainly determined by the odd-modes f_{o1} and f_{o2}. In addition, the odd-modes f_{o1} and f_{o2} move towards f_0 as Z_1 increases, and the 3-dB bandwidth of the differential mode increases as the coupling coefficient k_1 ($k_1 = (Z_{oe1}-Z_{oo1})/(Z_{oe1}+Z_{oo1})$) increases. The unwanted even/odd modes for the common mode can be suppressed less than -30 dB by the five transmission zeros. Four transmission zeros (f_{tz1}, f_{tz2}, f_{tz3}, f_{tz4}) move away from f_0 as the characteristic impedance Z_1 increases. In this way, the out-of-band harmonic suppression of the differential mode can be adjusted by the characteristic impedance Z_2 without changing the bandwidth of the differential mode. Next, to further improve the selectivity and the common mode suppression of the balanced filter with four transmission zeros, another high selectivity balanced filter structure with six transmission zeros close to the differential mode passband, and wideband common mode suppression will be presented.

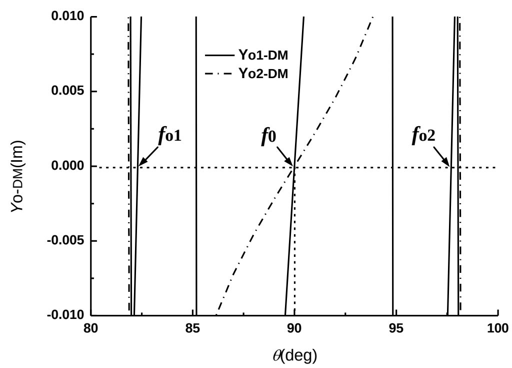

(a)

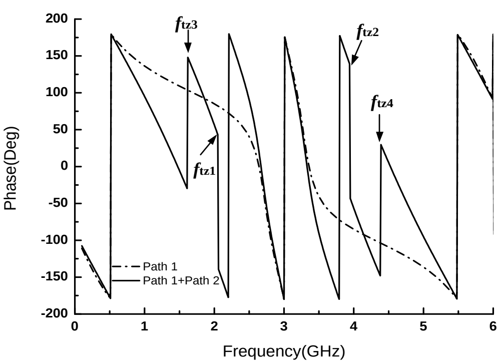

(b)

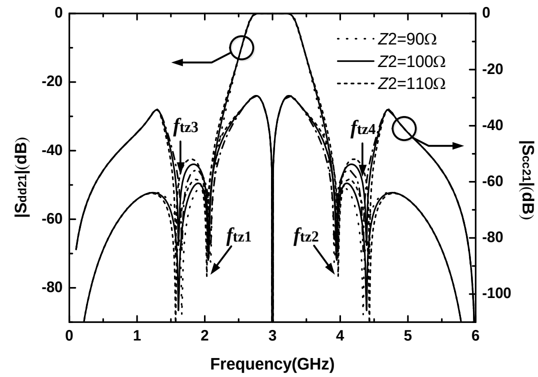

(c)

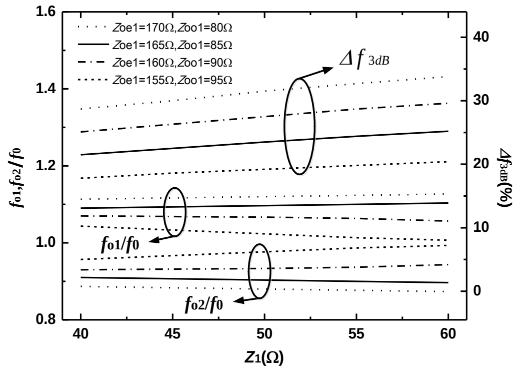

(d)

Fig. 3. (a) Analysis of resonator frequencies versus θ. (b) phase of $|S_{dd21}|$ ($Z_0 = 50\ \Omega$, $Z_1 = 50\ \Omega$, $Z_2 = 100\ \Omega$, $Z_{oe1} = 160\ \Omega$, $Z_{oo1} = 90\ \Omega$, $Z_{oe2} = 150\ \Omega$, $Z_{oo2} = 110\ \Omega$, $f_0 = 3.0$ GHz, $\theta = 90°$). (c) $|S_{dd21}|$& $|S_{cc21}|$ versus Z_2. (d) f_{o1}, f_{o2}/f_0, Δf_{3dB} versus Z_{oe1}, Z_{oo1}, Z_1. (*Structure I*).

B. Balanced filter analysis (Structure II)

Figure 4 (a) shows the ideal circuit of the balanced filter structure with two half-wavelength open stubs (Z_3, 2θ), instead of two quarter-wavelength short stubs (Z_1, θ), and the other part is the same as the balanced filter of *Structure I*.

As discussed in *Part A*, when the differential/ common mode are excited from ports 1 and 1' in Fig. 4 (a), a virtual short/open appears along the symmetric lines. The even/odd-mode equivalent circuits for the differential/common mode are shown Figs. 5 (a)-(b), and the input admittance for the differential mode of Fig. 5 (a) can be illustrated as:

$$Y_{o1-DM} = j\frac{Z_3(Z_{oe1}+Z_{oo1})\sin 2\theta\cos 2\theta + 4Z_{oe1}Z_{oo1}\sin 2\theta\cos^2\theta}{Z_3\cos 2\theta\left[(Z_{oe1}-Z_{oo1})^2-(Z_{oe1}+Z_{oo1})^2\cos^2\theta\right]-Z_{oe1}Z_{oo1}(Z_{oe1}+Z_{oo1})\sin^2 2\theta}$$
$$+ j\frac{-(Y_{oe2}+Y_{oo2})^2 Z_2\cos^2\theta+(Y_{oo2}-Y_{oe2})^2 Z_2+2(Y_{oe2}+Y_{oo2})\sin^2\theta}{(Y_{oe2}+Y_{oo2})^2 Z_2^{\,2}\sin\theta\cos\theta-(Y_{oo2}-Y_{oe2})^2 Z_2^{\,2}\tan\theta+(Y_{oe2}+Y_{oo2})Z_2\sin 2\theta}, \quad (6)$$

$$Y_{e1-DM} = \frac{-j[2(Z_{oe1}+Z_{oo1})\tan 2\theta+4Z_3\tan\theta]}{(Z_{oe1}+Z_{oo1})^2\tan\theta\tan 2\theta-2Z_3(Z_{oe1}+Z_{oo1})}$$
$$+\frac{j[Z_2(Z_{oe2}+Z_{oo2})+2Z_{oe2}Z_{oo2}]}{2Z_2Z_{oe2}Z_{oo2}\cot\theta-Z_2^{\,2}(Z_{oe2}+Z_{oo2})\tan\theta}. \quad (7)$$

When $Y_{e/o\text{-}DM}$=0, the resonator frequencies in the passband for the even -mode for the differential mode can be calculated as:

$$\theta_{e1} = \arctan\sqrt{\frac{-B \pm \sqrt{B^2 - 4AC}}{2A}}, \quad \theta_{e2} = \pi - \arctan\sqrt{\frac{-B \pm \sqrt{B^2 - 4AC}}{2A}},$$
$$A = -4Z_1Z_2^{\,2}(Z_{oe1} + Z_{oo1}),$$
$$B = (Z_{oe1} + Z_{oo1})^2[2Z_{oe2}Z_{oo2} + Z_2(Z_{oe2} + Z_{oo2})] + 2(Z_{oe1} + Z_{oo1})(Z_{oe2} + Z_{oo2})(Z_1Z_2 + Z_2^{\,2})$$
$$+4Z_1Z_{oe2}Z_{oo2}(Z_{oe1} + Z_{oo1}) + 8Z_1Z_2Z_{oe2}Z_{oo2},$$
$$C = -4Z_2Z_{oe2}Z_{oo2}(Z_{oe1} + Z_{oo1}). \tag{8}$$

Figures 6 (a)-(c) show the even/odd-mode resonant frequencies for the differential mode circuit versus θ and the simulated results of the circuit in Figs. 4 (b)-(c). Due to the superposition of signals for Paths 1 and 2, six transmission zeros (f_{tz1}, f_{tz2}, f_{tz3}, f_{tz4}, f_{tz5}, f_{tz6}) can be easily achieved for the proposed balanced filter [13]. Compared with the balanced filter of *Structure I*, two additional transmission zeros (f_{tz5}, f_{tz6}) are located at $0.5f_0$ and $1.5f_0$, which can be used to further improve the differential mode passband selectivity and the common mode suppression level from 0 to f_{tz1}, f_{tz2} to 2 f_0. In addition, the locations of two transmission zeros (f_{tz5}, f_{tz6}) do not change with all parameters of the circuit, and the locations of another four transmission zeros (f_{tz1}, f_{tz2}, f_{tz3}, f_{tz4}) do not change with Z_{oe1}, Z_{oo1}, Z_1 and Z_3. The 3-dB bandwidth of the differential mode is mainly determined by the even-modes f_{e1} and f_{e2}, and the 3-dB bandwidth of the differential mode decreases and differential/common mode suppression becomes better with the decrease of k_1 (k_1= (Z_{oe1}-Z_{oo1})/(Z_{oe1}+Z_{oo1})). The common mode can be suppressed less than -30 dB by the seven transmission zeros. Compared with the balanced filter of *Structure I*, the selectivity and common mode suppression of the balanced filter of *Structure II* has been further improved.

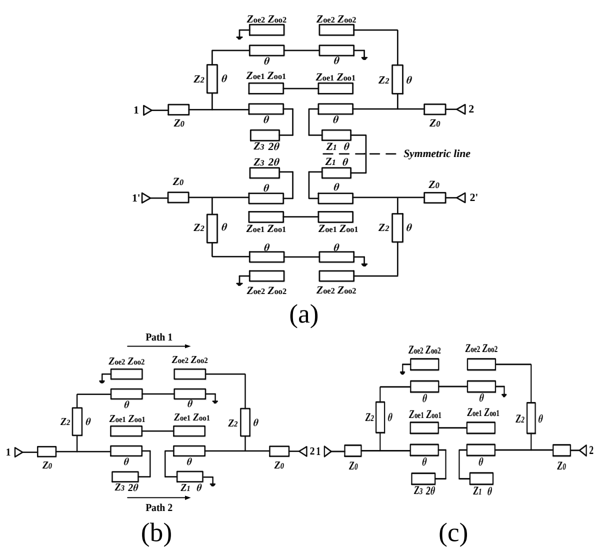

Fig. 4. (a) The ideal circuit of the balanced filter, (b) equivalent circuit for the differential mode, and (c) equivalent circuit for the common mode. (*Structure II*).

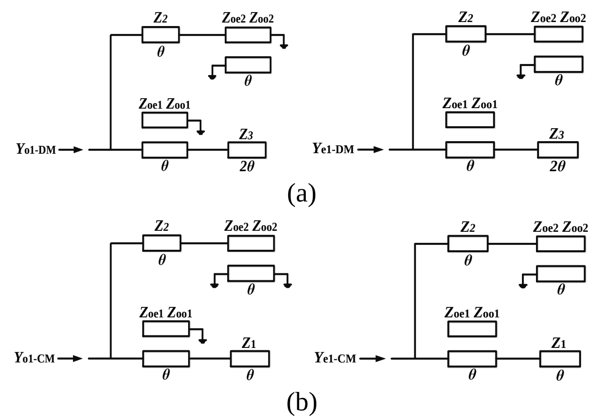

Fig. 5 (a) Even/odd-mode equivalent circuit of differential mode circuit, and (b) even/odd-mode equivalent circuit of common mode circuit. (*Structure II*).

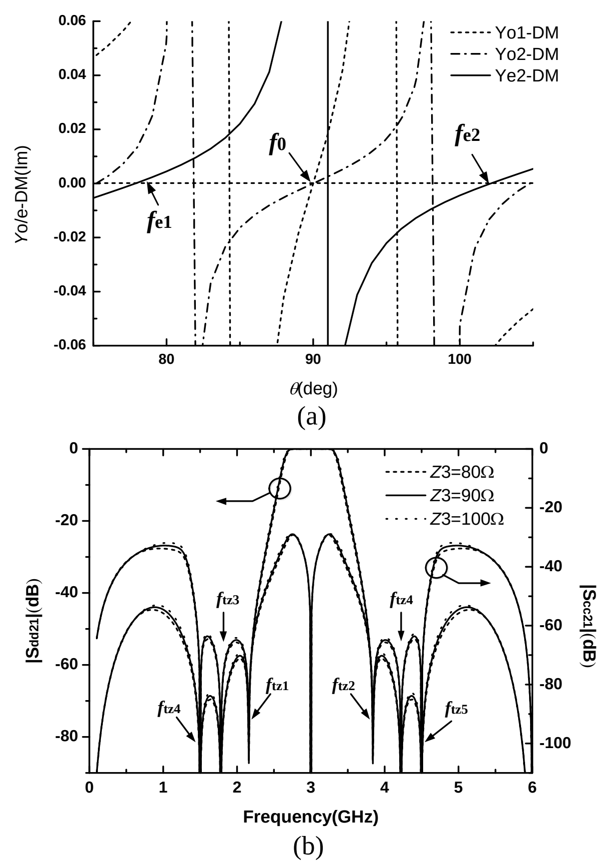

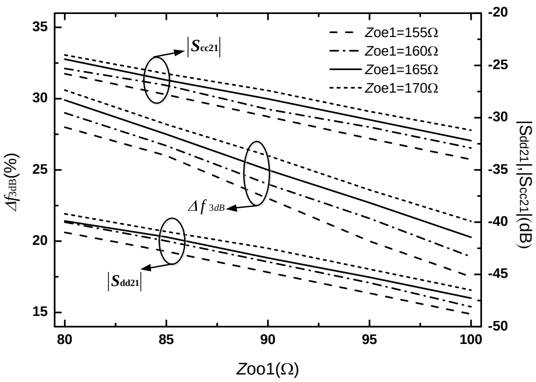

(c)

Fig. 6. (a) Analysis of resonator frequencies versus θ for the differential mode. (b) $|S_{dd21}|$& $|S_{cc21}|$ versus Z_3 ($Z_0 = 50\ \Omega$, $Z_1 = 50\ \Omega$, $Z_2 = 70\ \Omega$, $Z_{oe1} = 160\ \Omega$, $Z_{oo1} = 90\ \Omega$, $Z_{oe2} = 150\ \Omega$, $Z_{oo2} = 110\ \Omega$, $f_0 = 3.0$ GHz, $\theta = 90°$). (c) Δf_{3dB}, $|S_{dd21}|$, $|S_{cc21}|$ versus Z_{oe1}, Z_{oo1}. (*Structure II*).

C. Proposed two balanced bandpass filters

Referring to the discussions and the simulated results in *Part A and B*, the final parameters for the filters of Figs. 1, 4 are listed as below: $Z_0 = 50\ \Omega$, $Z_1 = 50\ \Omega$, $Z_2 = 100\ \Omega$, $Z_{oe1} = 160\ \Omega$, $Z_{oo1} = 90\ \Omega$, $Z_{oe2} = 150\ \Omega$, $Z_{oo1} = 110\ \Omega$; $Z_0 = 50\ \Omega$, $Z_1 = 50\ \Omega$, $Z_2 = 70\ \Omega$, $Z_3 = 90\ \Omega$, $Z_{oe1} = 160\ \Omega$, $Z_{oo1} = 90\ \Omega$, $Z_{oe2} = 150\ \Omega$, $Z_{oo1} = 110\ \Omega$. The structure parameters for two balanced filters (52.28 mm × 35.85 mm, 55.48 mm × 36.26 mm) shown in Figs. 7 (a)-(b) are: $l_1 = 15.31$ mm, $l_2 = 17.5$ mm, $l_3 = 6.66$ mm, $l_4 = 10.42$ mm, $l_5 = 15.46$ mm, $l_6 = 16.06$ mm, $l_7 = 10.6$ mm, $l_8 = 12.55$ mm, $l_9 = 11.65$ mm, $l_{10} = 4.2$ mm, $l_{11} = 9.42$ mm, $l_{12} = 4$ mm, $w_0 = w_3 = w_5 = 1.34$ mm, $w_1 = 0.2$ mm, $w_2 = 0.35$ mm, $w_4 = 0.3$ mm, $s_1 = s_2 = 0.2$ mm, $t_1 = t_2 = 1.89$ mm, $d = 0.7$ mm; $l_1 = 15.79$ mm, $l_2 = 17.5$ mm, $l_3 = 4.55$ mm, $l_4 = 10.42$ mm, $l_5 = 4$ mm, $l_6 = 18$ mm, $l_7 = 16.96$ mm, $l_8 = 17.56$ mm, $l_9 = 12.3$ mm, $l_{10} = 8.75$ mm, $l_{11} = 13.76$ mm, $l_{12} = 4.3$ mm, $l_{13} = 9.32$ mm, $l_{14} = 4$ mm, $w_0 = w_5 = 1.34$ mm, $w_1 = 0.2$mm, $w_2 = 0.76$ mm, $w_3 = 0.45$ mm, $w_4 = 0.3$ mm, $s_1 = s_2 = 0.2$ mm, $t_1 = t_2 = 1.89$ mm, $d = 0.7$ mm.

Figures 8-9 illustrate the simulated results of the two balanced filters with four/six transmission zeros (Simulated with ANSYS HFSS v.13.0). For the differential mode of balanced filter of *Structure I*, four simulated transmission zeros are located at 1.52, 2.23, 3.88 and 4.64 GHz, the in-band insertion loss is less than 0.5 dB with 3-dB bandwidth approximately 30.7% (2.54-3.46 GHz); for the common mode, the insertion loss is greater than 17 dB from 0 GHz to 8.5 GHz, indicating good wideband rejection. Moreover, for the differential mode of the balanced filter of *Structure II*, five simulated transmission zeros are located at 1.44, 2.29, 3.63, 4.1 and 4.87 GHz, the 3-dB bandwidth is 29% (2.44-3.31 GHz) with return loss greater than 13 dB (2.56-3.34 GHz); for the common mode, over 15-dB common mode suppression is achieved from 0 GHz to 8.92 GHz.

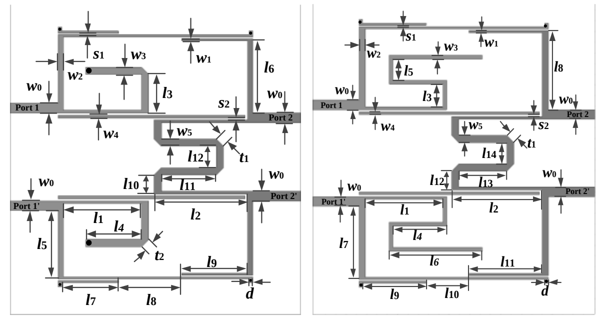

(a) (b)

Fig. 7. Geometries of two proposed balanced filters: (a) *Structure I*, and (b) *Structure II*.

III. MEASURED RESULTS AND DISCUSSIONS

For comparisons, the measured *S*-parameters of the two balanced filters are also illustrated in Figs. 8-9. For the differential mode of the balanced filter of *Structure I*, the 3-dB bandwidth is 31.3% (2.57-3.51 GHz) with return loss greater than 13 dB, four measured transmission zeros are located at 1.03, 2.32, 3.9 and 4.63 GHz, the insertion loss in the passband is less than 0.6 dB and greater than 20 dB from 3.75 to 8.9 GHz ($2.97f_0$); for the common mode, the insertion loss is greater than 15 dB from 0 GHz to 8.8 GHz ($2.93f_0$). For the differential mode of the balanced filter of *Structure II*, six measured transmission zeros are located at 1.21, 1.61, 2.26, 3.72, 4.14 and 4.96 GHz with 3-dB bandwidth of 32% (2.48-3.44 GHz), the insertion loss is less than 0.7 dB with return loss greater than 10 dB from 2.4 GHz and 3.53 GHz, an upper stopband with insertion loss greater than 20 dB is realized from 3.59 to 8.94 GHz ($2.98f_0$); in addition, the insertion loss for the common mode is greater than 15 dB from 0 to 9 GHz ($3f_0$). The slight frequency discrepancies of measured passbands for the differential mode are mainly caused by the imperfect soldering skill of the shorted stubs and folded transmission line of the two balanced filters.

To further illustrate the characteristics of the two balanced filters, Table 1 illustrates the comparisons of measured results for several balanced filter structures. Compared with other balanced filters [3]-[12], more transmission zeros near the passband are obtained for the two balanced filter structures, and the upper stopbands for the differential mode of the two balanced filters stretch up to $2.97f_0$ ($|S_{dd21}|$<-20 dB) and $2.98f_0$ ($|S_{dd21}|$<-20 dB). The insertion losses are lower with 0.6 dB and 0.7 dB for the proposed balanced filters.

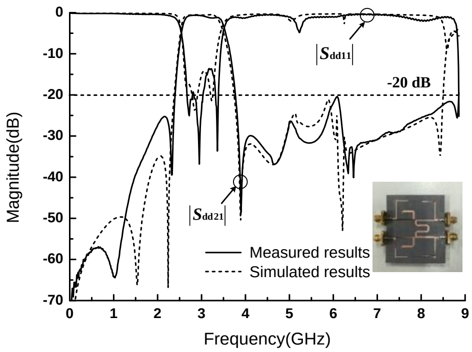

(a)

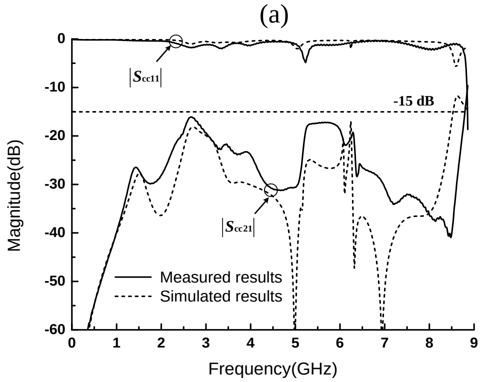

(b)

Fig. 8. Photograph, measured and simulated results of *Structure I*: (a) differential mode and (b) common mode.

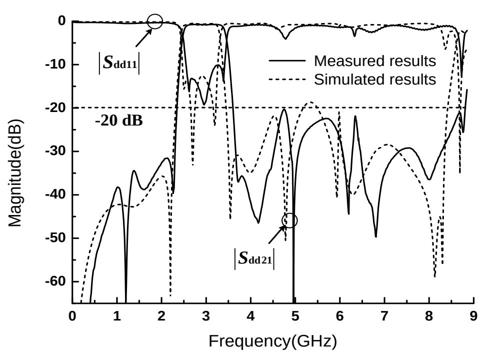

(a)

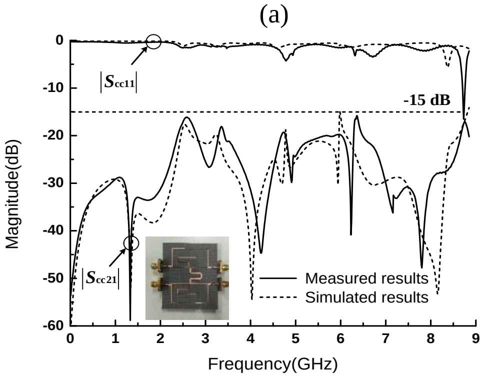

(b)

Fig. 9. Photograph, measured and simulated results of *Structure II*: (a) differential mode and (b) common mode.

Table 1: Comparisons of measured results for some balanced filters

Filter Structures	TZs, $\|S_{dd21}\|$ 0-2f_0, (f_0)	FBW $\|S_{dd21}\|$	Stopband $\|S_{dd21}\|$, dB	$\|S_{cc21}\|$, dB
Ref. [3]	0 (3.0 GHz)	110%	<-20, 2.2 f_0	<-15, (0-8)
Ref. [6] - II	2 (6.85 GHz)	70.7%	<-20, 2.77 f_0	<-13.5, (0-19.5)
Ref. [8]	4 (2.4 GHz)	17%	<-15, 2.75 f_0	<-18.8, (0-6.5)
Ref. [11] - I	3 (5.0 GHz)	67.6%	<-15, 2.7 f_0	<-15, (1.9-8.3)
Ref. [11] - II	5 (5.0 GHz)	37.8%	<-15,2.8 f_0	<-20, (1.2-9.3)
Ref. [12]	3 (3.0 GHz)	82%	<-15,2.1 f_0	<-10, (1.65-3.95)
Structure I	4 (3.0 GHz)	31.3%	<-20, 2.97f0	<-15, (0-8.8)
Structure II	6 (3.0 GHz)	32.0%	<-20, 2.98f0	<-15, (0-9)

IV. CONCLUSION

In this paper, two novel balanced filters based on transversal signal-interaction concepts with multiple transmission zeros are proposed. Four and six transmission zeros close to the differential mode passband can be easily achieved using the transversal signal-interaction concepts. In addition, wideband common mode suppression can easily realized by the multiple transmission zeros. High selectivity and wideband common mode suppression are obtained for the two balanced filters, indicating good candidates for microwave wireless applications.

ACKNOWLEDGMENT

This work is supported by the 2012 Distinguished Young Scientist awarded by the National Natural Science Foundation Committee of China (61225001), and by National Natural Science Foundation of China (6140010914), Natural Science Foundation of Jiangsu Province (BK20140791) and the 2014 Zijin Intelligent Program of Nanjing University of Science and Technology.

REFERENCES

[1] F. Broydé and E. Clavelier, “Crosstalk in balanced interconnections used for differential signal transmission,” *IEEE Trans. Circuits Syst. I, Reg. Papers*, vol. 54, no. 7, pp. 1562-1572, July 2007.

[2] T. B. Lim and L. Zhu, “A differential-mode wideband bandpass filter on microstrip line for UWB application,” *IEEE Microw. Wirel. Compon. Lett.*, vol. 19, no. 10, pp. 632-634, Oct. 2009.

[3] X. H. Wang, Q. Xue, and W. W. Choi, “A novel ultra-wideband differential filter based on double-sided parallel-strip line,” *IEEE Microw. Wireless Compon. Lett.*, vol. 20, no. 8, pp. 471-473, Oct. 2010.

[4] H. T. Zhu, W. J. Feng, W. Q. Che, and Q. Xue, "Ultra-wideband differential bandpass filter based on transversal signal-interference concept," *Electron. Lett.*, vol. 47, no. 18, pp. 1033-1035, Sep. 2011.

[5] J. Shi, C. Shao, J. X. Chen, Q. Y. Lu, Y. J. Peng, and Z. H. Bao, "Compact low-loss wideband differential bandpass filter with high common mode suppression," *IEEE Microw. Wireless Compon. Lett*., vol. 23, no. 9, pp. 480-482, Sep. 2013.

[6] W. J. Feng and W. Q. Che, "Novel wideband differential bandpass filters based on T-shaped structure," *IEEE Trans. Microw. Theory Tech.*, vol. 60, no. 6, pp. 1560-1568, June 2012.

[7] W. J. Feng, W. Q. Che, and Q. Xue, "Balanced filters with wideband common mode suppression using dual-mode ring resonators," *IEEE Trans. Circuits Syst. I*, vol. 62, no. 6, pp. 1499-1507, June 2015.

[8] L. L. Qiu and Q. X. Chu, "Balanced bandpass filter using stub-loaded ring resonator and loaded coupled feed-line," *IEEE Microw. Wireless Compon. Lett*., vol. 25, no. 10, pp. 654-656, Oct. 2015.

[9] Q. Y. Lu, J.-X. Chen, L.-H. Zhou, and H. Tang, "Novel varactor-tuned balanced bandpass filter with continuously high common-mode suppression," *ACES Jour.*, vol. 28, no. 7, pp. 628-632, July 2013.

[10] Q. Xiao, C. X. Zhou, "Design of balanced SIW filter with transmission zeroes and linear phase," *ACES Jour*., vol. 30, no. 9, pp. 1019-1023, Sep. 2015.

[11] W. J. Feng, X. Gao, W. Q. Che, W. C. Yang, and Q. Xue, "High selectivity wideband balanced filters with multiple transmission zeros," *IEEE Trans. Circuits Syst. II*, vol. PP, no. 99, pp. 1-1, May 2015.

[12] X. H. Wang, S. Hu, and Q. Y. Cao, "Differential broadband filter based on microstrip coupled line structures," *Electron. Lett.*, vol. 50, no. 15, pp. 1069-1070, July 2014.

[13] W. J. Feng, W. Q. Che, and Q. Xue, "Transversal signal interaction: Overview of high-performance wideband bandpass filters," *IEEE Microw. Magazine*, vol. 15, no. 2, pp. 84-96, Mar. 2014.

Wenjie Feng was born in Shangqiu, Henan Province, China, in 1985. He received the B.Sc. degree from the First Aeronautic College of the Airforce, Xinyang, China, in 2008, the M.Sc. and Ph.D. degrees from the Nanjing University of Science and Technology (NUST), Nanjing, China, in 2010, 2013.

From November 2009 to February 2010, March 2013 to September 2013, he was a Research Assistant with the City University of Hong Kong. From October 2010 to March 2011, he was an exchange student with the Institute of High-Frequency Engineering, Technische Universität München, Munich, Germany. He is currently an Associate Professor with the Nanjing University of Science and Technology, Nanjing, China. He has authored or co-authored over 110 internationally referred journal and conference papers. He has obtained the second class science and technology award and best dissertation award of Jiangsu Province in 2015. His research interests include ultra-wideband (UWB) circuits and technologies, substrate integrated components and systems, planar microstrip filters and power dividers, LTCC circuits.

Feng is a Reviewer for over twenty internationally referred journal and conference papers, including ten IEEE Transactions and three IEEE Letters. He now serves as an Associate Editor for the *International Journal of Electronics.*

Meiling Hong was born in Nantong, Jiangsu Province, China, in 1991. She received the B.E. degree from the Nanjing University of Science and Technology (NUST), Nanjing, China, in 2014. From September 2014, she went to Nanjing University of Science and Technology (NUST), Nanjing, China, for further study as a postgraduate. Her research interests include passive device and circuit.

Wenquan Che received the B.Sc. degree from the East China Institute of Science and Technology, Nanjing, China, in 1990, the M.Sc. degree from the Nanjing University of Science and Technology (NUST), Nanjing, China, in 1995, and the Ph.D. degree from the City University of Hong Kong (CITYU), Kowloon, Hong Kong, in 2003.

In 1999, she was a Research Assistant with the City University of Hong Kong. From March 2002 to September 2002, she was a Visiting Scholar with the Polytechnique de Montréal, Montréal, QC, Canada. She is currently a Professor with the Nanjing University of Science and Technology, Nanjing, China. From 2007 to 2008, she conducted academic research with the Institute of High Frequency Technology, Technische Universität München. During the summers of 2005–2006 and 2009–2012, she was with the City University of Hog Kong, as Research Fellow and Visiting Professor. She has authored or co-authored over 200 internationally referred journal papers and international conference papers. She has been a Reviewer for *IET Microwaves, Antennas and Propagation*. Her research interests include electromagnetic computation, planar/coplanar circuits and subsystems in RF/microwave frequency, microwave monolithic integrated circuits (MMICs) and medical application of microwave technology.

Che is a Reviewer for the IEEE Transactions on Microwave Theory and Techniques, IEEE Transactions on Antennas and Propagation, IEEE Transactions on Industrial Electronics, and IEEE Microwave and Wireless Components Letters. She was the recipient of the 2007 Humboldt Research Fellowship presented by the Alexander von Humboldt Foundation of Germany, the 5th China Young Female Scientists Award in 2008 and the recipient of Distinguished Young Scientist awarded by the National Natural Science Foundation Committee (NSFC) of China in 2012.